Improving the Quantification of Cerebral Haemodynamics using Optimally Sampled Arterial Spin Labelling MRI



Logan (Xin) Zhang

St. Cross College

University of Oxford

Supervisor: Michael Chappell

A thesis submitted for the degree of

Doctor of Philosophy

Trinity 2022

For both of my late grandfathers

Improving the Quantification of Cerebral Haemodynamics using Optimally Sampled Arterial Spin Labelling MRI

Logan (Xin) Zhang

St Cross College, University of Oxford

A thesis submitted for the degree of Doctor of Philosophy

Trinity 2022

Abstract

Arterial spin labelling (ASL) is a non-invasive magnetic resonance imaging (MRI) technique that utilises arterial blood water as an endogenous tracer to measure cerebral blood flow (CBF). While the ASL white paper recommends the clinical use of a single post-labelling delay (PLD) pseudo-continuous ASL (pCASL) method to robustly quantify CBF, there has been a growing body of research on multi-delay ASL which provides the ability to estimate for parameters other than CBF.

A framework applying optimal sampling strategy (OSS) to multi-PLD pCASL sequences has been developed to obtain optimised protocols by minimising the estimation uncertainty on both CBF and arterial transit time (ATT) or CBF only. Although this framework is flexible for designing ASL protocols with a variable number of target parameters, it adopted an idealised kinetic model and used a narrow range of prior values in the optimisation, rendering the optimised protocols susceptible to various sources of error during estimation.

This thesis seeks to systematically investigate the estimation sensitivity of existing optimised protocols to a number of physiological effects that are not accounted for in the idealised model. Additionally, it aims to extend the current framework and develop novel protocols optimised for both delay and echo times to improve the estimation of blood-brain barrier (BBB) water exchange.

Firstly, four pCASL protocols were examined for CBF and ATT estimation performance with the effects of flow dispersion, macrovascular signal contamination (MVC), and prolonged ATT. It was found that the protocol optimised for CBF estimation had the lowest CBF sensitivity to MVC, and extended kinetic models were beneficial to control for the presence of these effects. Results from simulation were validated using a previously acquired *in vivo* dataset.

Next, parameter sensitivity to MVC were evaluated for a comprehensive set of protocols optimised for CBF estimation. A wide range of tissue and macrovascular transit time ground truths was considered, and different assumptions regarding the relationship between the two transit times were compared and discussed. The resulting sensitivity maps further illustrated the benefit of adding an extra compartment in the analysis to account for MVC and could be used for data interpretation.

Finally, the OSS framework was extended to enable the combined optimisation of PLD and TE in multi-TE pCASL to measure water exchange time, $Texch$, across the BBB. Protocols were optimised with different optimality criteria under two multi-TE schemes and evaluated in terms of their theoretical estimation root-mean-square errors (RMSEs) using simulation. While the optimised protocols resulted in lower RMSEs of corresponding parameter estimation, reliably detecting a pathological level of $Texch$ change in an individual using the optimised protocols within five minutes remains challenging.

Acknowledgements

On 26th September 2018, the day I got off the plane from Beijing to London Heathrow Airport, I had little knowledge about what the four-year DPhil programme in Oxford encompasses, I was not sure how my journey in a completely foreign country will pan out, and I certainly would not have envisaged a global pandemic that rendered nearly everything to a halt - or online. Nonetheless I am fortunate. In an extremely difficult time for everyone, I was able to continue my pursuit for my dream since a very young age - a doctorate degree - not only as a title, but as an attitude: a rigorous, critical, learning attitude to any matter at hand. However, it is only possible with the tremendous help I received from a multitude of parties throughout the years, for which here I will acknowledge with my deepest gratitude.

First and foremost, I would like to express my most sincere gratefulness to my DPhil supervisor Michael Chappell. Like the ancient Chinese saying that goes ‘a teacher for a day is like a father for a lifetime’, Michael could not have been a more important figure in my DPhil, being an unstinting source of patience, guidance, and support. He is always able to explain intricate concepts in the simplest terms. He is constantly encouraging and inspiring new ideas and is happy to give me the freedom to pursue in topics and areas I feel most comfortable with. I can always rely on him to come back with timely and helpful comments on my writing. I almost attended every public lecture he gave about ASL - at conferences or FSL courses - which are more or less the same in nature, but each time I listen I could gain more knowledge from him. Following him to Nottingham was a big - but the right - choice I made in my second year, which opens up to me the diversity of experiences and great opportunities I would otherwise miss. I could never hope for a better, more understanding, and more professional supervisor than Michael.

I also cherished the time I have spent with my fellow labmates at PhysImAls, or formerly QuBIc, both at Oxford and Nottingham, in IBME and PI Beacon, in-person and on MS Teams. I always see people that came into the group earlier than me as role models: Martin Craig, Paula Croal, Tom Kirk, Flora Kennedey McConnell, Yuriko Suzuki, Jack Toner, Joe Woods, and Moss Zhao. They all have done amazing works and I have learned from all of them, be it programming, academic writing, or creative ideas, and I believe I still have a lot to learn. I also got great academic and moral support from my fellow Chinese labmates: Haodong He, Jian Hu, and Yechuan Zhang. Special thanks to Professors Stephen Payne, Thomas Okell and Daniel Bulte, who gave me a ton of useful comments on my paper and DPhil progression reports.

Some may envy historical and prestigious Oxford colleges with large spikes and quads, but never for a day have I regretted choosing St Cross College, a small but cosy college at the heart of Oxford. We have the best chefs and catering team and not once did they fail to deliver the most wonderful food and dining experiences. We also have the most responsive and caring staff members such as Lara Summerhill, Sharon Durno, Dr Joanna Ashbourn, and Professor Inge Daniels, the latter two of which were my personal tutors who gave me helpful zoom meetings during the pandemic.

Birds of a feather flock together. I am glad that despite the endless lockdowns, I managed to make friends along the way, who had given me invaluable emotional support throughout my DPhil. I am lucky to have shared a suite in Stonemason House with these

lovely persons: Deepak Kamlesh, Antonio Franchini, and Florian Titz. And a very special tribute goes to my amazing friend Sam Watkins who I got to know from a language buddy programme - miss our interesting discussions in the basement of St Cross Café. After moving to Nottingham, I am blessed to become friends with a group of wonderful people: Corine Cheong, Ruoyang Yuan, Lan Yao, and Wei Ye, with whom I spent a most unforgettable summer.

My parents in China provided me with the most unconditional love and support I can get in the world. Although we were being physically apart for more than 99% of the time during the four years, the numerous FaceTime calls constantly remind me that I always have their whole-hearted backup. I would not forget the joy on their face when I told them I got my first academic paper published. And my elder sister in the US - what a fabulous role model, an absolute paragon - no matter in life or in work. She is the earliest reason that I choose academia, and the person from whom I adopted the virtue of life-long learning. I will always look up to her as an inspiration.

Perhaps the most drastic change of lifestyle in ways I would never have imagined during my DPhil - or at all - is the addition of two new non-human family members: Nana and Hachi. The cute little (and huge) balls of fur always kept me company when I was burning the midnight oil. Also, I could not have emotionally gone through the lockdowns if it were not for their therapeutic cuddles and entertaining zoomies.

And last but not least, perhaps the not least of them all, my loving and beloved Ronnie Yan. Words fail to describe how I am indebted to you for your taking care of me when I was dealing with the passing of my grandfathers, when I was contracted with COVID, and other countless times when I was stressed about my academic progression. I simply cannot finish without your continuous love and affection bringing out the best of me. DPhil is hard, and life is hard, but being married to you in a lockdown wedding makes a hard time less intolerable. I will forever live up to our commitment to each other on our wedding - till death do us part.

Preface

List of Publications Arising from this Thesis

Journal Articles

1. **Zhang LX**, Woods JG, Okell TW, Chappell MA. Examination of optimized protocols for pCASL: Sensitivity to macrovascular contamination, flow dispersion, and prolonged arterial transit time. *Magn Reson Med.* 2021;86(4):2208-2219

Conference Abstracts

1. **Zhang X**, Kennedy McConnell F, Woods JG, Okell TW, Chappell MA. Examination of optimised PLD protocols for pCASL accounting for dispersion and macrovascular contamination over a prolonged ATT range. In: *Proceedings of the 36th Annual Meeting of the ESMRMB, Rotterdam, NL.* 2019;32 (Suppl 1) S1–S105:S63
2. **Zhang XL**, Woods JG, Kennedy McConnell F, Okell TW, Chappell MA. Examination of optimised PLD protocols for pCASL: accounting for dispersion and macrovascular contamination over a prolonged ATT range. In: *Proceedings of the 2020 ISMRM & SMRT Virtual Conference & Exhibition.* p3287
3. **Zhang LX**, Chappell MA. Systematic investigation of the sensitivity of optimised pCASL protocols to macrovascular contamination. In: *Proceedings of the 2021 ISMRM & SMRT Annual Meeting & Exhibition.* p2718
4. **Zhang LX**, Chappell MA. Combined optimisation of delays and echo times for blood-brain barrier permeability measurements using multi-TE pCASL MRI. In: *Proceedings of Joint ISMRM-ESMRMB ISMRT 31st Annual Meeting, London, England.* 2022; p907

Table of Contents

Table of Contents **1**

1 Introduction **6**

1.1 Background **6**

1.2 Thesis outline **9**

1.3 References **11**

2 Literature review **15**

2.1 Principles of magnetic resonance imaging **15**

2.1.1 The NMR effect and RF excitation 15

2.1.2 The Bloch equation and relaxation 18

2.1.3 Spatial encoding 21

2.1.4 *K*-space and *k*-space filling techniques 25

2.1.5 Common pulse sequences 28

2.2 Perfusion imaging using arterial spin labelling MRI **33**

2.2.1 Quantification of the cerebral blood flow using MRI 33

2.2.2 Principles of arterial spin labelling (ASL) 35

2.2.3 Kinetic modelling in ASL 43

2.2.4 Applications of ASL 55

2.3 Optimal sampling strategy in arterial spin labelling MRI **57**

2.3.1 Assumptions 57

2.3.2 Optimality criterion 59

2.3.3 Prior knowledge 61

2.3.4 Applications of optimal sampling strategy 62

2.4 Measuring water permeability across the blood-brain barrier 64

2.4.1 Water transportation across the blood-brain barrier 64

2.4.2 Measuring BBB permeability to water using contrast agent-based methods 67

2.4.3 Measuring BBB permeability to water using arterial spin labelling 69

2.5 References 77

3 Sensitivity of optimised protocols to macrovascular contamination, flow dispersion, and prolonged arterial transit time 89

3.1 Introduction 89

3.2 Methods 90

3.2.1 Kinetic Modelling 90

3.2.2 Simulation Experiments 92

3.2.3 In Vivo Experiments 96

3.3 Results 98

3.4 Discussion 105

3.4.1 Macrovascular Contamination 105

3.4.2 Flow Dispersion Effects 109

3.4.3 Prolonged ATT 110

3.4.4 Results From 3D-Readout Protocols 112

3.4.5 Limitations 115

3.5 Conclusion 116

3.6 References **117**

4 Sensitivity map of optimised protocols to macrovascular contamination **119**

4.1 Introduction **119**

4.2 Methods **120**

4.2.1 Protocol selection 120

4.2.2 Simulation Experiments 121

4.2.3 Sensitivity metrics 123

4.3 Results **124**

4.3.1 Assumption-based results 124

4.3.2 Map-based results 129

4.4 Discussion **131**

4.5 Conclusion **135**

4.6 References **136**

5 Combined optimisation of delays and echo times for blood-brain barrier permeability measurements using multi-TE pCASL MRI **137**

5.1 Introduction **137**

5.2 Optimisation **140**

5.2.1 Theory 140

5.2.2 Schemes 141

5.2.3 Optimisation methods 142

5.2.4 Optimisation results.....144

5.3 Evaluation.....**150**

5.3.1 Evaluation methods.....150

5.3.2 Evaluation results.....151

5.4 Discussions.....**154**

5.4.1 Implications for estimating $Texch$ accurately using OSS.....154

5.4.2 The theoretical RMSE - scan duration curve using the UST mode.....155

5.4.3 Parameter choices in optimisation and simulation evaluation.....157

5.4.4 Limitations and future work.....159

5.5 Conclusion.....**161**

5.6 References.....**162**

6 Summary of Findings and Future Prospects.....**164**

6.1 Summary of Findings.....**164**

6.2 Future Prospects.....**166**

6.2.1 *In vivo* validation of the results.....166

6.2.2 Change of simulation conditions.....167

6.2.3 Incorporating other parameters in the optimal sampling framework.....168

6.2.4 Developing the programme for target-based protocol selection.....169

6.3 References.....**171**

Appendix A Parameter estimation errors and sensitivity maps to MVC of protocols.....**173**

A.1 CBF and ATT estimation errors under the assumption 'percentage'.....**173**

A.2 CBF and ATT estimation errors under the assumption 'fixed' ... 177

A.3 CBF and ATT estimation errors under the assumption 'fixed_interval' ... 181

A.4 CBF, ATT, and aBV sensitivity maps to MVC ... 185

A.5 ATT sensitivity maps to MVC according to different metrics ... 192

1 Introduction

1.1 Background

The brain is a highly vascularised organ that requires more than a fifth of total-body oxygen consumption to support its function, despite only occupying about two percent of body mass[1]. The amount of blood that traverses through the arterioles and capillary vessels and reaches the destined tissue, a process called perfusion, per unit tissue volume per unit time is quantified by the cerebral blood flow (CBF)[2]. Disruption of CBF is correlated with various neuropathology, including stroke[3–7], multiple sclerosis[8,9], vascular malformations[10–12], dementia[13–16], and Alzheimer's disease[16–19], as well as neurologic disorders such as depression[20–23], post-traumatic stress disorder[24,25], and schizophrenia[26–28], etc. Measuring CBF is of great clinical value in routine screening, diagnosis, treatment, and long-term follow-ups of such diseases.

Although ^{15}O-water positron emission tomography (PET) is considered the gold standard of regional cerebral perfusion imaging[29], the limited availability of on-site cyclotrons, ionising radiation, and its expensive price poses health and social concerns for the patients. Perfusion computed tomography (CT) and single photon emission computed tomography (SPECT) are more widely available clinically, but suffer from restricted anatomical coverage and low spatial resolution, respectively[30]. Magnetic resonance imaging (MRI) plays an increasingly important role in the clinical evaluation of CBF without the use of radioactive isotopes, by methods such as dynamic susceptibility contrast (DSC) MRI, dynamic contrast-enhanced (DCE) MRI, and arterial spin labelling (ASL). DSC- and DCE-MRI require the intravenous injection of a gadolinium-based contrast agent (GBCA) to induce a change in T2* susceptibility or T1,

respectively, in the blood and tissue. Nevertheless, there are concerns about gadolinium deposition in the brain[31] and nephrogenic systemic fibrosis[32]; GBCA is also contraindicated to certain kidney diseases[33]. In contrast, ASL uses radiofrequency (RF) pulses to magnetically label the protons (^{1}H) in the blood water molecules that act as endogenous tracers, making it a completely non-invasive technique to provide absolute CBF measurements.

Since Detre et al. first proposed the concept of 'spin tagging' more than two decades ago[34,35], the field of ASL has undergone significant development in trying to produce reproducible and quantitative CBF maps within a clinically feasible scan time. In 2015, the ISMRM Perfusion Study Group published the 'ASL white paper', a consensus standardising the clinical implementations of ASL in terms of acquisition, quantification, and quality control[36]. It acknowledged its intrinsically low signal-to-noise ratio (SNR), since ASL signal only accounts for 1~2% of total image contrast in the acquired image. For this reason, the white paper's recommended use of ASL in clinical settings is a robust single post-labelling delay (PLD) pseudo-continuous ASL (pCASL) technique, with CBF quantified by the general kinetic model by Buxton et al.[37] While this method generates a CBF map relatively insensitive to arterial transit time (ATT) by use of a long delay, there has been growing interest in multi-delay ASL that enables multi-parametric and multi-compartmental modelling of the ASL signal. By sampling different time points on the kinetic curve and fitting the kinetic model to the signal-time series, parameters other than CBF, such as ATT or the exchange time of water across the blood-brain barrier, $Texch$, can be estimated [38–44]. These perfusion-related parameters have been shown of their clinical significance as potential biomarkers for various diseases[45–47]. Hence, it would be beneficial to non-invasively measure such parameters

complementary to CBF using multi-delay ASL techniques with the precision needed for clinical evaluation.

Recently, a framework of optimal sampling strategy (OSS) was proposed that is based on minimising the estimation variance of the parameters by optimising the PLDs of pCASL protocols[48]. It effectively changed the sampling points on the pCASL kinetic curve to an optimised schedule, instead of using the conventional evenly-sampled multi-PLD layout. As a result, the optimised protocols offered higher estimation accuracy of the parameters of interest without the penalty of prolonging the scan duration. Nevertheless, the dependency of the optimisation on the kinetic model and prior parameter ranges makes the optimised protocols potentially susceptible to other physiological effects that are not accounted for in the Buxton model but may be present *in vivo*. Therefore, the estimation performance of optimised protocols in the presence of such effects needs to be systematically examined. Furthermore, while the framework is versatile in the ability to incorporate other variables to optimise for, such as the label duration[49], so far it has not been demonstrated the application of OSS to optimise $Texch$ estimation. Addressing these issues will contribute to elucidating the utility of OSS in ASL, with the goal of improving the quantification of parameters related to cerebral haemodynamics.

In summary, ASL is a promising non-invasive MRI technique that provides quantitative estimations of CBF and other perfusion-related parameters, but it suffers from inherently low SNR. Optimal sampling strategy has been used to obtain optimised multi-delay ASL protocols that minimise the estimation uncertainty of the parameters of interest. Research is needed to explore the wider practicality of OSS in its sensitivity to kinetic model assumptions and the estimation of additional physiological parameters.

1.2 Thesis outline

This thesis set out to explore the usage of optimal sampling strategy in ASL MRI outside the general kinetic model by Buxton et al.[37], by testing the estimation performance of existing optimised protocols under various physiological effects, and by restructuring the optimisation framework to optimise both for delays and echo times which aims to improve the measurement of water exchange time across the blood-brain barrier using multi-TE multi-PLD pCASL. The findings of this work contribute to the knowledge and application of optimal sampling strategy in multi-PLD pCASL, in the aspects of examining an optimised protocol of its estimation accuracy of the parameters of interest and the sensitivity to potential artefacts before scanning, and checking the theoretical boundaries of the root-mean square errors of estimating $Texch$ using optimised multi-TE pCASL protocols.

Chapter 2 offers a review of literature on MRI and ASL principles, with a focus on ASL kinetic modelling, optimal sampling strategy in the ASL context, and measuring water exchange across the BBB using ASL methods.

Chapter 3 examines the performance of optimised pCASL protocols under different physiological effects that one may encounter *in vivo*, including dispersion, macrovascular signal contamination, and prolonged tissue arrival time (ATT) using simulated signals and a previously acquired *in vivo* dataset. The mean and standard deviation of CBF and ATT estimation errors in each scenario are calculated, while recommendations for choosing optimised protocols prior to imaging are suggested.

Chapter 4 takes the metric designed in Chapter 3 that describes the CBF estimation sensitivity to intra-voxel macrovascular signal and further tests it on existing CBF-optimised time-encoded pCASL protocols using simulated signals over a wide range of macrovascular arrival time (ATT_a) and ATT ground truths. Sensitivity maps are

generated for each optimised protocol. Different assumptions of the relationship between the two arrival times are compared and discussed.

Chapter 5 applies the optimal sampling strategy in multi-TE multi-PLD pCASL to measure the pre-exchange lifetime of water molecules across the BBB, $Texch$. The current optimisation framework is extended to optimise for both post-labelling delays (PLDs) and echo times (TEs) under two readout schemes: T2-Relaxation Under Spin-Tagging (TRUST) and multi-TE 3D-GRASE (mTE-GRASE). While the resulting optimised protocols are evaluated for their theoretical RMSEs of estimating the parameters, the implications are drawn for $Texch$ estimation accuracy and detectability of change.

Chapter 6 summarises the main findings and conclusions of the previous chapters and proposes future working directions of the current study.

1.3 References

1. Kety SS, Schmidt CF. The nitrous oxide method for the quantitative determination of cerebral blood flow in man: theory, procedure and normal values. *Journal of Clinical Investigation*. 1948;27(4):476-483.
2. Liu TT. Perfusion Imaging with Arterial Spin Labeling MRI. In: *Brain Mapping*. Vol 1. Elsevier; 2015:149-154.
3. Wang DJJ, Alger JR, Qiao JX, et al. Multi-delay multi-parametric arterial spin-labeled perfusion MRI in acute ischemic stroke — Comparison with dynamic susceptibility contrast enhanced perfusion imaging. *Neuroimage Clin*. 2013;3:1-7.
4. Viallon M, Altrichter S, Pereira VM, et al. Combined use of pulsed arterial spin-labeling and susceptibility-weighted imaging in stroke at 3T. *Eur Neurol*. 2010;64(5):286-296.
5. Zaharchuk G, el Mogy IS, Fischbein NJ, Albers GW. Comparison of Arterial Spin Labeling and Bolus Perfusion-Weighted Imaging for Detecting Mismatch in Acute Stroke. *Stroke*. 2012;43(7):1843-1848.
6. Bokkers RPH, Hernandez DA, Merino JG, et al. Whole-Brain Arterial Spin Labeling Perfusion MRI in Patients With Acute Stroke. *Stroke*. 2012;43(5):1290-1294.
7. Hernandez DA, Bokkers RPH, Mirasol R v., et al. Pseudocontinuous arterial spin labeling quantifies relative cerebral blood flow in acute stroke. *Stroke*. 2012;43(3):753-758.
8. Paling D, Thade Petersen E, Tozer DJ, et al. Cerebral Arterial Bolus Arrival Time is Prolonged in Multiple Sclerosis and Associated with Disability. *Journal of Cerebral Blood Flow & Metabolism*. 2014;34(1):34-42.
9. Wengler K, Ha J, Syritsyna O, et al. Abnormal blood-brain barrier water exchange in chronic multiple sclerosis lesions: A preliminary study. *Magn Reson Imaging*. 2020;70(April):126-133.
10. Wolf RL, Wang J, Detre JA, Zager EL, Hurst RW. Arteriovenous shunt visualization in arteriovenous malformations with arterial spin-labeling MR imaging. *American Journal of Neuroradiology*. 2008;29(4):681-687.
11. Le TT, Fischbein NJ, André JB, Wijman C, Rosenberg J, Zaharchuk G. Identification of venous signal on arterial spin labeling improves diagnosis of dural arteriovenous fistulas and small arteriovenous malformations. *American Journal of Neuroradiology*. 2012;33(1):61-68.
12. Iv M, Fischbein NJ, Zaharchuk G. Association of Developmental Venous Anomalies with Perfusion Abnormalities on Arterial Spin Labeling and Bolus Perfusion-Weighted Imaging. *Journal of Neuroimaging*. 2015;25(2):243-250.
13. Gao YZ, Zhang JJ, Liu H, Wu GY, Xiong L, Shu M. Regional Cerebral Blood Flow and Cerebrovascular Reactivity in Alzheimer's Disease and Vascular Dementia Assessed by Arterial Spinlabeling Magnetic Resonance Imaging. *Curr Neurovasc Res*. 2012;10(1):49-53.
14. Robertson AD, Messner MA, Shirzadi Z, et al. Orthostatic hypotension, cerebral hypoperfusion, and visuospatial deficits in Lewy body disorders. *Parkinsonism Relat Disord*. 2016;22:80-86.

15. Taylor JP, Firbank MJ, He J, et al. Visual cortex in dementia with Lewy bodies: Magnetic resonance imaging study. *British Journal of Psychiatry*. 2012;200(6):491-498.
16. Schuff N, Matsumoto S, Kmiecik J, et al. Cerebral blood flow in ischemic vascular dementia and Alzheimer's disease, measured by arterial spin-labeling magnetic resonance imaging. *Alzheimer's & Dementia*. 2009;5(6):454-462.
17. Yoshiura T, Hiwatashi A, Noguchi T, et al. Arterial spin labelling at 3-T MR imaging for detection of individuals with Alzheimer's disease. *Eur Radiol*. 2009;19(12):2819-2825.
18. Binnewijzend MAA, Kuijer JPA, Benedictus MR, et al. Cerebral Blood Flow Measured with 3D Pseudocontinuous Arterial Spin-labeling MR Imaging in Alzheimer Disease and Mild Cognitive Impairment: A Marker for Disease Severity. *Radiology*. 2013;267(1):221-230.
19. Zhang N, Gordon ML, Goldberg TE. Cerebral blood flow measured by arterial spin labeling MRI at resting state in normal aging and Alzheimer's disease. *Neurosci Biobehav Rev*. 2017;72:168-175.
20. Colloby SJ, Firbank MJ, He J, et al. Regional cerebral blood flow in late-life depression: Arterial spin labelling magnetic resonance study. *British Journal of Psychiatry*. 2012;200(2):150-155.
21. Ho TC, Wu J, Shin DD, et al. Altered Cerebral Perfusion in Executive, Affective, and Motor Networks During Adolescent Depression. *J Am Acad Child Adolesc Psychiatry*. 2013;52(10):1076-1091.e2.
22. Orosz A, Jann K, Federspiel A, et al. Reduced Cerebral Blood Flow Within the Default-Mode Network and Within Total Gray Matter in Major Depression. *Brain Connect*. 2012;2(6):303-310.
23. Lui S, Parkes LM, Huang X, et al. Depressive disorders: Focally altered cerebral perfusion measured with arterial spin-labeling MR imaging. *Radiology*. 2009;251(2):476-484.
24. Schuff N, Zhang Y, Zhan W, et al. Patterns of altered cortical perfusion and diminished subcortical integrity in posttraumatic stress disorder: An MRI study. *Neuroimage*. 2011;54(SUPPL. 1):S62-S68.
25. Li X, Spence JS, Buhner DM, et al. Hippocampal Dysfunction in Gulf War Veterans: Investigation with ASL Perfusion MR Imaging and Physostigmine Challenge 1. *radiology.rsna.org n Radiology*. 2011;261(1).
26. Ota M, Ishikawa M, Sato N, et al. Pseudo-continuous arterial spin labeling MRI study of schizophrenic patients. *Schizophr Res*. 2014;154(1-3):113-118.
27. Kindler J, Jann K, Homan P, et al. Static and dynamic characteristics of cerebral blood flow during the resting state in schizophrenia. *Schizophr Bull*. 2015;41(1):163-170.
28. Pinkham A, Loughead J, Ruparel K, et al. Resting quantitative cerebral blood flow in schizophrenia measured by pulsed arterial spin labeling perfusion MRI. *Psychiatry Res Neuroimaging*. 2011;194(1):64-72.
29. van Golen LW, Kuijer JPA, Huisman MC, et al. Quantification of cerebral blood flow in healthy volunteers and type 1 diabetic patients: Comparison of MRI arterial spin labeling and [15O]H2O positron emission tomography (PET). *Journal of Magnetic Resonance Imaging*. 2014;40(6):1300-1309.

30. Wintermark M, Sesay M, Barbier E, et al. Comparative Overview of Brain Perfusion Imaging Techniques. *Stroke*. 2005;36(9).
31. Pullicino R, Radon M, Biswas S, Bhojak M, Das K. A Review of the Current Evidence on Gadolinium Deposition in the Brain. *Clin Neuroradiol*. 2018;28(2):159-169.
32. Fraum TJ, Ludwig DR, Bashir MR, Fowler KJ. Gadolinium-based contrast agents: A comprehensive risk assessment. *Journal of Magnetic Resonance Imaging*. 2017;46(2):338-353.
33. Selby NM, Blankestijn PJ, Boor P, et al. Magnetic resonance imaging biomarkers for chronic kidney disease: a position paper from the European Cooperation in Science and Technology Action PARENCHIMA. *Nephrology Dialysis Transplantation*. 2018;33(suppl_2):ii4-ii14.
34. Detre JA, Leigh JS, Williams DS, Koretsky AP. Perfusion imaging. *Magn Reson Med*. 1992;23(1):37-45.
35. Detre JA, Zhang W, Roberts DA, et al. Tissue specific perfusion imaging using arterial spin labeling. *NMR Biomed*. 1994;7(1-2):75-82.
36. Alsop DC, Detre JA, Golay X, et al. Recommended implementation of arterial spin-labeled Perfusion mri for clinical applications: A consensus of the ISMRM Perfusion Study group and the European consortium for ASL in dementia. *Magn Reson Med*. 2015;73(1):102-116.
37. Buxton RB, Frank LR, Wong EC, Siewert B, Warach S, Edelman RR. A general kinetic model for quantitative perfusion imaging with arterial spin labeling. *Magn Reson Med*. 1998;40(3):383-396.
38. Gonzalez-At JB, Alsop DC, Detre JA. Cerebral perfusion and arterial transit time changes during task activation determined with continuous arterial spin labeling. *Magn Reson Med*. 2000;43(5):739-746.
39. Kramme J, Gregori J, Diehl V, et al. Improving perfusion quantification in arterial spin labeling for delayed arrival times by using optimized acquisition schemes. *Z Med Phys*. 2015;25(3):221-229.
40. Ishida S, Kimura H, Isozaki M, et al. Robust arterial transit time and cerebral blood flow estimation using combined acquisition of Hadamard-encoded multi-delay and long-labeled long-delay pseudo-continuous arterial spin labeling: a simulation and in vivo study. *NMR Biomed*. 2020;33(8):1-12.
41. Amemiya S, Watanabe Y, Takei N, et al. Arterial Transit Time-Based Multidelay Combination Strategy Improves Arterial Spin Labeling Cerebral Blood Flow Measurement Accuracy in Severe Steno-Occlusive Diseases. *Journal of Magnetic Resonance Imaging*. 2022;55(1):178-187.
42. Ohene Y, Harrison IF, Nahavandi P, et al. Non-invasive MRI of brain clearance pathways using multiple echo time arterial spin labelling: an aquaporin-4 study. *Neuroimage*. 2019;188:515-523.
43. Gregori J, Schuff N, Kern R, Günther M. T2-based arterial spin labeling measurements of blood to tissue water transfer in human brain. *Journal of Magnetic Resonance Imaging*. 2013;37(2):332-342.
44. Mahroo A, Buck MA, Huber J, et al. Robust Multi-TE ASL-Based Blood–Brain Barrier Integrity Measurements. *Front Neurosci*. 2021;15.

45. Rooney WD, Li X, Sammi MK, Bourdette DN, Neuwelt EA, Springer CS. Mapping human brain capillary water lifetime: High-resolution metabolic neuroimaging. *NMR Biomed*. 2015;28(6):607-623.
46. Soinne L, Helenius J, Tatlisumak T, et al. Cerebral hemodynamics in asymptomatic and symptomatic patients with high-grade carotid stenosis undergoing carotid endarterectomy. *Stroke*. 2003;34(7):1655-1661.
47. Kaneko K, Kuwabara Y, Mihara F, et al. Validation of the CBF, CBV, and MTT values by perfusion MRI in chronic occlusive cerebrovascular disease. *Acad Radiol*. 2004;11(5):489-497.
48. Woods JG, Chappell MA, Okell TW. A general framework for optimizing arterial spin labeling MRI experiments. *Magn Reson Med*. 2019;81(4):2474-2488.
49. Woods JG, Chappell MA, Okell TW. Designing and comparing optimized pseudo-continuous Arterial Spin Labeling protocols for measurement of cerebral blood flow. *Neuroimage*. 2020;223(August):117246.

2 Literature review

2.1 Principles of magnetic resonance imaging

2.1.1 The NMR effect and RF excitation

An atomic nucleus is made of nucleons such as protons and neutrons that each possesses an intrinsic spin angular momentum (or spin). The net spin of the nucleus $\boldsymbol{J}$ is the vector sum of all angular momenta of its consisting nucleons, which is quantised to allow only certain values:

$$\boldsymbol{J} = \hbar \boldsymbol{I}, \qquad \text{(Equation 2.1.1)}$$

where $\boldsymbol{I}$ is the spin quantum number that takes zero, integers and half integers; $\hbar = \boldsymbol{h}/2\pi$, where $\boldsymbol{h}$ is the Planck constant.

The nuclear magnetic moment is also quantised:

$$\boldsymbol{\mu} = \gamma \boldsymbol{J} = \gamma \hbar \boldsymbol{I}, \qquad \text{(Equation 2.1.2)}$$

where γ is the gyromagnetic ratio of the nucleus. Only nuclei that have non-zero spin values can interact with an external magnetic field and can be used in magnetic resonance (MR) studies. The hydrogen nucleus (^{1}H) with a nuclear spin of 1/2 is used as the most common nucleus to generate the MR signal, since hydrogen has very high natural abundance across various tissues that constitute our body[1].

Consider a tissue voxel that contains a large quantity of hydrogen atoms. In the absence of an external magnetic field, each hydrogen nucleus has the same magnetic moment amplitude $|\boldsymbol{\mu}|$. However, the orientations of these magnetic moments are randomly distributed under thermal equilibrium to give a net magnetisation of zero within the voxel. When an external magnetic field $\boldsymbol{B_0}$ is applied (usually along the z-axis), hydrogen nuclei would start to precess about $\boldsymbol{B_0}$ with an angle, with the axis of the

precession parallel with $\boldsymbol{B_0}$. The precession frequency of the spins is proportional to the external field strength:

$$\boldsymbol{\omega_0} = -\gamma \boldsymbol{B_0}, \qquad \text{(Equation 2.1.3)}$$

where $\boldsymbol{\omega_0}$ is called Lamour frequency.

In addition to precession, protons would tend to align their magnetic moments with the external field $\boldsymbol{B_0}$. However, because the energy associated with aligning individual spin orientation with $\boldsymbol{B_0}$ is much less than the thermal energy (due to e.g., collisions between nuclei) aiming to randomise the distribution of spin orientations, protons only gain a slightly higher tendency to orient towards the field direction, resulting in a small but non-zero net magnetisation $\boldsymbol{M}$ aligning with $\boldsymbol{B_0}$, as shown in Figure 2.1.1.

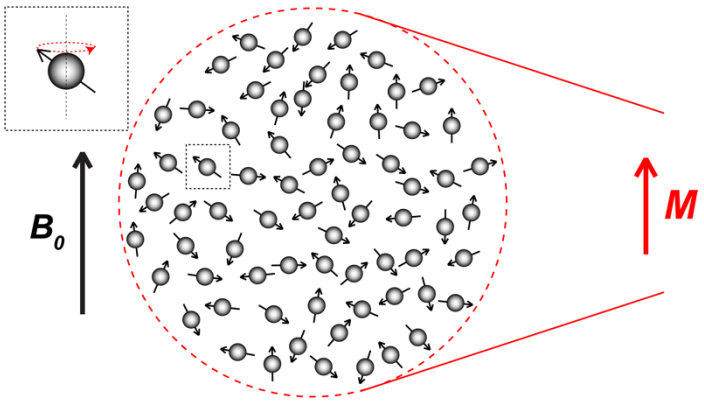


Figure 2.1.1 In the presence of an external magnetic field $\boldsymbol{B_0}$, magnetic moments of the proton spins that are previously randomly distributed start to precess in the field direction (figure shows the precession direction of one proton), and have a slightly higher tendency to align towards the direction of $\boldsymbol{B_0}$, forming a net magnetisation $\boldsymbol{M}$.

Without additional sources of energy, both the amplitude and the orientation of $\boldsymbol{M}$ are constant with time at equilibrium. When an oscillating magnetic field $\boldsymbol{B_1}$ perpendicular to $\boldsymbol{B_0}$ is present through the application of a radiofrequency (RF) pulse, $\boldsymbol{M}$ is tipped out of alignment with $\boldsymbol{B_0}$ and starts to precess around $\boldsymbol{B_0}$. However, the amplitude of $\boldsymbol{M}$ and the relative orientation of the spins are preserved, demonstrated in

Figure 2.1.2. The condition for this *resonance* of hydrogen nuclei to occur is that the frequency ω_0 of the RF pulse matches the Lamour frequency of the spins:

$$\omega_0 = \gamma B_0. \qquad \text{(Equation 2.1.4)}$$

This phenomenon is called the nuclear magnetic resonance (NMR) effect, and this process is also called RF excitation. The degree of rotation of $\boldsymbol{M}$ by excitation is known as the flip angle (FA) of the RF pulse. Specific flip angles can be achieved by carefully calibrating the amplitude and the duration of the RF pulse. For example, a 90° pulse tips the net magnetisation $\boldsymbol{M}$ to the transverse plane (Figure 2.1.2b), while after a 180° pulse $\boldsymbol{M}$ is tipped fully antiparallel with $\boldsymbol{B_0}$ (Figure 2.1.2c). The change of magnetisation in the transverse plane $M_\perp$ will induce a voltage in the receiver coil perpendicular to the transverse plane, according to Faraday's law of induction, which constitutes the detected NMR signal.

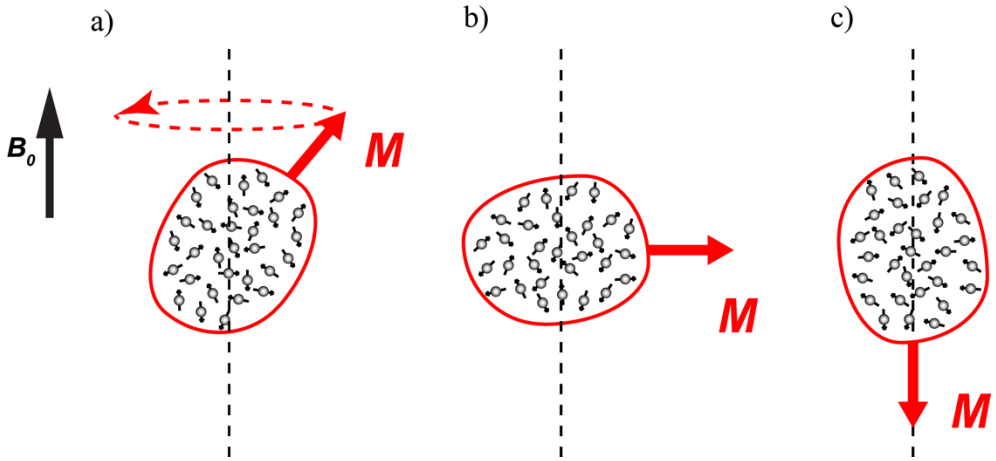


Figure 2.1.2 Different flip angles (FA) resulted from the oscillating magnetic field $\boldsymbol{B_1}$ during RF excitation, which preserves the amplitude of $\boldsymbol{M}$ and relative spin orientations. The red dashed line indicates the precession direction of $\boldsymbol{M}$. The direction of $\boldsymbol{B_1}$ is perpendicular to the figure plane and points towards the reader. (a) Arbitrary FA; (b) FA=90°; (c) FA=180°.

2.1.2 The Bloch equation and relaxation

The change of nuclear magnetisation $\boldsymbol{M}$ can be described by the Bloch equation[2], which in the laboratory frame of reference takes the form of:

$$\frac{d\boldsymbol{M}}{dt} = \gamma(\boldsymbol{M} \times \boldsymbol{B}) - \frac{M_x\boldsymbol{i} + M_y\boldsymbol{j}}{T_2} - \frac{M_z - M_0}{T_1}\boldsymbol{k}, \qquad \text{(Equation 2.1.5)}$$

where $\boldsymbol{B} = \boldsymbol{B_0} + \boldsymbol{B_1}$ when the RF pulse is switched on, and $\boldsymbol{B} = \boldsymbol{B_0}$ when the RF pulse is switched off; M_x, M_y and M_z are the components of $\boldsymbol{M}$ along the x-, y-, and z-axis, respectively; M_0 is the amplitude of $\boldsymbol{M}$ at equilibrium state before RF excitation; $\boldsymbol{i}$, $\boldsymbol{j}$, and $\boldsymbol{k}$ are unit vectors along the three axes.

Felix Bloch introduced two characteristic time constants T_1 and T_2 in Equation 2.1.5 to describe the process of nuclear spin relaxation in the longitudinal and transverse directions, respectively, after the RF pulse is switched off. T_1 is called the spin-lattice relaxation time, for during this process high-energy spins release energy into the surrounding molecular lattice, causing the longitudinal magnetisation M_z to recover back to M_0. T_1 is the time for M_z to recover to 63% of its original value. In the meantime, the energy from high-energy spins can also be transferred to other spins, leading to the loss of spin phase coherence. As a result, the transverse magnetisation $M_\perp$ begins to decrease. T_2, also termed spin-spin relaxation time, refers to the time for $M_\perp$ to have 37% left of its original value. T_2 decay is usually 5-10 times faster than T_1 decay[3]. Furthermore, dephasing of the spins may also occur due to $\boldsymbol{B_0}$ field inhomogeneities, causing an even faster T_2^* decay with the relation:

$$\frac{1}{T_2^*} = \frac{1}{T_2} + \frac{1}{2\gamma\Delta B_0}, \qquad \text{(Equation 2.1.6)}$$

where ΔB_0 is the variation of the magnetic field in parts per million (ppm).

The Bloch equation can be simplified when viewed in a rotating frame of reference with the same z-axis and an angular frequency $\omega = \omega_0$ in the transverse plane

relative to the stationary frame of reference. In the rotational frame, the Bloch equations can be expressed as:

$$\frac{dM_z}{dt} = -\frac{M_z - M_0}{T_1}, \qquad \text{(Equation 2.1.7)}$$

$$\frac{dM_\perp}{dt} = -\frac{M_\perp}{T_2}.$$

The solution to Equations 2.1.7 using a 90° pulse is an exponentially decaying signal in the transverse plane called the free induction decay (FID) signal:

$$M_z = M_0\left(1 - e^{-\frac{t}{T_1}}\right), \qquad \text{(Equation 2.1.8)}$$

$$M_\perp = M_{\perp max} e^{-\frac{t}{T_2}}.$$

In the laboratory frame of reference, the FID signal is an oscillating attenuating signal (Figure 2.1.3a) with a centre frequency ω_0 in the frequency domain (Figure 2.1.3b). If a 180° pulse is applied after a time duration τ following the FID signal, the phase of the spins is reversed, refocusing the transverse magnetisation after another duration τ, shown in Figure 2.1.4. This reappearing signal is known as the spin echo (SE). The time between the excitation pulse and the peak of the echo is the echo time (TE), while the time between consecutive excitation pulses is the repetition time (TR). TE and TR are fundamental parameters of an MR pulse sequence, for they control the extent of relaxation in the transverse and longitudinal directions, respectively. Since T_1 and T_2 values are tissue-specific, using different combinations of TE and TR can provide contrast in T1-weighted, T2-weighted, and proton-density (PD) weighted MR images (Figure 2.1.5).

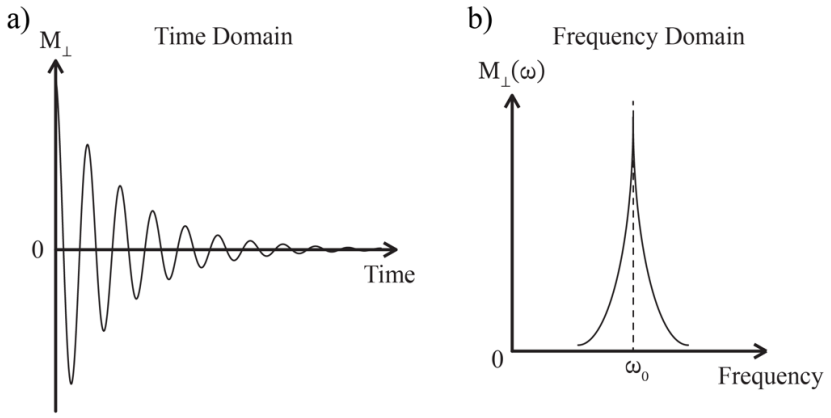


Figure 2.1.3 The free induction decay (FID) signal in the laboratory frame in (a) the time domain and (b) the frequency domain.

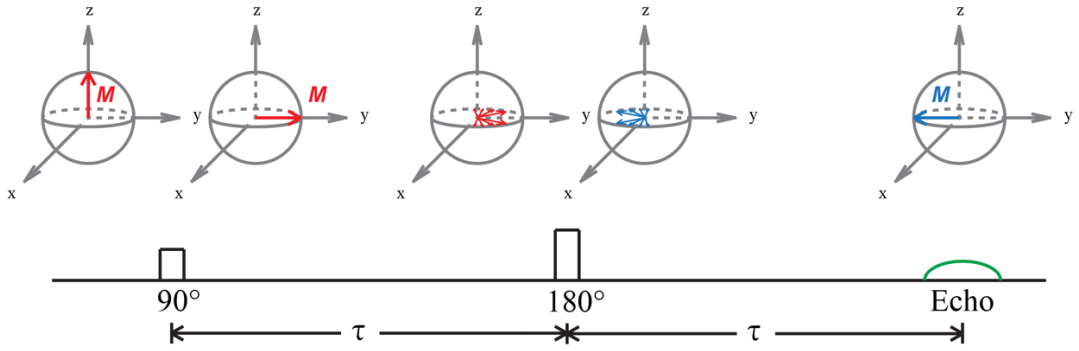


*Figure 2.1.4 Spin echo (SE) formation. Following the 90° excitation pulse, the magnetisation **M** is tipped to the transverse plane (red) and each spin constituting **M** start to lose phase coherence. After time τ, a 180° pulse is applied to add a 180° phase shift to each dephasing spin. Because the precession direction stays the same, the spins begin to regain phase coherence and, after the exact same time τ, recovers the transverse magnetisation (blue) and generates the spin echo (green).*

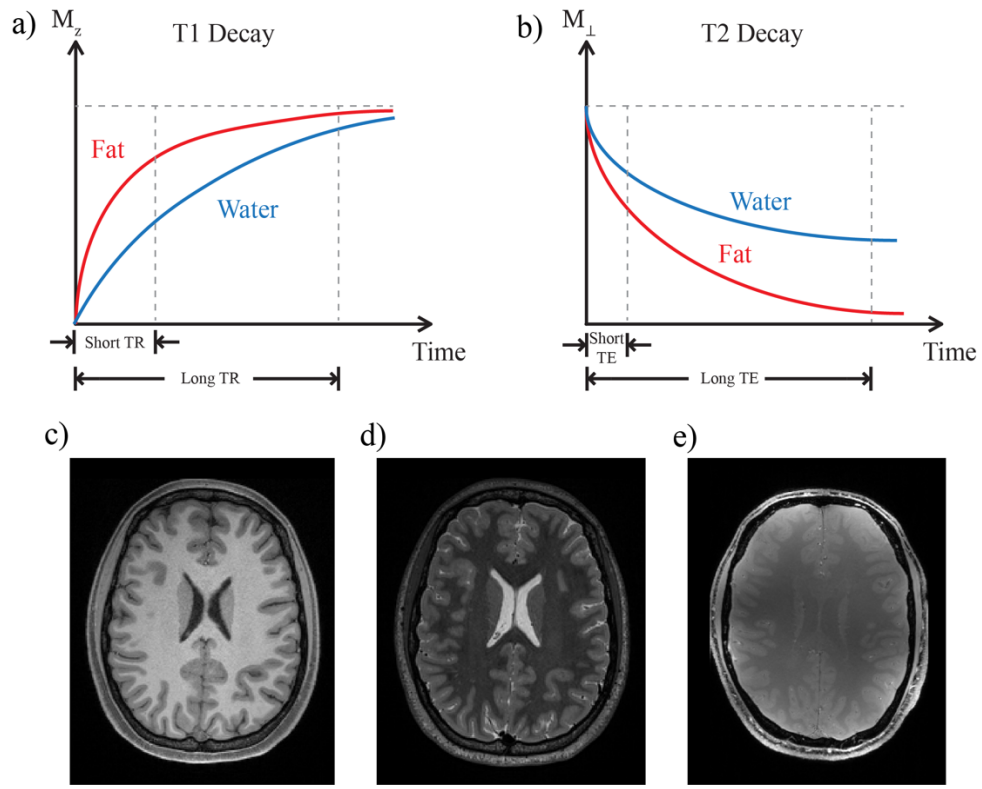


Figure 2.1.5 Characteristic T1 and T2 decay (a) and (b) in fat (red) and water (blue) providing different contrast images. (c) Short TR and short TE generate T1-weighted image. (d) Long TR and long TE generate T2-weighted image. (e) Long TR and short TE generate PD-weighted image, where the MR signal depends predominantly on the density of the protons, instead of T1 and T2 contrast between tissues.

2.1.3 Spatial encoding

As explained in Section 2.1.1, the resonance frequency ω_0 of the nuclear spins is associated with the strength of the external magnetic field. To spatially differentiate the signal contribution from the spins within different parts of the tissue, we could add linear gradients superimposed to the main field $\boldsymbol{B_0} = B_0\boldsymbol{k}$, creating a varying field strength dependent on the spatial location of the spins:

$$\boldsymbol{B_i} = \boldsymbol{B_0} + (\boldsymbol{G}\cdot\boldsymbol{r})\boldsymbol{k} = (B_0 + G_x\cdot x + G_y\cdot y + G_z\cdot z)\boldsymbol{k}, \quad \text{(Equation 2.1.9)}$$

where $\boldsymbol{G}$ is a vector specifying the gradient, and $\boldsymbol{B_i}$ is the local magnetic field at position $\boldsymbol{r}$. The amplitude of the gradient field is normally ~1% of the main field. The spins at two positions with a displacement of $\Delta\boldsymbol{r}$ will have a difference in resonance frequency:

$$\Delta\omega = \gamma \Delta B_i = \gamma \boldsymbol{G} \cdot \Delta \boldsymbol{r}. \qquad \text{(Equation 2.1.10)}$$

The first step of spatial encoding in MRI is called slice selection. Using a combination of G_x, G_y, and G_z, we could form a slice selective gradient $\boldsymbol{G_{SS}}$ with arbitrary amplitude and orientation. When an RF excitation pulse with a central frequency ω_c and a narrow bandwidth $\Delta\omega_{SS}$ is applied, only spins within a slice perpendicular to $\boldsymbol{G_{SS}}$ can absorb RF energy and achieve resonance, as shown in Figure 2.1.6. The location of the slice is determined by ω_c, whereas the thickness of the slice is determined by G_{SS} for a fixed transmit bandwidth $\Delta\omega_{SS}$, according to Equation 2.1.10:

$$\Delta\omega_{SS} = \gamma \cdot G_{SS} \cdot thickness. \qquad \text{(Equation 2.1.11)}$$

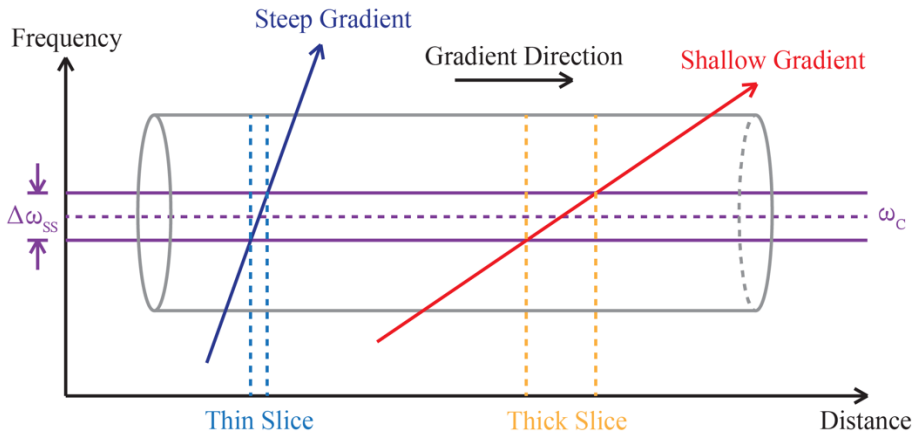


Figure 2.1.6 Slice selection process. With a constant central frequency ω_c and bandwidth $\Delta\omega_{SS}$, a steep gradient (blue) selects a thin slice while a shallow gradient (red) selects a thick slice. The slice is perpendicular to the gradient direction.

The slice direction is commonly chosen according to the orientation of the imaging tissue of interest. In brain MRI, the slice direction can be perpendicular to the x-, y-, or z-axis for sagittal, coronal, and axial view of the brain, respectively (Figure 2.1.7).

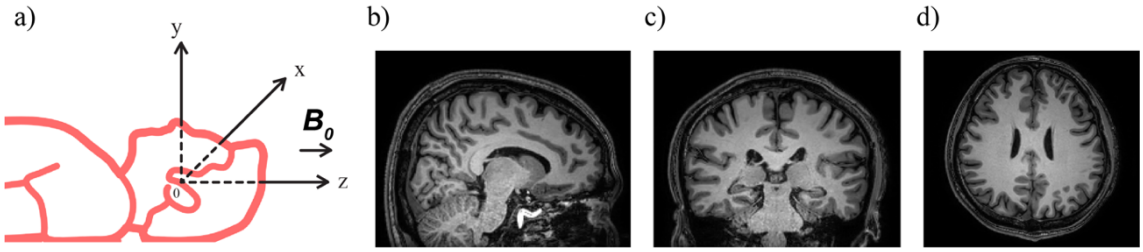


Figure 2.1.7 (a) The common axes used in brain MRI. Slice selection gradient along the x-, y- and z-axis leads to (b) sagittal, (c) coronal, and (d) axial view of the brain, respectively.

After defining an imaging slice, the localisation of spins along the other two orthogonal directions within the slice is accomplished by frequency encoding and phase encoding (Figure 2.1.8). The frequency encoding gradient, also known as the readout gradient $\boldsymbol{G_{RO}}$, is applied when the spin echo is forming after a 180° refocusing pulse. Similar to the slice selection process, spins originally precessing at the same resonance frequency ω_0 within the slice will slightly change in their precession frequency $\Delta\omega_{RO}$ based on the spin position. For a given receiver bandwidth of the receiver coil, which usually equals to the Nyquist sampling frequency ω_{NQ} of the image, the field-of-view FOV_{RO} along the frequency encoding direction is inversely proportional to the gradient amplitude:

$$2\omega_{NQ} = \gamma \cdot G_{RO} \cdot FOV_{RO}. \qquad \text{(Equation 2.1.12)}$$

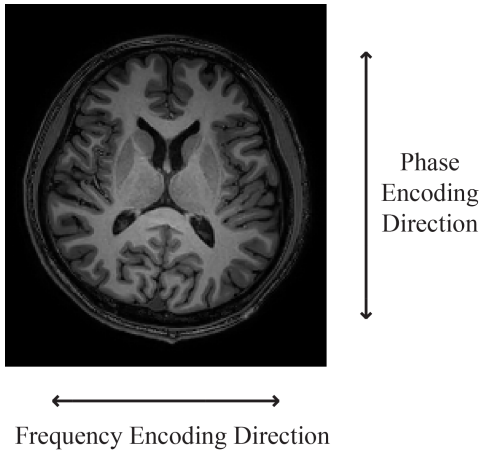


Figure 2.1.8 Frequency encoding and phase encoding directions shown in an image slice.

To separate the signals from the spins that have the same precession frequency in each readout line, different phase encoding gradients G_{PE} are administered alongside but perpendicular to G_{RO}. The application of G_{PE} will increase or decrease the precession frequency of the spins along the phase encoding direction, generating a phase shift $\Delta\phi$ when G_{PE} is switched off:

$$\Delta\phi = \gamma \cdot G_{PE} \cdot l \cdot t, \qquad \text{(Equation 2.1.13)}$$

where t is the duration of the gradient pulse, and l is the distance of the spin from the isocentre. The phase encoding process contains a number of steps N_{PE}, and in each step the spins at the edge of the phase encoding field-of-view FOV_{PE} will have a 180° phase shift from the last step, with spins close to the isocentre having less phase shift accordingly (Figure 2.1.9). After all steps, N_{PE} signals will be recorded, forming N_{PE} independent equations about the spins in each readout line. The maximum number of voxels that can be decoded along the phase-encoding direction is thus N_{PE}, and the size of each voxel VOX_{PE} is:

$$VOX_{PE} = FOV_{PE}/N_{PE}. \qquad \text{(Equation 2.1.14)}$$

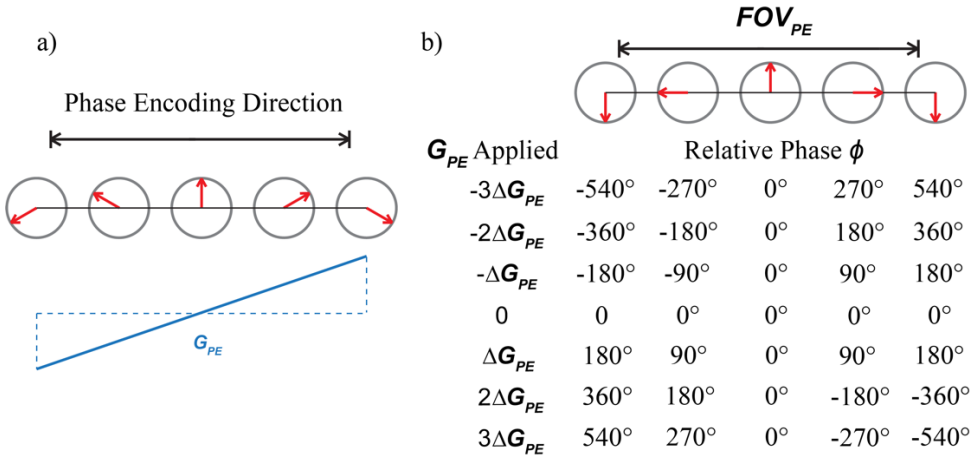


Figure 2.1.9 Phase encoding. (a) Five evenly spaced spins along the phase encoding direction will be introduced a phase shift $\Delta\phi$ between each two adjacent spins during the application of G_{PE}, where the centre spin does not change its phase. (b) Different G_{PE} are applied in each phase encoding step, with the spins at the edge of the field-of-view having a 180° phase ship from the previous step.

In a traditional multi-slice 2D MRI, signals from different spatial locations can be differentiated using slice selective, frequency encoding, and phase encoding gradients[4]. Higher signal-to-noise ratio (SNR) achieved from more contiguous slices can be realised using 3D MRI, where in the slice selective process, a thick volume instead of thin slices is excited by the RF pulse. A second phase encoding gradient $\boldsymbol{G_{PE2}}$ with N_{PE2} steps is added to the original slice selection direction during image readout to differentiate the signal contribution along that direction.

2.1.4 *K*-space and *k*-space filling techniques

For a given slice, the MR signal after each readout (or the 'raw data') is stored in a data matrix called *k*-space. The number of rows in *k*-space corresponds to the number of phase encoding steps, while the number of columns corresponds to the number of sampling points after digitisation in the frequency encoding direction. Each time a phase encoding gradient is selected, MR signals collected from the receiver coils experience frequency and amplitude modulation and analogue-to-digital conversion (ADC), eventually filling one row in *k*-space in each TR. The total scan time of an MR sequence is therefore proportional to TR and the number of phase encoding gradients used. Data with a lower $\boldsymbol{G_{PE}}$ amplitude is saved in the central rows of *k*-space, capturing features with low spatial frequencies within the slice, i.e., the main contrast in the image. On the other hand, data with a higher $\boldsymbol{G_{PE}}$ amplitude in the negative and positive polarities is saved in the bottom and upper rows of *k*-space, respectively, which represents features with high spatial frequencies, i.e., the edges and details in the image (Figure 2.1.10). The transformation from *k*-space to the native space is achieved by Inverse Fourier Transform (IFT).

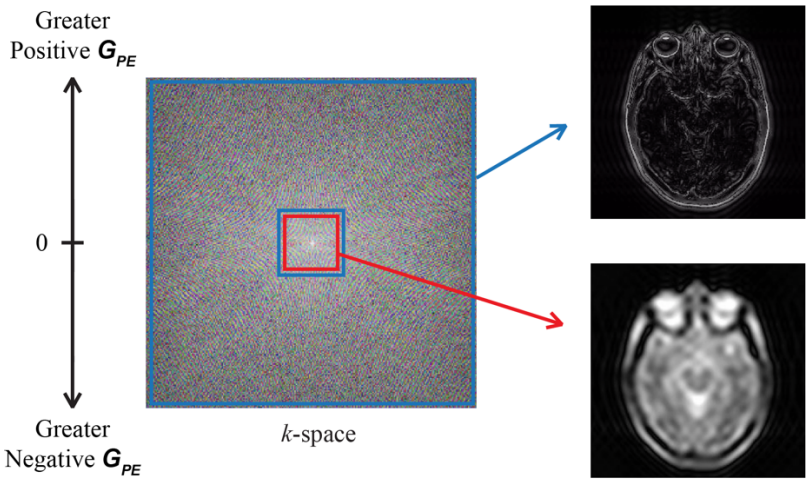


Figure 2.1.10 The relationship between phase encoding gradient $\boldsymbol{G_{PE}}$, k-space, and features in the image.

In the simplest form of data collection, the whole *k*-space is filled sequentially by each row from the most negative $\boldsymbol{G_{PE}}$ to the most positive $\boldsymbol{G_{PE}}$, and from the most negative $\boldsymbol{G_{RO}}$ to the most positive $\boldsymbol{G_{RO}}$, leaving the centre of *k*-space sampled at half of the scan. To reduce the total scan time, partial Fourier and partial echo techniques can be used where only over half of the *k*-space rows are filled in the phase encoding and frequency encoding directions (Figure 2.1.11a and b), respectively, and the image is reconstructed using the conjugate symmetrical property of *k*-space[5–7]. However, there is a sacrifice of SNR in the reconstructed image due to less signal acquired in *k*-space. Another method to reduce scan time is by parallel imaging[8], in which multiple receiver coils are positioned in an array to fill multiple rows in *k*-space simultaneously within one TR (Figure 2.1.11c). Because each coil only samples a part of *k*-space when the sequence is finished, the final image is obtained either by extrapolation of the entire *k*-space or combining the individual image of each coil through de-aliasing methods. Nevertheless, the final image is prone to geometric aliasing causing voxels equidistant to a receiver coil to have lower SNR than voxels closer to a receiver coil.

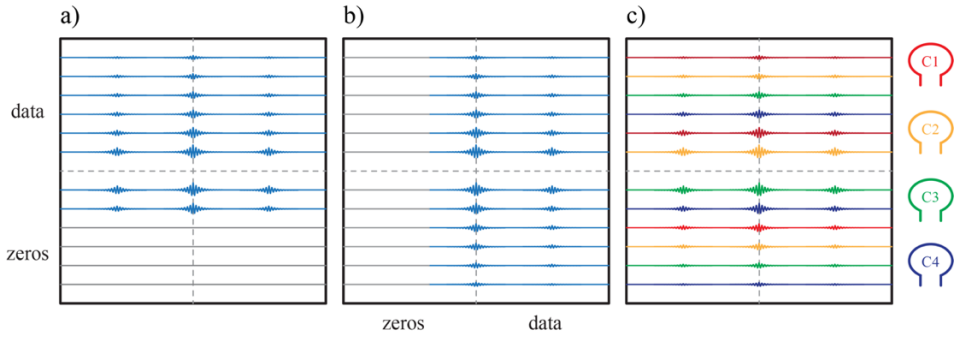


Figure 2.1.11 Time-saving k-space filling techniques. (a) Partial Fourier where k-space is sampled over half in the phase encoding direction. (b) Partial echo where k-space is sampled over half in the frequency encoding direction. (c) Parallel imaging where multiple k-space lines are filled simultaneously.

It is also possible to achieve contrast control by using other *k*-space traversal methods[9]. For example, centric filling and spiral filling start at the centre of *k*-space and work out on the peripheral in a rectilinear or spiral fashion (Figure 2.1.12a and b), respectively. Since the centre of *k*-space that contains high-signal intensity data is sampled first, it allows for fast contrast visualisation, especially beneficial in contrast-enhanced MR angiography (MRA). Alternatively, radial filling, provided by a constant $\boldsymbol{G_{RO}}$ amplitude but changing $\boldsymbol{G_{RO}}$ directions, traverses the centre of *k*-space in every acquisition (Figure 2.1.12c), giving each filling line the same SNR contribution to the final image. Because the centre is more densely sampled than the peripheral, radial filling techniques gives better image contrast in a short scan time and are relatively insensitive to motion artefacts. However, re-gridding of the raw data into a Cartesian matrix is required prior to the IFT to reconstruct the image.

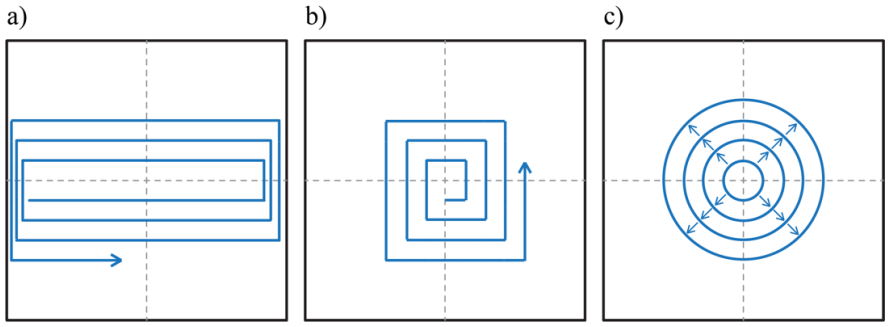


Figure 2.1.12 Other k-space filling techniques. (a) Centric filling; (b) spiral filling; (c) radial filling.

2.1.5 Common pulse sequences

As mentioned above, the MR signal comes from the induced voltage change by the refocused transverse magnetisation, i.e., the echo. An MR pulse sequence consists of a series of RF pulses and gradients that are carefully timed to achieve the desired echo. There are commonly two ways of generating an echo: using a 180° refocusing pulse or using a refocusing gradient, which corresponds to the spin-echo (SE) pulse sequence[10] or the gradient-echo (GRE) pulse sequence[11], respectively.

The basic spin echo sequence is shown in Figure 2.1.13, which has been explained in Section 2.1.2. Only one 180° refocusing pulse is applied within each TR to form one echo at TE. The simple SE sequence can produce good image quality and is considered the gold standard for generating image contrast and weighting. However, long scan time is required to repeat each TR through all phase encoding steps to fill the entire *k*-space.

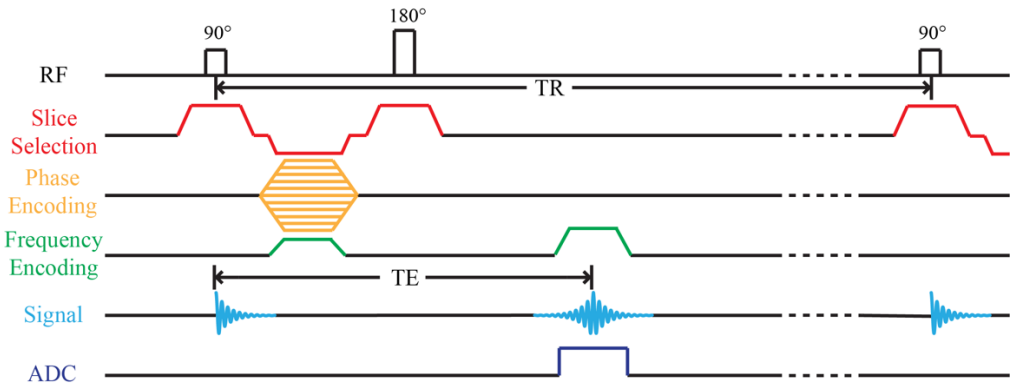


Figure 2.1.13 The basic spin echo (SE) sequence diagram.

To reduce scan time, the fast or turbo spin echo (FSE or TSE) sequence can be adopted[12], where two or more 180° pulses are used within one TR to generate more echoes, with each echo having a different phase encoding gradient (Figure 2.1.14). The number of echoes generated in one TR is called the turbo factor or echo train length (ETL), and it equals the number of rows in *k*-space that are filled in one TR. The FSE sequence enables higher T_2 weighting as a longer TR is used. However, it may be subject

to flow artefacts and image blurring due to low signal amplitude at long echo trains filling the edges of *k*-space.

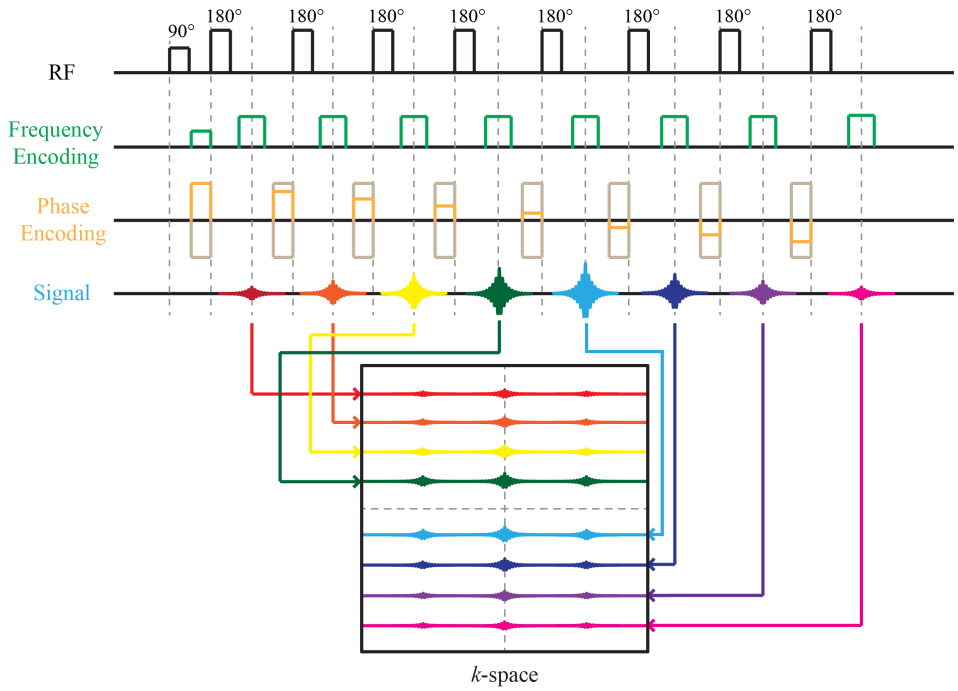


Figure 2.1.14 The turbo spin echo (TSE) sequence diagram with a turbo factor of 8.

The second method of rephasing the transverse magnetisation is by reversing the direction of the gradients called fast low angle shot (FLASH) imaging, first proposed by Haase *et al.* in 1986[13]. In the frequency encoding direction, a first gradient pulse dephases the spins while a second gradient pulse with the same duration and amplitude but opposite polarity rephases the spins at time TE, generating a gradient 'recalled' echo (GRE, or gradient echo, GE), shown in Figure 2.1.15. Similar to an SE sequence, a GRE sequence has to repeat many times depending on the expected spatial resolution in the phase encoding direction. However, since no 90° pulse is applied to tip the magnetisation onto the transverse plane, the flip angle of the excitation pulse is variable and typically smaller than 90°. This enables faster T_1 recovery and thus short TRs in the magnitude of hundreds of milliseconds, reducing the total scan time.

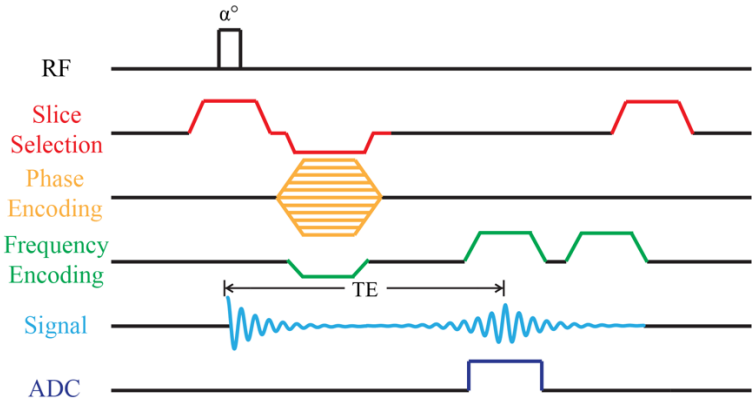


Figure 2.1.15 The basic gradient recalled echo (GRE) sequence (also called spoiled GE sequence) diagram. Note that a spoiler gradient is applied after echo formation in the slice selection direction to dephase the residual transverse magnetisation $M_{\perp,res}$.

Another group of GRE sequences is known for achieving a steady state of the transverse magnetisation $M_\perp$ using TRs that are shorter than the T_2 values of tissues[14]. Within each TR, only a single FA-variable RF pulse is applied. As a result, the $M_\perp$ does not experience full T_2 decay before the next TR starts, where the subsequent RF pulse rephases the residual $M_\perp$. After several TRs the system reaches a steady state, with a dynamic equilibrium of M_z and $M_\perp$. The signal at steady state comes from two components, shown in Figure 2.16, the pre-excitation signal formed of the spin echo S_{SE}^- produced by the former two RF pulses, and the post-excitation signal formed both by the spin echo S_{SE}^+ and the intrinsic FID produced by the current RF pulse S_{FID}^+. The signal component sampled during image readout determines the type of image weighting. Table 2.1.1 compares the characteristics of spoiled GRE and common steady-state sequences, and the nomenclature adopted by various manufacturers.

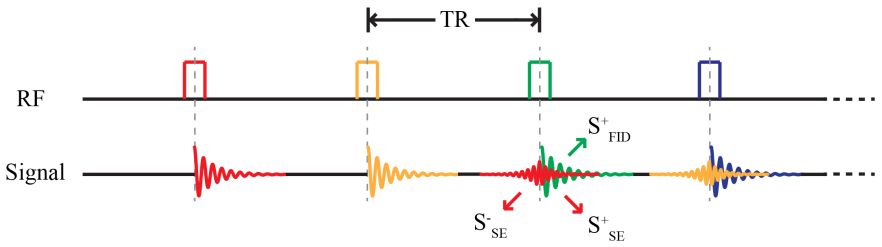


Figure 2.1.16 RF pulses and signals in steady state sequences.

Characteristics / Manufacturer	Spoiled GRE sequence	Steady-state sequences		
		Post-excitation refocused	Pre-excitation refocused	Fully refocused
Signal sampling	FID	$S_{FID}^{+} + S_{SE}^{+}$	S_{SE}^{-}	S_{SE}^{-}, $S_{FID}^{+} + S_{SE}^{+}$
Image weighting	T1	T2*	T2	T2/T1 ratio
Siemens	FLASH	FISP	PSIF (reversed FISP)	True-FISP
GE	SPGR	GRASS	SSFP	FIESTA
Philips	T1-FFE	FFE	T2-FFE	Balanced FFE
Note. FLASH = Fast Low-Angle SHot, FISP = Fast Imaging with Steady-state Precession, SPGR = SPoiled Gradient-Recalled, GRASS = Gradient-Recalled Acquisition in the Steady-State, SSFP = Steady-State Free Precession, FIESTA = Fast Imaging Employing STeady-state Acquisision, FFE = Fast Field Echo.				

Table 2.1.1 Characteristics of spoiled GRE sequence and steady-state sequences, and the nomenclature used by various MRI machine vendors.

A third category of pulse sequences utilises a rapid acquisition technique called echo planar imaging (EPI)[15–17]. In an EPI sequence, the set of excitation pulses can be either 90° and 180° pulses in an SE fashion (Figure 2.1.17a), or a variable flip angle in a GRE fashion (Figure 2.1.17b). A series of oscillating readout gradient follows, with each readout gradient companied by a 'blipped' low-amplitude phase encoding gradient. Hence, several lines or even the entire *k*-space can be sampled within one TR, termed multi-shot EPI or single-shot EPI, respectively. The nature of rapidness of EPI brings advantages such as shorter scan time, reduced motion artifacts, as well as enabling functional imaging. However, EPI sequences may still be prone to chemical shift artifacts, image blurring, and nerve stimulation because of the fast-oscillating gradients.

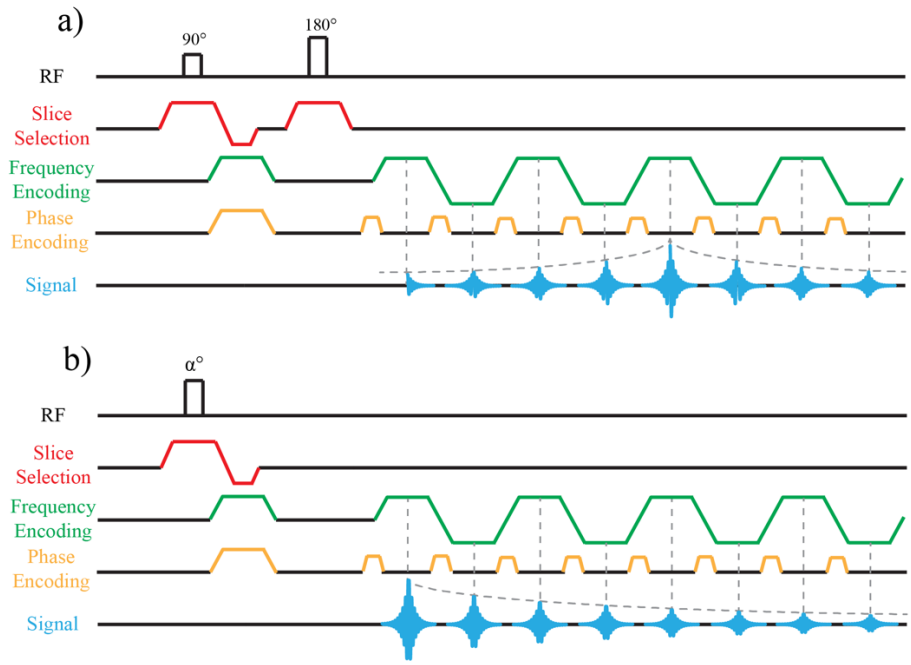


Figure 2.1.17 The echo planar imaging (EPI) sequence diagram. (a) Spin-echo EPI, the flip angle is 90° followed by another 180° pulse. (b) Gradient-echo EPI, the flip angle α is variable.

2.2 Perfusion imaging using arterial spin labelling MRI

2.2.1 Quantification of the cerebral blood flow using MRI

Perfusion is defined as the amount of blood delivered to a volume of tissue per unit time, which in the brain is quantified by the cerebral blood flow (CBF), with a unit of ml/(100g tissue)/min[18]. Quantitative CBF measurements can indicate the delivery of nutrition by blood to the brain tissue, thus providing information about physiological and pathological characteristics of the tissue. The gold standard of brain perfusion imaging is ^{15}O positron emission tomography[18] (PET), which is performed by intravenous injection of $H_2{}^{15}O$ or inhalation of $C^{15}O_2$. CBF is evaluated using the Kety-Schmidt model with blood sampling measuring the arterial input function[19]. However, the use of ionising radiation, the required access to on-site cyclotrons, and the expense of radiopharmaceuticals raise health and economic concerns for patients. As an alternative, magnetic resonance imaging (MRI) demonstrates great utility in clinical perfusion imaging.

The methods of clinical CBF measurement using MRI generally includes the injection of an exogenous contrast agent, as in dynamic susceptibility contrast-enhanced (DSC) MRI and dynamic contrast-enhanced (DCE) MRI, or using an endogenous tracer, such as blood water in arterial spin labelling (ASL). DSC-MRI captures the first pass of a non-diffusible gadolinium-based contrast agent (GBCA), after intravascular injection, through the blood vessels in the brain using T2 or T2*-weighted MR images[20,21]. Because of the paramagnetic property of the contrast agent, its magnetic field-susceptibility effect induces a loss to the MR signal. This appears in the form of contrast variation over time, as a voxelwise concentration-time curve, according to the principles of indicator dilution theory. Therefore, voxelwise and regional parametric maps of relative CBF or cerebral blood volume (CBV) measurements can be obtained from either

voxel-by-voxel or region-of-interest analysis. DCE-MRI similarly uses an extracellular low-molecular-weight MR contrast medium, often gadolinium-based, but monitors it with a series of T1-weighted MR images before, during, and after its administration[22,23]. Tissue perfusion, especially that reflecting vessel permeability, can be then derived using the signal intensity changes over time in the MR images. ASL, on the other hand, provides an inherently non-invasive approach to perfusion imaging, by employing the hydrogen molecules (spins) in the arterial blood water as an endogenous, freely diffusible tracer[24,25]. ASL uses a label-control subtraction scheme, in which a 'label image' is acquired after inversion of blood spins by adiabatic radio-frequency (RF) pulses, with a 'control image' acquired without the inversion. The difference image after subtraction is proportional to the delivery of blood, thus depicting the level of regional CBF.

ASL suffers from a substantially lower signal-to-noise ratio (SNR), mainly because the signal difference is quite small, usually 1~2% of the average signal intensity in the label/control image. Also, because the labelled blood needs to travel from the labelling site to the imaging site, T1 relaxation of the label during this arterial transit time (ATT) reduces the image contrast. For this reason, DSC-MRI remains the most widely used method in clinical cerebral perfusion MRI, with a much higher SNR and readily available post-processing software. However, ASL can provide measurements of CBF in absolute physiological units compared to contrast agent-based imaging. In addition, because of its non-invasive nature, ASL is safe for patients with acute kidney diseases (AKD) or having allergic reactions to exogenous contrast agents. Furthermore, it is relatively insensitive to abnormal permeability and have better access to paediatrics[26]. As a result, the ASL technique is now gaining popularity within the perfusion imaging community.

2.2.2 Principles of arterial spin labelling (ASL)

The time course of a conventional ASL acquisition is shown in Figure 2.2.1. An ASL signal image usually requires the acquisition of a pair of images, a label image and a control image, each consisting of a labelling stage, a post-labelling-delay (PLD), and a readout stage. For the label image, the spins in arterial blood are magnetically inverted using adiabatic RF pulses at the labelling stage, creating 'the label'. PLD then allows the blood to travel from the tagging location through the arteries and arterioles into the capillary bed, which then exchanges into extravascular space. At the imaging stage, signals from both labelled blood water and un-labelled static tissue water are acquired. The imaging location is often distal to the labelling location. The control image differs from the label image only in that the blood water remains uninverted in the labelling stage. The subtraction of labelled image from the controlled image cancels out the static tissue magnetisation and yields a perfusion-weighted image whose scale depends on factors such as scanner type, readout method, receiver coil configurations, etc.

Obtaining CBF in absolute units of ml/(100g tissue)/min requires the knowledge of the equilibrium magnetisation of arterial blood. This is often obtained from a separate calibration image acquired with a long TR to achieve a proton-density weighting. The calibration can either be voxelwise or based on a reference region (e.g., the CSF). The 'undesirable' static tissue signal can be reduced by applying one or more timed background suppression pulses in the imaging region during image readout to increase SNR.

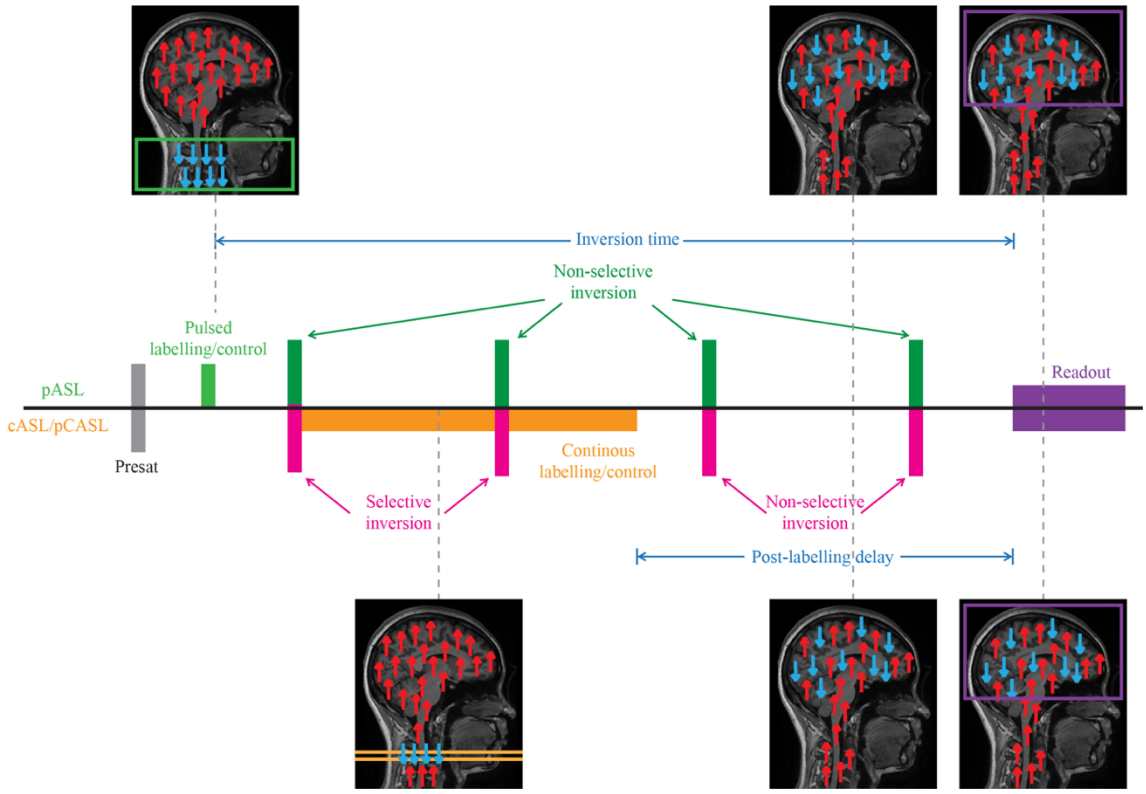


Figure 2.2.1 The time course of conventional arterial spin labelling.

According to different spatial and labelling profiles at the labelling stage, ASL can be divided into continuous ASL (cASL), pulsed ASL (pASL) and pseudo-continuous ASL (pCASL). More advanced labelling techniques such as time-encoded ASL (TE-ASL) and vessel-encoded ASL (VE-ASL) approach has been developed in recent years and will be briefly reviewed.

Continuous ASL

In continuous ASL, a constant RF pulse is applied in a proximal slice of the feeding arteries of the brain with a constant magnetic field gradient to induce flow-driven adiabatic inversions of blood spins[27]. This slice is defined as the labelling plane. As the blood spins travel from below the neck upwards to the labelling plane, they become less off-resonant with the RF pulse due to the field gradient. Then the RF pulse will invert the blood water when its off-resonance drops to zero and reaches the labelling plane. This creates a continuous supply of labelled blood water into the brain.

During the RF pulse, energy exchange between the free water pool and the macromolecular 'bound' water pool reduces the apparent T2 relaxation rate. This is known as magnetisation transfer (MT). To compensate for the MT effects, in the control image a labelling plane is added more distal to the imaging plane but symmetric to that in the labelling image[28]. However, this strategy effectively reduces the MT effects for only a single imaging slice, making it not applicable for multi-slice acquisition. There are two other solutions to correct the MT effects to tailor it for multi-slice imaging. One is using a separate RF coil for image acquisition, so that the imaging slices do not experience the MT effects produced by the constant RF pulse[29]. The disadvantages of this approach are that it induces a higher specific absorption rate (SAR) in local tissues, and it needs additional hardware setup that MRI scanners commonly lack. The other way is that by applying sine-modulated RF pulses on a second labelling plane in the control image, the blood water is inverted twice while obtaining the same amount of MT effects as in the label image[30]. The blood spins return to un-inverted after dual inversion at the expense of a loss in labelling efficiency and SNR.

The cASL approach has a well-defined temporal profile of labelling, and often can achieve more than 90% labelling efficiency. However, it requires a constant application of RF pulse and magnetic field gradient, which is not generally achievable in commercially available MRI scanners. Besides, the labelling efficiency of cASL is sensitive to the local blood velocity because of the finite labelling duration as the blood passes the labelling slice.

Pulsed ASL

Pulsed ASL differs from continuous ASL in that instead of setting a constant labelling slice, it inverts the blood water across a thicker spatial region using a very short RF pulse

(~10ms). A pre-defined delay following the labelling pulse allows the delivery of labelled blood water to the tissue.

The first sequence used to implement pASL was called EPI-based signal targeting with alternating RF pulses (EPISTAR)[31]. In EPISTAR, a thick slab of blood water is inverted proximal to the imaging slice to generate labelled tracers. Due to the close locality between the labelling slab and the imaging slice, a saturation pulse is often used on the imaging slice before image acquisition to prevent contamination by the labelling RF pulse. To compensate for the MT effects, there is an identical labelling slab in the control image only distal to the imaging plane. This, however, could result in labelled spins in veins and venules coming from the top of the imaging slice, producing focal dark spots in the subtracted perfusion-weighted ASL image. Multi-slice EPISTAR is made available by several methods: multi-slice STAR[32], PULSAR (PULsed StAR)[33], and QUASAR (QUantitative Star labelling of Arterial Regions)[34].

Later, the Proximal Inversion with Control of Off-Resonance Effects (PICORE) method was developed to avoid labelling in the control image[35]. The labelling image in PICORE is the same as in EPISTAR, but the control sequence uses a nonselective off-resonance pulse to create an equal amount of MT effects. Because there is no inversion of blood water in the control sequence, there is no signal of venous blood flow appearing in the image. Both EPISTAR and PICORE apply asymmetric pulsed labelling with respect to the imaging slice. A symmetric pASL approach is Flow-sensitive Alternating Inversion Recovery (FAIR)[36]. FAIR labelling utilises a nonselective non-resonance pulse to invert all the spins within the entire volume of the RF coil. In the control image, the same inversion pulse is used only in a range wider than the imaged slice to ensure uniform inversion. It has the advantage of capturing blood spins flowing in from multiple

directions, but venous blood water also tagged in the process will show as bright signals in the difference image.

Label duration in pASL is intrinsically ill-defined because of the near instantaneous labelling pulse duration compared to cASL. Long ATT and effects of dispersion will also cause a blunt profile near the leading and trailing edges of the labelled bolus. Therefore, in order to have a sharpened definition of the labelled slab, methods of Quantitative Imaging of Perfusion using a Single Subtraction (QUIPSS I), QUIPSS II[37], and QUIPSS II with Thin-slice TI_1 Periodic Saturation (Q2TIPS)[38] are adopted. QUIPSS I applies a saturation pulse to the imaging slice at time TI_1 after the inversion of the tagging region, creating a well-defined leading edge of the labelled slab. During a time delay ΔTI, blood starts to perfuse into the imaging slice, and the label image is acquired at time $TI_2 = TI_1 + \Delta TI$. In QUIPSS II, the saturation pulse is applied to the labelling slice, defining a sharp trailing edge. The Q2TIPS methods replaces the saturation pulse with a train of thin-slice periodic saturation at the distal end of the labelling region to reduce the sensitivity to B1 inhomogeneity and further improve the slice profile.

In contrast to cASL, pASL is much easier to implement on available MRI hardware since it does not require constant RF pulses and field gradients, which also minimises the power deposition in the tissue. The short pulse duration also makes pASL relatively insensitive to magnetisation transfer effects. However, signal from more proximal regions of the imaging slab decreases due to longer ATT and T1 relaxation. This effect limits the SNR of the pASL method.

Pseudo-continuous ASL

With an intention to achieve high SNR and labelling efficiency, as well as being able to implement on most MRI scanners, pseudo-continuous ASL (pCASL) method was

developed and is currently the recommended approach for clinical applications by the ASL White Paper[39]. PCASL resembles continuous ASL in that it also has a constant labelling plane which inverts the flowing spins as they pass through. However, the long radiofrequency pulses and magnetic gradients in cASL are substituted with a series of short, repeating pulses and matching gradients in pCASL[40], which facilitates the implementation of pCASL on MRI scanners without specialised hardware. It was reported that pCASL achieved a 50% increase in SNR than pASL, while having a higher labelling efficiency of 80% than cASL[41].

When conducting a specific study, it is always helpful to consider the advantages and disadvantages of pASL and pCASL so as to have the most suitable choice. The most prominent advantage of pCASL is its higher SNR, which is a significant benefit regarding the intrinsically low SNR nature of ASL. Furthermore, pCASL inherits the advantage of having a well-defined label duration from cASL, whereas in pASL the label duration is dependent on blood flow velocity except when using QUIPSS and Q2TIPS methods[42]. A greater degree of T1-relaxation is often considered in pASL, as some of the labelled spins travel from more proximal regions in the labelled slab. However, label efficiency in pCASL is typically lower than in pASL[43,44] (~85% in pCASL versus >90% in pASL).

Time-Encoded ASL

By varying the PLDs in the sequence in Figure 2.2.1, a kinetic model can be fitted to the ASL signals at multiple delays to obtain not only CBF, but also information about the arrival time of the labelled bolus, often called arterial transit time (ATT) or bolus arrival time (BAT) (see Section 2.2.3). For acquiring one repeat of N PLDs, one needs N label images and N control images thus $2N$ images in total. To increase the acquisition time efficiency while being able to measure ATT, time-encoded ASL method was proposed

where the whole label/control bolus was divided into sub-boli with different label or control conditions specified by a Hadamard matrix[45–48], as Figure 2.2.2a illustrates. The signal contribution from each sub-bolus can be subsequently decoded from the acquired images according to the signs in the Hadamard matrix, resulting in one effective PLD per block. In this case, N effective PLDs can be reconstructed from only $N + 1$ image acquisitions (also equal to the rank of the Hadamard encoding matrix), and each sub-bolus signal has been averaged $\frac{N+1}{2}$ times, reducing the total acquisition time.

The durations of sub-boli can be equal, which generates effective PLDs with an equal spacing (Figure 2.2.2a), or adjusted according to T1-decay, which preserves the same signal intensity for every effective PLD (Figure 2.2.2b), or targeted to measure the ATT using the 'Free Lunch' scheme, which inserts short encoding blocks in the idle time of standard single-delay ASL[49] (Figure 2.2.2c). A recent study optimised the timings of sub-boli durations and PLDs to minimise the estimation uncertainty of CBF and ATT[50]. Furthermore, time-encoded ASL can be combined with various readout methods to achieve simultaneous perfusion imaging and MR angiography[51,52]. Good reproducibility of CBF and ATT maps by time-encoded pCASL compared to conventional multi-PLD pCASL suggests it as a reliable approach to time-efficient measurement of these parameters[53,54].

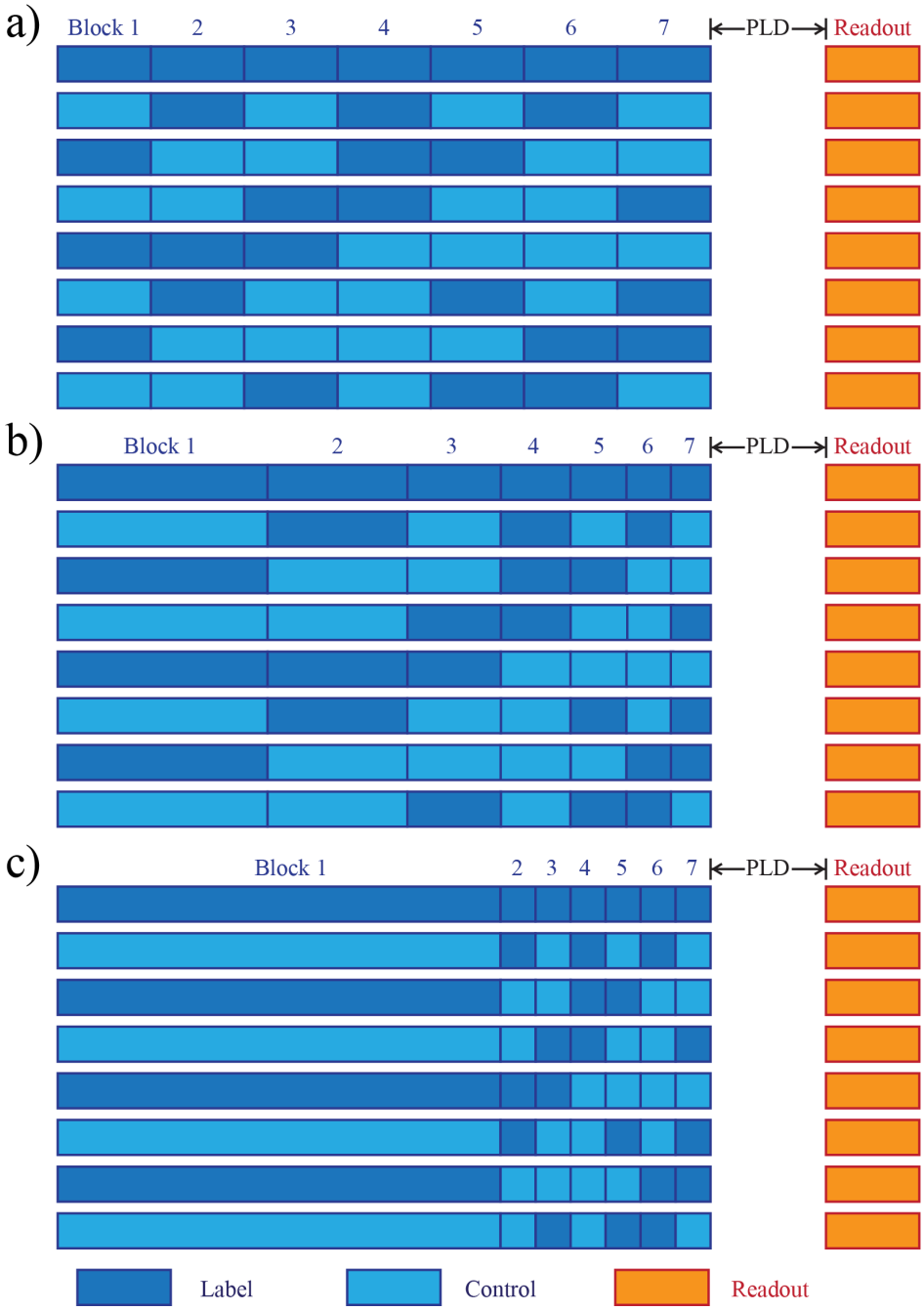


Figure 2.2.2 Example of time-encoded ASL sequence with 8 Hadamard encodings. Labelling block durations are a) equal, b) T1-adjusted, or c) consistent with standard single-delay ASL but inserted short block durations in the idle time ('Free Lunch' scheme). The signal from each block is decoded from the acquired image series according to the Hadamard matrix, e.g., bolus 2 = (image 1 + image 2 - image 3 - image 4 + image 5 + image 6 - image 7 - image 8)/4.

Vessel-Encoded ASL

Günther first proposed the idea of vessel-encoded ASL (VE-ASL), which allows ASL to label the blood water from specific feeding arteries of the brain, rather than labelling all

blood that comes through the labelling plane[55]. It is achieved by using transverse gradient pulses combined with a specific encoding matrix[56], often Hadamard for optimal encoding[55,57], to induce a phase shift between different vessels, which ensures specific vessels to remain in label or control condition during adiabatic inversion. A pseudo-inversion of the encoding matrix is then used in separating ASL signal contributions from different vessels. The method can generate vascular territory maps with high reproducibility[58] and comparable SNR to pCASL[57], which can provide accurate information about the perfusion of brain regions that can be attributed to a specific artery. Okell et al. later combined VEPCASL with a two-dimensional dynamic angiographic readout, allowing for the non-invasive acquisition of angiographic maps of major cerebral arteries[56]. This is useful for detecting delayed blood arrival times, thus assisting in clinical decision-making of potential stenosis or collateral flow[59]. However, if the flow territory maps were to be generated in a time-efficient manner, advanced post-processing methods are required, which are not often applicable in a clinical setting[60]. Overall, vessel-encoded ASL is a relatively new technique but is receiving more attention due to its non-invasive nature and the additional information obtained.

2.2.3 Kinetic modelling in ASL

The ASL technique uses hydrogen nuclei in the subject's blood water as an endogenous tracer. By monitoring magnetisation within each voxel after the inversion of the spins and subtracting with the static tissue signal without inversion, one can obtain a quantitative blood perfusion (or CBF) map. Since ASL effectively introduces a tracer in the blood, the magnetisation risen from labelled spins should conform to the principles of tracer kinetics.

The general kinetic model for ASL was first proposed by Buxton et al., stating that the magnetisation difference signal within a voxel could be accounted for by three functions[61]: the delivery function $c(t)$, the residue function $r(t)$, and the magnetisation relaxation function $m(t)$. In the label image, labelled blood water is constantly delivered to the tissue voxel by the major arteries and arterioles. The delivery function $c(t)$ thus represents the concentration of labelled spins delivered to the voxel by arterial blood at time t after delivery. However, upon arrival of the labelled spins, a portion of them is removed from the voxel due to further perfusion or venous clearance. The residue function $r(t)$ depicts the fraction of labelled spins still remaining at time t after delivery. Furthermore, the inverted magnetisation of blood water is subject to longitudinal relaxation at rate T1 of arterial blood. The magnetisation relaxation function $m(t)$ interprets the fraction of residual magnetisation owing to longitudinal decay within the voxel at time t after delivery. If the off-resonance and magnetisation transfer effects in the label and control images are the same, the ASL signal is then proportional to $\Delta M(t)$. Under these definitions, $\Delta M(t)$ can be expressed as:

$$\Delta M(t) = 2M_{0B} f\{c(t) * [r(t)m(t)]\}, \qquad \text{(Equation 2.2.1)}$$

where M_{0B} is the equilibrium magnetisation of arterial blood, f is the perfusion in ml/g/s, and $*$ denotes the convolution operation.

The expressions of these functions under conditions of PASL and cASL/pCASL are:

$$\begin{aligned} c(t) &= 0 && 0 < t < \Delta t \qquad \text{(Equation 2.2.2)} \\ &= \alpha e^{\frac{-t}{T_{1b}}} \text{ (pulsed)} && \Delta t < t < \tau + \Delta t \\ &= \alpha e^{\frac{-\Delta t}{T_{1b}}} \text{ (continuous)} \\ &= 0 && \tau + \Delta t < t \end{aligned}$$

$$r(t) = e^{\frac{-ft}{\lambda}}$$

$$m(t) = e^{\frac{-t}{T_{1t}}}$$

where α is the labelling efficiency, T_{1b} and T_{1t} are the longitudinal relaxation constants of blood and tissue, respectively, τ is the label duration, Δt is the arterial transit time (ATT), and λ is the brain/blood water partition coefficient in mL/g.

With each equation, the total magnetisation difference signal within the voxel can then be calculated as:

$$\Delta M_{\text{pulsed}}(t) = 0 \qquad 0 < t < \Delta t$$

$$= 2M_{0B} f \alpha e^{\frac{-t}{T_{1b}}} \frac{e^{kt}(e^{-k\Delta t} - e^{-kt})}{k} \qquad \Delta t < t < \tau + \Delta t, \quad \text{(Equation 2.2.3)}$$

$$= 2M_{0B} f \alpha e^{\frac{-t}{T_{1b}}} \frac{e^{kt}(e^{-k\Delta t} - e^{-k(\tau+\Delta t)})}{k} \quad \tau + \Delta t < t$$

and

$$\Delta M_{\text{continuous}}(t) = 0 \qquad 0 < t < \Delta t$$

$$= 2M_{0B} f \alpha T_1' e^{\frac{-\Delta t}{T_{1b}}} \left(1 - e^{\frac{-(t-\Delta t)}{T_1'}}\right) \quad \Delta t < t < \tau + \Delta t, \quad \text{(Equation 2.2.4)}$$

$$= 2M_{0B} f \alpha T_1' e^{\frac{-\Delta t}{T_{1b}}} e^{\frac{-(t-\tau-\Delta t)}{T_1'}} \left(1 - e^{\frac{-\tau}{T_1'}}\right) \quad \tau + \Delta t < t$$

where

$$k = \frac{1}{T_{1b}} - \frac{1}{T_1'}. \qquad \text{(Equation 2.2.5)}$$

$$\frac{1}{T_1'} = \frac{1}{T_{1t}} + \frac{f}{\lambda}$$

The general kinetic model offers a simple yet idealised solution to quantifying CBF which only holds true upon a few assumptions. Firstly, it assumes the flow of arterial blood into a voxel to be of uniform plug flow. This ignores the scenario of dispersion within the arterial blood profile. Secondly, it assumes that the concentration

ratio of labelled blood water in the tissue to that in the venous flow is constant and equal to the brain/blood water partition coefficient λ, conforming to single-compartment kinetics. Thirdly, it assumes that the water in arterial blood exchanges with the tissue blood instantaneously and completely upon entering a voxel, and decays with the relaxation constant $T1$ of tissue, T_{1t}. Before applying the general kinetic model, these assumptions need to be carefully validated.

In 2015, Alsop et al. published a paper (also called the ASL White Paper) summarising the consensus of the implementation of ASL technique in the clinical environment adopted by the community of International Society for Magnetic Resonance in Medicine (ISMRM) and the European consortium ASL in Dementia (AID)[39]. In this paper, the general kinetic model was further simplified from Buxton et al.'s model by assuming that T1 of tissue is similar to T1 of blood. The absolute quantification of CBF using pCASL can therefore be derived using a series of label-control paired ASL images and a proton density (PD)-weighted image, and is given by the following equation:

$$CBF_{\text{pASL}} = \frac{6000\lambda(SI_{\text{control}} - SI_{\text{label}})e^{\frac{TI}{T_{1b}}}}{2\alpha TI_1 SI_{\text{PD}}}, \qquad \text{(Equation 2.2.6)}$$

and

$$CBF_{\text{pCASL}} = \frac{6000\lambda(SI_{\text{control}} - SI_{\text{label}})e^{\frac{PLD}{T_{1b}}}}{2\alpha T_{1b} SI_{\text{PD}}\left(1 - e^{\frac{-\tau}{T_{1b}}}\right)}, \qquad \text{(Equation 2.2.7)}$$

where SI_{control} and SI_{label} are the repetition-averaged signal intensity values in the control and label images, respectively, SI_{PD} is the signal intensity value in the PD-weighted image. TI, TI_1, and PLD are defined in the previous section.

Although the concept of 'kinetic modelling' intuitively involves some sort of 'modelling' process, Petersen et al. proposed a 'model-free' approach of CBF quantification in ASL using single value decomposition (SVD) deconvolution methods

commonly applied in DSC-MRI[34]. The expression of ASL difference signal in discretized form is:

$$\Delta M(t_j) = \Delta TI \cdot f \cdot \sum_{i=0}^{j} AIF(t_i) \cdot r(t_j - t_i), \qquad \text{(Equation 2.2.8)}$$

where ΔTI is the interval of multiple inversion times in pASL, AIF is the arterial input function, and $r(t)$ is the residue function. Since the residue function $r(t)$, by definition, satisfies $r(0) = 1$, CBF estimates can be obtained by performing deconvolution of a measured AIF from ΔM and selecting the maximum value. However, deconvolution methods tend to produce an underestimation of CBF values than those estimated by the general kinetic model[34,62]. The fundamental trade-off between model-free and model-based approaches is the degrees of freedom each one can offer. CBF estimation using the model-free approach does not require such strict conformity to the mathematical expressions each function has as the model-based approach does, thus the estimation relies more on the data and has higher specificity to the signal shape of each individual. The model-free approach is less regularised, and therefore does not result in systematic bias in estimation if some of the assumptions were violated. In contrast, model-based approaches have less sensitivity to physiological noise, and the estimated parameters have clearer physiological interpretations.

Since the original proposal of the general kinetic model, progress has been made towards the better accuracy of perfusion quantification by accounting for different effects that are neglected in the simplest model but are often present *in vivo*, such as dispersion effects[63–65], macrovascular signal contamination[66–68], restricted water permeability[69–72], magnetisation transfer effects[73,74], cardiac pulsatility[75–77], partial volume effects[78–80], apparent transverse relaxation time[81], and dynamic transit time[82] etc. To the interest of this thesis, we will review the extensions of the general kinetic model

to account for dispersion and macrovascular contamination in the next two subsections, and will review the techniques in measuring water permeability using ASL in Section 2.4.

2.2.3.1 Accounting for Flow Dispersion Effects

Before the labelled blood water in the main arteries reaches its target tissue, it will traverse through small arterioles and the capillary bed, where it experiences numerous branching and bifurcation. Cardiac pulsation will affect the regional blood flow speed by periodically changing the blood pressure. As a result, blood water that starts at the same voxel in the main arteries and arrives at the same voxel in the target tissue may have travelled through multiple paths with different flow speeds. Furthermore, occlusions in arteries and arterioles seen in cerebral stenosis and thrombosis can cause obstructions of blood perfusion. Therefore, the labelled bolus will arrive at the target tissue at slightly different time points. This effect of desynchronization in bolus arrival times, caused by branching vasculature, cardiac pulsation, and possible blood vessel occlusions is collectively termed flow dispersion.

An arterial input function (AIF) can be used to describe the profile of the labelled bolus entering the imaging plane. For pulsed ASL, all blood water within the slab is inversed simultaneously, with a well-defined rectangular profile at the labelling site using QUIPSS methods. Then, blood water in different locations within the bolus will experience different durations of T1 relaxation, according to the distance between the labelling site and the imaging plane. However, for continuous ASL, this distance is fixed as blood water is continuously being labelled through passage of a labelling plane. Therefore, in an ideal condition, pASL has an AIF subject to exponential decay with

time, while pCASL has an AIF of a boxcar shape, which can both be expressed in mathematical terms:

$$\begin{aligned} a(t) &= 0 && 0 < t < \Delta t \qquad \text{(Equation 2.2.9)} \\ &= 2M_{0B}e^{\frac{-(t-\Delta t)}{T_{1b}}} \quad \text{(pulsed)} && \Delta t < t < \tau + \Delta t, \\ &= 2M_{0B}e^{\frac{-\Delta t}{T_{1b}}} \quad \text{(continuous)} \\ &= 0 && \tau + \Delta t < t \end{aligned}$$

where M_{0B}, Δt, τ, and T_{1b} are defined as above.

Flow dispersion will in effect smooth the shape of the ideal arterial input function (AIF). Therefore, to account for dispersion effects can be achieved by applying a smoother AIF in model-based methods or use model-free approaches to directly incorporate dispersion. Up to now, a number of studies have proposed more realistic shapes of the AIF. Hrabe and Lewis first considered two scenarios in pASL where the AIF experiences uniform or Gaussian dissipation[63]. The dissipation can be characterised by a scaling factor $W(t)$. In the simplest approximation of uniform dissipation, in which point-based labels dissipate into a homogenous sphere with radius σ, $W(t)$ takes the form of a trapezoid function:

$$\begin{aligned} W(t) &= 0 && t < \Delta t - \sigma_1 \qquad \text{(Equation 2.2.10)} \\ &= \frac{1}{2} + \frac{1}{2\sigma_1(t-\tau_1)} && \Delta t - \sigma_1 < t < \Delta t + \sigma_1 \\ &= 1 && \Delta t + \sigma_1 < t < (\Delta t + \tau) - \sigma_2 \\ &= \frac{1}{2} - \frac{1}{2\sigma_2(t-\tau_2)} && (\Delta t + \tau) - \sigma_2 < t < (\Delta t + \tau) + \sigma_2 \\ &= 0 && (\Delta t + \tau) + \sigma_2 < t \end{aligned}$$

where σ_1 and σ_2 are the dissipation radius for the leading and trailing edge of the bolus, respectively. In the case of Gaussian dissipation, where the leading and trailing edges of the bolus are shaped by Gaussian smoothing, $W(t)$ has the expression of:

$$W(t) = \frac{1}{2}\left[\text{erf}\left(\frac{t-\Delta t}{\sqrt{2}\sigma_1}\right) - \text{erf}\left(\frac{t-(\Delta t+\tau)}{\sqrt{2}\sigma_2}\right)\right], \qquad \text{(Equation 2.2.11)}$$

where $\text{erf}(x)$ denotes the error function, and σ_1 and σ_2 are the standard deviation characterising the Gaussian smoothing that is experienced by the leading and trailing wavefront of the bolus, respectively.

Although the AIFs in these models are effectively smoothed, uniform dissipation of blood is hardly seen under biological conditions, and Gaussian dissipation can lead to physiologically implausible results where magnetisation starts to rise even when $t < 0$. Ozyurt et al. later modified this model by making the standard deviation of the Gaussian smoothing time-dependent[83], resulting in a new $W(t)$:

$$W(t) = \frac{1}{2}\left[\text{erf}\left(\frac{t-\Delta t}{k\sqrt{t}}\right) - \text{erf}\left(\frac{t-(\Delta t+\tau)}{k\sqrt{t}}\right)\right], \qquad \text{(Equation 2.2.12)}$$

where $k = 2\sqrt{D}/\bar{v}$, D is the diffusion constant in the blood adopted from diffusion equation, and $\bar{v}$ is the average velocity of the bolus. This model corrected the early rise of the signal-time curve, as well as achieving a better fit in real data.

Gallichan and Jezzard proposed a method assuming laminar flow of the blood based on a geometrical model[76]. The velocity of blood takes a parabolic shape according to the distance from the centre of the vessel:

$$v(r) = V_m(1 - r^2), \qquad \text{(Equation 2.2.13)}$$

where V_m is the maximum velocity of blood in the mid-axial point, r is the normalised radius. Therefore, the proportion of labelled blood in the cross-section of the vessel at the imaging site at time t, $P(t)$, represents the proportion of blood input at the imaging slice, i.e., the AIF:

$$P(t) = 0 \qquad 0 < t < \frac{x}{V_m} \qquad \text{(Equation 2.2.14)}$$

$$= 1 - \frac{x}{V_m t} \qquad \frac{x}{V_m} < t < \frac{X + x}{V_m},$$

$$= \frac{x}{V_m t} \qquad \frac{X + x}{V_m} < t$$

where x is the distance from the leading edge of the bolus to the imaging slice, X is the length of the labelled bolus. However, the bolus arrival time in this model is dependent on the dispersion parameter x/V_m unless an additional time offset Δt is introduced, which assumes the blood undergoes no dispersion for some time before dispersion occurs.

In other perfusion imaging modalities such as DSC-MRI, a gamma variate function is found to be related to the solution of the tracer signal-time curve under a one-dimensional convective dispersion model[84]. It is also implemented in the model-free approach[34], and validated using ASL-based angiography[65]. In the normalised form adopted by Chappell et al., the AIF can be expressed as[65]:

$$a(t) = 0 \qquad t < \Delta t. \qquad \text{(Equation 2.2.15)}$$

$$= \tau e^{\frac{-t}{T_{1b}}} \frac{s^{1+sp}}{\Gamma(1+sp)} (t - \Delta t)^{sp} e^{-s(t-\Delta t)} \quad \Delta t < t,$$

where s is the sharpness of the curve, p is the time-to-peak of the curve, and $\Gamma(x)$ is the Gamma function.

Instead of finding the explicit expression of the AIF, the distortion of flow dispersion on the AIF could also be described by mathematically convolving the AIF with a vascular transport function $VTF(t)$ (also called dispersion kernel)[85]:

$$AIF_{\text{dispersion}}(t) = AIF_{\text{ideal}}(t) * VTF(t). \qquad \text{(Equation 2.2.16)}$$

The Gaussian dissipation model of Hrabe and Lewis is essentially convolving the AIF with a Gaussian kernel[63]:

$$VTF_{\text{Gaussian}}(t) = \frac{1}{\sqrt{2\pi\sigma}} e^{\frac{-t^2}{2\sigma^2}}, \qquad \text{(Equation 2.2.17)}$$

where σ is the standard deviation of the Gaussian distribution. Chappell et al. proposed a Gamma dispersion kernel, which provides both good fit to the data and computational simplicity[65]:

$$VTF_{\text{Gamma}}(t) = \frac{s^{1+sp}}{\Gamma(1+sp)} t^{sp} e^{-st}, \qquad \text{(Equation 2.2.18)}$$

where s and p resembles the parameters in the Gamma variate function, and larger p and smaller s are associated with greater dispersion. This model only introduces two free parameters to describe dispersion, thus is more preferable considering the inherently low SNR of ASL data.

However, it is still under debate whether a dispersion kernel independent to spatial location can accurately describe the level of flow dispersion within the voxel, or worse, whether using convolution kernels can describe dispersion effects at all[86]. Mouannes et al. used a delay-dependent exponential kernel to relate dispersion with arterial-tissue delay (ATD), which is the bolus arrival time difference between the voxel-of-interest and tissue[87]:

$$VTF_{\text{exponential}}(t) = \frac{A}{ATD+1} e^{\frac{-\beta t}{ATD}}, \qquad \text{(Equation 2.2.19)}$$

where ATD is the arterial tissue delay, and parameters A and β are determined by model fitting. However, this method has only been tested in DSC-MRI but not using ASL. In theory, determining an AIF that is upstream to the voxel can eliminate the dispersion effect. By using a local AIF that is close to tissue input, CBF measurements are reported to be overestimated and transit time underestimated[88], corresponding to a decrease in dispersion effects. This is particularly useful when significant levels of dispersion are expected, as in severe vascular diseases[89].

In summary, dispersion refers to the temporal delaying effect on the arterial input functions. Using a smoother AIF or convolving the ideal AIF with a vascular transit function (or dispersion kernel) can reduce the underestimation of CBF and overestimation of ATT caused by dispersion effects. It can be minimised, in principle, by measuring a local AIF.

2.2.3.2 Accounting for Macrovascular Contamination

Ideally, ASL signal only comes from the perfused tissue. However, labelled blood water will take a finite amount of time to reach the tissue. If the PLD is not long enough, labelled blood water could still remain in the macrovasculature, creating an artefact around the major arteries, such as the middle cerebral artery (MCA) and the circle of Willis. Intravascular signal, where blood is destined to perfuse into the more distal tissue, can also hinder the accurate quantification of tissue perfusion. These two effects are commonly referred to as macrovascular contamination.

This effect can be accounted for by inherently eliminating the signal in the macrovasculature. The long PLD suggested by the White Paper[39] using a single-PLD imaging protocol can largely ensure the arrival of labels in the tissue, but this comes with a loss of signal due to T1 relaxation, thus decreasing the SNR and image quality. Another approach to minimise macrovascular signal is to use bipolar crusher gradients to selectively saturate spins within a threshold of encoded velocity V_{enc}[90]. However, bipolar crusher gradients can only saturate the spins within a single direction, which leaves the macrovascular signal perpendicular to the gradient direction unaffected. Also, it is hard to determine the velocity threshold for different individuals, as choosing very small V_{enc} values could lead to inaccuracy of perfusion quantification due to the extended TE and a decreased SNR[34], and the removal of important arterial signal might result in a loss of

clinical indicators such as delayed blood flow and arteriovenous shunting[39]. Due to these reasons, the use of crusher gradients is not recommended by the White Paper.

Whereas the above-mentioned model-free approaches can largely bypass the problem of macrovascular contamination, macrovascular component signal can be mathematically estimated by fitting the signal-time curve to the kinetic model with the help of multi-PLD (or multi-TI) ASL. This gives us more information about the physiological parameters of the patient, such as arterial blood volume fraction aBV% and arterial bolus arrival time Δt_a, which are both important cerebral hemodynamic indicators in cerebral pathology such as multiple sclerosis[91] and hyperacute stroke[92]. Chappell et al. included both a tissue and an arterial component in the kinetic model using a variational Bayesian method[66]. The ASL difference signal of the arterial component takes the shape similar to that of the AIF:

$$\begin{aligned}
\Delta M_{\text{arterial}}(t) &= 0 && 0 < t < \Delta t_a \qquad \text{(Equation 2.2.20)} \\
&= 2\alpha M_{0B} e^{\frac{-(t-\Delta t_a)}{T_{1b}}} \cdot aBV\% \ \text{(pulsed)} && \Delta t_a < t < \tau + \Delta t_a, \\
&= 2\alpha M_{0B} e^{\frac{-\Delta t_a}{T_{1b}}} \cdot aBV\% \qquad \text{(continuous)} \\
&= 0 && \tau + \Delta t_a < t
\end{aligned}$$

where $aBV\%$ is the arterial blood volume fraction, and Δt_a is the bolus arrival time of the arterial component, which depicts the first arrival of labelled blood water in the arteries in the voxel. The variational Bayesian method adopts a probabilistic approach, which includes prior information about parameters such as ATT, so as to ensure the result of estimation being within the physiologically plausible range. This method has proven to remove most of the macrovascular signal compared to using crusher gradients with high reproducibility[93]. However, it is worth noting that this expression of arterial component only applies to the magnetisation of the major arteries, where flow velocity is likely to be high with minimal amount of water transportation into the extravascular

space. Signal arisen from a capillary compartment, which has fractional water exchange with the tissue compartment, is not in the scope of this discussion, and will be considered in Section 2.4.

Furthermore, independent component analysis (ICA) is often used to eliminate the contribution of macrovascular component in other perfusion imaging techniques such as DSC-MRI. This model-free approach has the ability of separating different sources of signal components, such as those from arterial flow, venous flow, tissue perfusion, etc., without prior knowledge of the shape of the signal. With ICA, significant reduction of macrovascular signal contamination has been achieved[94,95], with reported robustness in obtaining perfusion maps with respect to different temporal resolution and SNR levels[96]. Compared to early thresholding and model-based methods, ICA has the advantage of inherently correcting for partial volume effects, because of its separation of signal components solely according to different flow patterns. However, it remains arguable whether the independent components can be reliably derived in clinical practice, especially within severe vascular diseases such as stroke, where a delayed contrast bolus is expected[95].

2.2.4 Applications of ASL

Although DSC-MRI remains the favoured method in clinical cerebral perfusion imaging, ASL use is rapidly growing in clinical applications owing to the increasing availability of high-field MRI scanners, improved pulse sequences and multichannel receive coils[97]. Whereas nuclear perfusion imaging techniques such as PET and SPECT may be expensive and contra-indicated, the main advantage of ASL is its reproducibility in providing absolute CBF measurements in a comparatively cheap and completely non-invasive manner[98,99].

Patterns of hypoperfusion have been detected by ASL in cases of various neurodegenerative diseases such as Alzheimer's Disease[100–102], vascular dementia[103,104], and Lewy body dementia[105,106], corresponding to the hypometabolism found by fluorine 18 fluorodeoxyglucose (FDG) PET[107]. ASL also shows potential in epilepsy for localising the epileptogenic region[108,109], and in neoplasms for identifying high-grade CNS tumour such as glioblastoma multiforme[110,111]. In terms of cerebrovascular diseases, ASL has produced promising results in measuring perfusion alterations in stroke[112,113] and Moyamoya disease[114]. Multi-delay ASL is particularly useful in carotid stenosis and occlusion when correcting for abnormal ATT and even mapping the transit time directly[115]. In diagnosing psychiatric disorders, ASL has higher sensitivity than other MR imaging techniques in detecting subtle perfusion changes in post-traumatic stress disorder (PTSD)[116,117], mild traumatic brain injury[118,119], or schizophrenia[120,121]. Furthermore, ASL imaging can be used in perfusion quantification in extra-cerebral regions. Perfusion measurements from renal cortical regions[122–124], pancreas[125], and regions with low perfusion rates such as the prostate[126,127], have been reported.

2.3 Optimal sampling strategy in arterial spin labelling MRI

In 1948, C. E. Shannon published the landmark paper 'A Mathematical Theory of Communication', which laid the groundwork for the development of information theory[128]. Corresponding to Shannon's depiction of a general communication system, the MRI machine is, in essence, a signal transmitter and receiver that generate and harvest the MR signal from the information source, for example, the body, and then transform the signal into human-interpretable images. A challenge therefore exists that we aim to design an MR experiment so that it gathers the most amount of information within a reasonable acquisition time. This notion of information is closely associated with uncertainty. That is, an informative measurement would be able to reduce the uncertainty about the biophysiological parameters of interest, and the optimal experiment design would, at least theoretically, give rise to the least possible uncertainty. In the context of multi-delay ASL, an aspect of optimal experiment design by finding the optimal sampling times, i.e., inversion times (TI) in PASL or post-labelling delays (PLD) in PCASL, that lead to the least uncertainty in parameter estimation, has received increased attention in recent years.

A well-defined optimisation process of the optimal sampling strategy (OSS) would require the formalisation of a few aspects: assumptions, optimality, and prior knowledge. The following sections will address these aspects respectively.

2.3.1 Assumptions

The number of assumptions that an optimisation process is based on is inversely correlated to the generalisability of the results. According to Haldar, MR optimisation methods can be categorised into three groups from less to more assumptions made[129]: model-free, data-driven, and model-based. Model-free methods concern the basic

characteristics of an MR image, such as optimising for signal-to-noise ratio (SNR) or finding the optimal trade-off between spatial resolution and noise variance, usually within a constrained scan duration. The minimal number of assumptions involved in the optimisation process enables the resulting configurations to be used across dataset and experiments. A data-driven optimisation is normally based on prior information about a specific modality, but independent of the model within that modality. While the extraction of prior information can be assisted using machine learning and deep learning approaches, data-driven methods may struggle with interpretability and selection bias of the training data[130].

Conversely, model-based approaches require the most explicit model assumptions of the experiment structure, allowing for statistical optimisation of a specific problem. The optimal sampling strategy falls into the category of model-based methods, and it is based on the theoretical concept of the Cramér-Rao Lower Bound (CRLB).

Let $\boldsymbol{\theta} = [\theta_1, \theta_2, \dots, \theta_n]^T$ be a column vector of n parameters of interest, which is aimed to be estimated from m independent samples of x following the same probability density function $f(x; \boldsymbol{\theta})$. The CRLB theory identifies the lower bound of the covariance matrix for $\boldsymbol{\theta}$ as the inverse of the Fisher information matrix (FIM), $I(x, \boldsymbol{\theta})$:

$$\text{cov}(\boldsymbol{\theta}) \geq I(x, \boldsymbol{\theta})^{-1}. \qquad \text{(Equation 2.3.1)}$$

The FIM is an $n \times n$ matrix with each element $I(\boldsymbol{\theta})_{jk}$ defined as:

$$I(x, \boldsymbol{\theta})_{jk} = E\left[\frac{\partial}{\partial \theta_j} \log f(x; \boldsymbol{\theta}) \cdot \frac{\partial}{\partial \theta_k} \log f(x; \boldsymbol{\theta})\right], \qquad \text{(Equation 2.3.2)}$$

where $E[x]$ denotes the expectation of x; θ_j and θ_k are the j-th and k-th parameter of interest in $\boldsymbol{\theta}$, respectively, with $I(x, \boldsymbol{\theta})_{jk}$ representing the diagonal elements of the FIM when $j = k$. Regarding to ASL experiments, the FIM takes the form of:

$$I(\boldsymbol{t},\boldsymbol{\theta})_{jk} = \frac{A}{\sigma^2}\sum_{i=1}^{m}\frac{\partial\Delta M(t_i;\boldsymbol{\theta};\rho)}{\partial\theta_j}\frac{\partial\Delta M(t_i;\boldsymbol{\theta};\rho)}{\partial\theta_k}, \qquad \text{(Equation 2.3.3)}$$

where A is the number of repeats accommodated in the acquisition time, σ^2 is the variance of the assumed Gaussian noise in each image (assuming each image has the same noise variance), ΔM is the magnetisation difference in the ASL signal model, $\boldsymbol{t}$ is the column vector of sampling times, ρ is the collection of nuisance parameters that are assumed to be fixed during optimisation, and $\frac{\partial\Delta M}{\partial\theta_i}$ is referred to as the sensitivity functions of parameter θ_i. Therefore, minimising the variance-covariance matrix of model parameters is equivalent to maximising the 'information' contained in the FIM.

The fact that the sensitivity functions depend on specific ASL kinetic model expressions (such as those introduced in Subsection 2.2.3) gives OSS the flexibility of generating customised protocol timings aimed for different purposes. For example, a set of sensitivity functions using kinetic models that incorporate flow dispersion or macrovascular contamination can be used to design protocols that are optimised for estimating dispersion or macrovascular parameters. Meanwhile, it is important to note that assumptions underlying the model expressions still need to be satisfied if the resulting optimal sampling scheme were to be adopted in practice.

2.3.2 Optimality criterion

The aim of the optimal sampling design is to minimise the estimation uncertainty of a list of parameters. However, even if an algorithm (e.g., least squares or Bayesian methods) is able to provide uncertainty estimates on each parameter, we are often more interested in minimising the uncertainty of a subset of parameters over others under different circumstances. In the context of ASL, for example, while one would always want an estimation of CBF and its uncertainty, ATT is more desired when studying delayed bolus

arrival in cerebral pathology, and the exchange time $Texch$ characterising vascular permeability to water is preferred when investigating the integrity of the blood-brain barrier. The nuisance parameters - ones that may have an impact on the estimation of focused parameters but not at the centre of our goals - can be given lower weightings in the optimisation based on the loss function, which is also named the optimality criterion in the context of optimal experiment design.

Based on the purpose of the optimisation, optimality criteria can be categorised into ones that are aimed for the precision of estimation of model parameters or 'estimation-oriented', such as D-optimality and A-optimality, and ones that are aimed for the precision of prediction of input response or 'prediction-oriented', such as G-optimality and I-optimality[131]. In the scope of this thesis, only estimation-oriented optimality criteria are considered.

D-optimality

The D-optimality criterion $\Phi_{\mathrm{D-optimal}}$ is the determinant of the variance-covariance matrix $\mathrm{cov}(\boldsymbol{\theta})$, which is proportional to the volume of the n-dimensional confidence ellipsoid of model parameters $\boldsymbol{\theta}$. According to CRLB, it is equivalent to maximising the determinant of the Fisher information matrix. A D-optimal design is achieved when $\Phi_{\mathrm{D-optimal}}$ is minimised:

$$\min\Phi_{\text{D-optimal}} = \min \det\left(\mathrm{cov}(\boldsymbol{\theta})\right) = \max \det(I(\boldsymbol{t};\boldsymbol{\theta}))\,. \qquad \text{(Equation 2.3.4)}$$

A-optimality

The A-optimality criterion $\Phi_{\mathrm{A-optimal}}$ is the average variance of the n model parameters, denoted by the trace of the variance-covariance matrix $\mathrm{cov}(\boldsymbol{\theta})$. An A-optimal design is achieved when $\Phi_{\mathrm{A-optimal}}$ is minimised:

$$\min\Phi_{\text{A-optimal}} = \min \mathrm{trace}\left(\mathrm{cov}(\boldsymbol{\theta})\right) = \min \mathrm{trace}(I(\boldsymbol{t};\boldsymbol{\theta})^{-1})\,. \qquad \text{(Equation 2.3.5)}$$

L-optimality

In addition to A-optimality, we could give different weights to the parameters by placing a diagonal non-negative definite matrix $\boldsymbol{W}$ in front of $\mathrm{cov}(\boldsymbol{\theta})$, which is termed the local-optimality, or L-optimality, criterion $\Phi_{\mathrm{L-optimal}}$. Positive weightings are assigned to the parameters according to the degree of interest we take in their variances, while low or zero weightings are given to the nuisance parameters that we treat as confounds. An L-optimal design is achieved when $\Phi_{\mathrm{L-optimal}}$ is minimised:

$$\min\Phi_{\text{L-optimal}} = \min \mathrm{trace}\,(\boldsymbol{W}\mathrm{cov}(\boldsymbol{\theta})) = \min \mathrm{trace}(\boldsymbol{W}I(\boldsymbol{t};\boldsymbol{\theta})^{-1})\,. \quad \text{(Equation 2.3.6)}$$

2.3.3 Prior knowledge

As shown in Equation 2.3.3, the value of the FIM depends on the values of the parameters of interest, so much so that the resulting optimised sampling times are only optimal under one set of selected parameters. However, in medical imaging such parameters may lie in a range of physiologically plausible values obtainable as prior information, either from literature or prior studies on a particular subject group. Therefore, it is important that we incorporate such information in the optimisation, so that the output timings would perform optimally within a range of parameters of interest values encountered *in vivo*, which we termed 'optimised range'.

A common approach to incorporate prior information is the pseudo-Bayesian method[132], in which the optimality criterion $\Phi(\boldsymbol{t};\boldsymbol{\theta})$ is integrated over a probability distribution of $\boldsymbol{\theta}$, $\rho(\boldsymbol{\theta})$:

$$\min\Psi(\boldsymbol{t};\boldsymbol{\theta}) = \min \int \Phi(\boldsymbol{t};\boldsymbol{\theta})\rho(\boldsymbol{\theta})\,d\boldsymbol{\theta}\,. \quad \text{(Equation 2.3.7)}$$

To simplify the computation, a discrete form of the prior distribution is often used to approximate for $\Psi(\boldsymbol{t};\boldsymbol{\theta})$:

$$\min\widetilde{\Psi}(\boldsymbol{t};\boldsymbol{\theta}) = \min \frac{1}{|\boldsymbol{\Theta}|}\sum_{\boldsymbol{\theta_i}\in\boldsymbol{\Theta}} \Phi(\boldsymbol{t};\boldsymbol{\theta_i}) \approx \min\Psi(\boldsymbol{t};\boldsymbol{\theta}), \quad \text{(Equation 2.3.8)}$$

where $\boldsymbol{\Theta}$ is the set of the combinations of the parameters of interest chosen from an evenly spaced sample range, and $|\boldsymbol{\Theta}|$ is the number of combinations in the set $\boldsymbol{\Theta}$.

2.3.4 Applications of optimal sampling strategy

Since its first appearance in parametric time series analysis in 1969[133], using CRLB for designing optimal sampling strategies has been extensively applied in both linear and nonlinear biophysical systems such as the identification of thyroid hormone kinetics[134,135], insulin kinetics[136], and pharmacokinetics[137,138]; the measurement of protein relaxation times[139], and neural recruitment curves in transcranial magnetic stimulation[140] (TMS). Apart from minimising parameter estimation variances, the application of OSS has the advantage of reducing the number of sampling times required and shortening the total sampling duration, especially when harvesting time-series data invasively in SNR-challenging scenarios[134].

In the MR community, the OSS was adopted by many modalities to assist quantitative model fitting, from T2 measurement[141] to diffusion MRI[142], from magnetisation transfer MRI[143–145] to functional MRI[146], and from chemical exchange saturation transfer (CEST) MRI[147] to the more recently developed MR fingerprinting[148–150]. In arterial spin labelling, specifically, the optimal sampling strategy was earlier utilised in pulsed ASL to obtain optimised TIs[151–153], resulting in improved precision in CBF and ATT estimations. An adaptive process was later proposed to be incorporated into the optimisation, so that the prior information on the parameters of interest could be updated by real-time parameter estimations from existing data, thereby updating the optimised protocol timings used in later data acquisitions[154]. With the advantage of easier implementation and higher SNR, pseudo-continuous ASL (pCASL) became the recommended ASL technique in a clinical setting by the ASL consensus paper[39]. Woods

et al. applied the OSS in multi-delay pCASL[155] and later in time-encoded pCASL[156], generating optimised protocols that had significantly higher parameter estimation accuracy than conventional protocols with equally spaced timings.

2.4 Measuring water permeability across the blood-brain barrier

2.4.1 Water transportation across the blood-brain barrier

The blood-brain barrier (BBB) is a dynamic interface that lies between the brain tissue and the cerebral blood circulation. As shown in Figure 2.4.1, endothelial cells that are adjoined by tight junctions encompass the vessel lumen, and are surrounded by pericytes and the basement membrane, which are in turn anchored by the foot processes of astrocytes to obtain structural and biochemical support[157]. The semi-selective nature of the BBB gives it the indispensable role of regulating the transportation of solutes from the blood vessel into the brain, while protecting the brain from harmful toxins and pathogens. The transport of substances across the endothelial barrier takes place via two permeability pathways: the paracellular pathway and the transcellular pathway. Some ions and small hydrophilic molecules can traverse through the tight junctions via the paracellular pathway, in a passive transport fashion driven by the concentration gradients. In contrast, other substances rely on ion channels and protein receptors on the endothelial surface via the transcellular pathway, either by passive transport (e.g., diffusion, facilitated diffusion, filtration, and osmosis) or by active transport that requires energy.

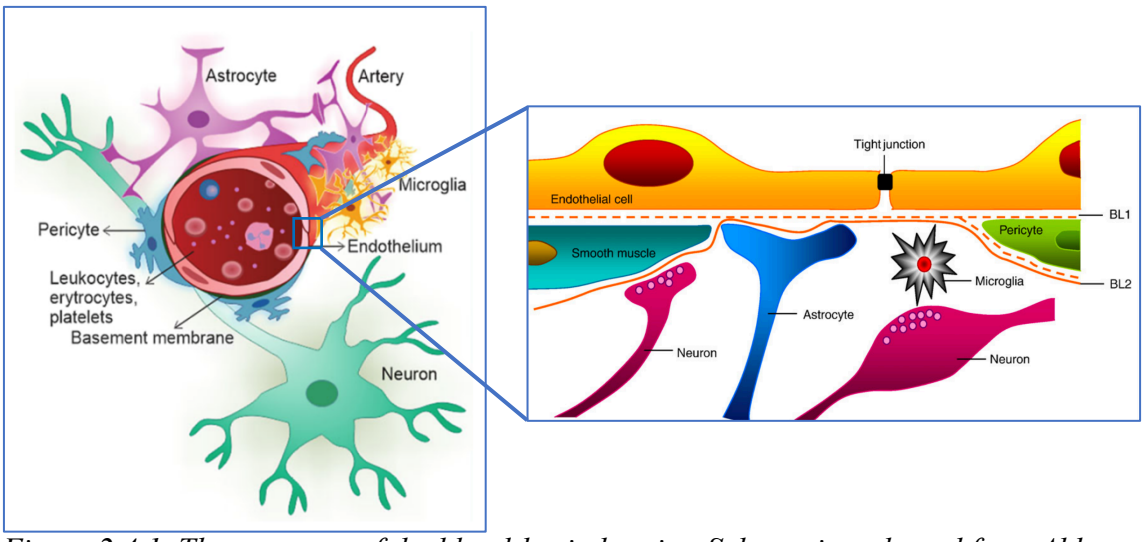


Figure 2.4.1. The structure of the blood-brain barrier. Schematics adapted from Abbott et al.[157] *and Barichello et al.*[158]

The structural and functional intactness of the BBB is crucial to the maintenance of neuronal function and cerebral homeostasis. Also, damage to the blood-brain barrier has been shown to be associated with pathological conditions such as stroke[159–162], multiple sclerosis[163,164], and neurodegenerative diseases[165–168]. Therefore, much effort has been directed to measuring the BBB integrity using medical imaging methods, which can be achieved by monitoring the cerebral uptake of intravenously injected agents such as fluorescent dyes in microscopy and radioactive substances in positron emission tomography (PET). However, not only are these methods invasive and may lead to allergic reactions or cumulative ionising radiation, but they also lack quantification sensitivity in subtle BBB pathology cases and specificity in localising the mechanism of BBB breakdown[169,170]. Consequently, using MRI to measure BBB permeability to water, which is an endogenous tracer abundant in the brain, stands out as a promising and accessible way of probing BBB function.

Water molecules are believed to freely cross the endothelial membranes mainly via filtration in other parts of the body, such as the muscle capillary endothelium. However, due to the lack of pores and slits in the tight junctions, the exchange of water molecules across the BBB is believed to occur via diffusion and active transport mainly

through the Aquaporin 4 protein (AQP4) channel, which largely restricts the BBB permeability to water[171,172]. Furthermore, the extra coating of astrocytic endfeet and basement membranes, as well as the deficiency in endocytotic vesicles modulating transcellular flux, also contributes to the low water permeability in the BBB.

Quantification of restricted water permeability can be achieved by estimating characteristic parameters such as the permeability-surface area product of water, PS_w, and the pre-exchange lifetime of water molecules, $Texch$[172]. As implied by its name, PS_w is the product of the permeability of BBB to water (P_w) and the surface area of the vessels (S) where water exchange takes place. Therefore, it is a parameter of interest that accounts for both structural and functional integrity of the BBB. PS_w product is also related to the cerebral blood flow f by the extraction fraction E, which is much less than one considering the restricted BBB permeability to water:

$$PS_w = -ln\,(1 - E) \cdot f. \qquad \text{(Equation 2.4.1)}$$

On the other hand, $Texch$ is average time that water molecules spend in the blood compartment before exchanging through the BBB. It is the reciprocal of the first-order water exchange rate constant k_w, which is defined as the fraction of water exchanged from blood to brain through capillary walls per minute[173]. Furthermore, $Texch$ is linked to PS_w by the capillary water distribution volume V_c, which equals to the fraction of blood volume V_b to tissue volume V_t:

$$Texch = \frac{V_c}{PS_w} = \frac{V_b}{V_t PS_w}. \qquad \text{(Equation 2.4.2)}$$

Abnormal values of parameters characterising the exchange of water are important indicators for cerebral pathology. For example, lower water exchange fractions can be associated with high CBF values in tumorous regions[71], while reduced levels of

$Texch$ are possible indications of ischemic stroke[161], cerebral small vessel diseases (SVD) or dementia[174].

MRI approaches to estimate BBB permeability to water typically fall into two categories: those that require injections of exogenous contrast agents (CA) (e.g., dynamic contrast-enhanced, DCE-MRI) and those are completely non-invasive (e.g., arterial spin labelling, ASL). The following sections will discuss these approaches respectively, with a focus on the non-invasive ASL methods.

2.4.2 Measuring BBB permeability to water using contrast agent-based methods

In the absence of CA, the signal difference in intra- and extravascular compartments due to compartmental T1 relaxation rate differences ΔR_1 is masked by the order-of-magnitude higher water exchange rates k_w, resulting in a mono-exponential 'water exchange rate independent' T1 relaxation of the total signal[172]. The aim of a paramagnetic intravascular CA is to shorten the blood water T1, thus increasing ΔR_1 (also termed the relaxographic NMR 'shutter speed'[175]) and enabling the sampled signal to be fitted with a bi-exponential T1 decay model. However, the choice of CA based on molecular size and chemical structure needs to ensure the CA is largely confined to intravascular space, i.e., no or only small BBB leakage of the agent is permitted. For this reason, gadolinium-based contrast agents (GBCA) in DCE-MRI are the most suitable and widely available type of CA administered clinically and in research.

Tissue T1 values were measured by T1-weighted signals both prior to the injection of GBCA and during the first pass of the infused GBCA bolus through the tissue. In the meantime, tissue longitudinal relaxation rate constant, $R_1(t)$, the reciprocal of tissue T1, is a function of CA concentration across time $[CA_b](t)$, given by the two-compartment Shutter-Speed Paradigm (SSP) [167,176,177]:

$$R_1(t) = \frac{1}{2}\left\{\left[R_{1b}(t) + R_{1exv} + k_{po} + \frac{k_{po}p_b}{(1-p_b)}\right]\right.$$

$$\left. - \left[\left(R_{1exv} - R_{1b}(t) - k_{po} + \frac{k_{po}p_b}{(1-p_b)}\right)^2 + \frac{4{k_{po}}^2 p_b}{(1-p_b)}\right]^{\frac{1}{2}}\right\}, \text{(Equation 2.4.3)}$$

where

$$R_{1exv} = \frac{R_1(0) - R_{1b}(0)p_b}{1-p_b}$$

$$R_{1b}(t) = R_{1b}(0) + r_1(1-h)[CA_b](t), \qquad \text{(Equation 2.4.4)}$$

$$p_b = V_b/f_w$$

in which $R_1(0)$, $R_{1b}(0)$, $R_1(t)$, and $R_{1b}(t)$ are the longitudinal relaxation rates for tissue and blood before GBCA injection and at measured time points t, respectively; r_1 is the GBCA relaxivity; h is the haematocrit; p_b is the mole fraction of tissue water in blood; f_w is the tissue volume fraction accessible to mobile aqueous solutes. Voxel-wise estimation of blood volume fraction V_b and water molecule capillary efflux rate constant k_{po} in Equations 2.4.3 and 2.4.4 gives the quantification of the water permeability surface area product of the capillary wall: $PS_w \equiv V_b \cdot k_{po}$.

In a recent study, this shutter-speed-DCE-MRI (SS-DCE-MRI) method demonstrated significantly reduced k_{po} in progressive multiple sclerosis compared to healthy controls[177]. However, the application is hindered by the fact that high temporal resolution of the images is required to capture the rapid change of GBCA concentration, therefore brain coverage is limited to a single-slice acquisition[176,177].

2.4.3 Measuring BBB permeability to water using arterial spin labelling

In the ASL general kinetic model, it is assumed that the labelled blood water acts as the freely diffusible tracer across the capillary wall into the perfused tissue. Also, this one-compartment model treats the labelled bolus as a well-mixed composite of arterial, capillary, and tissue labelled spins, with an instantaneous extraction of blood water from the intravascular space into the extravascular space[61], shown in Figure 2.4.2a. However, as introduced in the previous section, it is since acknowledged that the free passage of water molecules through the blood-brain barrier is limited by semi-permeable tight junctions and AQP4 channels[172]. Meanwhile, arterial blood water tends to remain in the vasculature for a period of time before being extracted into the perfused tissue, violating the assumptions above[178]. Therefore, early work has attempted to improve CBF measurement by incorporating an additional vascular compartment in the kinetic model, hence accounting for water exchange across the BBB.

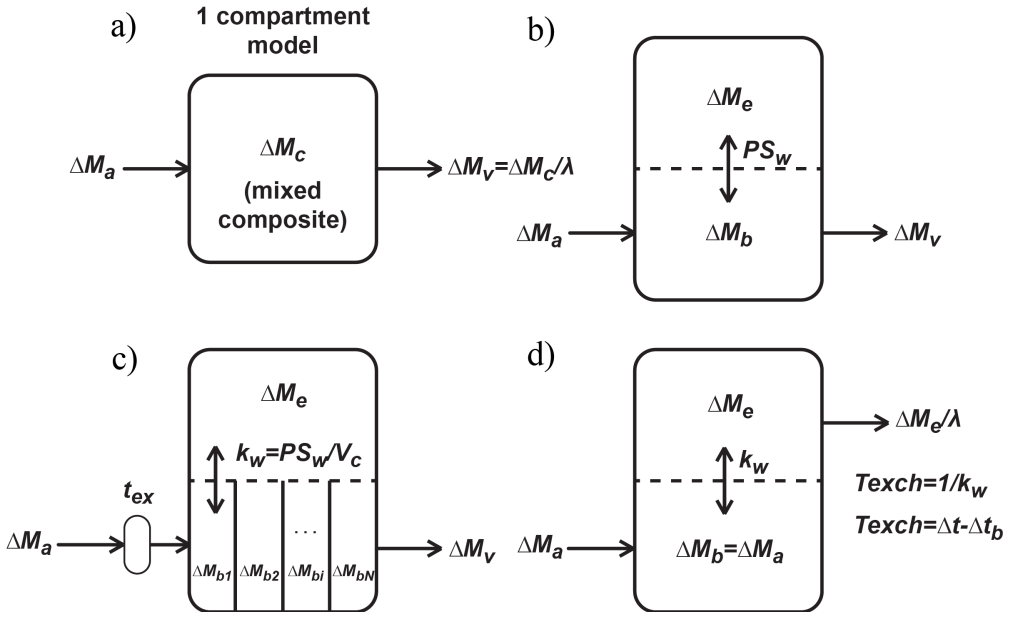


Figure 2.4.2. Kinetic models used in literature in measuring BBB permeability to water. a) The one-compartment general kinetic model by Buxton et al.[61] b) The two-compartment model by Zhou et al.[179], St Lawrence et al.[72], and Parkes et al.[69] c) The four-phase-single-capillary-stepwise (FPSCS) model by Li et al.[117] d) The two-compartment model by Gregori et al.[178], Wells et al.[180], and Ohene et al.[171]

For example, the work of Zhou et al. included a microvascular compartment based on a two-compartment PET model (Figure 2.4.2b), and showed that, in the case of restricted water exchange, the single compartment model will underestimate CBF at 4.7T in animal brain, which has higher CBF levels than human brain[179]. However, Ewing et al. interpreted the difference between the two compartments as a change in effective T1 value, and thereby concluded that with the flow rate of up to 150 mL/100g/min, the one-compartment Kety model will overestimate CBF[181]. St Lawrence et al. used a single-pass approximation (SPA) model to consider the effects of capillary and even venous contributions to the impulse residue function[182]. This study found that using the one-compartment model to interpret data that has capillary and venous contributions will lead to overestimation of CBF at lower flow rates and underestimation of CBF at higher flow rates in grey matter, as well as constant overestimation of CBF in white matter. The large discrepancies among these results are possibly due to the intrinsically low SNR of ASL, as well as a lack of consensus in the values of parameters used.

Parkes et al. later identified two opposite effects that influence on the quantification of CBF with restricted permeability[69,183]. The *T1 effect* is related to the fact that blood water will remain in the vasculature for a finite amount of time before being exchanged to the extravascular space. The longer T1 in blood will result in the slower decay of spin magnetisation, thus an overestimation of perfusion when labelled spins enter the extravascular space. The *outflow effect* regards the water molecules that flow straight into venous blood without exchanging, which causes an underestimation of perfusion in the single-compartment model. The true value of CBF is therefore the compromise between the two effects. In the study of Parkes et al., the total magnetisation is the sum of that from vascular and extravascular compartments[69]:

$$\Delta M(t) = v_{bw}\Delta m_b(t) + v_{ew}\Delta m_e(t), \qquad \text{(Equation 2.4.4)}$$

where v_{bw} and v_{ew} are the corresponding volume of blood water in the vascular and extravascular space, while $\Delta m_b(t)$ and $\Delta m_e(t)$ are the magnetisation difference per unit volume in the vascular and extravascular space, respectively. The revised Bloch equations to express the magnetisation of the two compartments are:

$$\frac{d\left(v_{bw}\Delta m_b(t)\right)}{dt} = -\frac{v_{bw}\Delta m_b(t)}{T_{1b}} + PS_w\left(\Delta m_e(t) - \Delta m_b(t)\right) + f\left(\Delta m_a(t) - \Delta m_v(t)\right)$$

$$\frac{d\left(v_{ew}\Delta m_e(t)\right)}{dt} = -\frac{v_{ew}\Delta m_e(t)}{T_{1t}} - PS_w\left(\Delta m_e(t) - \Delta m_b(t)\right), \qquad \text{(Equation 2.4.5)}$$

where $\Delta m_a(t)$ and $\Delta m_v(t)$ are the corresponding magnetisation difference per unit volume in the arterial and venous side, PS_w is the permeability-surface area produce of the capillary wall, and T_{1b} and T_{1t} are the T1 relaxation rates in the blood and tissue, respectively. The validity of the model was tested under different assumptions to obtain different solutions. In the simplified solution, the results in grey matter were found to be consistent with previous research[182].

Instead of modelling for a vascular compartment, Li et al. proposed a method that takes into account restricted water exchange by incorporating additional parameters such as the arrival time of labelled bolus Δt_a, the time interval before exchange of blood water occurs in the capillary bed Δt_{ex}, and the label duration τ, termed the Four-Phase Single-Capillary Stepwise (FPSCS) model[70] (Figure 2.4.2c). In this model, the entire time-course of the magnetisation within a voxel is segmented into four phases: transit phase ($0 < t < \Delta t_a$), arterial phase ($\Delta t_a < t < \Delta t_a + \Delta t_{ex}$), arterial-capillary transitional phase ($\Delta t_a + \Delta t_{ex} < t < \Delta t_a + \Delta t_{ex} + \tau$), and capillary phase ($\Delta t_a + \Delta t_{ex} + \tau < t$). The total magnetisation in the voxel $\Delta M(t)$ can be expressed as:

$$\begin{aligned} \Delta M(t) &= 0 && 0 < t < \Delta t_a \qquad \text{(Equation 2.4.6)} \\ &= 2M_{0B} f \alpha e^{\frac{-t}{T_{1b}}} \cdot \min(t - \Delta t_a, \tau) && \Delta t_a < t < \Delta t_a + \Delta t_{ex}, \\ &= \Delta M_a(t) + \Delta M_c(t) + \Delta M_e(t) && \Delta t_a + \Delta t_{ex} < t < \Delta t_a + \Delta t_{ex} + \tau \end{aligned}$$

$$= \Delta M_c(t) + \Delta M_e(t) \qquad \Delta t_a + \Delta t_{ex} + \tau < t_a$$

where $\min(x, y)$ returns the smaller value between the arguments, and $\Delta M_a(t)$, $\Delta M_c(t)$, and $\Delta M_e(t)$ are the magnetisation contributions in the voxel from arterial, capillary, and extravascular space, respectively. Their expressions under the corresponding phases are:

$$\Delta M_a(t) = 2M_{0B} f \alpha e^{\frac{-t}{T_{1b}}} \min(\Delta t_a + \Delta t_{ex} + \tau - t, \Delta t_{ex}) \qquad \text{(Equation 2.4.7)}$$

$$\Delta M_c(t) = 2M_{0B} f \alpha e^{\frac{-t}{T_{1b}}} \int_{t_{cl}}^{t} e^{-k_w(t' - \Delta t_a - \Delta t_{ex})} dt' ,$$

$$\Delta M_e(t) = 2M_{0B} f \alpha k_w \int_{t_{cl}}^{t} \int_{\Delta t_a + \Delta t_{ex}}^{t'} e^{-k_w(t_c - \Delta t_a - \Delta t_{ex}) - \frac{t_c + t - t'}{T_{1b}} - \frac{t' - t_c}{T_{1t}}} dt_c dt'$$

where k_w is the water extraction rate in min^{-1}, and $t_{cl} = max(\Delta t_a + \Delta t_{ex}, t - \tau)$, with $\max(x, y)$ returning the greater value between the arguments.

Although compartmental models have achieved improvement in CBF quantification, the estimation of water exchange rates *per se* has been challenging and inconsistent. This is because of the small T1 difference between blood and tissue compartments, which is the contrast that compartmental modelling relies on, and low estimation sensitivity to changes in PS_w[184]. Therefore, other contrast mechanisms to separate the two signal compartments were later exploited, such as T2 relaxation rates using multi-TE ASL and intrinsic diffusivity using diffusion-weighted ASL.

Wells et al. first used multi-TE ASL to plot the origin of the labelled spins and measure the BBB exchange time of water in mouse cortex at 9.4 Tesla[180,185]. The ASL difference signal was fitted with a biexponential decay model as a function of both post-labelling delays (PLDs) and echo times:

$$\Delta M(PLD, TE) = \Delta M_{IV}(PLD) e^{-\frac{TE}{T2_{IV}}} + \Delta M_{EV}(PLD) e^{-\frac{TE}{T2_{EV}}}, \qquad \text{(Equation 2.4.8)}$$

where signal contributions from IV and EV compartments, ΔM_{IV} and ΔM_{EV}, were estimated and fitted to the respective kinetic model for each compartment to obtain the bolus arrival times for blood (Δt_b) and tissue (Δt) (Figure 2.4.2d). The exchange time $Texch$ is defined as the difference between the two arrival times:

$$Texch = \Delta t - \Delta t_b, \qquad \text{(Equation 2.4.9)}$$

which indicates the average time for water to transit through the blood brain barrier into the parenchyma. A more complete model was later applied to human brain at 3T by Gregori et al. that accounted for both T1 and T2 decays[178]. The mean $Texch$ in grey matter was estimated to be about 440ms.

However, the accurate estimation of $Texch$ is hindered by the ill-posed bi-exponential fitting of the four free parameters in Equation 2.4.8: $T2_{IV}$, $T2_{EV}$, ΔM_{IV}, and ΔM_{IV}. A common approach to constrain the fitting for ΔM_{IV} and ΔM_{IV} is to fit the control images, rather than the difference images after pairwise subtraction, at different echo times with a mono-exponential $T2_{EV}$ decay model to obtain a mean $T2_{EV}$ for grey matter[171,186,187], the rationale being that static GM signals predominate in control images and are independent to PLD choices[180]. Other simplifications to increase estimation robustness include fitting short-PLD multi-TE data with a mono-exponential $T2_{IV}$ decay model[171,186], and fitting short-TE multi-PLD data with a ΔM_{IV} kinetic model to obtain Δt_b[188].

Besides the conventional multi-TE readout that took multiple images after one excitation but suffers from rapid T2* decay, T2 weightings can be created by the T2-relaxation-under-spin-tagging (TRUST) technique, where a T2-preparation module consisting of composite 90° and 180° pulses is inserted during the PLD and just before image readout[189], shown in Figure 2.4.3. Depending on the number of 180° pulses within the module, different effective TEs (eTEs) are generated. The TRUST technique can be

combined with time-encoded ASL to increase time efficiency while preserving estimation accuracy of $Texch$[187,190].

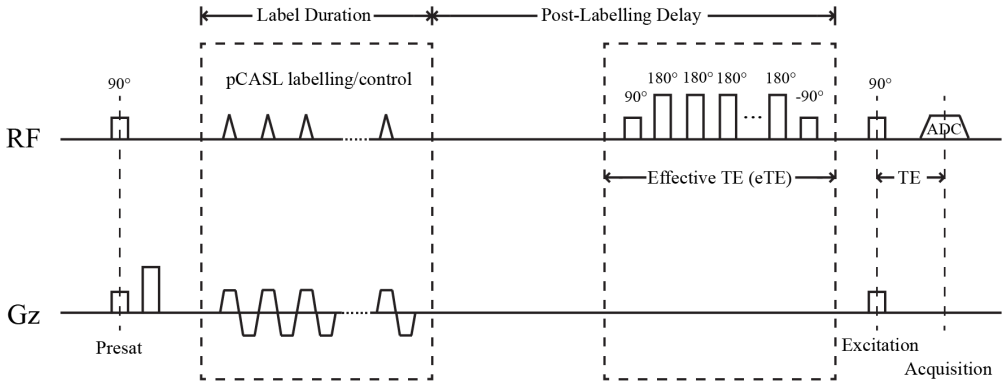


Figure 2.4.3 The schematic of the T2-relaxation-under-spin-tagging (TRUST) ASL technique to create a T2 weighting.

As mentioned above, a number of assumptions have been made in the kinetic models that might not hold true *in vivo*, such as no backflow from EV to IV compartment, no venous outflow, and instantaneous start of exchange when labelled blood reaches the voxel[178], which have possibly resulted in the discrepancies of $Texch$ measurements in different studies[172]. Therefore, models in the future need to take into account the underlying physiological processes and be carefully examined for systematic biases if the assumptions were not met. For example, a recent study tried to account for the delay when arterial labels traverse the arterioles before getting into the extravascular space by including a third pre-capillary compartment and an "intra-voxel transit time" (ITT), and achieved $Texch$ estimation with less variations and good reproducibility[191]. On the other hand, it is debated that whether the T2 variations could be completely attributed to water exchange from capillary to tissue. Other effects might also alter the T2 relaxation rate in the vicinity of the labelled spins, such as field inhomogeneity, and changing oxygenation or haematocrit in the tissue[192,193].

Another method to measure the water exchange rate is to use diffusion-aided ASL to distinguish the intravascular and extravascular signal according to their fast and

slow diffusion properties. Different b-values in diffusion-weighted (DW) ASL sequence are used to generate different levels of diffusion effects[71,72]. Consequently, the contributions from fast- and slow-moving compartments can be fitted to a biexponential decay model using the magnetisation under each b-value:

$$\frac{\Delta M(b)}{\Delta M(0)} = A_1 e^{-bD_1} + A_2 e^{-bD_2}, \qquad \text{(Equation 2.4.10)}$$

where $\Delta M(b)$ is the magnetisation difference under diffusion weighting determined by b, $\Delta M(0)$ is the magnetisation difference without the diffusion gradients, A_1 and A_2 are the signal fractions from fast-and slow-moving compartments, respectively (with $A_1 + A_2 = 1$), and D_1 and D_2 are the respective apparent diffusion coefficients. A_1 and A_2 are then used in a two-compartment model to estimate the water extraction rate k_w [71,174]. In a more recent study, the intrinsic diffusivity of water can be encoded in k-space by modulating the point-spread functions (PSF) to achieve separation of the two compartments[194]. However, the diffusion gradient pulses are conventionally added between ASL preparation and 2D EPI sequence, which yields a long TE that might harm the SNR. Furthermore, the assumption that fast- and slow-moving spins are completely attributed to intravascular and tissue compartments may itself cause systematic bias.

Due to the limitations of the methods described above, Lin et al. proposed a unique method for measuring PS, using a combination of spatial location (phase-contrast) and flow velocity to separate the vascular and extravascular compartments[195]. However, the PS values obtained in this study were confined to the superior sagittal sinus (SSS) without further spatial information, thus could not provide water exchange rate maps as previous studies did.

Up to now, research towards measuring BBB water permeability using ASL techniques is still largely under the assumption that capillary bed is the only microvascular compartment that exchanges water with the tissue. Nevertheless,

discoveries have been made that terminal arterioles and post-capillary venules can be sources of BBB water transportation through aquaporins and other water cotransporters[157]. Also, completed extraction process of water from vascular space to extravascular space is often assumed by using a long PLD in healthy cohorts[194]. However, if prolonged ATT is expected as in elderly cohorts and in cerebrovascular disease models, estimation of PS_w and $Texch$ might be biased or have less sensitivity.

In summary, ASL is intuitively the 'ideal' way of measuring blood-brain barrier permeability to water in a non-invasive manner *in vivo*, compared to PET that uses radioactively labelled $H_2{}^{15}O$ molecules as contrast agents. Nevertheless, the low SNR of ASL images and various assumptions made in the model fitting suggest that further research is needed to validate the reliability of this method, especially its applicability in clinical settings.

2.5 References

1. Armstrong P, Keevil SF. Magnetic resonance imaging--1: Basic principles of image production. *BMJ*. 1991;303(6793):35-40.
2. Bloch F. Nuclear Induction. *Physical Review*. 1946;70(7-8):460-474.
3. Stanisz GJ, Odrobina EE, Pun J, et al. T1, T2 relaxation and magnetization transfer in tissue at 3T. *Magn Reson Med*. 2005;54(3):507-512.
4. Mansfield P, Maudsley AA. Medical imaging by NMR. *Br J Radiol*. 1977;50(591):188-194.
5. MacFall JR, Pelc NJ, Vavrek RM. Correction of spatially dependent phase shifts for partial Fourier imaging. *Magn Reson Imaging*. 1988;6(2):143-155.
6. Feinberg DA, Hale JD, Watts JC, Kaufman L, Mark A. Halving MR imaging time by conjugation: demonstration at 3.5 kG. *Radiology*. 1986;161(2):527-531.
7. McGibney G, Smith MR, Nichols ST, Crawley A. Quantitative evaluation of several partial fourier reconstruction algorithms used in mri. *Magn Reson Med*. 1993;30(1):51-59.
8. Deshmane A, Gulani V, Griswold MA, Seiberlich N. Parallel MR imaging. *Journal of Magnetic Resonance Imaging*. 2012;36(1):55-72.
9. Mezrich R. A perspective on K-space. *Radiology*. 1995;195(2):297-315.
10. Hahn EL. Spin Echoes. *Physical Review*. 1950;80(4):580-594.
11. Elster AD. Gradient-echo MR imaging: techniques and acronyms. *Radiology*. 1993;186(1):1-8.
12. Hennig J, Nauerth A, Friedburg H. RARE imaging: A fast imaging method for clinical MR. *Magn Reson Med*. 1986;3(6):823-833.
13. Haase A, Frahm J, Matthaei D, Hanicke W, Merboldt KD. FLASH imaging. Rapid NMR imaging using low flip-angle pulses. *Journal of Magnetic Resonance*. 1986;67(2):258-266.
14. Carr HY. Steady-State Free Precession in Nuclear Magnetic Resonance. *Physical Review*. 1958;112(5):1693-1701.
15. Mansfield P. Multi-planar image formation using NMR spin echoes. *Journal of Physics C: Solid State Physics*. 1977;10(3):L55-L58.
16. Stehling MK, Turner R, Mansfield P. Echo-Planar Imaging: Magnetic Resonance Imaging in a Fraction of a Second. *Science (1979)*. 1991;254(5028):43-50.
17. Poustchi-Amin M, Mirowitz SA, Brown JJ, McKinstry RC, Li T. Principles and Applications of Echo-planar Imaging: A Review for the General Radiologist. *RadioGraphics*. 2001;21(3):767-779.
18. Wintermark M, Sesay M, Barbier E, et al. Comparative Overview of Brain Perfusion Imaging Techniques. *Stroke*. 2005;36(9).
19. Kety SS, Schmidt CF. The nitrous oxide method for the quantitative determination of cerebral blood flow in man: theory, procedure and normal values. *Journal of Clinical Investigation*. 1948;27(4):476-483.
20. Vonken EJ, van Osch MJ, Bakker CJ, Viergever MA. Measurement of cerebral perfusion with dual-echo multi-slice quantitative dynamic susceptibility contrast MRI. *J Magn Reson Imaging*. 1999;10(2):109-117.

21. Kiselev VG. On the theoretical basis of perfusion measurements by dynamic susceptibility contrast MRI. *Magn Reson Med*. 2001;46(6):1113-1122.
22. Tofts PS, Brix G, Buckley DL, et al. Estimating kinetic parameters from dynamic contrast-enhanced t1-weighted MRI of a diffusable tracer: Standardized quantities and symbols. *Journal of Magnetic Resonance Imaging*. 1999;10(3):223-232.
23. Buckley DL. Uncertainty in the analysis of tracer kinetics using dynamic contrast-enhancedT1-weighted MRI. *Magn Reson Med*. 2002;47(3):601-606.
24. Detre JA, Leigh JS, Williams DS, Koretsky AP. Perfusion imaging. *Magn Reson Med*. 1992;23(1):37-45.
25. Detre JA, Zhang W, Roberts DA, et al. Tissue specific perfusion imaging using arterial spin labeling. *NMR Biomed*. 1994;7(1-2):75-82.
26. Essig M, Shiroishi MS, Nguyen TB, et al. Perfusion MRI: The Five Most Frequently Asked Technical Questions. *American Journal of Roentgenology*. 2013;200(1):24-34.
27. Maccotta L, Detre JA, Alsop DC. The efficiency of adiabatic inversion for perfusion imaging by arterial spin labeling. *NMR Biomed*. 1997;10(4-5):216-221.
28. Pekar J, Jezzard P, Roberts DA, Leigh JS, Frank JA, McLaughlin AC. Perfusion imaging with compensation for asymmetric magnetization transfer effects. *Magn Reson Med*. 1996;35(1):70-79.
29. Silva AC, Zhang W, Williams DS, Koretsky AP. Multi-Slice MRI of Rat Brain Perfusion During Amphetamine Stimulation Using Arterial Spin Labeling. *Magn Reson Med*. 1995;33(2):209-214.
30. Alsop DC, Detre JA. Multisection cerebral blood flow MR imaging with continuous arterial spin labeling. *Radiology*. 1998;208(2):410-416.
31. Edelman RR, Siewert B, Darby DG, et al. Qualitative mapping of cerebral blood flow and functional localization with echo-planar MR imaging and signal targeting with alternating radio frequency. *Radiology*. 1994;192(2):513-520.
32. Golay X, Stuber M, Pruessmann KP, Meier D, Boesiger P. Transfer insensitive labeling technique (TILT): Application to multislice functional perfusion imaging. *Journal of Magnetic Resonance Imaging*. 1999;9(3):454-461.
33. Golay X, Petersen ET, Hui F. Pulsed star labeling of arterial regions (PULSAR): A robust regional perfusion technique for high field imaging. *Magn Reson Med*. 2005;53(1):15-21.
34. Petersen ET, Lim T, Golay X. Model-free arterial spin labeling quantification approach for perfusion MRI. *Magn Reson Med*. 2006;55(2):219-232.
35. Wong EC, Buxton RB, Frank LR. Implementation of quantitative perfusion imaging techniques for functional brain mapping using pulsed arterial spin labeling. *NMR Biomed*. 1997;10(4-5):237-249.
36. Kim SG, Tsekos N v. Perfusion imaging by a flow-sensitive alternating inversion recovery (Fair) technique: Application to functional brain imaging. *Magn Reson Med*. 1997;37(3):425-435.
37. Wong EC, Buxton RB, Frank LR. Quantitative imaging of perfusion using a single subtraction (QUIPSS and QUIPSS II). *Magn Reson Med*. 1998;39(5):702-708.
38. Luh WM, Wong EC, Bandettini PA, Hyde JS. QUIPSS II with thin-slice TI1 periodic saturation: A method for improving accuracy of quantitative perfusion

imaging using pulsed arterial spin labeling. *Magn Reson Med*. 1999;41(6):1246-1254.

39. Alsop DC, Detre JA, Golay X, et al. Recommended implementation of arterial spin-labeled Perfusion mri for clinical applications: A consensus of the ISMRM Perfusion Study group and the European consortium for ASL in dementia. *Magn Reson Med*. 2015;73(1):102-116.
40. Dai W, Garcia D, de Bazelaire C, Alsop DC. Continuous flow-driven inversion for arterial spin labeling using pulsed radio frequency and gradient fields. *Magn Reson Med*. 2008;60(6):1488-1497.
41. Wu WC, Fernández-Seara M, Detre JA, Wehrli FW, Wang J. A theoretical and experimental investigation of the tagging efficiency of pseudocontinuous arterial spin labeling. *Magn Reson Med*. 2007;58(5):1020-1027.
42. Haller S, Zaharchuk G, Thomas DL, Lovblad KO, Barkhof F, Golay X. Arterial Spin Labeling Perfusion of the Brain: Emerging Clinical Applications. *Radiology*. 2016;281(2):337-356.
43. Aslan S, Xu F, Wang PL, et al. Estimation of labeling efficiency in pseudocontinuous arterial spin labeling. *Magn Reson Med*. 2010;63(3):765-771.
44. Gardener AG, Gowland PA, Francis ST. Implementation of quantitative perfusion imaging using pulsed arterial spin labeling at ultra-high field. *Magn Reson Med*. 2009;61(4):874-882.
45. Guenther M. *Highly Efficient Accelerated Acquisition of Perfusion Inflow Series by Cycled Arterial Spin Labeling*.; 2007.
46. Wells JA, Lythgoe MF, Gadian DG, Ordidge RJ, Thomas DL. In vivo Hadamard encoded Continuous arterial spin labeling (H-CASL). *Magn Reson Med*. 2010;63(4):1111-1118.
47. Dai W, Shankaranarayanan A, Alsop DC. Volumetric measurement of perfusion and arterial transit delay using hadamard encoded continuous arterial spin labeling. *Magn Reson Med*. 2013;69(4):1014-1022.
48. Hirschler L, Munting LP, Khmelinskii A, et al. Transit time mapping in the mouse brain using time-encoded pCASL. *NMR Biomed*. 2018;31(2).
49. Teeuwisse WM, Schmid S, Ghariq E, Veer IM, van Osch MJP. Time-encoded pseudocontinuous arterial spin labeling: Basic properties and timing strategies for human applications. *Magn Reson Med*. 2014;72(6):1712-1722.
50. Woods JG, Chappell MA, Okell TW. Designing and comparing optimized pseudo-continuous Arterial Spin Labeling protocols for measurement of cerebral blood flow ☆. *Neuroimage*. 2020;223:117246.
51. Suzuki Y, Helle M, Koken P, van Cauteren M, van Osch MJP. Simultaneous acquisition of perfusion image and dynamic MR angiography using time-encoded pseudo-continuous ASL. *Magn Reson Med*. 2018;79(5):2676-2684.
52. Plas MCE, Schmid S, Versluis MJ, Okell TW, Osch MJP. Time-encoded golden angle radial arterial spin labeling: Simultaneous acquisition of angiography and perfusion data. *NMR Biomed*. 2021;34(7).
53. Guo J, Holdsworth SJ, Fan AP, et al. Comparing accuracy and reproducibility of sequential and Hadamard-encoded multidelay pseudocontinuous arterial spin labeling for measuring cerebral blood flow and arterial transit time in healthy subjects: A simulation and in vivo study. *Journal of Magnetic Resonance Imaging*. 2018;47(4):1119-1132.

54. Neumann K, Schidlowski M, Günther M, Stöcker T, Düzel E. Reliability and Reproducibility of Hadamard Encoded Pseudo-Continuous Arterial Spin Labeling in Healthy Elderly. *Front Neurosci*. 2021;15.
55. Günther M. Efficient visualization of vascular territories in the human brain by cycled arterial spin labeling MRI. *Magn Reson Med*. 2006;56(3):671-675.
56. Okell TW, Chappell MA, Woolrich MW, Günther M, Feinberg DA, Jezzard P. Vessel-encoded dynamic magnetic resonance angiography using arterial spin labeling. *Magn Reson Med*. 2010;64(3):698-706.
57. Wong EC. Vessel-encoded arterial spin-labeling using pseudocontinuous tagging. *Magn Reson Med*. 2007;58(6):1086-1091.
58. Gevers S, Bokkers RP, Hendrikse J, et al. Robustness and Reproducibility of Flow Territories Defined by Planning-Free Vessel-Encoded Pseudocontinuous Arterial Spin-Labeling. *American Journal of Neuroradiology*. 2012;33(2):E21-E25.
59. Okell TW, Chappell MA, Kelly ME, Jezzard P. Cerebral Blood Flow Quantification Using Vessel-Encoded Arterial Spin Labeling. *Journal of Cerebral Blood Flow & Metabolism*. 2013;33(11):1716-1724.
60. van Osch MJ, Teeuwisse WM, Chen Z, Suzuki Y, Helle M, Schmid S. Advances in arterial spin labelling MRI methods for measuring perfusion and collateral flow. *Journal of Cerebral Blood Flow & Metabolism*. 2018;38(9):1461-1480.
61. Buxton RB, Frank LR, Wong EC, Siewert B, Warach S, Edelman RR. A general kinetic model for quantitative perfusion imaging with arterial spin labeling. *Magn Reson Med*. 1998;40(3):383-396.
62. Chappell MA, Woolrich MW, Petersen ET, Golay X, Payne SJ. Comparing model-based and model-free analysis methods for QUASAR arterial spin labeling perfusion quantification. *Magn Reson Med*. 2013;69(5):1466-1475.
63. Hrabe J, Lewis DP. Two analytical solutions for a model of pulsed arterial spin labeling with randomized blood arrival times. *Journal of Magnetic Resonance*. 2004;167(1):49-55.
64. Kazan SM, Chappell MA, Payne SJ. Modeling the Effects of Flow Dispersion in Arterial Spin Labeling. *IEEE Trans Biomed Eng*. 2009;56(6):1635-1643.
65. Chappell MA, Woolrich MW, Kazan S, Jezzard P, Payne SJ, MacIntosh BJ. Modeling dispersion in arterial spin labeling: Validation using dynamic angiographic measurements. *Magn Reson Med*. 2013;69(2):563-570.
66. Chappell MA, MacIntosh BJ, Donahue MJ, Günther M, Jezzard P, Woolrich MW. Separation of macrovascular signal in multi-inversion time arterial spin labelling MRI. *Magn Reson Med*. 2010;63(5):1357-1365.
67. Mildner T, Müller K, Hetzer S, Trampel R, Driesel W, Möller HE. Mapping of arterial transit time by intravascular signal selection. *NMR Biomed*. 2014;27(5):594-609.
68. Su P, Mao D, Liu P, et al. Multiparametric estimation of brain hemodynamics with MR fingerprinting ASL. *Magn Reson Med*. 2017;78(5):1812-1823.
69. Parkes LM, Tofts PS. Improved accuracy of human cerebral blood perfusion measurements using arterial spin labeling: Accounting for capillary water permeability. *Magn Reson Med*. 2002;48(1):27-41.
70. Li K loh, Zhu X, Hylton N, Jahng GH, Weiner MW, Schuff N. Four-phase single-capillary stepwise model for kinetics in arterial spin labeling MRI. *Magn Reson Med*. 2005;53(3):511-518.

71. Wang J, Fernández-Seara MA, Wang S, Lawrence KSS. When Perfusion Meets Diffusion: in vivo Measurement of Water Permeability in Human Brain. *Journal of Cerebral Blood Flow & Metabolism*. 2007;27(4):839-849.
72. st. Lawrence KS, Owen D, Wang DJJ. A two-stage approach for measuring vascular water exchange and arterial transit time by diffusion-weighted perfusion MRI. *Magn Reson Med*. 2012;67(5):1275-1284.
73. McLaughlin AC, Ye FQ, Pekar JJ, Santha AKS, Frank JA. Effect of magnetization transfer on the measurement of cerebral blood flow using steady-state arterial spin tagging approaches: A theoretical investigation. *Magn Reson Med*. 1997;37(4):501-510.
74. Petr J, Schramm G, Hofheinz F, Langner J, van den Hoff J. Modeling magnetization transfer effects of Q2TIPS bolus saturation in multi-TI pulsed arterial spin labeling. *Magn Reson Med*. 2014;72(4):1007-1014.
75. Wu WC, Mazaheri Y, Wong EC. The Effects of Flow Dispersion and Cardiac Pulsation in Arterial Spin Labeling. *IEEE Trans Med Imaging*. 2007;26(1):84-92.
76. Gallichan D, Jezzard P. Modeling the effects of dispersion and pulsatility of blood flow in pulsed arterial spin labeling. *Magn Reson Med*. 2008;60(1):53-63.
77. Kazan SM, Chappell MA, Payne SJ. Modelling the effects of cardiac pulsations in arterial spin labelling. *Phys Med Biol*. 2010;55(3):799-816.
78. Wiersma J, Deichmann R, Ordidge R, Turner R. Removing the effects of CSF partial voluming on fitted CBF and arterial transit times using FAIR, a pulsed arterial spin labelling technique. *Magnetic Resonance Materials in Physics, Biology and Medicine*. 2006;19(3):115-123.
79. Chappell MA, Groves AR, MacIntosh BJ, Donahue MJ, Jezzard P, Woolrich MW. Partial volume correction of multiple inversion time arterial spin labeling MRI data. *Magn Reson Med*. 2011;65(4):1173-1183.
80. Zhao MY, Mezue M, Segerdahl AR, et al. A systematic study of the sensitivity of partial volume correction methods for the quantification of perfusion from pseudo-continuous arterial spin labeling MRI. *Neuroimage*. 2017;162:384-397.
81. st. Lawrence KS, Wang J. Effects of the apparent transverse relaxation time on cerebral blood flow measurements obtained by arterial spin labeling. *Magn Reson Med*. 2005;53(2):425-433.
82. Hernandez-Garcia L, Lee GR, Vazquez AL, Yip CY, Noll DC. Quantification of perfusion fMRI using a numerical model of arterial spin labeling that accounts for dynamic transit time effects. *Magn Reson Med*. 2005;54(4):955-964.
83. Ozyurt O, Dincer A, Ozturk C. A Modified Version of Hrabe-Lewis Model to Account Dispersion of Labeled Bolus in Arterial Spin Labeling. *Proceedings of the 18th Annual Meeting of ISMRM*. 2010;18:4065.
84. Harpen MD, Lecklitner ML. Derivation of gamma variate indicator dilution function from simple convective dispersion model of blood flow. *Med Phys*. 1984;11(5):690-692.
85. Calamante F, Yim PJ, Cebral JR. Estimation of bolus dispersion effects in perfusion MRI using image-based computational fluid dynamics. *Neuroimage*. 2003;19(2):341-353.
86. Calamante F. Arterial input function in perfusion MRI: A comprehensive review. *Prog Nucl Magn Reson Spectrosc*. 2013;74:1-32.

87. Mouannes-Srour JJ, Shin W, Ansari SA, et al. Correction for arterial-tissue delay and dispersion in absolute quantitative cerebral perfusion DSC MR imaging. *Magn Reson Med*. 2012;68(2):495-506.
88. Calamante F, Mørup M, Hansen LK. Defining a local arterial input function for perfusion MRI using independent component analysis. *Magn Reson Med*. 2004;52(4):789-797.
89. Willats L, Christensen S, K Ma H, A Donnan G, Connelly A, Calamante F. Validating a Local Arterial Input Function Method for Improved Perfusion Quantification in Stroke. *Journal of Cerebral Blood Flow & Metabolism*. 2011;31(11):2189-2198.
90. Ye FQ, Mattay VS, Jezzard P, Frank JA, Weinberger DR, McLaughlin AC. Correction for vascular artifacts in cerebral blood flow values measured by using arterial spin tagging techniques. *Magn Reson Med*. 1997;37(2):226-235.
91. Paling D, Thade Petersen E, Tozer DJ, et al. Cerebral Arterial Bolus Arrival Time is Prolonged in Multiple Sclerosis and Associated with Disability. *Journal of Cerebral Blood Flow & Metabolism*. 2014;34(1):34-42.
92. Sorensen AG, Copen WA, Østergaard L, et al. Hyperacute Stroke: Simultaneous Measurement of Relative Cerebral Blood Volume, Relative Cerebral Blood Flow, and Mean Tissue Transit Time. *Radiology*. 1999;210(2):519-527.
93. Sousa I, Vilela P, Figueiredo P. Reproducibility of the quantification of arterial and tissue contributions in multiple postlabeling delay arterial spin labeling. *Journal of Magnetic Resonance Imaging*. 2014;40(6):1453-1462.
94. Carroll TJ, Haughton VM, Rowley HA, Cordes D. Confounding effect of large vessels on MR perfusion images analyzed with independent component analysis. *AJNR Am J Neuroradiol*. 2002;23(6):1007-1012.
95. Reishofer G, Koschutnig K, Enzinger C, et al. Automated macrovessel artifact correction in dynamic susceptibility contrast magnetic resonance imaging using independent component analysis. *Magn Reson Med*. 2011;65(3):848-857.
96. Reishofer G, Fazekas F, Keeling S, et al. Minimizing macrovessel signal in cerebral perfusion imaging using independent component analysis. *Magn Reson Med*. 2007;57(2):278-288.
97. Ferré JC, Bannier E, Raoult H, Mineur G, Carsin-Nicol B, Gauvrit JY. Arterial spin labeling (ASL) perfusion: Techniques and clinical use. *Diagn Interv Imaging*. 2013;94(12):1211-1223.
98. Petersen ET, Mouridsen K, Golay X. The QUASAR reproducibility study, Part II: Results from a multi-center Arterial Spin Labeling test–retest study. *Neuroimage*. 2010;49(1):104-113.
99. Wang Y, Saykin AJ, Pfeuffer J, et al. Regional reproducibility of pulsed arterial spin labeling perfusion imaging at 3T. *Neuroimage*. 2011;54(2):1188-1195.
100. Yoshiura T, Hiwatashi A, Noguchi T, et al. Arterial spin labelling at 3-T MR imaging for detection of individuals with Alzheimer's disease. *Eur Radiol*. 2009;19(12):2819-2825.
101. Binnewijzend MAA, Kuijer JPA, Benedictus MR, et al. Cerebral Blood Flow Measured with 3D Pseudocontinuous Arterial Spin-labeling MR Imaging in Alzheimer Disease and Mild Cognitive Impairment: A Marker for Disease Severity. *Radiology*. 2013;267(1):221-230.

102. Zhang N, Gordon ML, Goldberg TE. Cerebral blood flow measured by arterial spin labeling MRI at resting state in normal aging and Alzheimer's disease. *Neurosci Biobehav Rev*. 2017;72:168-175.
103. Schuff N, Matsumoto S, Kmiecik J, et al. Cerebral blood flow in ischemic vascular dementia and Alzheimer's disease, measured by arterial spin-labeling magnetic resonance imaging. *Alzheimer's & Dementia*. 2009;5(6):454-462.
104. Gao YZ, Zhang JJ, Liu H, Wu GY, Xiong L, Shu M. Regional Cerebral Blood Flow and Cerebrovascular Reactivity in Alzheimer's Disease and Vascular Dementia Assessed by Arterial Spinlabeling Magnetic Resonance Imaging. *Curr Neurovasc Res*. 2012;10(1):49-53.
105. Robertson AD, Messner MA, Shirzadi Z, et al. Orthostatic hypotension, cerebral hypoperfusion, and visuospatial deficits in Lewy body disorders. *Parkinsonism Relat Disord*. 2016;22:80-86.
106. Taylor JP, Firbank MJ, He J, et al. Visual cortex in dementia with Lewy bodies: Magnetic resonance imaging study. *British Journal of Psychiatry*. 2012;200(6):491-498.
107. Chen Y, Wolk DA, Reddin JS, et al. Voxel-level comparison of arterial spin-labeled perfusion MRI and FDG-PET in Alzheimer disease. *Neurology*. 2011;77(22):1977-1985.
108. Pendse N, Wissmeyer M, Altrichter S, et al. Interictal arterial spin-labeling MRI perfusion in intractable epilepsy. *Journal of Neuroradiology*. 2010;37(1):60-63.
109. Storti SF, Boscolo Galazzo I, del Felice A, et al. Combining ESI, ASL and PET for quantitative assessment of drug-resistant focal epilepsy. *Neuroimage*. 2014;102:49-59.
110. Wolf RL, Wang J, Wang S, et al. Grading of CNS neoplasms using continuous arterial spin labeled perfusion MR imaging at 3 Tesla. *Journal of Magnetic Resonance Imaging*. 2005;22(4):475-482.
111. Kim MJ, Kim HS, Kim JH, Cho KG, Kim SY. Diagnostic accuracy and interobserver variability of pulsed arterial spin labeling for glioma grading. *Acta radiol*. 2008;49(4):450-457.
112. Wang DJJ, Alger JR, Qiao JX, et al. Multi-delay multi-parametric arterial spin-labeled perfusion MRI in acute ischemic stroke — Comparison with dynamic susceptibility contrast enhanced perfusion imaging. *Neuroimage Clin*. 2013;3:1-7.
113. Bokkers RPH, Hernandez DA, Merino JG, et al. Whole-Brain Arterial Spin Labeling Perfusion MRI in Patients With Acute Stroke. *Stroke*. 2012;43(5):1290-1294.
114. Zaharchuk G, Do HM, Marks MP, Rosenberg J, Moseley ME, Steinberg GK. Arterial Spin-Labeling MRI Can Identify the Presence and Intensity of Collateral Perfusion in Patients With Moyamoya Disease. *Stroke*. 2011;42(9):2485-2491.
115. Bokkers RPH, van Laar PJ, van de Ven KCC, Kapelle LJ, Klijn CJM, Hendrikse J. Arterial Spin-Labeling MR Imaging Measurements of Timing Parameters in Patients with a Carotid Artery Occlusion. *American Journal of Neuroradiology*. 2008;29(9):1698-1703.
116. Schuff N, Zhang Y, Zhan W, et al. Patterns of altered cortical perfusion and diminished subcortical integrity in posttraumatic stress disorder: An MRI study. *Neuroimage*. 2011;54:S62-S68.

117. Li X, Spence JS, Buhner DM, et al. Hippocampal Dysfunction in Gulf War Veterans: Investigation with ASL Perfusion MR Imaging and Physostigmine Challenge. *Radiology*. 2011;261(1):218-225.
118. Kim J, Whyte J, Patel S, et al. Resting Cerebral Blood Flow Alterations in Chronic Traumatic Brain Injury: An Arterial Spin Labeling Perfusion fMRI Study. *J Neurotrauma*. 2010;27(8):1399-1411.
119. Lin CM, Tseng YC, Hsu HL, et al. Arterial Spin Labeling Perfusion Study in the Patients with Subacute Mild Traumatic Brain Injury. Hendrikse J, ed. *PLoS One*. 2016;11(2):e0149109.
120. Pinkham A, Loughead J, Ruparel K, et al. Resting quantitative cerebral blood flow in schizophrenia measured by pulsed arterial spin labeling perfusion MRI. *Psychiatry Res Neuroimaging*. 2011;194(1):64-72.
121. Ota M, Ishikawa M, Sato N, et al. Pseudo-continuous arterial spin labeling MRI study of schizophrenic patients. *Schizophr Res*. 2014;154(1-3):113-118.
122. Roberts DA, Detre JA, Bolinger L, et al. Renal perfusion in humans: MR imaging with spin tagging of arterial water. *Radiology*. 1995;196(1):281-286.
123. Tan H, Koktzoglou I, Prasad P v. Renal perfusion imaging with two-dimensional navigator gated arterial spin labeling. *Magn Reson Med*. 2014;71(2):570-579.
124. Karger N, Biederer J, Lüsse S, et al. Quantitation of renal perfusion using arterial spin labeling with FAIR-UFLARE. *Magn Reson Imaging*. 2000;18(6):641-647.
125. Schraml C, Schwenzer NF, Martirosian P, Claussen CD, Schick F. Perfusion imaging of the pancreas using an arterial spin labeling technique. *Journal of Magnetic Resonance Imaging*. 2008;28(6):1459-1465.
126. Li X, Metzger GJ. Feasibility of measuring prostate perfusion with arterial spin labeling. *NMR Biomed*. 2013;26(1):51-57.
127. Cai W, Li F, Wang J, et al. A comparison of arterial spin labeling perfusion MRI and DCE-MRI in human prostate cancer. *NMR Biomed*. 2014;27(7):817-825.
128. Shannon CE. A Mathematical Theory of Communication. *Bell System Technical Journal*. 1948;27(3):379-423.
129. Haldar JP. Optimal Sampling & Reconstruction: Theory and Applications. *J Chem Inf Model*. 2019;2(1):5-7.
130. Lundervold AS, Lundervold A. An overview of deep learning in medical imaging focusing on MRI. *Z Med Phys*. 2019;29(2):102-127.
131. Jones B, Allen-Moyer K, Goos P. A-optimal versus D-optimal design of screening experiments. *Journal of Quality Technology*. 2021;53(4):369-382.
132. Gilmour SG, Trinca LA. Bayesian L-optimal exact design of experiments for biological kinetic models. *J R Stat Soc Ser C Appl Stat*. 2012;61(2):237-251.
133. Åström KJ. On the choice of sampling rates in parametric identification of time series. *Inf Sci (N Y)*. 1969;1(3):273-278.
134. Mori F, DiStefano J. Optimal nonuniform sampling interval and test-input design for identification of physiological systems from very limited data. *IEEE Trans Automat Contr*. 1979;24(6):893-900.
135. DiStefano JJ. Optimized blood sampling protocols and sequential design of kinetic experiments. *Am J Physiol Regul Integr Comp Physiol*. 1981;9(3).

136. Cobelli C, Ruggeri A, Distefano JJ, Landaw EM. Optimal Design of Multioutput Sampling Schedules— Software and Applications to Endocrine-Metabolic and Pharmacokinetic Models. *IEEE Trans Biomed Eng*. 1985;BME-32(4):249-256.
137. Graham G, Aarons L. Optimum blood sampling time windows for parameter estimation in population pharmacokinetic experiments. *Stat Med*. 2006;25(23):4004-4019.
138. Daimon T, Goto M. Curvature-adjusted optimal design of sampling times for the inference of pharmacokinetic compartment models. *Stat Med*. 2007;26(14):2799-2812.
139. Jones JA. Optimal Sampling Strategies for the Measurement of Relaxation Times in Proteins. *Journal of Magnetic Resonance*. 1997;126(2):283-286.
140. Alavi SMM, Goetz SM, Peterchev A v. Optimal Estimation of Neural Recruitment Curves Using Fisher Information: Application to Transcranial Magnetic Stimulation. *IEEE Transactions on Neural Systems and Rehabilitation Engineering*. 2019;27(6):1320-1330.
141. Jones JA, Hodgkinson P, Barker AL, Hore PJ. Optimal Sampling Strategies for the Measurement of Spin–Spin Relaxation Times. *J Magn Reson B*. 1996;113(1):25-34.
142. Brihuega-Moreno O, Heese FP, Hall LD. Optimization of Diffusion Measurements Using Cramer-Rao Lower Bound Theory and Its Application to Articular Cartilage. *Magn Reson Med*. 2003;50(5):1069-1076.
143. Samson RS, Symms MR, Cercignani M, et al. Optimisation of quantitative Magnetisation Transfer (qMT) sequence acquisition parameters INTRODUCTION : METHODS : RESULTS : *Brain Res*. 2006;14(4):2493-2493.
144. Cercignani M, Alexander DC. Optimal acquisition schemes for in vivo quantitative magnetization transfer MRI. *Magn Reson Med*. 2006;56(4):803-810.
145. Battiston M, Grussu F, Ianus A, et al. An optimized framework for quantitative magnetization transfer imaging of the cervical spinal cord in vivo. *Magn Reson Med*. 2018;79(5):2576-2588.
146. Maus B, van Breukelen GJP. Optimal design for functional magnetic resonance imaging experiments: Methodology, challenges, and future perspectives. *Zeitschrift fur Psychologie / Journal of Psychology*. 2013;221(3):174-189.
147. Tee YK, Khrapitchev AA, Sibson NR, Payne SJ, Chappell MA. Optimal sampling schedule for chemical exchange saturation transfer. *Magn Reson Med*. 2013;70(5):1251-1262.
148. Zhao B, Haldar JP, Liao C, et al. Optimal experiment design for magnetic resonance fingerprinting: Cramér-rao bound meets spin dynamics. *IEEE Trans Med Imaging*. 2019;38(3):844-861.
149. Lahiri A, Fessler JA, Hernandez-Garcia L. Optimizing MRF-ASL scan design for precise quantification of brain hemodynamics using neural network regression. *Magn Reson Med*. 2020;83(6):1979-1991.
150. Mickevicius NJ, Nencka AS, Paulson ES. Reducing the Dimensionality of Optimal Experiment Design for Magnetic Resonance Fingerprinting. Published online October 1, 2020.
151. Xie J, Gallichan D, Gunn RN, Jezzard P. Optimal design of pulsed arterial spin labeling MRI experiments. *Magn Reson Med*. 2008;59(4):826-834.

152. Sanches J, Sousa I, Figueiredo P. Bayesian fisher information criterion for sampling optimization in ASL-MRI. In: *2010 IEEE International Symposium on Biomedical Imaging: From Nano to Macro*. IEEE; 2010:880-883.
153. Santos N, Sanches JM, Sousa I, Figueiredo P. Optimal Sampling and Estimation in PASL Perfusion Imaging. *IEEE Trans Biomed Eng*. 2011;58(11):3165-3174.
154. Xie J, Clare S, Gallichan D, Gunn RN, Jezzard P. Real-time adaptive sequential design for optimal acquisition of arterial spin labeling MRI data. *Magn Reson Med*. 2010;64(1):203-210.
155. Woods JG, Chappell MA, Okell TW. A general framework for optimizing arterial spin labeling MRI experiments. *Magn Reson Med*. 2019;81(4):2474-2488.
156. Woods JG, Chappell MA, Okell TW. Designing and comparing optimized pseudo-continuous Arterial Spin Labeling protocols for measurement of cerebral blood flow. *Neuroimage*. 2020;223(August):117246.
157. Abbott NJ, Patabendige AAK, Dolman DEM, Yusof SR, Begley DJ. Structure and function of the blood-brain barrier. *Neurobiol Dis*. 2010;37(1):13-25.
158. Barichello T, Collodel A, Hasbun R, Morales R. An Overview of the Blood-Brain Barrier. In: *Neuromethods*. Vol 142. Humana Press Inc.; 2019:1-8.
159. Kassner A, Merali Z. Assessment of Blood–Brain Barrier Disruption in Stroke. *Stroke*. 2015;46(11):3310-3315.
160. Chen H, Zhu G, Liu N, Li Y, Xia Y. Applications and development of permeability imaging in ischemic stroke (Review). *Exp Ther Med*. 2018;16(3):2203-2207.
161. Tiwari Y v, Lu J, Shen Q, Cerqueira B, Duong TQ. Magnetic resonance imaging of blood–brain barrier permeability in ischemic stroke using diffusion-weighted arterial spin labeling in rats. *Journal of Cerebral Blood Flow & Metabolism*. 2017;37(8):2706-2715.
162. Niibo T, Ohta H, Miyata S, Ikushima I, Yonenaga K, Takeshima H. Prediction of blood-brain barrier disruption and intracerebral hemorrhagic infarction using arterial spin-labeling magnetic resonance imaging. *Stroke*. 2017;48(1):117-122.
163. Minagar A, Alexander JS. Blood-brain barrier disruption in multiple sclerosis. *Multiple Sclerosis*. 2003;9(6):540-549.
164. Wengler K, Ha J, Syritsyna O, et al. Abnormal blood-brain barrier water exchange in chronic multiple sclerosis lesions: A preliminary study. *Magn Reson Imaging*. 2020;70(April):126-133.
165. Lin Z, Sur S, Liu P, et al. Blood–Brain Barrier Breakdown in Relationship to Alzheimer and Vascular Disease. *Ann Neurol*. 2021;90(2):227-238.
166. Chagnot A, Barnes SR, Montagne A. Magnetic Resonance Imaging of Blood–Brain Barrier permeability in Dementia. *Neuroscience*. 2021;474:14-29.
167. Anderson VC, Lenar DP, Quinn JF, Rooney WD. The Blood-Brain Barrier and Microvascular Water Exchange in Alzheimer's Disease. *Cardiovasc Psychiatry Neurol*. 2011;2011:1-9.
168. Desai BS, Monahan AJ, Carvey PM, Hendey B. Blood-Brain Barrier Pathology in Alzheimer's and Parkinson's Disease: Implications for Drug Therapy. *Cell Transplant*. 2007;16:285-299.

169. Saunders NR, Dziegielewska KM, Møllgård K, Habgood MD. Markers for blood-brain barrier integrity: How appropriate is Evans blue in the twenty-first century and what are the alternatives? *Front Neurosci*. 2015;9(OCT).
170. Yang FY, Chang WY, Chen JC, Lee LC, Hung YS. Quantitative assessment of cerebral glucose metabolic rates after blood-brain barrier disruption induced by focused ultrasound using FDG-MicroPET. *Neuroimage*. 2014;90:93-98.
171. Ohene Y, Harrison IF, Nahavandi P, et al. Non-invasive MRI of brain clearance pathways using multiple echo time arterial spin labelling: an aquaporin-4 study. *Neuroimage*. 2019;188:515-523.
172. Dickie BR, Parker GJM, Parkes LM. Measuring water exchange across the blood-brain barrier using MRI. *Prog Nucl Magn Reson Spectrosc*. 2020;116:19-39.
173. Davoodi-Bojd E, Chopp M, Soltanian-Zadeh H, Wang S, Ding G, Jiang Q. An Analytical Model for Estimating Water Exchange Rate in White Matter Using Diffusion MRI. Jung RE, ed. *PLoS One*. 2014;9(5):e95921.
174. Shao X, Ma SJ, Casey M, D'Orazio L, Ringman JM, Wang DJJ. Mapping water exchange across the blood-brain barrier using 3D diffusion-prepared arterial spin labeled perfusion MRI. *Magn Reson Med*. 2019;81(5):3065-3079.
175. Landis CS, Li X, Telang FW, et al. Equilibrium transcytolemmal water-exchange kinetics in skeletal muscle in vivo. *Magn Reson Med*. 1999;42(3):467-478.
176. Rooney WD, Li X, Sammi MK, Bourdette DN, Neuwelt EA, Springer CS. Mapping human brain capillary water lifetime: high-resolution metabolic neuroimaging. *NMR Biomed*. 2015;28(6):607-623.
177. Tagge IJ, Anderson VC, Springer CS, et al. Gray matter blood-brain barrier water exchange dynamics are reduced in progressive multiple sclerosis. *Journal of Neuroimaging*. 2021;31(6):1111-1118.
178. Gregori J, Schuff N, Kern R, Günther M. T2-based arterial spin labeling measurements of blood to tissue water transfer in human brain. *Journal of Magnetic Resonance Imaging*. 2013;37(2):332-342.
179. Zhou J, Wilson DA, Ulatowski JA, Traystman RJ, van Zijl PCM. Two-compartment exchange model for perfusion quantification using arterial spin tagging. *Journal of Cerebral Blood Flow and Metabolism*. 2001;21(4):440-455.
180. Wells JA, Siow B, Lythgoe MF, Thomas DL. Measuring Biexponential Transverse Relaxation of the ASL Signal at 9.4 T to Estimate Arterial Oxygen Saturation and the Time of Exchange of Labeled Blood Water into Cortical Brain Tissue. *Journal of Cerebral Blood Flow & Metabolism*. 2013;33(2):215-224.
181. Ewing JR, Cao Y, Fenstermacher J. Single-coil arterial spin-tagging for estimating cerebral blood flow as viewed from the capillary: Relative contributions of intra- and extravascular signal. *Magn Reson Med*. 2001;46(3):465-475.
182. St Lawrence KS, Frank JA, McLaughlin AC. Effect of restricted water exchange on cerebral blood flow values calculated with arterial spin tagging: A theoretical investigation. *Magn Reson Med*. 2000;44(3):440-449.
183. Parkes LM. Quantification of cerebral perfusion using arterial spin labeling: Two-compartment models. *Journal of Magnetic Resonance Imaging*. 2005;22(6):732-736.
184. Carr JP, Buckley DL, Tessier J, Parker GJM. What levels of precision are achievable for quantification of perfusion and capillary permeability surface area product using ASL? *Magn Reson Med*. 2007;58(2):281-289.

185. Wells J, Thomas D, Saga T, Kershaw J, Aoki I. MRI of cerebral micro-vascular flow patterns: A multi-direction diffusion-weighted ASL approach. *Journal of Cerebral Blood Flow & Metabolism*. 2017;37(6):2076-2083.
186. Ohene Y, Harrison IF, Evans PG, Thomas DL, Lythgoe MF, Wells JA. Increased blood–brain barrier permeability to water in the aging brain detected using noninvasive multi-TE ASL MRI. *Magn Reson Med*. 2021;85(1):326-333.
187. Petitclerc L, Schmid S, Hirschler L, van Osch MJP. Combining T2 measurements and crusher gradients into a single ASL sequence for comparison of the measurement of water transport across the blood–brain barrier. *Magn Reson Med*. 2021;85(5):2649-2660.
188. Schidlowski M, Boland M, Rüber T, Stöcker T. Blood–brain barrier permeability measurement by biexponentially modeling whole-brain arterial spin labeling data with multiple T2-weightings. *NMR Biomed*. 2020;33(10):1-12.
189. Lu H, Ge Y. Quantitative evaluation of oxygenation in venous vessels using T2-relaxation-under-spin-tagging MRI. *Magn Reson Med*. 2008;60(2):357-363.
190. Schmid S, Teeuwisse WM, Lu H, Osch MJP van. Time-efficient determination of spin compartments by time-encoded pCASL T2-relaxation-under-spin-tagging and its application in hemodynamic characterization of the cerebral border zones. *Neuroimage*. 2015;123:72-79.
191. Mahroo A, Breutigam NJ, Gunther M. Assessing Repeatability of Blood Brain Barrier Permeability Measure Using Contrast-free MRI. In: *Proc. Intl. Soc. Mag. Reson. Med. 28*. ; 2021:2020-2022.
192. Liu P, Chalak LF, Krishnamurthy LC, et al. T1 and T2 values of human neonatal blood at 3 Tesla: Dependence on hematocrit, oxygenation, and temperature. *Magn Reson Med*. 2016;75(4):1730-1735.
193. Portnoy S, Milligan N, Seed M, Sled JG, Macgowan CK. Human umbilical cord blood relaxation times and susceptibility at 3 T. *Magn Reson Med*. 2018;79(6):3194-3206.
194. Wengler K, Bangiyev L, Canli T, Duong TQ, Schweitzer ME, He X. 3D MRI of whole-brain water permeability with intrinsic diffusivity encoding of arterial labeled spin (IDEALS). *Neuroimage*. 2019;189:401-414.
195. Lin Z, Li Y, Su P, et al. Non-contrast MR imaging of blood-brain barrier permeability to water. *Magn Reson Med*. 2018;80(4):1507-1520.

3 Sensitivity of optimised protocols to macrovascular contamination, flow dispersion, and prolonged arterial transit time

3.1 Introduction

Arterial spin labelling (ASL) is gaining popularity for its inherently non-invasive ability to quantify brain perfusion, i.e., regional cerebral blood flow (CBF)[1]. ASL image acquisition adopts a label-control subtraction approach. In the label image, arterial-blood water spins are labelled by inversion[2], followed by one or multiple post-labelling delays (PLD) to allow blood to perfuse the target tissue before image readout. The same procedure is administered in the control image but without inversion of the spins. An ASL image is obtained by subtracting the label image from the control image. Perfusion quantification using a single PLD is the general recommendation of the community for clinical applications[3], due to its robustness to arterial transit time (ATT) and relatively simple implementation. However, there is a trade-off between the recommended long PLD which ensures a more complete arrival of blood into long ATT regions and ASL signal loss due to T1 relaxation. Therefore, there has been increasing interest in the greater accuracy available from multi-PLD ASL[4]. In multi-PLD ASL, a series of paired label-control images can be acquired by incrementing the PLD or by use of a Look-Locker acquisition scheme[5]. Signals from different time points are then fit with a tracer kinetic model depicting the dynamic concentration of the labelled blood water[6], enabling simultaneous quantification of CBF and other parameters such as ATT.

Recently, a general framework was proposed by Woods *et al*. for optimising multi-PLD sampling protocols[7]. This framework yielded two optimised multi-PLD

protocols: CBF-ATTopt and CBFopt, which were optimised for combined CBF and ATT estimation and CBF estimation only, respectively. Both optimised protocols achieved better parameter estimation performance than the more commonly used evenly spaced multi-PLD and single-PLD protocols[7]. However, as multi-PLD ASL tends to use some short PLDs, when labelled blood may not have reached the target tissue but still remain in the major arteries, artefacts caused by macrovascular signal contamination (MVC) might arise[8]. Furthermore, flow dispersion due to blood traversing the vascular branches and cardiac pulsation will compromise the idealised arterial input function (AIF) in the kinetic model used in this framework[9]. The effects of macrovascular contamination and flow dispersion might be more prominent in the presence of prolonged ATTs seen in cerebrovascular disease[10] and deep white matter[11].

In this chapter, we tested the performance for CBF and ATT estimation of the previously proposed protocols, CBF-ATTopt and CBFopt, along with a reference multi-PLD protocol and a single-PLD protocol, under the effects of MVC and dispersion over a prolonged ATT range, using both simulated and *in vivo* data. We examined CBF and ATT estimation errors across a range of arterial blood volumes (aBV) to investigate the sensitivity to MVC of each protocol, while also comparing the results with an extended kinetic model that explicitly accounts for MVC effects. Furthermore, estimation errors of each protocol across different levels of dispersion, as well as over a prolonged ATT range, were also examined.

3.2 Methods

3.2.1 Kinetic Modelling

The kinetic model used in this work was based on the general kinetic model proposed by Buxton *et al.*[6] incorporating a macrovascular compartment[8] and a Gamma dispersion

kernel[12]. In the general kinetic model, the ASL difference signal of the tissue compartment $\Delta M_t(t)$ can be expressed by:

$$\Delta M_t(t) = 2M_{0B} f\{c(t) * [r(t) \cdot m(t)]\}, \qquad \text{(Equation 3.2.1)}$$

where M_{0B} is the equilibrium magnetisation of arterial blood and f is the CBF in (ml blood)/(ml tissue)/s; $c(t)$, $r(t)$, and $m(t)$ denote the delivery function, residue function, and magnetisation relaxation function, respectively. The $*$ denotes convolution operation. For pseudo-continuous ASL (pCASL), these functions take the form of:

$$\begin{aligned} c(t) &= 0 && 0 < t < \Delta t \qquad \text{(Equation 3.2.2)} \\ &= \alpha e^{\frac{-\Delta t}{T_{1b}}} && \Delta t < t < \tau + \Delta t \\ &= 0 && \tau + \Delta t < t \\ r(t) &= e^{\frac{-ft}{\lambda}} \\ m(t) &= e^{\frac{-t}{T_{1t}}} \end{aligned}$$

where α is the labelling efficiency, Δt is the ATT of tissue, τ is the label duration, T_{1b} and T_{1t} are the longitudinal relaxation constants of arterial blood and tissue, respectively, and λ is the blood-tissue partition coefficient of water.

The form of the difference signal of the macrovascular compartment[8] is related to the delivery function $c(t)$ but has its own transit time Δt_a:

$$\begin{aligned} \Delta M_a(t) &= 0 && 0 < t < \Delta t_a \qquad \text{(Equation 3.2.3)} \\ &= 2\alpha M_{0B} e^{\frac{-\Delta t_a}{T_{1b}}} \cdot aBV\% && \Delta t_a < t < \tau + \Delta t_a, \\ &= 0 && \tau + \Delta t_a < t \end{aligned}$$

where aBV is the arterial blood volume fraction in percentage. The total signal in a voxel is the sum of its tissue compartment and macrovascular compartment, i.e., $\Delta M(t) = \Delta M_t(t) + \Delta M_a(t)$.

Flow dispersion can be accounted for by convolving the delivery function $c(t)$ with a dispersion kernel $k(t)$ to change its shape. Therefore,

$$c'(t) = c(t) * k(t). \qquad \text{(Equation 3.2.4)}$$

Here we chose a Gamma dispersion kernel for its physiologically plausible shape and relatively low computational complexity[12]:

$$k(t) = \frac{s^{1+sp}}{\Gamma(1+sp)} t^{sp} e^{-st}, \qquad \text{(Equation 3.2.5)}$$

where $\Gamma(x)$ is the Gamma function, and s, p depict the "sharpness" and time-to-peak characteristics of the dispersion kernel. The lower the value of s, the less sharp the Gamma kernel is, and the higher degree of dispersion the kernel adds to the signal. In this study, we used the same dispersion parameters for both tissue and macrovascular components.

By switching whether dispersion or macrovascular contamination is included, four types of signals were simulated: no dispersion no macrovascular contamination ($\mathrm{D}-\mathrm{M}-$), no dispersion with macrovascular contamination ($\mathrm{D}-\mathrm{M}+$), with dispersion no macrovascular contamination ($\mathrm{D}+\mathrm{M}-$), and with dispersion with macrovascular contamination ($\mathrm{D}+\mathrm{M}+$).

3.2.2 Simulation Experiments

Four different PLD protocols from Woods *et al*. were investigated: single-PLD, reference multi-PLD, CBF-ATTopt, and CBFopt[7]. These protocols were optimised for CBF and/or ATT accuracy for an ATT range of 0.5 s to 1.8 s in the absence of dispersion and macrovascular signal. Table 3.2.1 lists the PLDs and number of averages for each protocol obtained by optimisation. For each protocol, pCASL signals were simulated in MATLAB (The Mathworks, Natick, MA) using the four models specified in the previous

section. Two factors were varied in simulation: ATTs from 0.5s to 3.0s with 0.05s interval, which includes ATT values much longer than those which had been optimised for, and an aBV range from 0 to 2% with 0.05% interval.

Protocol	**Post-labelling delays (s)**	**PLDs (N)**	**Repeats (N)**
Single-PLD	1.8	1	33
Reference multi-PLD	0.25, 0.5, 0.75, 1, 1.25, 1.5	6	7
CBF-ATTopt	0.2, 0.2, 0.225, 0.3, 0.375, 0.45, 0.5, 0.55, 0.6, 0.6, 0.625, 0.625, 0.65, 0.65, 0.675, 0.675, 0.7, 0.7, 0.7, 0.7, 1.25, 1.275, 1.3, 1.35, 1.375, 1.4, 1.425, 1.425, 1.475, 1.5, 1.675, 1.75, 1.8, 1.825, 1.85, 1.875, 1.9, 1.925, 1.95, 1.975	40	1
CBFopt	0.2, 0.7, 0.825, 1, 1.125, 1.25, 1.325, 1.4, 1.475, 1.55, 1.625, 1.675, 1.7, 1.725, 1.75, 1.775, 1.8, 1.825, 1.85, 1.85, 1.875, 1.9, 1.925, 1.925, 1.95, 1.975, 1.975, 2, 2.025, 2.025, 2.05, 2.075, 2.075	34	1

Table 3.2.1 Protocol timings from Woods et al[7].

To test the effects of flow dispersion, simulations were performed under three conditions based on different values of s (and a constant $p_0 = 0.17s$) in the Gamma kernel: $s_0 = 1/0.13$ s^{-1}, $s_0/2$, and $s_0/4$, each with a higher degree of flow dispersion. Figure 3.2.1 illustrates the effect of different dispersion kernels on both tissue and macrovascular signals.

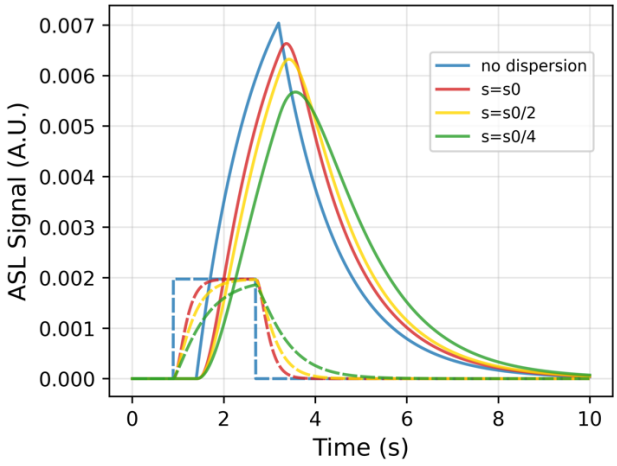


Figure 3.2.1 The effect of different dispersion kernels to the tissue (solid lines) and macrovascular signals (dashed lines). A smaller parameter s indicates a higher level of flow dispersion. Parameters used in this simulation: ATT_t = 1.4s, ATT_a = 0.9s.

Gaussian white noise was then added to all signals, with its standard deviation defined by the maximum signal intensity sampled across all PLDs in a typical condition (ATT = 1.4s, aBV = 0.2%) over an SNR of 9.37 under common MR acquisition environment[13], i.e., $SD_{noise} = \Delta M_{\text{samp_max}}/SNR$. Each condition was repeated for 2000 times. See Table 3.2.2 for all simulation parameters.

Parameter	**Value**
Cerebral blood flow (f)	60 ml/100g/min
Blood-tissue partition coefficient of water (λ)	0.9 ml/g
T1 of arterial blood (T_{1b})	1.65s
T1 of tissue (T_{1t})	1.3s
Labelling efficiency (α)	0.85
Label duration (τ)	1.4s
ATT of macrovascular compartment (Δt_a)	Δt-0.5s
Arterial blood volume (aBV) when varying tissue ATT	0.2%
Tissue ATT (Δt) when varying aBV	1.4s
Sharpness of Gamma dispersion kernel (s_0)	1/0.13s^{-1}
Time-to-peak of Gamma dispersion kernel (p_0)	0.17s

Table 3.2.2 Parameters used for simulations.

For the purposes of simplification in this study, macrovascular ATT was fixed relative to tissue ATT by 0.5s, this implicitly assumes that the mechanism that prolongs the ATT (e.g., pathology in the feeding arteries) affects both the macrovascular and tissue blood supply by the same amount, but the reality *in vivo* may be more complex than this in practice.

Noisy signals for each protocol were then fit with different kinetic models to obtain CBF and ATT (only for multi-PLD protocols) estimates and errors using the BASIL toolkit from the Oxford Centre for Functional MRI of the Brain (FMRIB)'s software library (FSL)[14], which uses a variational Bayesian inference method with estimation priors applied to each parameter. See Table 3.2.3 for a list of parameter priors used.

Parameter	**Mean**	**SD**
$f\ (ml/100g/min)$	0	10^3
$\Delta t\ (s)$	1.3	10^3
$\tau\ (s)$	1.8	0.3
$aBV\ (\%)$	0	10^3
$\Delta t_a\ (s)$	0.9	10^3
$s_0\ (s^{-1})$	1/0.13	0.3
$p_0\ (s)$	0.17	0.3
$T_{1b}\ (s)$	1.65	0.3
$T_{1t}\ (s)$	1.3	0.3

Table 3.2.3 Specifications of the estimation priors (as mean and standard deviation by a normal distribution) used in the variational Bayesian inference method for simulation experiments.

All signals were fit with the general kinetic model (denoted gkm). $\mathrm{D-M+}$, $\mathrm{D+M-}$, and $\mathrm{D+M+}$ data were also fitted with the extended kinetic model by accounting for macrovascular contamination (denoted gkm + mvc), dispersion (denoted gkm + disp), or both (denoted gkm + disp + mvc). For the full list of models fit used, see

Table 3.2.4. Apart from estimating for CBF and ATT in gkm, aBV and Δt_a were estimated in gkm + mvc and gkm + disp + mvc, while s and p were estimated in gkm + disp and gkm + disp + mvc. Other parameters assumed the values of the priors in Table 3.2.3 when an estimation was not possible. For model fitting of the single-PLD protocol in simulation, we assumed an ATT of 1.25s[7]. CBF and ATT estimation error using each model was calculated by '(estimated value - ground truth value)/ground truth value * 100'. Results were compared both across models and across protocols. As a measure of each protocol's sensitivity to macrovascular contamination, we calculated the slopes of the CBF and ATT estimation error line of best fit when aBV > 0.5% for D − M + signals fitted with gkm and gkm + mvc.

Signals	**Models used for fitting**
No dispersion no macrovascular contamination (D − M −)	general kinetic model (gkm)
No dispersion with macrovascular Contamination (D − M +)	gkm, gkm + mvc
With dispersion no macrovascular contamination (D + M −)	gkm, gkm + disp
With dispersion with macrovascular Contamination (D + M +)	gkm, gkm + mvc, gkm + disp, gkm + disp + mvc

Table 3.2.4 Models used for fitting each signal.

3.2.3 In Vivo Experiments

A dataset from 7 healthy subjects (3 female, 23-27 years old) from Woods *et al.* was retrospectively analysed to examine the consistency between the results of simulations and *in vivo* acquisition[7]. The pCASL imaging parameters were: 2D-EPI readout, 5 slices, voxel size = 3.4 x 3.4 x 5 mm^3, 1.4s label duration, and flow crusher gradients with a cut-off velocity of 4 cm/s. A full list of imaging parameters and pre-processing methods can be found in Woods *et al*[7]. Grey matter (GM) masks were obtained from the T1

structural image using the FAST tool from FSL[15]. CBF and ATT estimates were obtained by fitting the data of each protocol with the four models. The estimates were then binned and averaged with 0.05s ATT or 0.05% aBV interval across all subjects, so as to match the sampling points in simulation.

Another four sets of CBF and ATT estimates were obtained by fitting the four models (gkm, gkm + disp, gkm + mvc, gkm + disp + mvc) to the combined data from all four protocols, giving an equal weighting to each protocol. Voxels were excluded if the CBF and ATT estimated by gkm from the combined data had standard deviations higher than 15 ml/100g/min and 1.0s, respectively, and were restricted by the parameter range of interest (0.5s < ATT < 3.0s, 0.0 < aBV < 2.0%). These sets of estimates were used in place of ground-truth estimates in calculating estimation errors of each protocol, since there was no independent gold-standard protocol or universal ground-truth for the *in vivo* data. For example, the CBF error of Reference Multi-PLD estimated by gkm with respect to the CBF estimated by gkm+mvc from the combined data was calculated by

$$\text{CBF Error\%}^{\text{gkm+mvc}}_{\text{Ref-multi, gkm}} = \frac{\text{CBF}_{\text{Ref-multi, gkm}} - \text{CBF}_{\text{combined, gkm+mvc}}}{\text{CBF}_{\text{combined, gkm+mvc}}} \times 100. \quad \text{(Equation 3.2.6)}$$

The resulting estimation errors were compared to the errors in the equivalent simulation study. For example, the above CBF estimation error was compared to the CBF error of Reference Multi-PLD using $\mathrm{D-M+}$ signals fit by gkm. This allowed an assessment of whether differences seen using the gkm on real data when compared to using a more sophisticated model matched with the errors seen in simulation when dispersion and/or macrovascular contamination were included in the signal.

Similar to the sensitivity to MVC measure obtained in simulation, slopes of CBF and ATT estimation errors fit with gkm and gkm + mvc (with respect to $\text{CBF}_{\text{combined, gkm+mvc}}$ and $\text{ATT}_{\text{combined, gkm+mvc}}$) were generated by linear regression when aBV > 0.5%.

All statistical tests were performed using two-sample t-tests (one-tailed, with Bonferroni correction for multiple comparisons, p-value thresholded at 0.05) between estimations by different protocols.

3.3 Results

Using the four models to fit *in vivo* data of different protocols, whole brain and segmented GM CBF and ATT maps were obtained. Across all subjects, 1216 voxels were identified as having prolonged ATT (ATT > 1.8s, 6.19% of all GM voxels), and 1268 voxels as having high macrovascular signal (aBV > 0.25%, 6.46% of all GM voxels). Representative whole-brain CBF and ATT estimation maps and absolute error maps (protocols – combined) from one subject are shown in Figure 3.3.1. Reasonably good visual agreement was found between different protocols and fitting models. Evidence of macrovascular contamination could be seen in some cortical voxels in Reference Multi-PLD and CBF-ATTopt, which appeared as higher CBF estimation. CBFopt appeared to be in best agreement with the CBF estimation from the combined data among the three multi-PLD protocols.

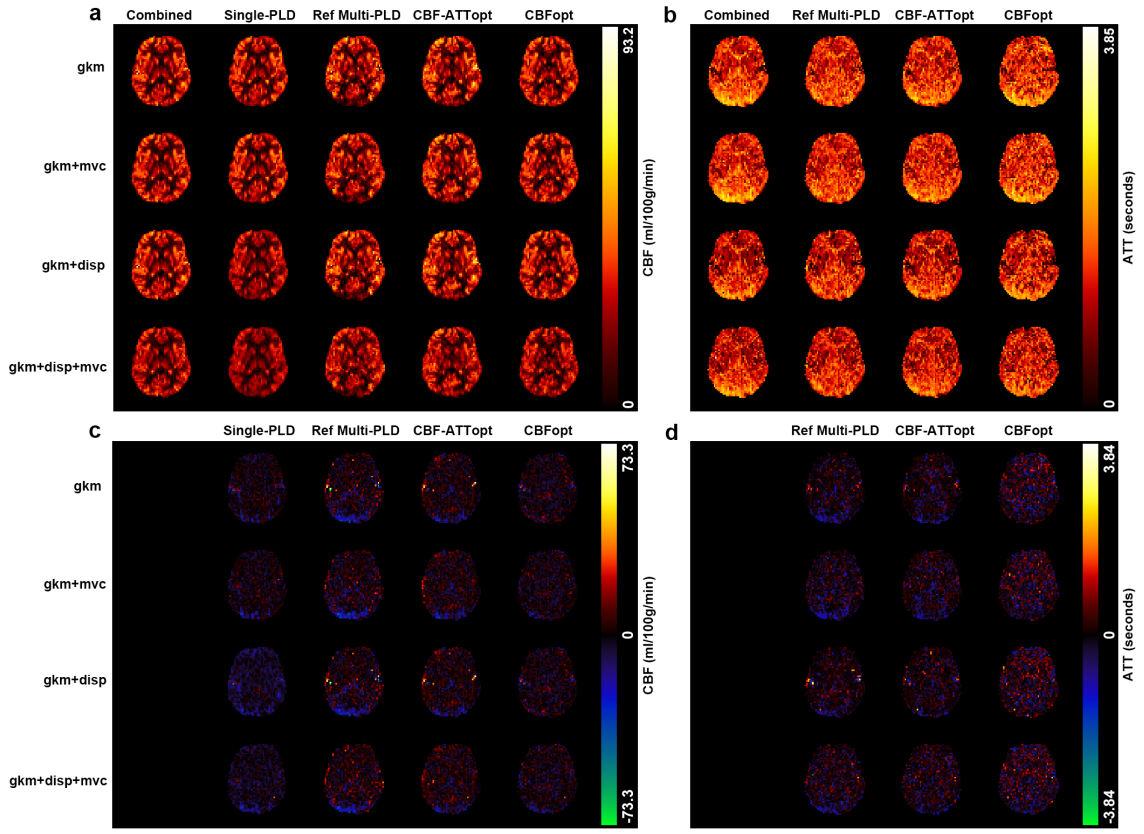


Figure 3.3.1 Representative whole-brain CBF and ATT estimation maps and absolute error maps (protocols – combined) for the 4 protocols tested and combined data estimates (by column), and for the 4 estimation models (by row). The maps show one axial slice from a single subject. (a): CBF estimation map; (b): ATT estimation map; (c): CBF absolute error map; (d): ATT absolute error map.

Figure 3.3.2 shows CBF estimation errors for the different protocols with and without macrovascular contamination both in simulation and *in vivo* using gkm as the fitting model. The general trends were consistent between simulation and *in vivo* data. All three multi-PLD protocols performed reasonably well within a normal range of ATT (ATT < 1.8s), with only Ref Multi-PLD protocol exhibiting substantial error from macrovascular contamination within that range. In the absence of MVC, multi-PLD protocols could retain CBF accuracy beyond an ATT of 2.0s up to 2.5s for CBFopt (Figure 3.3.2a and 3.3.2c). No protocol had a consistently better performance than others when macrovascular contamination was present over the wider ATT range (Figure 3.3.2b and 3.3.2d). ATT estimation errors of the three multi-PLD protocols under the

same conditions are shown in Figure 3.3.3. ATT was underestimated by all three protocols both in simulation and *in vivo* when ATT was prolonged. Despite having higher ATT estimation errors at short ATTs, CBFopt had the lowest ATT errors among all protocols at prolonged ATTs.

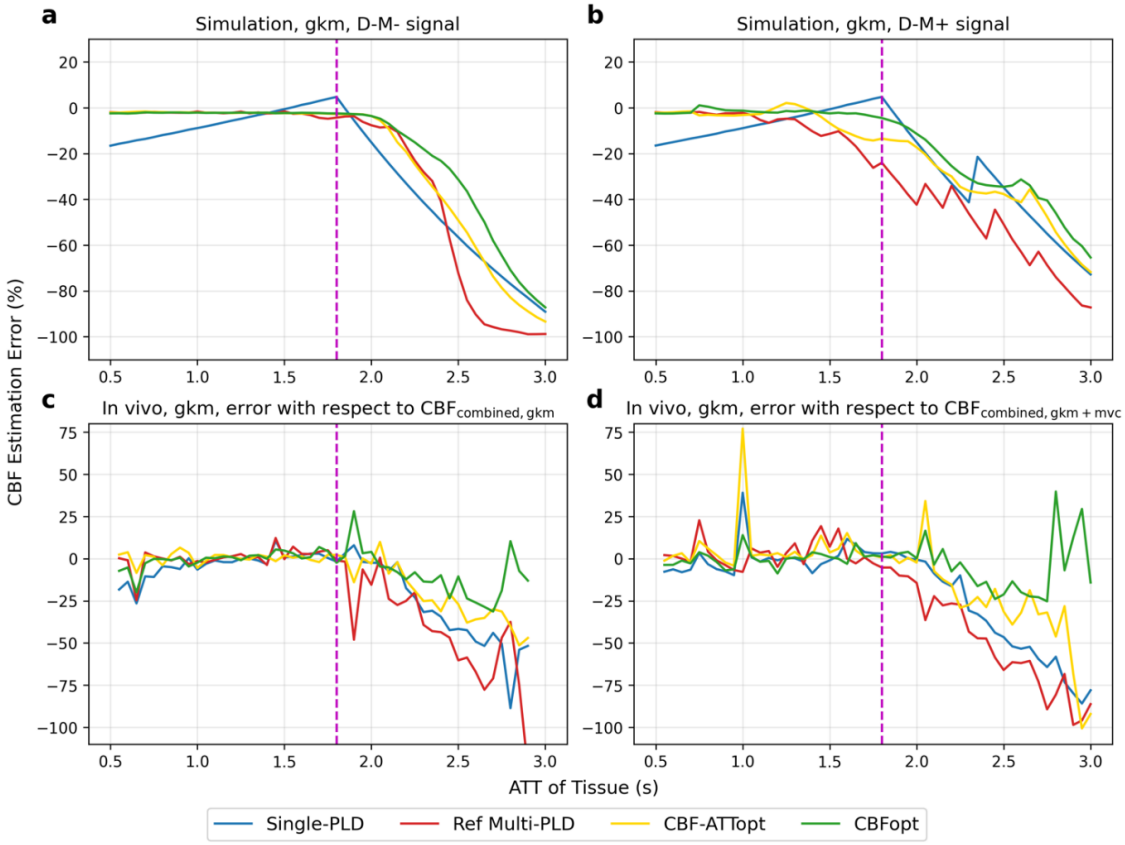


Figure 3.3.2 CBF estimation mean errors for the 4 protocols fit with gkm. (a): simulation data using $D-M-$; (b): simulation data using $D-M+$, with aBV=0.2%; (c): in vivo estimation error with respect to $CBF_{combined,\ gkm}$; (d): in vivo estimation error with respect to $CBF_{combined,\ gkm+mvc}$. The dashed magenta line indicates the upper limit of the range of ATT that CBF-ATTopt and CBFopt was optimised for.

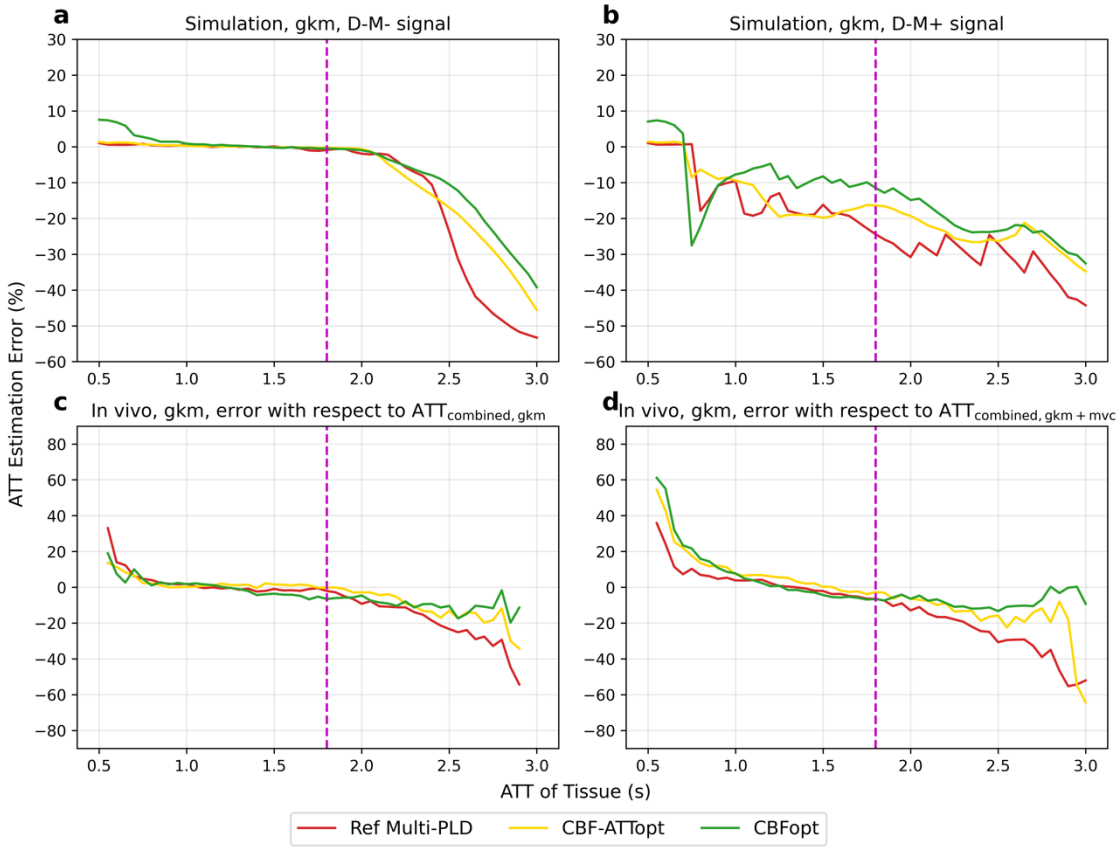


Figure 3.3.3 ATT estimation errors for the 3 multi-PLD protocols fitted with gkm over a prolonged ATT range. (a): simulation data using $D-M-$; (b): simulation data using $D-M+$; (c): in vivo estimation error with respect to $ATT_{combined,\ gkm}$; (d): in vivo estimation error with respect to $ATT_{combined,\ gkm+mvc}$. The dashed magenta line indicates the upper limit of the range of ATT that CBF-ATTopt and CBFopt was optimised for.

Figure 3.3.4 shows CBF and ATT estimation errors over a range of aBV both in simulation and *in vivo* using gkm and gkm + mvc as fitting models. The bar chart in Figure 3.3.5 shows the sensitivity values to macrovascular contamination, measured by the slope of error against aBV. When aBV was varied, all three multi-PLD protocols were sensitive to macrovascular contamination when fitted with gkm, overestimating CBF and underestimating ATT (see dashed lines in Figure 3.3.4a, 3.3.4b and star marks in Figure 3.3.4c, 3.3.4d). For CBF estimation in simulation, CBFopt had the smallest sensitivity value to macrovascular contamination (33.47% error per 1% aBV) among multi-PLD protocols using gkm. For ATT estimation, the three multi-PLD protocols all significantly underestimated ATT, but were not significantly different from each other.

Despite having different ground truth CBF values from simulation, similar relations were seen using *in vivo* data, where CBF sensitivity to macrovascular contamination of CBFopt (60.21% error per 1% aBV) was much smaller than the Reference Multi-PLD (88.73% error per 1% aBV) and CBF-ATTopt (96.5% error per 1% aBV). By fitting the signal with an extended kinetic model gkm + mvc, all multi-PLD protocols showed a notable decrease in CBF and ATT estimation error in simulation (solid lines in Figure 3.3.4a and 3.3.4b) and *in vivo* (triangle marks in Figure 3.3.4c and 3.3.4d). Absolute CBF and ATT sensitivity values to macrovascular contamination were all lowered except for the absolute ATT sensitivity for the reference multi-PLD protocol with *in vivo* data (Figure 3.3.5).

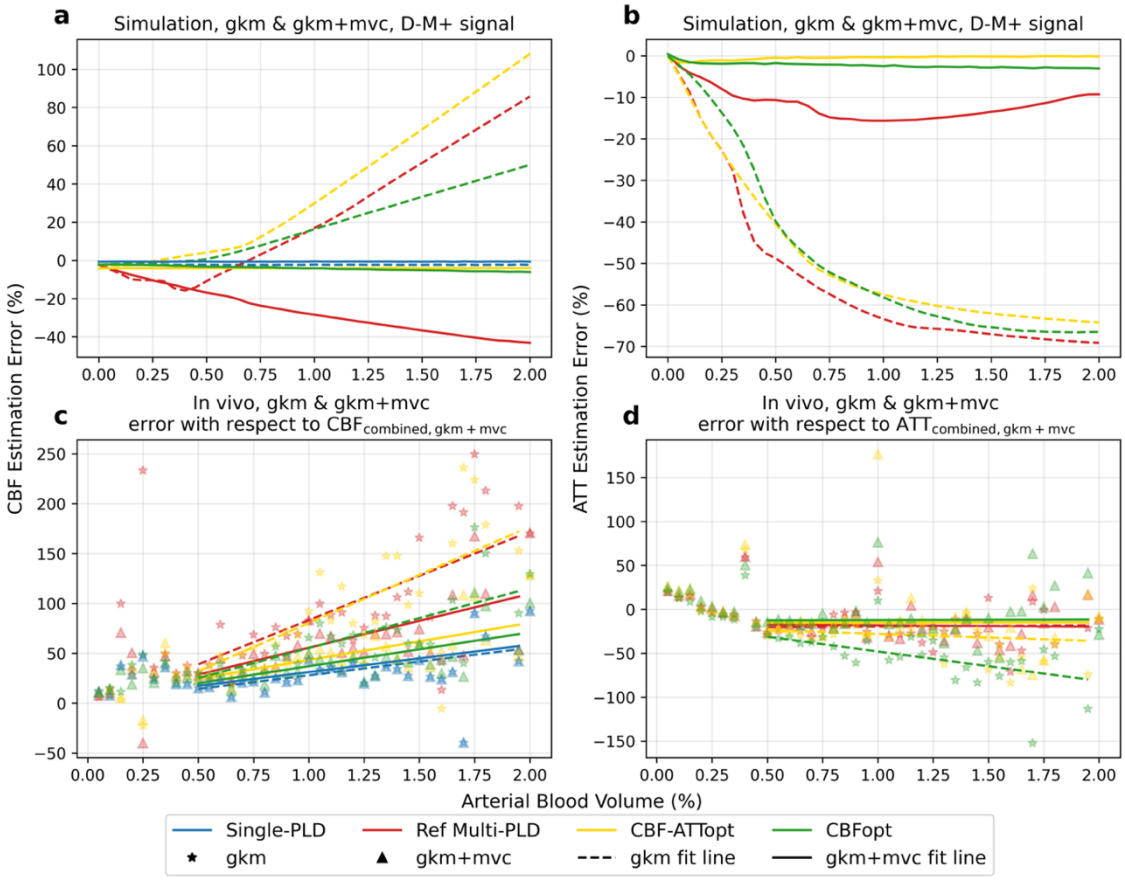


Figure 3.3.4 CBF and ATT estimation errors for the 4 protocols fitted with gkm and gkm + mvc over a range of aBV values. ATT was held constant at 1.4s in simulation across all aBVs. (a): CBF errors of simulation data on D − M + signals; (b): ATT errors of simulation data on D − M + signals; (c): CBF errors of in vivo data; (d): ATT

errors of in vivo data. In vivo estimation errors were calculated with respect to $CBF_{combined,\ gkm+mvc}$ *and* $ATT_{combined,\ gkm+mvc}$*. The star and triangle markers in (c) and (d) represent the mean errors at each binned value of aBV fit by* gkm *and* $gkm + mvc$*, respectively, while the dashed and solid lines represent the linear fit of errors when* $aBV > 0.5\%$ *by* gkm *and* $gkm + mvc$*, respectively.*

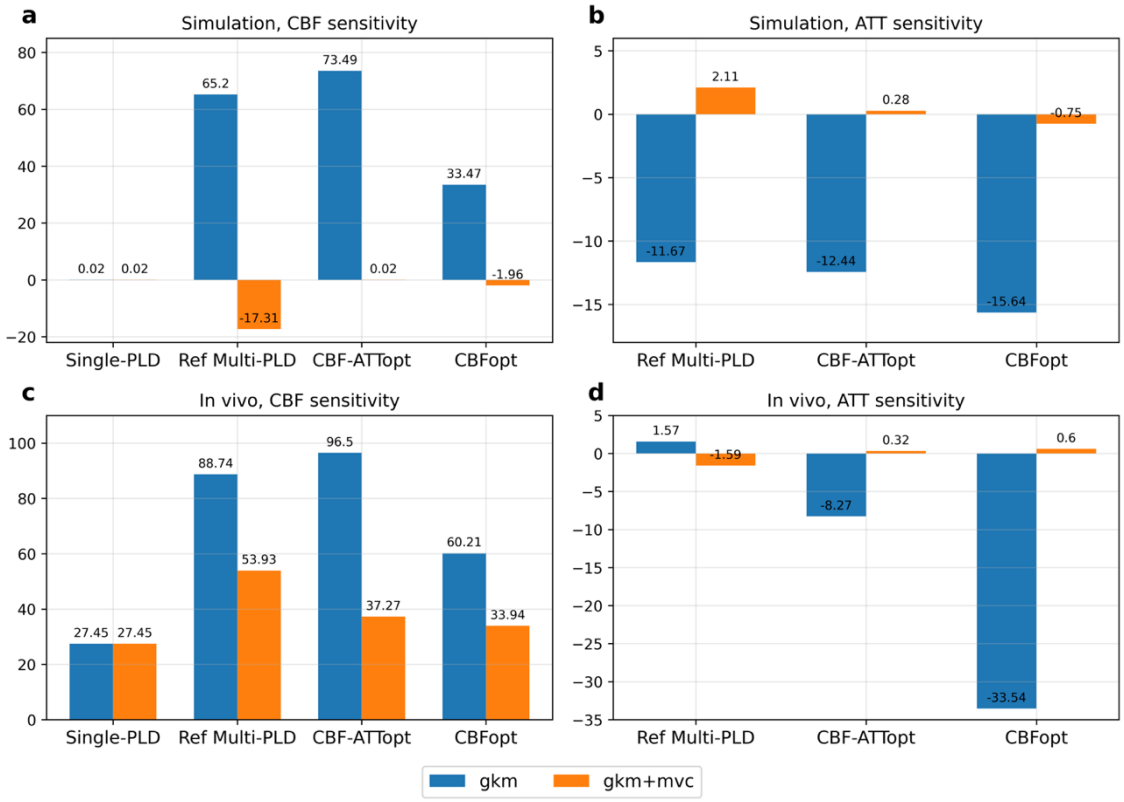


Figure 3.3.5 CBF and ATT sensitivity (unit: % error per 1% aBV) to macrovascular contamination for the 4 protocols with conditions in Figure 5.5. Sensitivity values represent the slopes of the lines of best fit when aBV > 0.5%.

When the degree of dispersion was varied in $D + M -$ signals in simulation but not accounted for in the model fitting, as shown in Figure 3.3.6, both CBF and ATT were overestimated at shorter ATT and CBF was underestimated at prolonged ATT by all protocols. The CBF and ATT overestimation errors increased with a higher degree of dispersion, with the highest increase by CBFopt being 7.82% and 15.23% in CBF estimation and 29.07% and 73.42% in ATT estimation when $s = s_0/2$ and $s = s_0/4$, respectively. The largest error of CBF underestimations all reached nearly -100% at the longest ATT, when the protocols could hardly detect meaningful signals due to the prolonged arrival time. When dispersion was accounted for in the model fitting by

$gkm + disp$, which is shown in Figure 3.3.7, Reference Multi-PLD could retain CBF estimation accuracy up to 2.0s, while optimised protocols up to 2.5s. ATT estimation errors were significantly reduced when ATT < 1.8s. Beyond the ATT range of 2.5s, however, the three protocols did not show consistent increase or reduction of CBF and ATT errors.

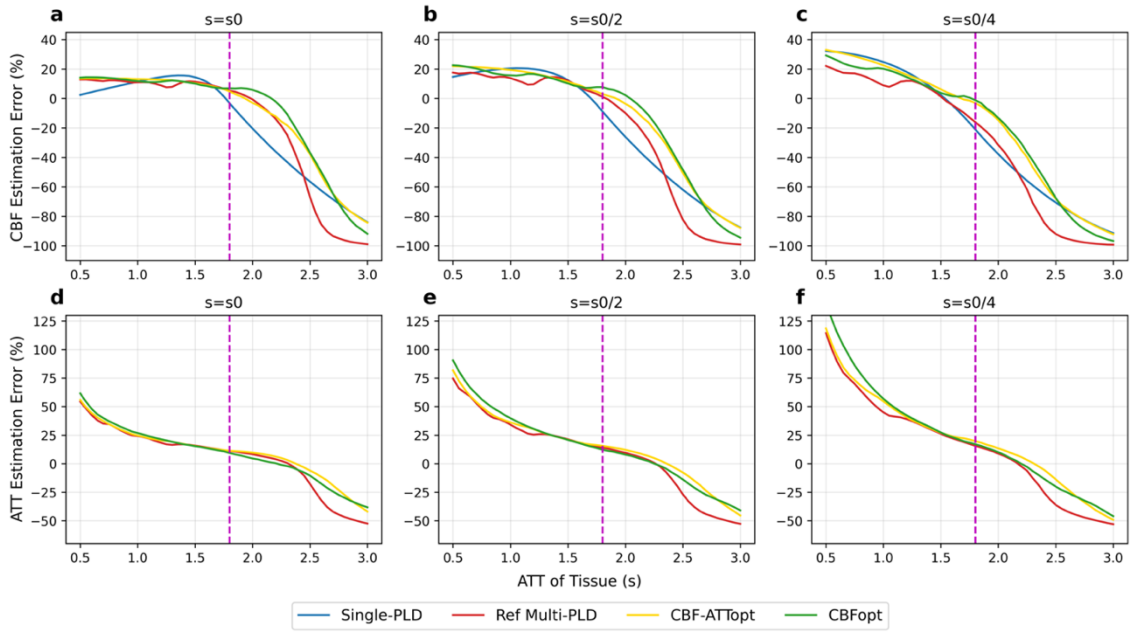


Figure 3.3.6 CBF and ATT estimation fitted with gkm over a prolonged ATT range on $D + M -$ signals with different degrees of dispersion. (a), (d): $s = s_0$, low degree of dispersion; (b), (e): $s = s_0/2$, moderate degree of dispersion; (c), (f): $s = s_0/4$, high degree of dispersion. The dashed magenta line indicates the upper limit of the range of ATT that CBF-ATTopt and CBFopt was optimised for.

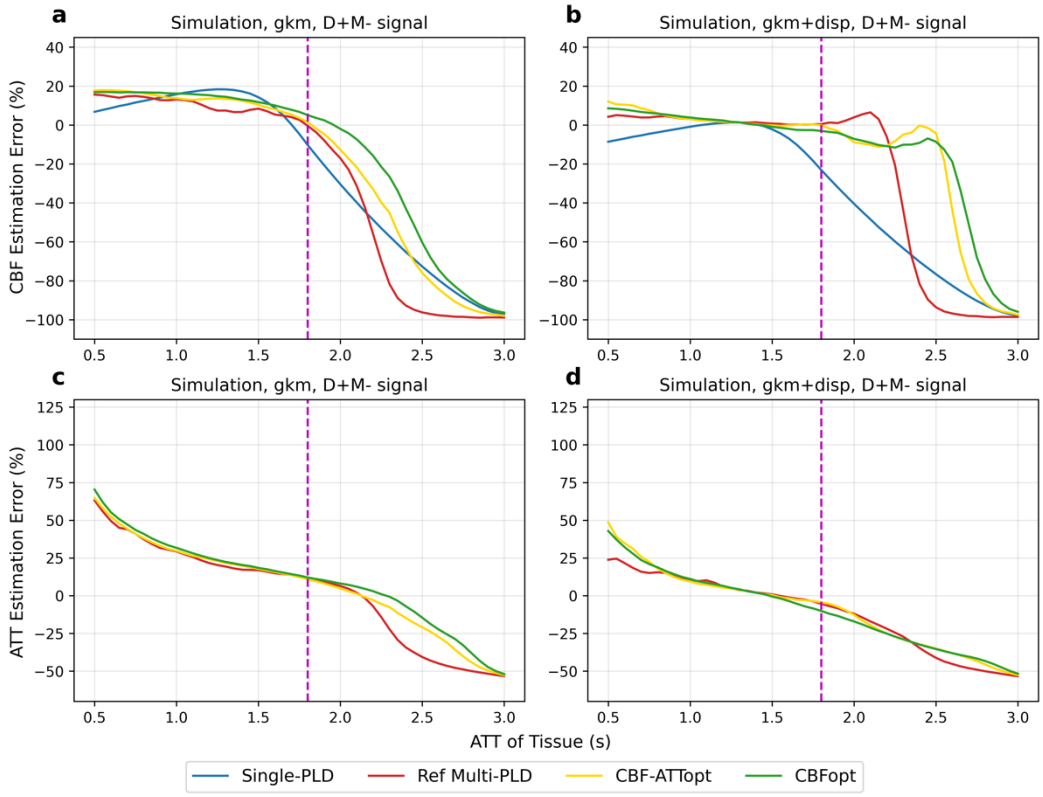


Figure 3.3.7 Simulation CBF and ATT estimation errors for the 4 protocols fit with gkm or gkm+disp using $D + M -$ signals (kernel sharpness $s = s_0$) over a prolonged ATT range. (a): CBF errors fit with gkm; (b): CBF errors fit with $gkm + disp$; (c): ATT errors fit with gkm; (d): ATT errors fit with $gkm + disp$.

3.4 Discussion

In this chapter, we have explored the performance of several pCASL imaging protocols in CBF and ATT estimation under the effects of macrovascular signal contamination, flow dispersion, and prolonged ATT.

3.4.1 Macrovascular Contamination

The single PLD value recommended by the ASL consensus paper[3] and tested in this study is 1800ms, a trade-off between incomplete arrival of blood to the tissue voxels and a loss of ASL signal due to T_1 relaxation. If the PLD is too short, part of the labelled blood may remain in the macrovasculature, leading to false interpretation of tissue

perfusion by macrovascular signals. This is particularly problematic in multi-PLD ASL, since short PLDs are often used to capture the arrival time information. When macrovascular contamination was included (Figure 3.3.4), CBF was overestimated and ATT was underestimated across all protocols at high aBV when using gkm, i.e., not accounting for macrovascular contamination in the analysis. CBFopt had the least sensitivity to MVC of the multi-PLD protocols when gkm was used for analysis, as indicated by the smallest slope value against an increasing aBV, most probably because it mainly includes long PLDs within the sampling schedule. The three multi-PLD protocols yielded similar but high ATT estimation errors, significantly underestimating the ATT when macrovascular compartment was included in the model. This would be consistent with the model treating the macrovascular signal as tissue perfusion with a shorter ATT. When the extended model gkm + mvc was used, i.e., the analysis explicitly attempted to correct for macrovascular contamination, all protocols showed big improvement in CBF and ATT estimation. This was seen by a decrease of almost all CBF and ATT sensitivity values by multi-PLD protocols using gkm + mvc than the original gkm in Figure 3.3.5. CBF-ATTopt showed significantly lower error in estimating arterial blood volume than Reference multi-PLD and CBFopt using gkm + mvc, shown by Figure 3.4.1. This benefit could be due to the short ATTs within the CBF-ATTopt protocol.

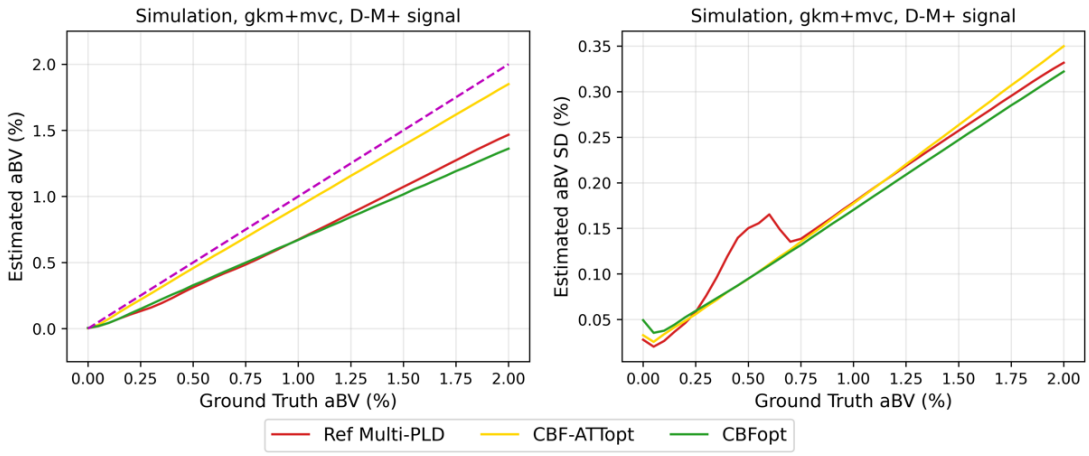


Figure 3.4.1 Arterial blood volume (aBV) estimation mean and standard deviation for the 3 multi-PLD protocols fitted with $gkm + mvc$ using $D - M +$ signals. The dashed magenta line indicates identity.

When MVC was present in a prolonged ATT range, shown in Figure 3.3.2b and Figure 3.3.3b, no protocol exhibited consistently better performance than others in CBF and ATT estimation. It is worth noting that, because flow crusher gradients were used to eliminate most of the macrovascular signal in the *in vivo* data, estimation errors with respect to $CBF_{combined,\ gkm+mvc}$ (Figure 3.3.2d, Figure 3.3.3d) was not the *in vivo* equivalent of estimation using simulated $D - M +$ signals. A more direct comparison would be to use gkm+mvc to fit $D - M -$ signals, which is presented in Figure 3.4.2. For both CBF and ATT estimation, fitting with $gkm + mvc$ led to higher errors when ATT < 1.3s, while the errors remained comparable to fitting with gkm when ATT > 1.3s, with CBFopt achieving smaller estimation standard deviation. This, together with the fact that the *in vivo* results using $CBF_{combined,\ gkm+mvc}$ in error calculation were not substantially different from the results using $CBF_{combined,\ gkm}$ (Figure 3.3.2d, Figure 3.3.2c), suggests that explicitly including a macrovascular compartment in the model used for analysis could be a successful strategy for controlling for MVC, without necessarily having the knowledge of whether or not MVC was present.

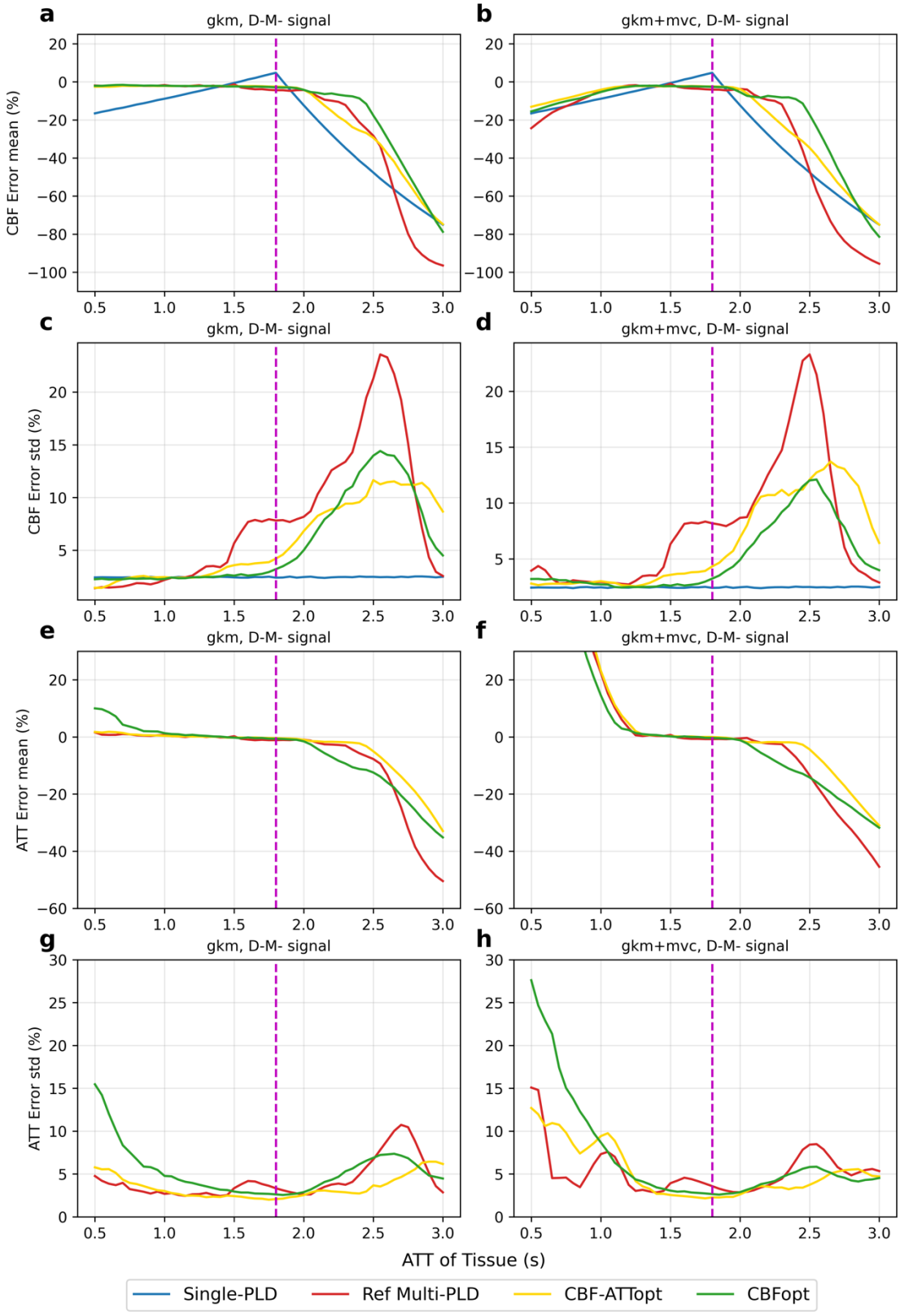


Figure 3.4.2 Simulation CBF and ATT estimation error means and standard deviations for the 4 protocols fitted with gkm or $gkm + mvc$ using $D - M -$ signals over a prolonged ATT range.

The *in vivo* data used in this study included flow crusher gradients, as the original study from which the data originated sought to test protocols without any macrovascular signal. Bipolar crusher gradients can be used to eliminate flowing labelled spins in one direction above a cut-off velocity. However, the macrovascular signals perpendicular to the gradient direction are unaffected and present in the image. Thus in practice macrovascular contamination remains, as has been seen previously[8], and has been exploited here to examine the sensitivity to macrovascular contamination. In general, the ASL white paper discouraged the use of flow crusher gradients[3], concerning that important clinical information might be removed, but leading to more prominent macrovascular signal contamination. Therefore, we would recommend the use of the two-compartment model in multi-PLD acquisitions to control, as well as potentially estimate for, the effect of MVC.

3.4.2 Flow Dispersion Effects

We investigated the effects of flow dispersion by varying the sharpness parameter s in the Gamma kernel to control the degree of dispersion. All protocols showed overestimation of CBF and ATT at short ATT and underestimation of CBF and ATT at prolonged ATT. This CBF overestimation is contrary to previous pulsed-ASL findings[9,16,17], in which dispersion effects were reported to cause an underestimation of CBF. A possible explanation is that while the dispersion kernel attenuates the peak of the signal curve, the protocols examined in this study were mainly sampling the trailing edge of the curve when ATT was short, where dispersion increases the signal magnitudes compared to the non-dispersed case using the dispersion model implemented here. Across the three dispersion parameters tested, $s = s_0/4$ generated the greatest dispersion which in turn led to the highest error of CBF and ATT overestimation at short ATT,

shown by Figure 3.3.6c and 3.3.6f. However, the bias due to dispersion was fairly consistent between different protocols. This suggests that while flow dispersion does influence CBF and ATT estimation, the presence of dispersion would not alter the appropriateness of the existing optimal sampling framework, and our choice of an optimal protocol *per se* would not lead to particularly egregious errors.

In this study we chose a Gamma-shaped dispersion kernel, which has a relative advantage in physiological plausibility and computational simplicity[12]. Other shapes of dispersion kernels or vascular transport functions (VTFs) have also been proposed, such as the Gaussian kernel[16,18] and the delay-dependent exponential kernel used in dynamic susceptibility contrast (DSC) imaging[19]. Furthermore, there is debate as to whether one dispersion kernel independent to spatial location could accurately describe the profile of flow dispersion within every voxel. For instance, the macrovascular component was seen to show a higher sensitivity to the choice of dispersion kernel than the tissue component[12]. Future work could look into the effects of having different levels of dispersion between tissue and macrovascular compartments. Besides, the effects of dispersion could be controlled by determining an AIF that is upstream to the voxel, i.e., a local AIF. Methods, such as subtraction of signals with and without flow crusher gradients[20] or by using independent component analysis[21], have been developed to obtain a local AIF, thus reducing the errors arising from dispersion effects.

3.4.3 Prolonged ATT

The ATT range used in the optimisation of CBF-ATTopt and CBFopt was [0.5s, 1.8s]. In this study, we tested the performance of the protocols with an extended ATT range [0.5s, 3.0s] to reflect potential unexpected deviations from this narrow range in practice,

although for application in cohorts where longer ATTs are expected, the optimisation range should be adjusted (e.g., see Woods *et al*.[7] Supporting Table S1).

For CBF estimation, all four protocols underestimated CBF at prolonged ATT, as expected. We could see from Figure 3.3.2 that the single-PLD protocol was much more sensitive to the change of tissue ATT than the multi-PLD protocols in the normal ATT range. Although the consensus paper recommended the use of a 1800ms single-PLD protocol for young and healthy adults, and 2000ms single-PLD for elderly subjects or pathological conditions[3], our results showed a worse performance of the single-PLD protocol than multi-PLD protocols under the tested SNR. In keeping with the study of Woods *et al*[7], the estimation by the optimised multi-PLD protocols, CBF-ATTopt and CBFopt, was quite satisfactory until tissue ATT was out of their initial optimised range. CBFopt and CBF-ATTopt remained reasonably accurate up to ATT = 2.5s for CBF and ATT estimation, respectively (Figure 3.3.2a and Figure 3.3.3a). The standard deviations of CBF and ATT estimation errors in simulation are shown in Figure 3.4.3. Estimation SDs by gkm + mvc were significantly smaller than those by gkm in the prolonged ATT range. This might be because the presence of the extra signal from the macrovascular component gives a higher SNR, leading to a more consistent parameter fitting. In the *in vivo* results, CBFopt had significantly lower absolute errors in CBF estimation than all other protocols in the extended ATT range, whether the errors were calculated with respect to $CBF_{combined,\ gkm}$ or $CBF_{combined,\ gkm+mvc}$ (average reduction of 4.96% or 9.45% CBF estimation error compared to CBF-ATTopt, respectively), and without having significant differences in ATT errors compared to CBF-ATTopt. In accordance with the lowest sensitivity value to MVC of CBFopt, we therefore argue that CBFopt is the least sensitive protocol to MVC and unexpectedly prolonged ATT for CBF estimation, while maintaining reasonably good performance in estimating ATT. We may further conclude

that the optimisation framework can still be used where some prolonged ATTs (up to 2.5s) might be expected, particularly where the majority of the voxels are likely to fall within the optimal range. Beyond this ATT range, the protocols would become overly sensitive to the long ATTs, and the optimisation range should be reconsidered.

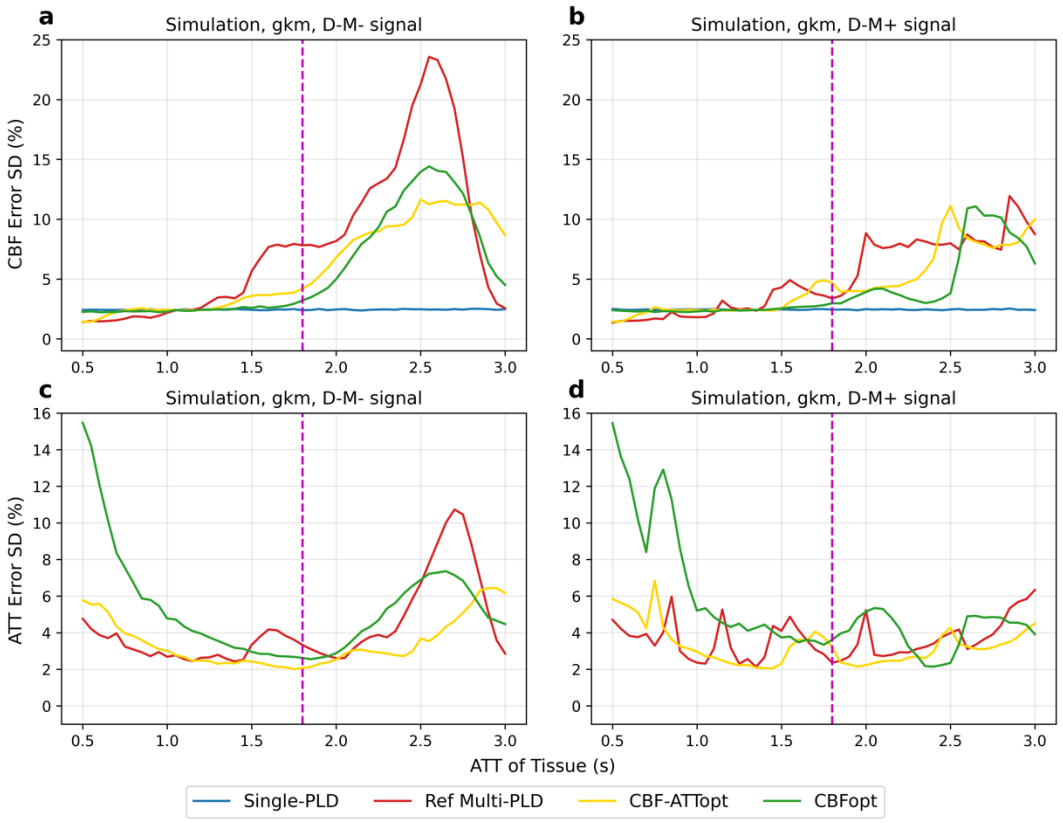


Figure 3.4.3 Simulation CBF and ATT estimation error standard deviations for the 4 protocols fitted with gkm over a prolonged ATT range. (a): CBF error std using $D-M-$; (b): CBF error std using $D-M+$; (c): ATT error std using $D-M-$; (d): ATT error std using $D-M+$. The dashed magenta line indicates the upper limit of the range of ATT that CBF-ATTopt and CBFopt was optimised for.

3.4.4 Results From 3D-Readout Protocols

To investigate further the effects of using a protocol outside of its optimised range, more simulations were performed using the optimal protocols designed for segmented 3D-readout[7], which are listed in Table 3.4.1. These two sets of protocols were optimised for a normal ATT range (NAR) [0.5s, 2.0s] and a prolonged ATT range (PAR) [1.0s, 3.0s],

and were both tested under the same simulation conditions across the aBV range [0.0, 2.0] and the ATT range [0.5s, 3.0s] as the 2D-readout case.

Protocol	**Post-labelling delays (s)**	**PLDs (N)**	**Averages (N)**
$0.5 \leq ATT \leq 2.0s$			
Reference Multi-PLD	0.5, 0.725, 0.925, 1.15, 1.35, 1.575, 1.775, 2	8	6
CBF-ATTopt	0.2, 0.9, 0.9, 1.15, 2, 2.2	6	8
CBFopt	0.2, 0.925, 1.425, 1.85, 2.025, 2.15, 2.25, 2.3, 2.3, 2.3	10	4
$1.0 \leq ATT \leq 3.0s$			
Reference Multi-PLD	1, 1.25, 1.5, 1.75, 2, 2.25, 2.75, 3	9	4
CBF-ATTopt	0.7, 1.875, 1.9, 1.9, 1.925, 2.75, 2.95, 3.1, 3.3	9	4
CBFopt	0.7, 1.8, 2.5, 2.875, 3.075, 3.3, 3.3, 3.325	8	4

Table 3.4.1 Protocols timings of 3D readout from Woods et al[7]. Two sets of protocols were developed, one for a normal range of $0.5 \leq ATT \leq 2.0s$*, the other one for a prolonged range of* $1.0 \leq ATT \leq 3.0s$*.*

CBF and ATT estimation errors across the aBV range can be found in Figure 3.4.4. PAR protocols appeared to be more predictable than NAR protocols, giving near-linear sensitivity to aBV in both estimations when aBV > 1.25% (Figure 3.4.4b). Furthermore, PAR protocols produced more consistent results when using $\mathrm{gkm} + \mathrm{mvc}$, clearly reducing the estimation error, whereas in NAR protocols the results were more variable. CBF and ATT estimation errors across the prolonged ATT range can be found in Figure 3.4.5. Within the overlapping ATT range of [1.0s, 2.0s], there were similar CBF and ATT estimation errors between NAR and PAR versions of CBF-ATTopt and CBFopt. However, NAR protocols had a consistently lower standard deviation than PAR protocols for CBF-ATTopt and CBFopt in this range. Expectedly, NAR protocols had better performance when ATT < 1.0s, while PAR protocols did better when ATT > 2.0s. This indicates that optimised protocols would evidently yield higher accuracy within

their optimised range, but could only work sub-optimally outside this range. Choosing the appropriate optimised protocol is thus critical in controlling estimation errors. In the meantime, if prior knowledge of the ATT profile of the dataset is provided, a non-uniform ATT distribution can be used in the optimisation process to give different weights to the ATTs within the optimised range.

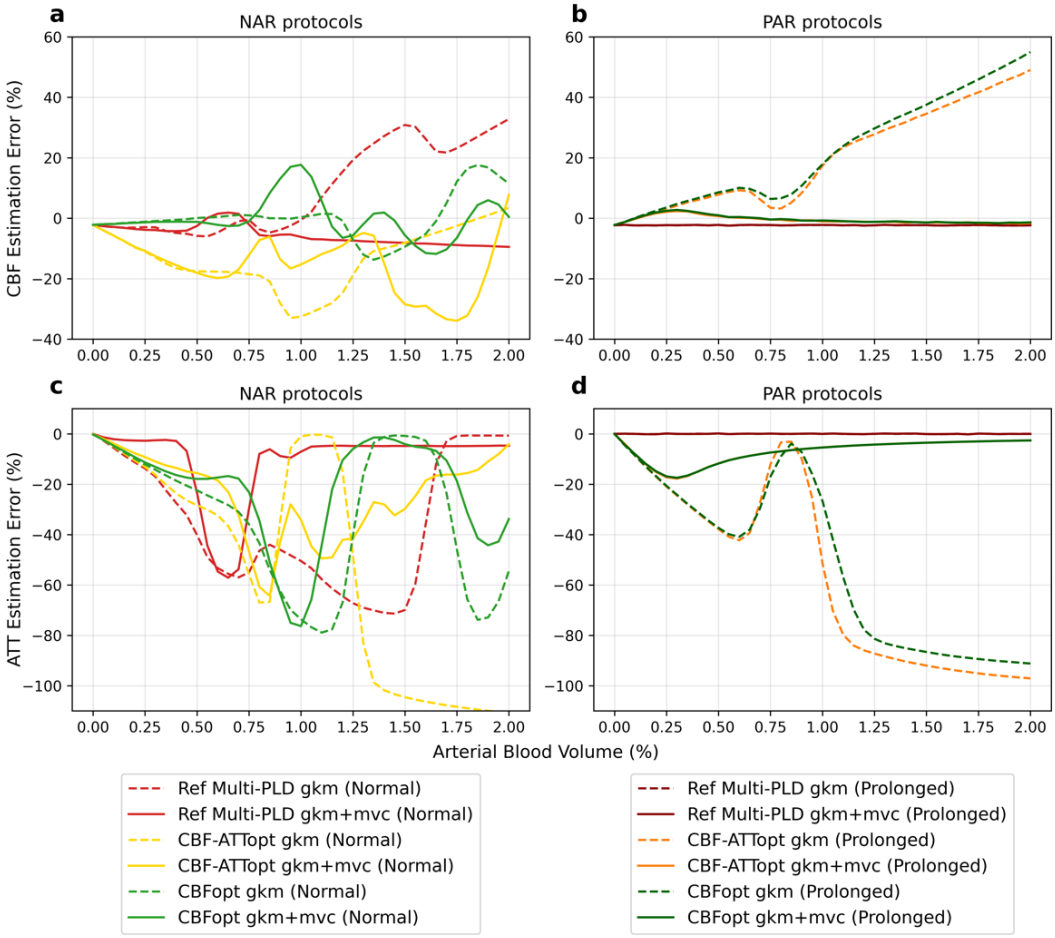


Figure 3.4.4. Simulation CBF and ATT estimation errors for the 3 normal-range protocols and 3 prolonged-range protocols fit with gkm over a range of aBV using $D-M+$ signals. ATT was held constant at 1.4s in simulation across all aBVs. (a): CBF errors of normal-range protocols; (b): CBF errors of prolonged-range protocols; (c) ATT errors of normal-range protocols; (d): ATT errors of prolonged-range protocols.

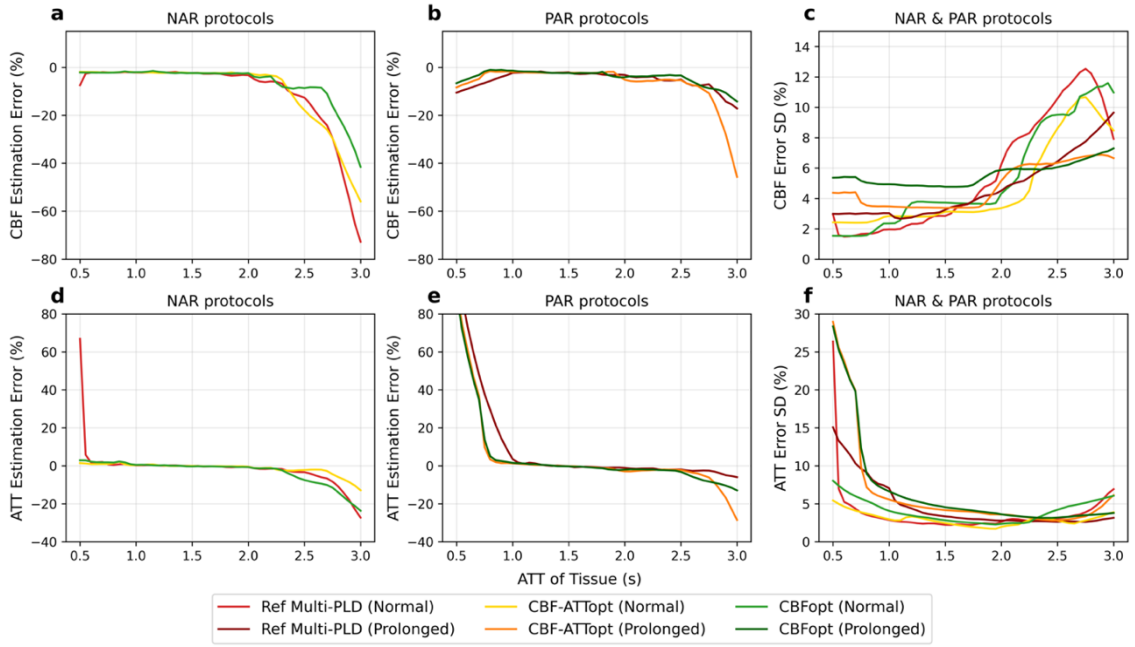


Figure 3.4.5. Simulation CBF and ATT estimation error means and standard deviations for the 3 normal-ATT-range (NAR) protocols and 3 prolonged-ATT-range (PAR) protocols fitted with gkm over a prolonged ATT range using $D-M-$ signals. (a): CBF errors of NAR protocols; (b): CBF errors of PAR protocols; (c) CBF errors std of NAR & PAR protocols; (d) ATT errors of NAR protocols; (e): ATT errors of PAR protocols; (f): ATT errors std of NAR & PAR protocols.

3.4.5 Limitations

This study has a few limitations. Firstly, the results are based on the estimation from the extended kinetic model that assumes a specific shape of dispersion kernel and macrovascular AIF. Meanwhile, other artefacts might also be present in real data, further confounding the accurate quantification of perfusion and ATT. For example, T2* differences between capillary and tissue might cause an underestimation of CBF using the one-compartment model; partial volume effects in which different composites of the brain tissue share the same voxel will underestimate perfusion in the grey matter and overestimate perfusion in the white matter.

Secondly, assumptions have been made at various stages in simulation that might be violated *in vivo*. For example, the difference between bolus arrival times of the

macrovascular signal and the tissue signal is assumed to remain a constant of 0.5s in this study. Further research is needed to investigate how this assumption might affect the outcome. It is also worth noting that the improvement of CBF estimation seen in simulated data using gkm + mvc should not be over-interpreted as implying that the observed benefit will necessarily be achieved in real data since these are idealised experiments in which the same model is used to fit the model-generated data.

Thirdly, the optimised protocols so far have only been applied to a young and healthy population, who typically have the ATTs in the optimised range. This work did preliminary analyses on a small dataset which included limited voxels that had prolonged ATT. Future work could explicitly focus on elderly or pathological groups, investigate the effects of these protocols on long ATTs, and compare them to appropriately optimised protocols for these groups. This could help establish the importance of protocol optimisation for each sub-population due to their varying ATT ranges.

3.5 Conclusion

In conclusion, we have examined four ASL protocols under the effects of dispersion and macrovascular contamination over a prolonged ATT range. Explicitly including a macrovascular component in the kinetic model was shown to be a feasible approach in controlling for MVC. Furthermore, we argue that among all protocols, CBFopt was the least sensitive protocol to MVC and unexpectedly prolonged ATT for CBF estimation while maintaining reasonably good performance in estimating ATT.

3.6 References

1. Jezzard P, Chappell MA, Okell TW. Arterial spin labeling for the measurement of cerebral perfusion and angiography. *Journal of Cerebral Blood Flow and Metabolism*. 2018;38(4):603-626.
2. Dai W, Garcia D, de Bazelaire C, Alsop DC. Continuous flow-driven inversion for arterial spin labeling using pulsed radio frequency and gradient fields. *Magn Reson Med*. 2008;60(6):1488-1497.
3. Alsop DC, Detre JA, Golay X, et al. Recommended implementation of arterial spin-labeled Perfusion mri for clinical applications: A consensus of the ISMRM Perfusion Study group and the European consortium for ASL in dementia. *Magn Reson Med*. 2015;73(1):102-116.
4. Gonzalez-At JB, Alsop DC, Detre JA. Cerebral perfusion and arterial transit time changes during task activation determined with continuous arterial spin labeling. *Magn Reson Med*. 2000;43(5):739-746.
5. Günther M, Bock M, Schad LR. Arterial spin labeling in combination with a look-locker sampling strategy: Inflow turbo-sampling EPI-FAIR (ITS-FAIR). *Magn Reson Med*. 2001;46(5):974-984.
6. Buxton RB, Frank LR, Wong EC, Siewert B, Warach S, Edelman RR. A general kinetic model for quantitative perfusion imaging with arterial spin labeling. *Magn Reson Med*. 1998;40(3):383-396.
7. Woods JG, Chappell MA, Okell TW. A general framework for optimizing arterial spin labeling MRI experiments. *Magn Reson Med*. 2019;81(4):2474-2488.
8. Chappell MA, MacIntosh BJ, Donahue MJ, Günther M, Jezzard P, Woolrich MW. Separation of macrovascular signal in multi-inversion time arterial spin labelling MRI. *Magn Reson Med*. 2010;63(5):1357-1365.
9. Wu WC, Mazaheri Y, Wong EC. The Effects of Flow Dispersion and Cardiac Pulsation in Arterial Spin Labeling. *IEEE Trans Med Imaging*. 2007;26(1):84-92.
10. Paling D, Thade Petersen E, Tozer DJ, et al. Cerebral Arterial Bolus Arrival Time is Prolonged in Multiple Sclerosis and Associated with Disability. *Journal of Cerebral Blood Flow & Metabolism*. 2014;34(1):34-42.
11. van Gelderen P, de Zwart JA, Duyn JH. Pittfalls of MRI measurement of white matter perfusion based on arterial spin labeling. *Magn Reson Med*. 2008;59(4):788-795.
12. Chappell MA, Woolrich MW, Kazan S, Jezzard P, Payne SJ, MacIntosh BJ. Modeling dispersion in arterial spin labeling: Validation using dynamic angiographic measurements. *Magn Reson Med*. 2013;69(2):563-570.
13. Mehta RR, Chappell MA. Quantification of errors in cerebral blood flow measurements due to dispersion in arterial spin labelling. In: *2015 37th Annual International Conference of the IEEE Engineering in Medicine and Biology Society (EMBC)*. Vol 2015-Novem. IEEE; 2015:7917-7920.
14. Chappell MA, Groves AR, Whitcher B, Woolrich MW. Variational Bayesian Inference for a Nonlinear Forward Model. *IEEE Transactions on Signal Processing*. 2009;57(1):223-236.

15. Zhang Y, Brady M, Smith S. Segmentation of brain MR images through a hidden Markov random field model and the expectation-maximization algorithm. *IEEE Trans Med Imaging*. 2001;20(1):45-57.
16. Hrabe J, Lewis DP. Two analytical solutions for a model of pulsed arterial spin labeling with randomized blood arrival times. *Journal of Magnetic Resonance*. 2004;167(1):49-55.
17. Gallichan D, Jezzard P. Modeling the effects of dispersion and pulsatility of blood flow in pulsed arterial spin labeling. *Magn Reson Med*. 2008;60(1):53-63.
18. Ozyurt O, Dincer A, Ozturk C. A Modified Version of Hrabe-Lewis Model to Account Dispersion of Labeled Bolus in Arterial Spin Labeling. *Proceedings of the 18th Annual Meeting of ISMRM*. 2010;18:4065.
19. Mouannes-Srour JJ, Shin W, Ansari SA, et al. Correction for arterial-tissue delay and dispersion in absolute quantitative cerebral perfusion DSC MR imaging. *Magn Reson Med*. 2012;68(2):495-506.
20. Petersen ET, Lim T, Golay X. Model-free arterial spin labeling quantification approach for perfusion MRI. *Magn Reson Med*. 2006;55(2):219-232.
21. Calamante F, Mørup M, Hansen LK. Defining a local arterial input function for perfusion MRI using independent component analysis. *Magn Reson Med*. 2004;52(4):789-797.

4 Sensitivity map of optimised protocols to macrovascular contamination

4.1 Introduction

In Chapter 3, it was demonstrated that while the optimised protocols may perform better under an ideal kinetic model than the conventionally used single-PLD and evenly-spaced multi-PLD protocols, they could still be sensitive to macrovascular contamination (MVC), leading to high CBF and ATT estimation errors. We developed a metric denoting the parameter estimation sensitivity of protocols to MVC by calculating the slope of the line of best fit of CBF and ATT estimation error against an increasing arterial blood volume (aBV). CBFopt was found to be the least sensitive multi-PLD protocol to macrovascular contamination in CBF estimation while having reasonable performance in ATT estimation. By adding a macrovascular compartment in the estimation model, the CBF and ATT sensitivity values to MVC were reduced in almost all multi-PLD protocols.

The simulation in the previous chapter to investigate the effect of MVC was limited to one set of combination of tissue ATT and macrovascular ATT, i.e., ATT_t = 1.4s and ATT_a = 0.9s. The *in vivo* data we used to investigate the relationship between CBF and ATT estimation errors and aBV did not take into account the values of ATT_t and ATT_a. This chapter would focus on the sensitivity metrics using a more comprehensive group of CBF-optimised protocols to MVC and examine a complete set of combinations of tissue and macrovascular transit times.

4.2 Methods

4.2.1 Protocol selection

We selected eight representative optimised pCASL protocols from a more recent study[1], which were all optimised for CBF estimation accuracy. They consist of a sequential multi-PLD protocol (Seq_singleLD), four time-encoded multi-LD protocols with various label duration (LD) block types (Had_fixed, Had_T1adj, Had_freeLunch, Had_variable), and three time-encoded multi-LD multi-PLD ('Hybrid') protocols (Hybrid_fixed, Hybrid_T1adj, Hybrid_variable). The protocol schematics and timings are shown in Figure 4.2.1 and Table 4.2.1, respectively.

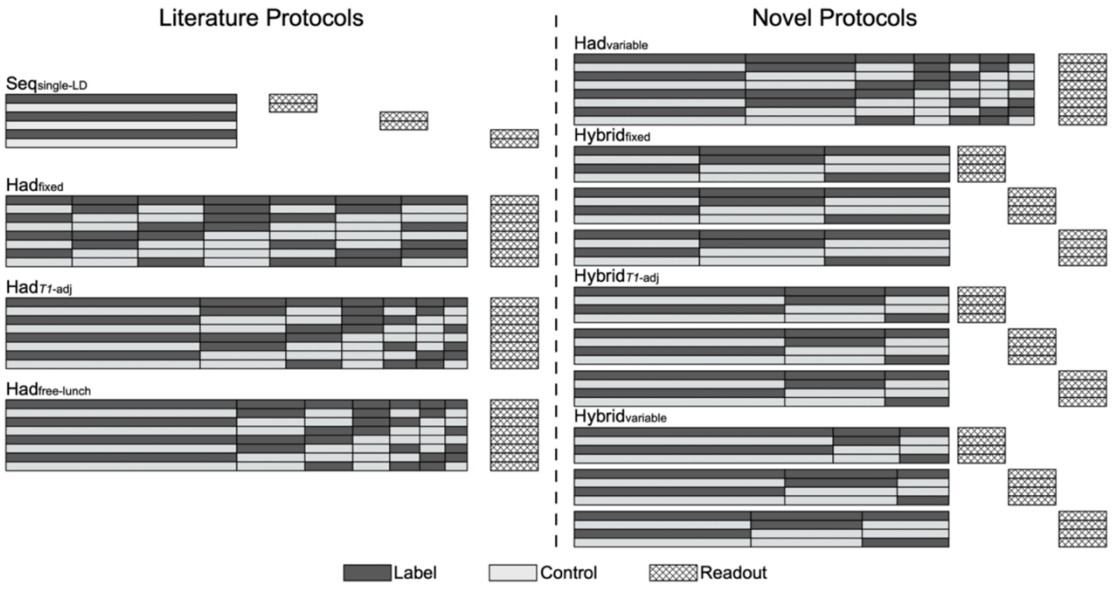


Figure 4.2.1 The optimised protocol timing schematics for the protocols from Woods et al.[1] compared in this study.

Protocol	Label durations (ms)	Post-label delays (ms)	N_T	N_{Ave}	N_{Acq}	Scan duration (min)
Seq_singleLD	1800	175, 1050, 1425, 1725, 2075, 2200, 2300, 2300, 2300	7	4	72	5:00
Had_fixed	550, 550, 550, 550, 550, 550, 550	100	7	8	64	4:54

Had_T1adj	1150, 675, 475, 375, 300, 250, 225	75	7	9	72	5:00
Had_freeLunch	1800, 625, 450, 350, 300, 250, 225	125	7	8	64	5:05
Had_variable	1725, 750, 650, 375, 150, 150, 125	100	7	8	64	4:58
Hybrid_fixed	1275, 1275, 1275	75, 150, 600, 850, 1000	15	3	60	5:00
Hybrid_T1adj	1800, 850, 550	200, 650, 900, 900	12	4	64	4:48
Hybrid_variable	1800, 1050, 775 1800, 1225, 550 1800, 850, 750 1800, 800, 800	100 525 575 700	12	4	64	4:55

Table 4.2.1 The optimised protocol timings for the protocols from Woods et al.[1] *compared in this study. N_T is the number of effective PLDs; N_{Ave} is the number of averages; N_{Acq} is the number of acquired volumes for each scan.*

4.2.2 Simulation Experiments

4.2.2.1 Assumption-based Simulations

PCASL signals using the general kinetic model[2] (gkm) with a macrovascular component[3] were simulated and added Gaussian white noise to give an SNR of 9.37 under common MR acquisition environment[4]. This signal is equivalent to the $\mathrm{D}-\mathrm{M}+$ signal type described in Section 3.2.2. The aBV of the macrovascular component varied between 0 and 2.0% with 0.05% interval. Additionally, we made three assumptions of the relationship between $\mathrm{ATT_t}$ and $\mathrm{ATT_a}$:

a) $\mathrm{ATT_a}$ is a constant percentage of $\mathrm{ATT_t}$, i.e., $ATT_a = \delta * ATT_t$, termed 'Percentage';

b) $\mathrm{ATT_a}$ is a fixed value irrelevant of $\mathrm{ATT_t}$, i.e., $ATT_a = \delta[s]$, termed 'Fixed';

c) ATT_a has a fixed interval to ATT_t, i.e., $ATT_a = ATT_t - \delta[s]$, termed 'Fixed-interval'.

Under each assumption, two scenarios were investigated where either ATT_t or δ was hold constant while the other parameter varied within a plausible range. Specifically, these scenarios were:

a-1) Percentage: $\delta = 0.5$, $ATT_t = [0.5: 0.25: 3.0]s$;

a-2) Percentage: $\delta = [0.0: 0.1: 0.9]$, $ATT_t = 1.4s$;

b-1) Fixed: $\delta = 0.5$, $ATT_t = [0.5: 0.25: 3.0]s$;

b-2) Fixed: $\delta = [0.0: 0.1: 1.3]$, $ATT_t = 1.4s$;

c-1) Fixed-interval: $\delta = 0.5$, $ATT_t = [0.5: 0.25: 3.0]s$;

c-2) Fixed-interval: $\delta = [0.0: 0.1: 1.3]$, $ATT_t = 1.4s$.

Other simulation parameters can be found in Table 4.2.2.

Parameter	Value
Cerebral blood flow (f)	60 ml/100g/min
Blood-tissue partition coefficient of water (λ)	0.9 ml/g
T1 of arterial blood (T_{1b})	1.65s
T1 of tissue (T_{1t})	1.3s
Labelling efficiency (α)	0.85

Table 4.2.2 Parameters used for simulations.

The noisy signals were then fitted with two models using the BASIL toolkit of FSL[5]: gkm and gkm + mvc, the latter explicitly accounting for the macrovascular signal. CBF and ATT estimates and uncertainties from the BASIL output were obtained and averaged over 500 simulations. CBF and ATT estimation errors were calculated by (estimate - ground truth) / ground truth *100. Within this chapter, the name 'ATT' will unequivocally denote tissue transit time, i.e., ATT_t. Arterial blood volume (aBV) estimates were obtained using the gkm + mvc model.

4.2.2.2 Map-based Simulations

In addition to assumption-based simulations, a map-based simulation was also conducted, where ATT_t and ATT_a values were chosen from a grid forming a complete set of possible combinations. ATT_t ranged from 0.5s to 3.0s with 0.1s interval, with ATT_a varied between 0 and each ATT_t with 0.1s interval, acknowledging the fact that the macrovascular transit time would always be shorter than the tissue transit time. The simulation parameters and the estimation process were the same as in the assumption-based approach. Under each combination of ATT_t and ATT_a, CBF and ATT estimation errors and absolute aBV estimates were obtained from the models gkm and gkm + mvc.

4.2.3 Sensitivity metrics

In Chapter 3, the metrics of sensitivity to MVC for CBF and ATT estimation were developed, using the slope values of the line of best fit by the corresponding error curves. We would follow that definition here, and have considered other types of sensitivity metrics in the discussion Section 4.4. For the aBV sensitivity metric, the slope value of the line of best fit by the absolute estimation curve was used. To sum up, the sensitivity metrics for different parameters are listed as follows:

a) CBF sensitivity (Θ_{CBF}): The slope of the line of best fit of the mean CBF estimation error curves (unit: error% per 1% aBV).

b) ATT sensitivity (Θ_{ATT}): The slope of the line of best fit of the mean ATT estimation error curves (unit: error% per 1% aBV).

c) aBV sensitivity (Θ_{aBV}): The slope of the line of best fit of the mean absolute aBV estimation curves (unit: 1).

The sensitivity values were obtained by the 'polyfit' function of the NumPy package. Under each of the three assumptions outlined in Section 4.2.2.1, CBF sensitivity values were plotted for each protocol with varying ATT_t or δ. In addition, CBF, ATT, and aBV sensitivity maps were generated for each protocol across the ATT_t and ATT_a ranges.

4.3 Results

4.3.1 Assumption-based results

Although the estimation errors were different across the eight protocols, they showed similar characteristics when ATT_t or δ varied. Here taking Seq_singleLD as an example, CBF and ATT estimation errors using gkm (dashed lines) and gkm + mvc (solid lines) under the assumptions 'percentage', 'fixed', and 'fixed_interval' are shown by Figures 4.3.1, 4.3.2, and 4.3.3, respectively. The estimation results by protocols other than Seq_singleLD are listed in Appendix A.1-A.3. In general, the simple model gkm led to more variable estimation, if not higher estimation errors, than the extended model gkm + mvc.

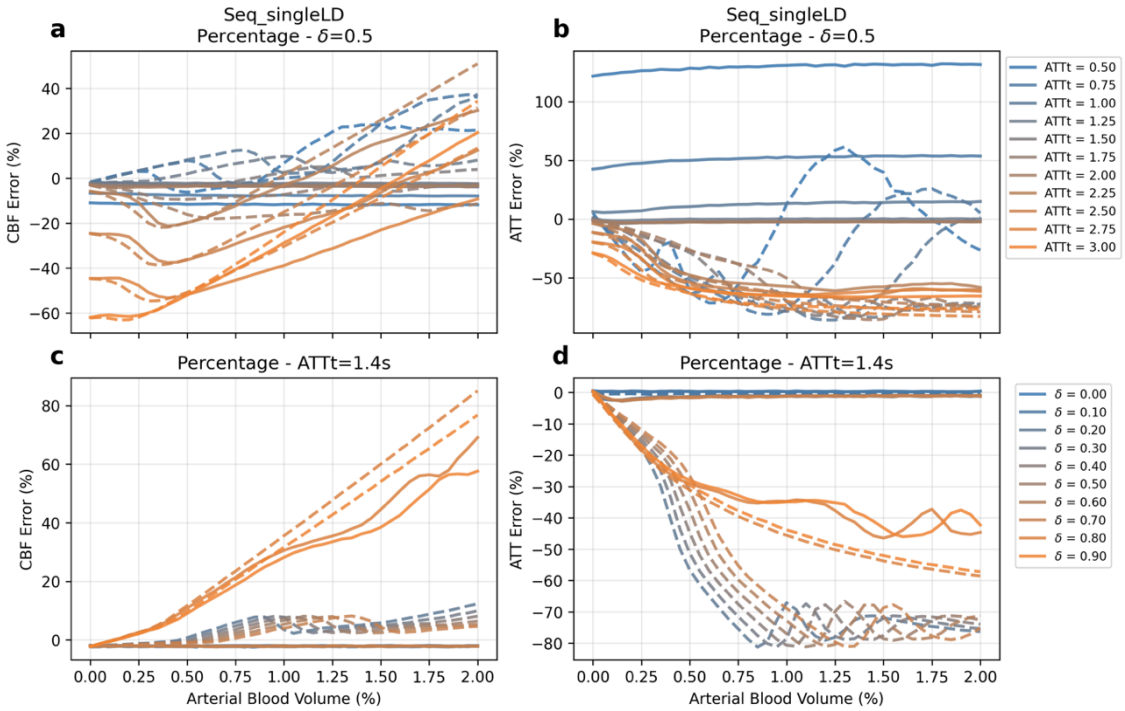


Figure 4.3.1 CBF and ATT estimation errors of Seq_singleLD using gkm (dashed lines) and gkm + mvc (solid lines) under the percentage assumption. (a) and (b): δ = 0.5 while varying ATT_t; (c) and (d): ATT_t = 1.4s while varying δ.

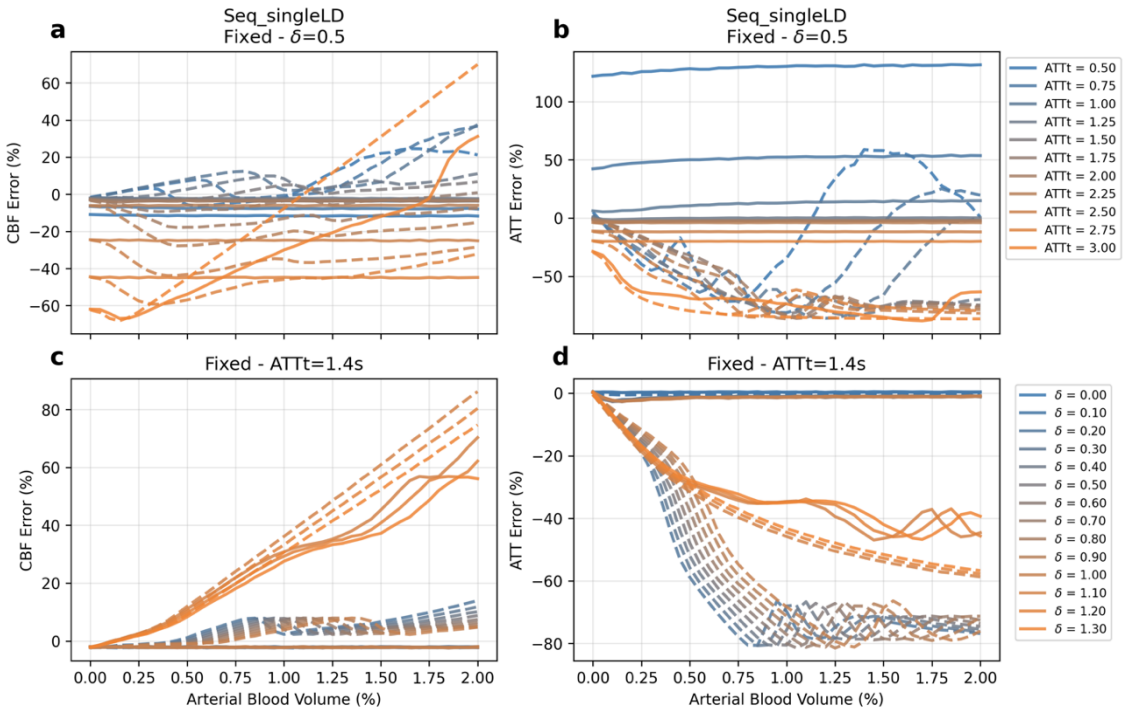


Figure 4.3.2 CBF and ATT estimation errors of Seq_singleLD using gkm (dashed lines) and gkm + mvc (solid lines) under the fixed assumption. (a) and (b): δ = 0.5 while varying ATT_t; (c) and (d): ATT_t = 1.4s while varying δ.

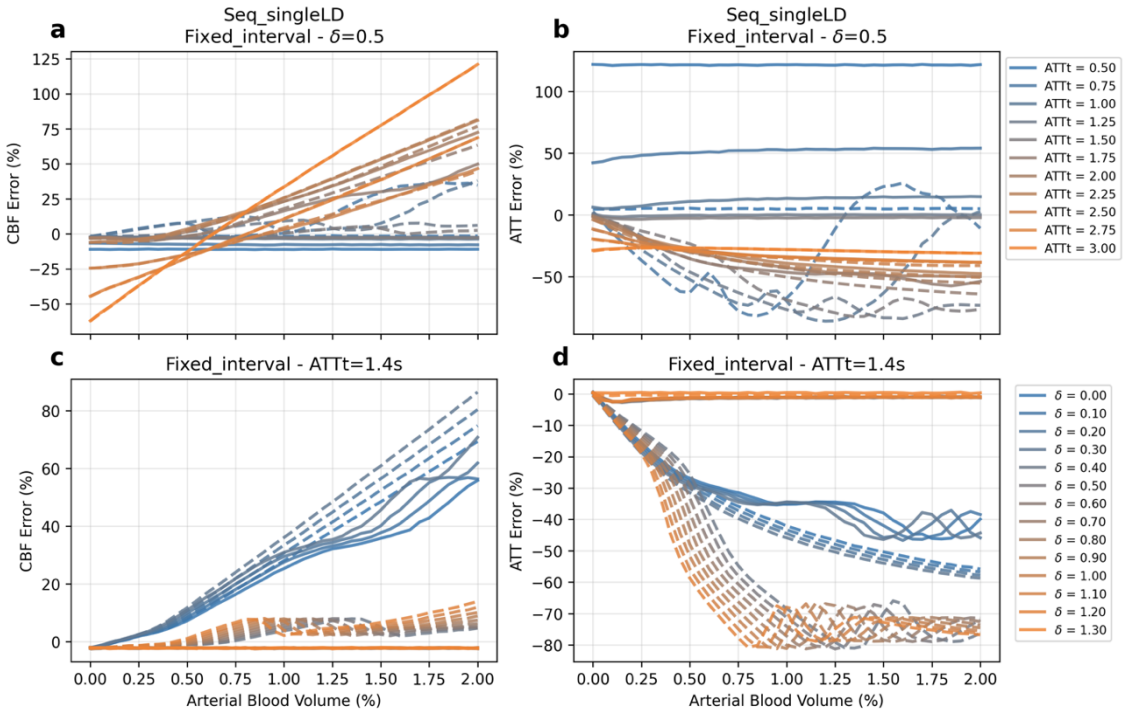


Figure 4.3.3 CBF and ATT estimation errors of Seq_singleLD using gkm (dashed lines) and gkm + mvc (solid lines) under the fixed_interval assumption. (a) and (b): δ = 0.5 while varying ATT_t; (c) and (d): ATT_t = 1.4s while varying δ.

When each δ was held constant and ATT_t varied, the results from all three assumptions agreed reasonably well (Figure 4.3.1ab, Figure 4.3.2ab, Figure 4.3.3ab). The extended model gkm + mvc gave more consistent CBF and ATT estimation across different levels of aBV when ATT_t was short and up to 2.25s. When ATT_t was longer than 2.25s, CBF was underestimated at low aBV and overestimated at high aBV, while ATT was underestimated across all aBVs.

When ATT_t was held constant at 1.4s and δ varied, 'percentage' and 'fixed' assumptions showed similar patterns, with a higher δ (i.e., a shorter interval between ATT_a and ATT_t) leading to higher CBF and ATT errors (Figure 4.3.1cd, Figure 4.3.2cd), while the 'fixed_interval' assumptions showed reverse patterns, since a higher δ means a longer interval between macrovascular and tissue transit times (Figure 4.3.3cd). CBF was overestimated and ATT was underestimated with an increasing aBV. The simpler model gkm performed relatively well in CBF estimation (with errors less than 20%)

when ATT_a < 1.1s, corresponding to δ < 1.1 under the 'fixed' assumption, with a cost of ATT estimation accuracy. Using a two-compartment model within this ATT_a range greatly reduces CBF and ATT estimation error. However, both models had high CBF and ATT errors beyond ATT_a = 1.1s.

CBF sensitivity (Θ_{CBF}) to macrovascular contamination using gkm and gkm + mvc, as well as their differences (gkm + mvc - gkm) under the assumptions of 'percentage', 'fixed', and 'fixed_interval' for all protocols are shown by Figures 4.3.4, 4.3.5, and 4.3.6, respectively. The fact that Θ_{CBF} differences between the two models were largely below zero indicates the extended model could reduce CBF sensitivity to MVC. However, it is worth noting that this effect of reduction is more prominent when ATT_t was in the range [1.2s, 2.3s], while small or nearly no reduction of Θ_{CBF} was achieved when ATT_t was either very short or very long in the examined range.

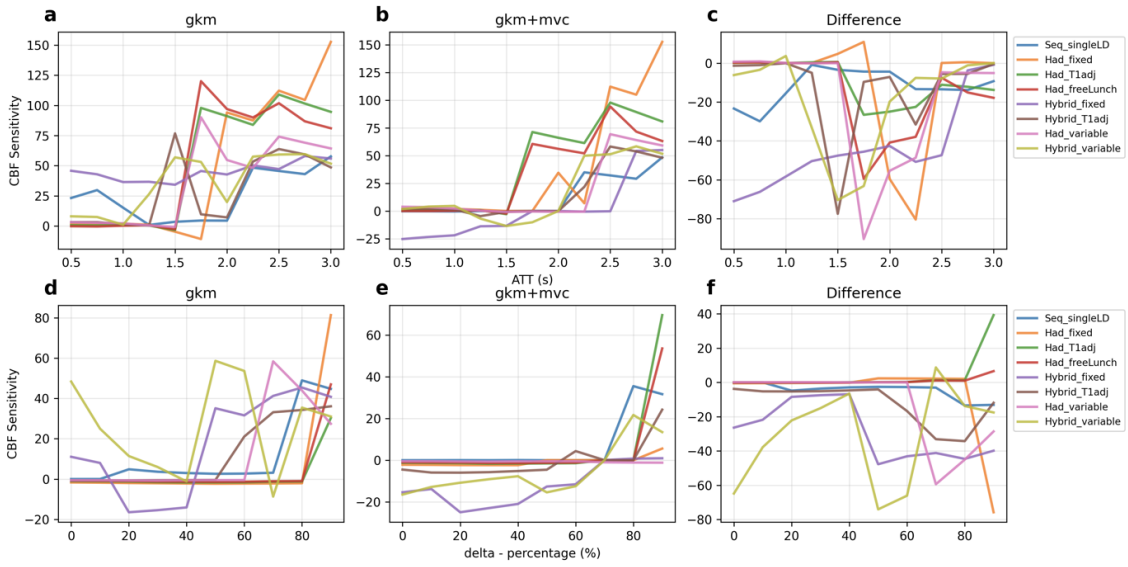


Figure 4.3.4 CBF sensitivity to macrovascular contamination using gkm (first column), gkm + mvc (second column), and their difference (gkm + mvc - gkm, third column) under the percentage assumption by all eight protocols. (a)(b) and (c): δ = 0.5 while varying ATT_t; (d)(e) and (f): ATT_t = 1.4s while varying δ.

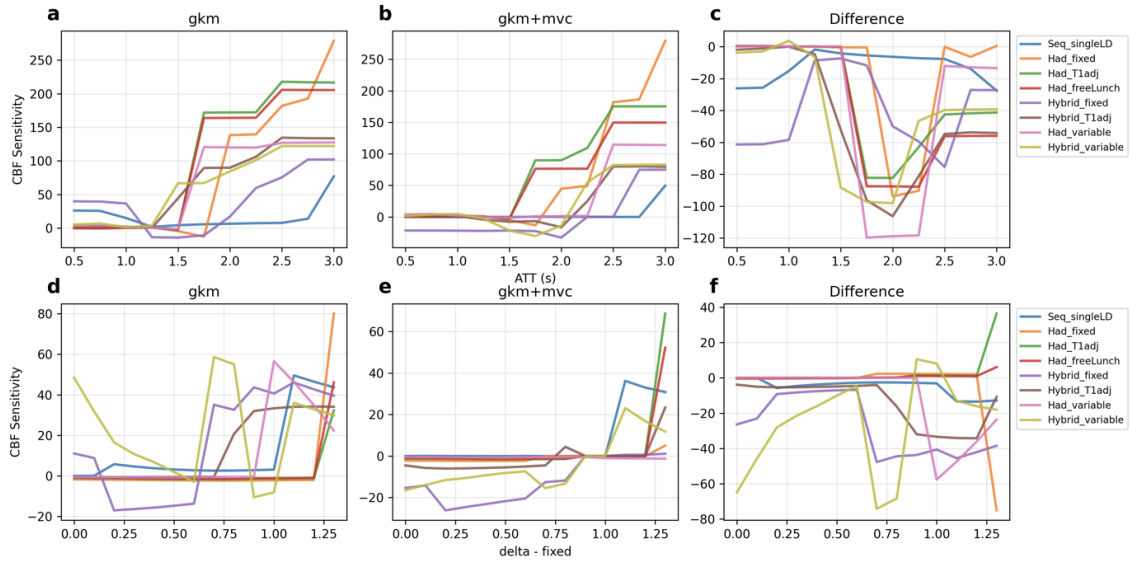


Figure 4.3.5 CBF sensitivity to macrovascular contamination using gkm (first column), gkm + mvc (second column), and their difference (gkm + mvc - gkm, third column) under the fixed assumption by all eight protocols. (a)(b) and (c): δ = 0.5 while varying ATT_t; (d)(e) and (f): ATT_t = 1.4s while varying δ.

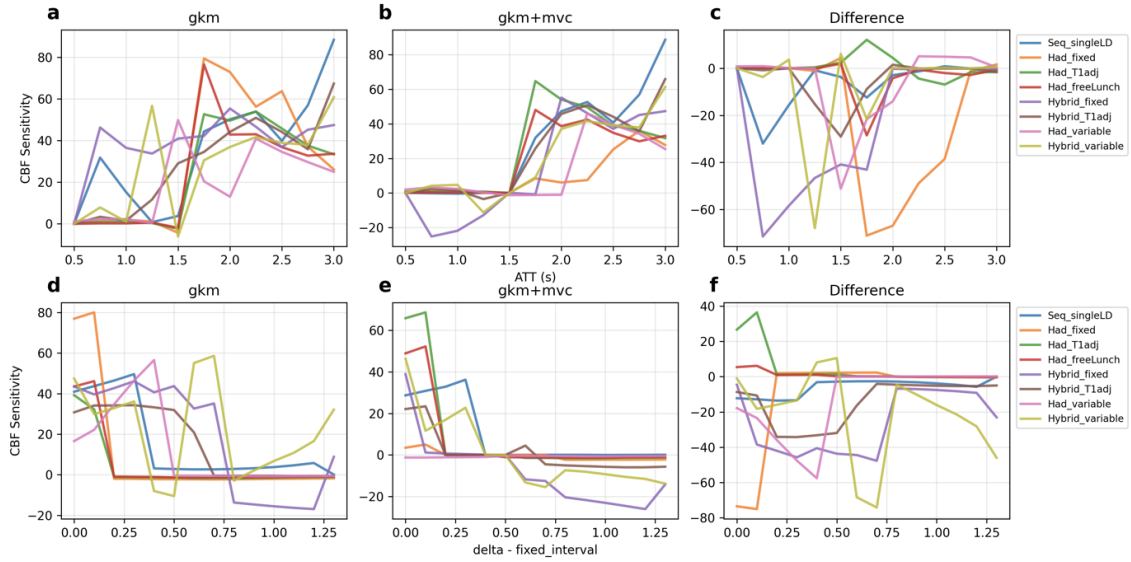


Figure 4.3.6 CBF sensitivity to macrovascular contamination using gkm (first column), gkm + mvc (second column), and their difference (gkm + mvc - gkm, third column) under the fixed_interval assumption by all eight protocols. (a)(b) and (c): δ = 0.5 while varying ATT_t; (d)(e) and (f): ATT_t = 1.4s while varying δ.

Across all three assumptions, when δ was held constant, Θ_{CBF} increased with a longer ATT_t (first rows of Figures 4.3.4, 4.3.5, and 4.3.6). When ATT_t was held constant, Θ_{CBF} was relatively low for smaller δ under 'percentage' and 'fixed' assumptions (second rows of Figures 4.3.4 and 4.3.5). The reverse is true under the

'fixed_interval' assumption (second row of Figure 4.3.6). This means a smaller difference between ATT_a and ATT_t typically leads to higher Θ_{CBF}, especially when gkm + mvc was used in model fitting.

4.3.2 Map-based results

CBF, ATT, and aBV sensitivity maps to MVC using gkm, gkm + mvc, as well as their difference (gkm + mvc - gkm) for the protocol Had_fixed as an example are shown by Figure 4.3.7. Sensitivity maps by protocols other than Had_fixed are listed in Appendix A4. For CBF sensitivity, both gkm and gkm + mvc had the highest Θ_{CBF} values when ATT_t = 3.0s and ATT_a = 0, i.e., the most extreme simulated condition where the transit times had the largest difference. Both models had relatively low Θ_{CBF} when ATT_t < 1.8s, corresponding with the optimised ATT_t range of [0.5s, 2.0s] of the protocols. The two-compartment model reduced Θ_{CBF} most prominently when 1.8s < ATT_t < 2.3s and 0 < ATT_a < 0.6s. The ATT sensitivity difference map showed largely consistent features with the CBF sensitivity difference map, except in smaller regions such as 2.6s < ATT_t < 2.9s and 0 < ATT_a < 1.2s. The aBV sensitivity map shows that aBV estimation was possible when ATT_t > 1.2s and ATT_a < 1.2s. In addition, aBV was most accurately estimated for each ATT_t when ATT_a = 0, indicated by the highest Θ_{aBV} value, since Θ_{aBV} closer to one would mean perfect aBV estimation.

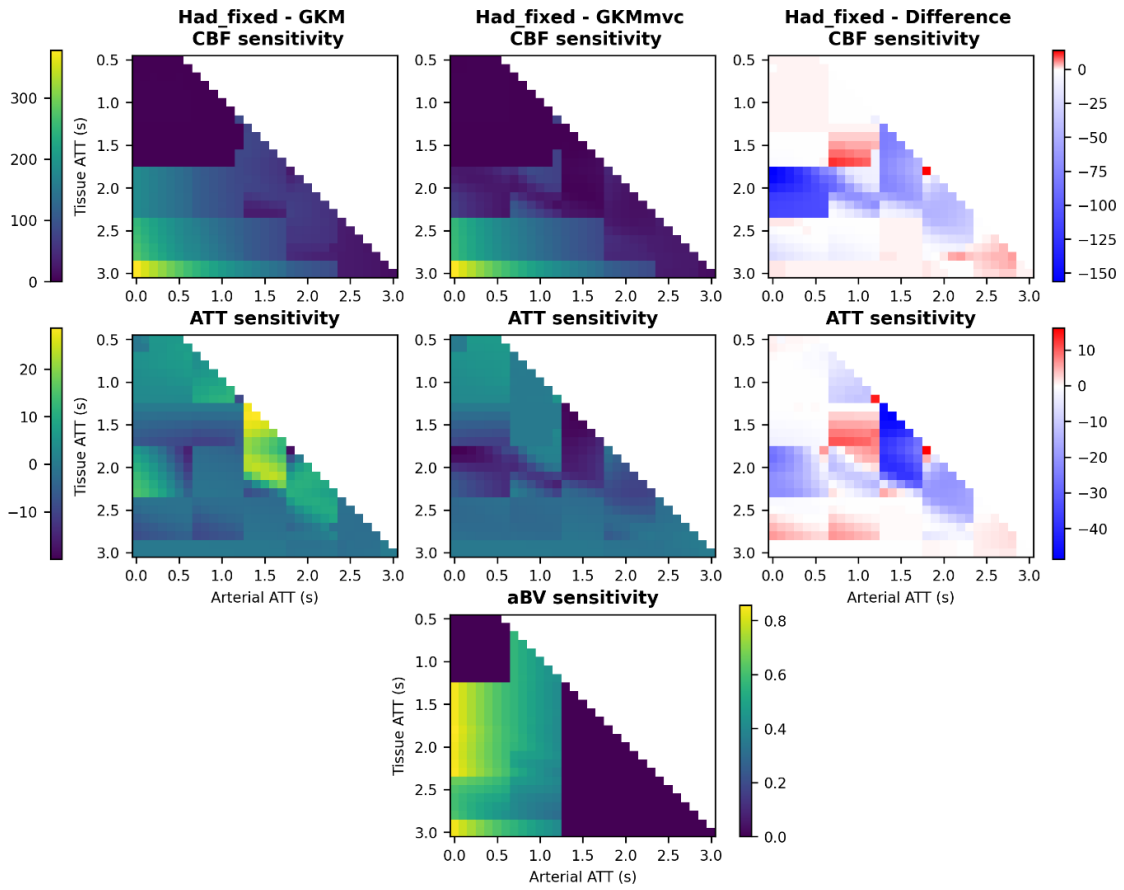


Figure 4.3.7 CBF, ATT, and aBV sensitivity maps to macrovascular contamination using gkm (first column), gkm + mvc (second column), and their difference (gkm + mvc - gkm, third column) by the protocol Had_fixed.

To examine the overall performance of different optimal protocols, the sensitivity maps were averaged across eight protocols and shown by Figure 4.3.8. Consistent features with protocol Had_fixed (Figure 4.3.7) in Θ_{CBF} could be observed, with the largest difference when 1.6s < ATT_t < 2.3s and 0 < ATT_a < 0.8s. For Θ_{ATT}, using the extended model had variable effects across the map. However, the sensitivity values in the map using gkm + mvc were closer to zero compared to those in the map using gkm, demonstrating the effect of reducing absolute Θ_{ATT} and providing more consistent estimation. Θ_{aBV} was the highest at ATT_t = 2.0s and ATT_a = 0, but it dropped to zero beyond ATT_a = 1.5s, indicating the poor performance in estimating aBV in this range.

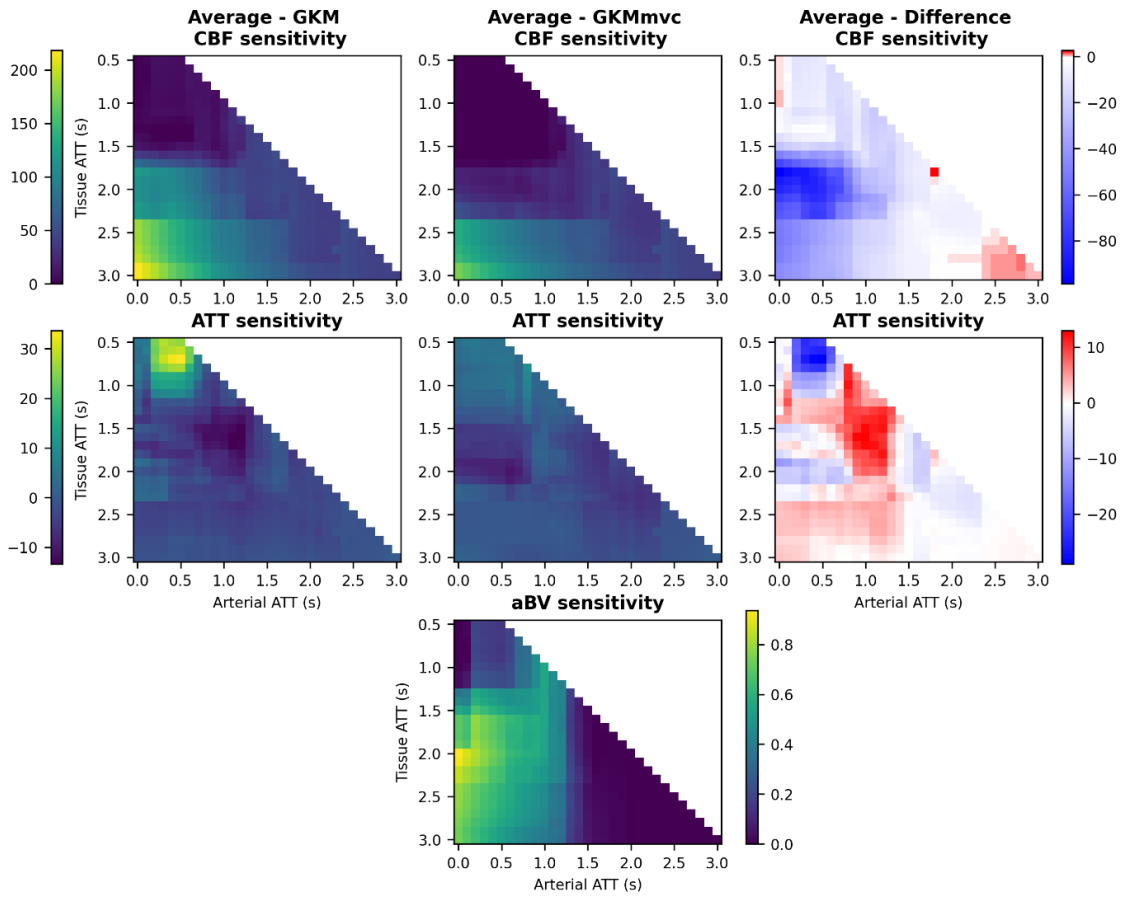


Figure 4.3.8 CBF, ATT, and aBV sensitivity maps to macrovascular contamination using gkm (first column), gkm + mvc (second column), and their difference (gkm + mvc - gkm, third column) averaged over all protocols.

4.4 Discussion

In this chapter, we investigated the parameters' sensitivity to macrovascular contamination using one- and two-compartment models by eight optimised protocols. Building on the findings in Chapter 3, this study offers a holistic analysis under a complete set of possible combinations of macrovascular and tissue transit times, thus providing more support to the recommendations made in the previous chapter on the application of the extended model.

Because there is limited literature regarding the relationships between ATT_a and ATT_t *in vivo*, the assumption-based analysis would allow us to evaluate different

conditions one might encounter in real data. The 'percentage' assumption may be more intuitive and representative, while 'fixed' and 'fixed_interval' assumptions are more extreme cases where ATT_a or the interval remains constant when ATT_t changes. From Figure 4.3.4a, there were no consistent patterns across protocols using gkm. When fitted with gkm + mvc (Figure 4.3.4b), four Hadamard-encoded protocols were nearly insensitive to MVC in the range of $ATT_t < 1.5$s, whereas hybrid protocols may have negative CBF sensitivity values. The negative Θ_{CBF} may be due to overfitting of the macrovascular component by gkm + mvc, thus underestimating CBF with increasing aBV. Under 'percentage' and 'fixed' assumptions, hybrid protocols generally had lower Θ_{CBF} values than Hadamard-encoded protocols when $ATT_t > 2.0$s, which is beyond the optimised ATT_t range of all protocols. This is consistent with the results in the previous study[1], which found Hybrid_T1adj to be the most accurate and robust CBF estimation protocol.

The sensitivity maps obtained for CBF, ATT, and aBV provide a systematic investigation into the sensitivity to MVC of the parameters of interest. Θ_{CBF} using gkm increased with a longer ATT_t and a shorter ATT_a, which is probably because the increased interval between the two compartments confounds CBF estimation, leading to the macrovascular signal interpreted as tissue perfusion. The extended model gkm + mvc could generally reduce Θ_{CBF} across the map, and was especially effective when 1.8s $< ATT_t < 2.3$s and $0 < ATT_a < 0.6$s. However, there were still individual differences by each protocol, shown by different features and regions where the extended model had the most reduction effects in Appendix A.4. Therefore, the sensitivity maps may be useful in examining a protocol for possible MVC effects and the benefits of using more complicated models prior to scanning, so as to choose a protocol that best matches the expected ATT_t values within a subject group. In addition, they could be used

retrospectively after data collection for interpreting results, when MVC effects are more prominently observed using certain protocols than others.

Since a Bayesian inference method was used to fit the simulated data, when estimation is not possible, the model output will rely largely on the prior information of the parameters. This was especially true in estimating ATT, e.g., shown in Figure 4.3.1b when ATT_t is short. The ATT estimation means would plateau around the prior value of ATT = 1.3s. Besides, given the nonlinearity of ATT in the general kinetic model outlined in Section 3.2.1, the ATT errors were hardly linear to aBV as CBF errors. Therefore, our current Θ_{ATT} might not be as good a metric as CBF sensitivity to MVC. To address this problem, three metrics for Θ_{ATT} were derived in search for a more consistent comparison to Θ_{CBF}:

a) $\Theta_{ATT-linear}$: The slope of the line of best fit of ATT estimation error mean curves (unit: error% per 1% aBV), which is the one used above.

b) $\Theta_{ATT-error}$: The mean absolute error of ATT estimation across the entire range of aBV (unit: error %).

c) $\Theta_{ATT-exponential}$: The decay term b of a negative exponential fit ($y = Ae^{-bx} + C$) of ATT estimation error mean curves (unit: $(1\%\ aBV)^{-1}$).

The definitions of $\Theta_{ATT-error}$ and $\Theta_{ATT-exponential}$ may be easier to understand, in that $\Theta_{ATT-error}$ represents the average level of ATT error the model would give if the aBV is within the simulated range, and $\Theta_{ATT-exponential}$ indicates how fast the ATT error curve would plateau to a constant or to the priors. The $\Theta_{ATT-exponential}$ values were obtained by the 'curve_fit' function of the SciPy package. The average ATT sensitivity maps by all protocols according to these metrics are shown in Figure 4.4.1. The ATT sensitivity maps by each protocol are provided in Appendix A.5.

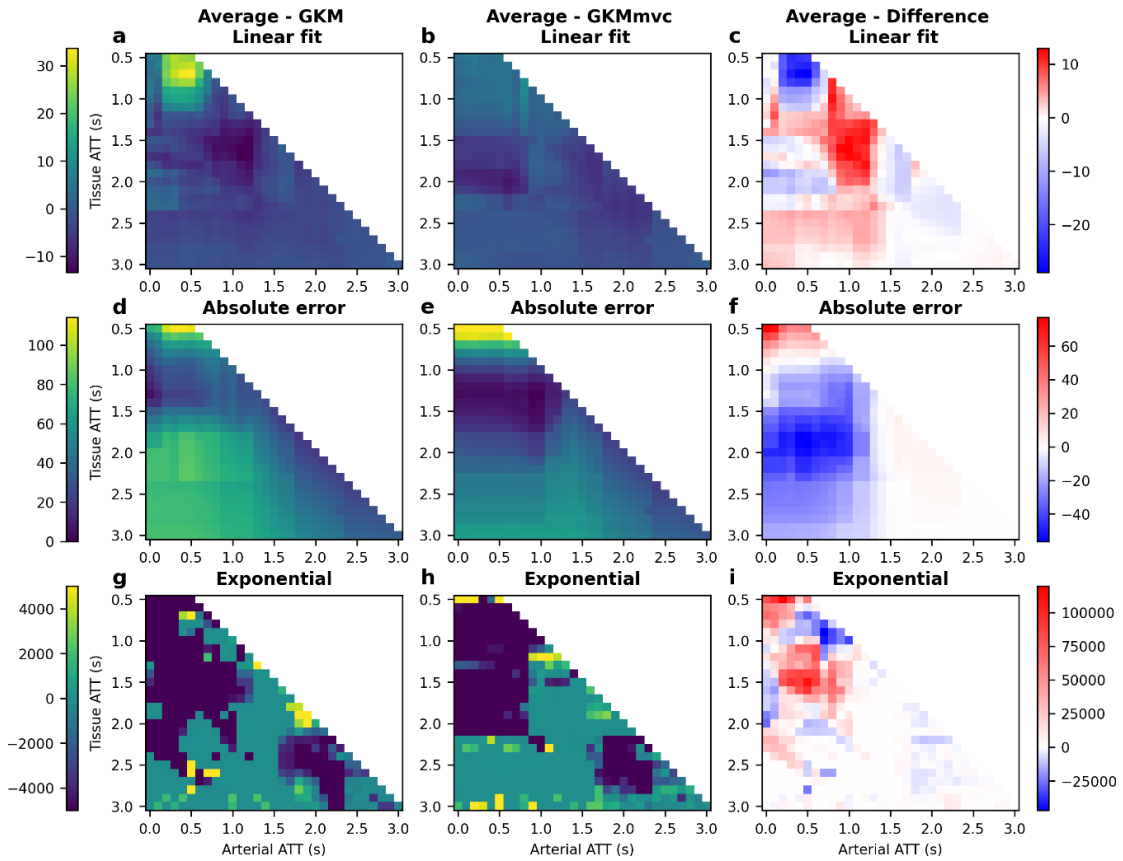


Figure 4.4.1 ATT sensitivity maps using gkm (first column), gkm + mvc (second column), and their difference (gkm + mvc - gkm, third column) averaged over all protocols. (a), (b), (c): linear fitting; (d), (e), (f): mean absolute error; (g), (h), (i): negative exponential fitting.

$\Theta_{ATT-error}$ exhibits more consistent features with Θ_{CBF}. The difference map Figure 4.4.1f shows a region around 1.5s < ATT_t < 2.3s and 0 < ATT_a < 1.0s that had the most benefit of reducing absolute estimation errors when the extended model was used. This coincided with the region seen in Θ_{CBF} difference map. The fact that this range corresponds with the ATT_t and ATT_a values appeared in literature[6,7] gives weight to the claim that adding a macrovascular component in the analysis could reduce estimation error. However, when ATT_t was shorter than 0.8s or ATT_a was longer than 1.5s, corresponding to abnormal cases one might observe in various pathology, choosing the simpler gkm would not lead to severe penalties due to MVC. In contrast, the gkm and gkm + mvc maps of $\Theta_{ATT-exponential}$ appeared to be noisier and more inconsistent in

Figure 4.4.1gh. Overall, it was found that due to the nonlinearity of ATT estimation, and that the protocols examined here were not optimised for estimating ATT, Θ_{ATT} were more expectedly nonlinear and provided less meaningful implications than Θ_{CBF}.

4.5 Conclusion

In this chapter, we conducted simulation experiments and obtained sensitivity maps to macrovascular contamination for different parameters over a more complete set of combinations of ATT_t and ATT_a. More evidence was found to support the claim in Chapter 3 that the two-compartment model gkm + mvc could reduce CBF sensitivity to MVC as well as ATT estimation errors within certain transit time ranges. The sensitivity maps could be used when one needs to examine a protocol for potential MVC effects before imaging, or interpret the results after data analysis.

4.6 References

1. Woods JG, Chappell MA, Okell TW. Designing and comparing optimized pseudo-continuous Arterial Spin Labeling protocols for measurement of cerebral blood flow. *Neuroimage*. 2020;223(August):117246.
2. Buxton RB, Frank LR, Wong EC, Siewert B, Warach S, Edelman RR. A general kinetic model for quantitative perfusion imaging with arterial spin labeling. *Magn Reson Med*. 1998;40(3):383-396.
3. Chappell MA, MacIntosh BJ, Donahue MJ, Günther M, Jezzard P, Woolrich MW. Separation of macrovascular signal in multi-inversion time arterial spin labelling MRI. *Magn Reson Med*. 2010;63(5):1357-1365.
4. Mehta RR, Chappell MA. Quantification of errors in cerebral blood flow measurements due to dispersion in arterial spin labelling. In: *2015 37th Annual International Conference of the IEEE Engineering in Medicine and Biology Society (EMBC)*. Vol 2015-Novem. IEEE; 2015:7917-7920.
5. Chappell MA, Groves AR, Whitcher B, Woolrich MW. Variational Bayesian Inference for a Nonlinear Forward Model. *IEEE Transactions on Signal Processing*. 2009;57(1):223-236.
6. Chen Y, Wang DJJ, Detre JA. Comparison of arterial transit times estimated using arterial spin labeling. *Magnetic Resonance Materials in Physics, Biology and Medicine*. 2012;25(2):135-144.
7. Mildner T, Müller K, Hetzer S, Trampel R, Driesel W, Möller HE. Mapping of arterial transit time by intravascular signal selection. *NMR Biomed*. 2014;27(5):594-609.

5 Combined optimisation of delays and echo times for blood-brain barrier permeability measurements using multi-TE pCASL MRI

5.1 Introduction

The blood-brain barrier (BBB) plays an indispensable role in the homeostasis of the central nervous system. Disruption of the BBB is considered as a precursor to vascular changes in many cerebral pathologies, such as stroke[1], multiple sclerosis[2], and neurodegenerative diseases[3]. Therefore, the measurement of BBB structural and functional integrity is potentially of great clinical value.

Blood water in the capillary vessel lumen is transported across the semi-permeable BBB into the extravascular space via diffusion or active transport through the aquaporin channels[4]. The average time water molecules spend before exchanging into the perfused tissue, $Texch$, can be used as a surrogate measure of blood-brain barrier integrity. Pseudo-continuous arterial spin labelling (pCASL), a non-invasive MRI technique that uses magnetically labelled blood water as an endogenous tracer to provide quantitative cerebral blood flow (CBF) measurements, can be used with multiple post-labelling delays (multi-PLD) to capture the early signals when the labelled bolus arrives and exchanges at the imaging voxel[5–11]. Subsequently, $Texch$ can be measured by resolving the signal fractions from the two spin compartments, the intravascular (IV) and the extravascular (EV) compartment, as a function of time, according to their differences in diffusion characteristics using diffusion-weighted ASL, or transverse relaxation times (T2) using multi-TE ASL, the latter of which is the focus of this study. A review of literature on these methods can be found in Section 2.4.3.

In multi-TE multi-PLD pCASL, a bi-exponential T2 decay model is fitted to the ASL signal ΔM to estimate signal contributions from IV and EV compartments as a function of PLDs and TEs:

$$\Delta M(PLD, TE) = \Delta M_{IV}(PLD)e^{-\frac{TE}{T2_{IV}}} + \Delta M_{EV}(PLD)e^{-\frac{TE}{T2_{EV}}}, \quad \text{(Equation 5.1.1)}$$

where $\Delta M_{IV}(t)$, $\Delta M_{EV}(t)$, $T2_{IV}$, and $T2_{EV}$ are the signal and T2 values from the IV and EV compartments, respectively.

To constrain the four 'free' parameters in the bi-exponential model (Equation 5.1.1), $T2_{EV}$ is often estimated with a mono-exponential decay model on the control image, under the assumption that the EV tissue signal dominates in the control image[12]. Next, ΔM_{IV} and ΔM_{EV} are fitted with compartmental kinetic models to obtain separate arrival times of each compartment (Figure 5.1.1a). $Texch$ is then defined as either the difference between IV and EV arrival times[13–15] or the exponential transfer rate between the compartments[16], and thus can be quantitively measured.

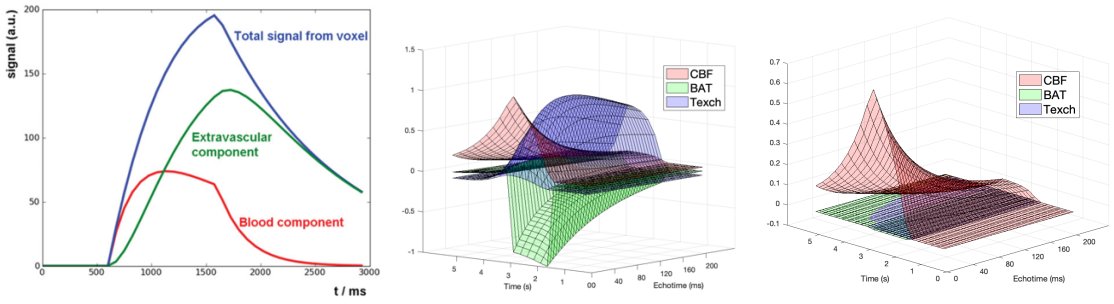


Figure 5.1.1 (a) The IV and EV compartmental contributions of the ASL signal using the kinetic model from Gregori et al.[16] (b) Normalised sensitivity functions of ΔM_{IV} and ΔM_{EV} to CBF, bolus arrival time (BAT), and $Texch$. (c) Absolute sensitivity functions of ΔM_{IV} and ΔM_{EV} to CBF, BAT, and $Texch$. Sensitivity functions were simulated using ground truth CBF = 60ml/100g/min, BAT = 1.4s, $Texch$ = 0.3s, using the kinetic model from Gregori et al.[16]

Previous research using multi-PLD multi-TE ASL was able to obtain reliable estimates of $Texch$ only in the cortex of rodents and in grey matter of humans[10,13,16]. This may be due to several reasons: a) ASL images have inherently low signal-to-noise

ratio (SNR). ASL signal only accounts for 1~2% of the MR signal in the label/control image, but adding more repeats to each PLD comes at a cost of increasing the total scan duration. b) The relatively small compartmental T2 difference leads to low sensitivity to changes of $Texch$ in the kinetic models compared to CBF, as illustrated in absolute values in Figure 5.1c. This makes the estimation accuracy of $Texch$ prone to error propagation in the post-processing pipeline. c) T2 differences are more sensitive to blood oxygenation or haematocrit, adding to experiment noise[12,17,18]. Therefore, methods such as increasing the SNR or optimising of the acquisition are needed to improve $Texch$ quantification accuracy using multi-PLD multi-TE ASL, with the goal of measuring this potential biomarker within a clinically practical scan duration (e.g., 5 minutes).

As introduced in previous chapters, the optimal sampling strategy (OSS), which determines the optimal set of sampling times of an unknown signal-time course, aims to maximise the estimability of the parameters of interest. Multi-PLD pCASL protocols with optimised PLDs, as well as simultaneously optimised PLDs and label durations (LDs) with Hadamard encoding, have been shown to reduce the estimation uncertainty of CBF and arterial transit time (ATT) or bolus arrival time (BAT)[19–21]. Additionally, the optimisation framework could accommodate different optimalities and incorporate prior information of the parameters, i.e., the optimised ranges, so as to obtain optimised protocols that are targeted at specific parameters of interests and subject groups. However, there has been little research that uses OSS to simultaneously optimise the PLDs and TEs to measure BBB permeability to water using multi-TE multi-PLD pCASL. This chapter aims to extend the current OSS framework by optimising PLDs and TEs, and examine the utility and potential benefits of OSS in estimating $Texch$.

5.2 Optimisation

5.2.1 Theory

The underlying theory of optimal sampling strategy is the Cramer-Rao Lower Bound, which states that the lower bound of the covariance matrix of an unbiased estimator is the inverse of the Fisher Information Matrix (FIM). The FIM in ASL is defined in Equation 5.2.1 using the Hessian matrix of the parameters of interest vector $\boldsymbol{\theta}$, which in this study $\boldsymbol{\theta} = \{CBF, BAT, Texch\}$, multiplied by the number of repetitions and divided by the noise variance:

$$FIM(\boldsymbol{\theta}; \boldsymbol{PLD}; \boldsymbol{TE}) = \frac{A}{\sigma^2} \cdot \left(\frac{\partial \Delta M(\boldsymbol{\theta}; \boldsymbol{PLD}; \boldsymbol{TE})}{\partial \boldsymbol{\theta}}\right)^T \left(\frac{\partial \Delta M(\boldsymbol{\theta}; \boldsymbol{PLD}, \boldsymbol{TE})}{\partial \boldsymbol{\theta}}\right). \text{(Equation 5.2.1)}$$

Based on the A-optimality criterion reviewed in Chapter 2, minimising the estimation SD is equivalent to minimising the trace of the Hadamard square root of the FIM inverse. To eliminate the effect of parameter means, the optimality criterion is normalised elementwise by dividing the FIM with a normalisation matrix $N(\boldsymbol{\theta}) = (\boldsymbol{\theta}^{0.5})^T(\boldsymbol{\theta}^{0.5})$, effectively minimising the sum of coefficients of variation (CoV) of the parameters of interest[22]. Different weights are assigned to each parameter in the weighting matrix $\boldsymbol{W}$, changing the optimality of the resulting protocol. A discrete pseudo-Bayesian method was adopted where CBF, BAT, and $Texch$ were given uniform distributions, and the optimality criterion was averaged over these prior distributions. As a result, the optimised PLDs and TEs are those minimising the optimality criterion:

$$\widehat{\boldsymbol{PLD}}, \widehat{\boldsymbol{TE}} = \underset{\substack{\boldsymbol{PLD} \in \boldsymbol{X} \\ \boldsymbol{TE} \in \boldsymbol{Y}}}{\arg\min} \frac{1}{|\boldsymbol{\Theta}|^3} \sum_{\boldsymbol{\theta} \in \boldsymbol{\Theta}} \mathrm{Tr}\left(\boldsymbol{W} \cdot \left(\frac{|FIM^{-1}(\boldsymbol{\theta}; \boldsymbol{PLD}; \boldsymbol{TE})|^{0.5}}{N(\boldsymbol{\theta})}\right) \cdot \boldsymbol{W}\right), \text{ (Equation 5.2.2)}$$

where $\boldsymbol{X}$, $\boldsymbol{Y}$ are the set of all plausible PLDs and TEs, respectively, and $|\boldsymbol{\Theta}|$ is the number of points in the prior distributions of the parameters of interest for the pseudo-Bayesian evaluation.

5.2.2 Schemes

The optimisation was tested with two multi-TE pCASL schemes, T2-Relaxation-Under-Spin-Tagging (TRUST)[23] and multi-TE 3D GRASE (Gradient- and Spin-Echo) readout[24], the latter of which we termed mTE-GRASE.

In a TRUST sequence (Figure 5.2.1), T2-weightings are generated by inserting a series of non-selective T2-preparation RF pulses during the PLD and just before the excitation pulse to create an effective TE (eTE). The same eTE is used in label and control images for pairwise subtraction and can be used across multiple repeats. To minimise the imperfect pulse profiles caused by B0 and B1 inhomogeneities, the T2-preparation pulses are arranged in a Malcolm-Levitt (MLEV) pattern. For this reason, the first non-zero eTE, eTE_1, is determined by the number and interval of CPMG pulses (e.g., a τ_{CPMG} of 10ms and four 180° pulses will result in an eTE_1 of 40ms) and subsequent eTEs are limited to eTE_1 multiplied by the powers of 2 (e.g., 80ms, 160ms, etc.). Because only one image with a single T2-weighting is obtained during an acquisition, the conventional multi-TE TRUST is time-consuming, and the total number of PLDs is equal to the total number of eTEs (which equals to half of the number of acquisitions). TRUST with Hadamard-encoded labelling schemes were used to improve time efficiency[25].

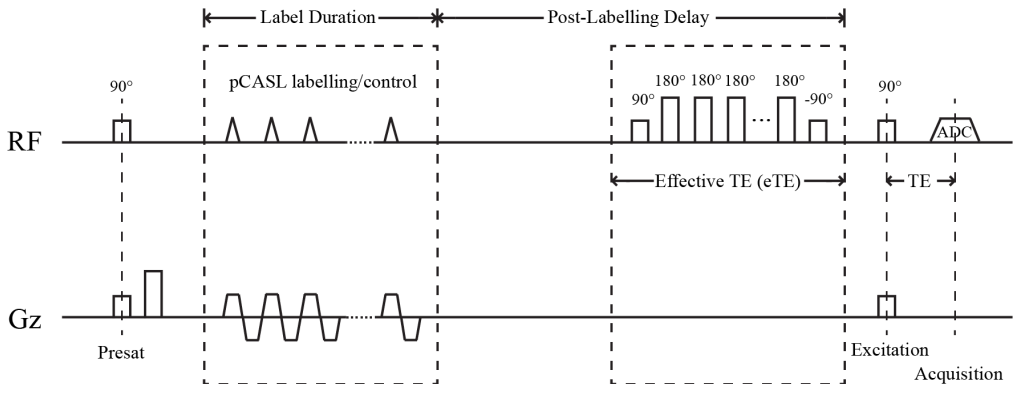


Figure 5.2.1 A schematic of the multi-echo TRUST pCASL scheme.

The mTE-GRASE scheme is similar to a multi-echo spin echo sequence, where multiple images of different TEs were acquired after a single excitation. Unlike TRUST, individual TE can be chosen freely as long as it does not incur significant T2-weighted signal loss, but it cannot be repeated within one TR. The number of PLDs can differ from the number of TEs, which is usually fixed and limited by the scanner settings.

5.2.3 Optimisation methods

Based on the parameters of interest vector $\boldsymbol{\theta} = \{CBF, BAT, Texch\}$, four optimality criteria were developed according to the different weighting matrices in the FIM listed in Table 5.2.1. As a result, protocols ALLopt, CBFopt, BATopt and Texopt were obtained from optimisation under each scheme, reflecting the respective parameters that the protocols were optimised for. Other parameters used in the simulation are listed in Table 5.2.2. Two reference protocols Ref-TRUST and Ref-mTE-GRASE, listed in Table 5.2.3 for the TRUST scheme and Table 5.2.5 for the mTE-GRASE scheme, represent the typical evenly spaced multi-PLD multi-TE pCASL protocols. In Ref-TRUST, each PLD has four repeats with eTEs being the available values administered in TRUST (0ms, 40ms, 80ms, 160ms). These two reference protocols are intended for the comparison of the optimised protocols against protocols commonly used in literature.

Protocols	ALLopt	CBFopt	BATopt	Texopt
Weighting matrix in FIM	$\begin{pmatrix} 1/3 & 0 & 0 \\ 0 & 1/3 & 0 \\ 0 & 0 & 1/3 \end{pmatrix}$	$\begin{pmatrix} 0.98 & 0 & 0 \\ 0 & 0.01 & 0 \\ 0 & 0 & 0.01 \end{pmatrix}$	$\begin{pmatrix} 0.01 & 0 & 0 \\ 0 & 0.98 & 0 \\ 0 & 0 & 0.01 \end{pmatrix}$	$\begin{pmatrix} 0.01 & 0 & 0 \\ 0 & 0.01 & 0 \\ 0 & 0 & 0.98 \end{pmatrix}$

Table 5.2.1 Weighting matrices in the optimality criterion in corresponding protocols.

Parameter	Value	Parameter	Value
Labelling efficiency (α)	0.85	PLD search limit	0.1s to 3.5s with 0.05s interval
Blood-tissue partition coefficient of water (λ)	0.9 mL/g	TE search limit	[0, 40, 80, 160] ms (TRUST); 5ms to 200ms with 5ms interval (mTE-GRASE)

T1 of blood	1.65s	Pseudo-Bayesian prior for CBF	$u[10, 90]$ mL/100g/min
T1 of tissue	1.3s	Pseudo-Bayesian prior for BAT	$u[1.0, 2.5]$ s
T2 of blood	300ms	Pseudo-Bayesian prior for $Texch$	$u[0.1, 0.8]$ s
T2 of tissue	47ms	Total scan time in LST mode	300s
Label duration (τ)	1.4s	Numbers of optimised PLDs	10 to 35
Readout time	0.8s	Numbers of optimised TEs	10 to 35 (TRUST) 10 (mTE-GRASE)

Table 5.2.2 List of parameters used in simulation. $u[a, b]$ denotes the uniform distribution between a and b.

The whole optimisation process is illustrated by the flow chart in Figure 5.2.2. Firstly, the numbers of PLDs and TEs to be optimised were input into the protocol generator, which consists of four steps of optimisation, with each step optimising for PLDs, TEs, PLDs, and TEs, respectively. The initialisation of PLDs and TEs in the first and second steps were evenly spaced between the lower and upper limits of the PLD and TE listed in Table 5.2.2. The output of each step was used as the initialisation of the next step. Within each step of optimisation, the series of PLDs and TEs were updated sequentially, meaning one PLD (or TE) was optimised before moving to the next PLD (or TE). The protocol generator would output the optimised PLDs from Step 3 and the optimised TEs from Step 4, as well as the loss function value from Step 4, which was calculated from the optimality criterion Equation 5.2.2. After updating the numbers of PLDs and TEs to be optimised and repeating the protocol generation, the global optimal PLDs and TEs were chosen as the set that gave the minimum loss. During the optimisation, it was observed that the output protocol converges after four steps. Namely, if the output PLD/TE were used as initialisations for further optimisation steps,

the output PLD/TE would stay the same. For simplicity, we used this empirical observation as the stopping criterion for the optimisation process.

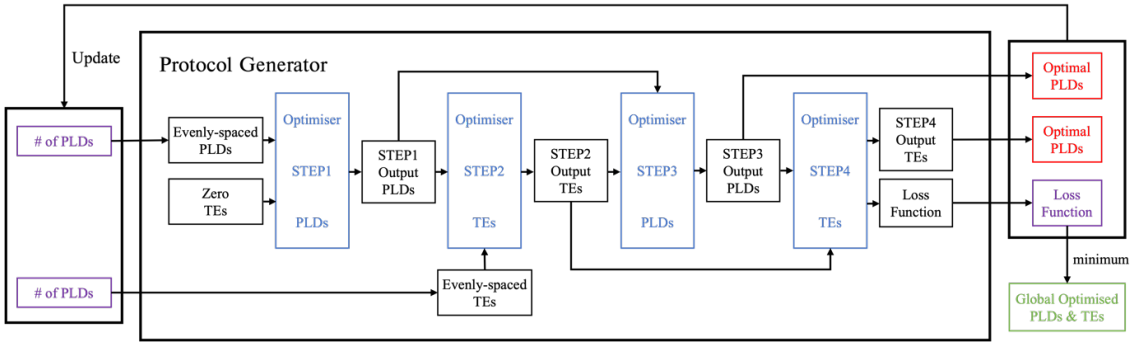


Figure 5.2.2 The optimisation process.

Furthermore, the optimisation can be performed under two modes: limited scan time (LST) and unlimited scan time (UST). The LST mode is the default mode, which sets a limit to the total scan duration defined by the user (e.g., 5 minutes), with higher numbers of PLDs (and TEs in TRUST) leading to lower numbers of repeats. The UST mode sets the number of repeats constant (in this study, two), ensuring the same SNR of each PLD/TE, and outputs the total scan duration. The latter was used to investigate the potential benefit of reducing the scan duration required to achieve a certain level of estimation uncertainty of the parameters of interest, which will be discussed in detail in Section 5.4.2.

5.2.4 Optimisation results

The output of optimisation in LST mode was a single protocol for each optimality criterion, which gave the minimum loss function value based on the optimality criterion, while not exceeding the total scan duration limit. To maintain sufficient SNR on each sampling time, each PLD was set to have at least two repeats. The protocols are listed in Tables 5.2.3 and 5.2.5 for TRUST and mTE-GRASE schemes, respectively. The

schematic PLD and TE timings of the protocols are illustrated in Figures 5.2.3 (TRUST) and 5.2.4 (mTE-GRASE).

The output in UST mode was a series of protocols, as well as the variable total scan time, that differed in the number of PLDs/TEs for each optimality criterion. The protocols with UST mode listed in Tables 5.2.4 and 5.2.6 were in the maximum number of PLDs/TEs examined, which was 35 under both TRUST and mTE-GRASE schemes.

- TRUST scheme with LST mode

Optimality	#PLDs/TEs	Optimised Timings		#Rep	#Acq	Scantime(s)
ALLopt	19	PLDs (s)	0.95, 0.95, 0.95, 1.15, 1.15, 1.15, 1.5, 1.5, 1.7, 1.85, 1.85, 2, 2, 2.05, 2.05, 2.05, 2.35, 2.55, 2.55	2	76	296.4
		eTEs (ms)	0, 80, 80, 0, 80, 80, 80, 80, 80, 0, 80, 80, 80, 0, 0, 80, 0, 0, 80			
CBFopt	18	PLDs (s)	1, 1, 1.35, 1.55, 1.55, 1.55, 1.85, 1.85, 1.85, 2.2, 2.2, 2.35, 2.35, 2.55, 2.55, 2.55, 2.55, 2.55	2	72	300
		eTEs (ms)	0, 160, 0, 0, 0, 160, 0, 0, 160, 0, 0, 0, 0, 0, 0, 0, 0, 0			
BATopt	20	PLDs (s)	0.3, 0.45, 0.45, 0.45, 0.8, 0.95, 0.95, 1.15, 1.2, 1.2, 1.55, 1.55, 1.55, 1.55, 1.7, 2.05, 2.2, 2.35, 2.55, 2.55	2	80	286
		eTEs (ms)	0, 0, 0, 0, 0, 0, 40, 0, 0, 0, 0, 0, 0, 80, 0, 0, 0, 0, 0, 0			
Texopt	19	PLDs (s)	0.95, 0.95, 0.95, 0.95, 1.15, 1.3, 1.5, 1.5, 1.7, 1.85, 1.85, 1.85, 1.95, 2, 2, 2, 2, 2, 2	2	76	289
		eTEs (ms)	0, 80, 80, 80, 80, 80, 80, 80, 80, 0, 80, 80, 160, 0, 0, 160, 160, 160, 160			
Ref-TRUST	20	PLDs (s)	0.5, 0.5, 0.5, 0.5, 1.0, 1.0, 1.0, 1.0, 1.5, 1.5, 1.5, 1.5, 2.0, 2.0, 2.0, 2.0, 2.5, 2.5, 2.5, 2.5	2	80	296

		eTEs (ms)	0, 40, 80, 160, 0, 40, 80, 160, 0, 40, 80, 160, 0, 40, 80, 160, 0, 40, 80, 160			

Table 5.2.3 Optimised protocols under the TRUST scheme with LST mode.

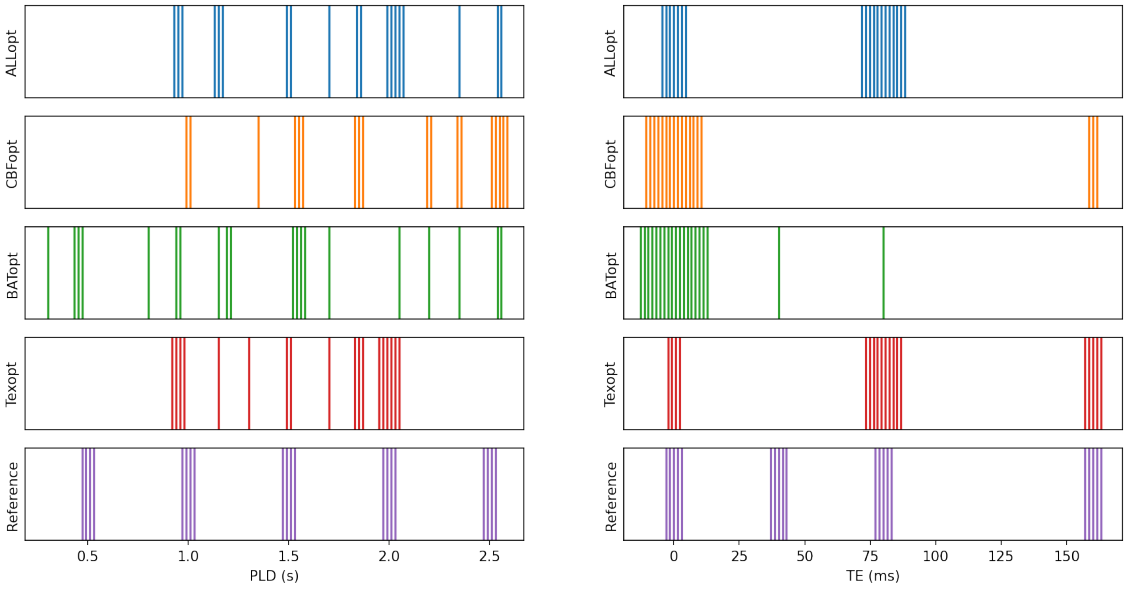


Figure 5.2.3 A schematic of the timings of optimised protocols and reference protocol under the TRUST scheme with LST mode. Repeated timings were shown as densely distributed lines centred at the corresponding timings.

- TRUST scheme with UST mode

Optimality	**#PLDs/TEs**	**Optimised Timings**		**#Rep**	**#Acq**	**Scantime(s)**
ALLopt	35	PLDs (s)	0.95, 0.95, 0.95, 0.95, 0.95, 1, 1.15, 1.15, 1.15, 1.2, 1.35, 1.35, 1.35, 1.35, 1.65, 1.65, 1.7, 1.85, 1.85, 1.85, 1.85, 1.85, 2, 2, 2, 2, 2.05, 2.2, 2.2, 2.2, 2.2, 2.2, 2.35, 2.55, 2.55	2	140	542.4
		eTEs (ms)	0, 80, 80, 80, 80, 80, 80, 80, 0, 80, 0, 80, 0, 80, 80, 80, 80, 80, 0, 80, 0, 80, 80, 160, 80, 80, 0, 0, 80, 80, 0, 80, 0, 0, 0			
CBFopt	35	PLDs (s)	0.95, 1.15, 1.15, 1.2, 1.3, 1.35, 1.7, 1.7, 1.7, 1.7, 1.7, 1.7, 1.8, 1.8, 1.85, 1.95, 2.05, 2.2, 2.2, 2.2, 2.35, 2.35, 2.35, 2.35, 2.35, 2.55, 2.55, 2.55, 2.55,	2	140	590.4

			2.55, 2.55, 2.55, 2.55, 2.55, 2.55			
		eTEs (ms)	0, 0, 160, 0, 160, 0, 0, 0, 0, 0, 0, 0, 0, 160, 160, 0, 160, 0, 0, 0, 0, 0, 0, 0, 0, 0, 0, 0, 0, 0, 0, 0, 0, 0, 0, 0, 0, 0, 0, 0, 0, 0, 0			
BATopt	35	PLDs (s)	0.15, 0.15, 0.3, 0.45, 0.45, 0.45, 0.45, 0.65, 0.8, 0.8, 0.95, 0.95, 1.15, 1.15, 1.15, 1.2, 1.2, 1.2, 1.2, 1.35, 1.65, 1.7, 1.7, 1.7, 1.7, 1.85, 2.05, 2.2, 2.2, 2.35, 2.35, 2.55, 2.55, 2.55, 2.55	2	140	499.2
		eTEs (ms)	0, 0, 0, 0, 0, 0, 0, 0, 0, 0, 40, 0, 0, 0, 0, 0, 0, 0, 0, 0, 0, 80, 0, 0, 0, 0, 0, 0, 0, 0, 0, 0, 0, 0, 0, 0, 0, 0, 0, 0, 0, 0, 0			
Texopt	35	PLDs (s)	0.95, 0.95, 0.95, 0.95, 0.95, 0.95, 0.95, 0.95, 1.2, 1.35, 1.35, 1.35, 1.5, 1.5, 1.5, 1.7, 1.7, 1.85, 1.85, 1.85, 1.85, 2, 2, 2, 2, 2, 2, 2, 2, 2, 2, 2, 2, 2, 2, 2, 2, 2	2	140	532.6
		eTEs (ms)	80, 80, 80, 80, 80, 80, 80, 0, 80, 80, 0, 80, 80, 80, 80, 80, 80, 160, 80, 80, 80, 160, 0, 160, 160, 160, 160, 0, 160, 160, 0, 160, 0, 0, 160			

Table 5.2.4 Optimised protocols of under the TRUST scheme with UST mode.

- mTE-GRASE scheme with LST mode

Optimality	**#PLDs/TEs**	**Optimised Timings**		**#Rep**	**#Acq**	**Scantime(s)**
ALLopt	19	PLDs (s)	0.95, 0.95, 0.95, 1.15, 1.15, 1.2, 1.35, 1.55, 1.7, 1.7, 1.85, 1.85, 2.05, 2.05, 2.2, 2.2, 2.2, 2.35, 2.55	2	76	295
	10	TEs (ms)	5, 10, 15, 95, 100, 105, 110, 115, 120, 125			
CBFopt	18	PLDs (s)	0.95, 1.2, 1.2, 1.35, 1.7, 1.7, 1.85, 1.85, 2.05, 2.05, 2.2, 2.35, 2.35, 2.35, 2.55, 2.55, 2.55, 2.55	2	72	299.8
	10	TEs (ms)	5, 10, 15, 20, 25, 30, 145, 150, 155, 160			

BATopt	21	PLDs (s)	0.15, 0.3, 0.45, 0.45, 0.65, 0.8, 0.95, 1.15, 1.15, 1.2, 1.2, 1.2, 1.35, 1.35, 1.7, 1.85, 2.05, 2.2, 2.35, 2.35, 2.55	2	84	294.4
	10	TEs (ms)	5, 10, 15, 20, 25, 30, 35, 40, 45, 50			
Texopt	19	PLDs (s)	0.95, 0.95, 0.95, 1, 1.15, 1.15, 1.35, 1.5, 1.65, 1.65, 1.8, 1.85, 2, 2, 2, 2, 2.15, 2.15, 2.15	2	76	288.8
	10	TEs (ms)	5, 10, 100, 105, 110, 115, 120, 125, 130, 135			
Ref-mTE-GRASE	5	PLDs (s)	0.5, 1.0, 1.5, 2.0, 2.5	8	80	296
	10	TEs (ms)	16, 32, 48, 64, 80, 96, 112, 128, 144, 160			

Table 5.2.5 Optimised protocols under the mTE-GRASE scheme with LST mode.

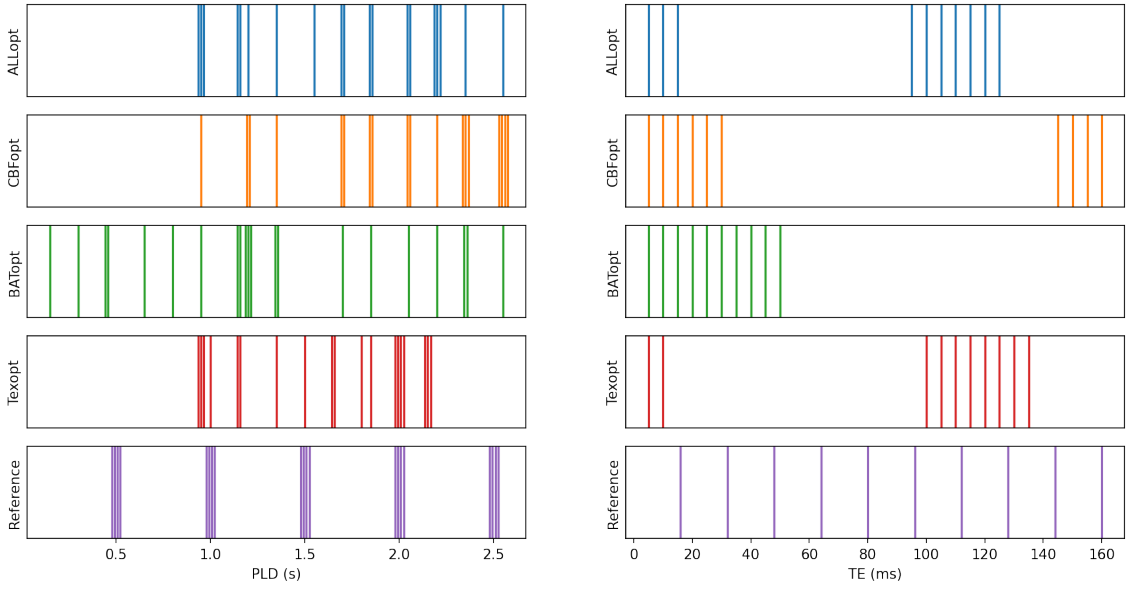


Figure 5.2.4 A schematic of the timings of optimised protocols and reference protocol under the mTE-GRASE scheme with LST mode. Repeated timings were shown as densely distributed lines centred at the corresponding timings.

- mTE-GRASE scheme with UST mode

Optimality	**#PLDs/TEs**	**Optimised Timings**		**#Rep**	**#Acq**	**Scantime(s)**
ALLopt	35	PLDs (s)	0.95, 0.95, 0.95, 0.95, 0.95, 1.15, 1.15, 1.15, 1.15, 1.15, 1.2, 1.2, 1.35,	2	140	541

			1.35, 1.55, 1.7, 1.7, 1.7, 1.85, 1.85, 1.85, 1.85, 1.85, 2.05, 2.05, 2.05, 2.2, 2.2, 2.2, 2.2, 2.2, 2.2, 2.35, 2.35, 2.35, 2.55			
	10	TEs (ms)	5, 10, 15, 95, 100, 105, 110, 115, 120, 125			
CBFopt	35	PLDs (s)	0.95, 1.15, 1.2, 1.35, 1.35, 1.55, 1.7, 1.7, 1.85, 1.85, 1.85, 1.85, 1.85, 2.05, 2.05, 2.2, 2.2, 2.2, 2.2, 2.35, 2.35, 2.35, 2.35, 2.35, 2.35, 2.55, 2.55, 2.55, 2.55, 2.55, 2.55, 2.55, 2.55, 2.55, 2.55, 2.55	2	140	598.8
	10	TEs (ms)	5, 10, 15, 20, 25, 30, 140, 145, 150, 155			
BATopt	35	PLDs (s)	0.15, 0.15, 0.15, 0.3, 0.45, 0.45, 0.45, 0.45, 0.65, 0.8, 0.8, 0.95, 0.95, 1.15, 1.15, 1.15, 1.2, 1.2, 1.2, 1.2, 1.2, 1.35, 1.35, 1.35, 1.7, 1.7, 1.85, 2.05, 2.05, 2.2, 2.2, 2.35, 2.35, 2.55 2.55	2	140	483
	10	TEs (ms)	5, 10, 15, 20, 25, 30, 35, 40, 45, 50			
Texopt	35	PLDs (s)	0.95, 0.95, 0.95, 0.95, 0.95, 1, 1, 1.15, 1.15, 1.15, 1.15, 1.3, 1.35, 1.5, 1.65, 1.65, 1.65, 1.65, 1.8, 1.8, 1.8, 1.8, 1.95, 1.95, 2, 2, 2, 2, 2, 2.15, 2.15, 2.15, 2.15, 2.15, 2.15	2	140	532.4
	10	TEs (ms)	5, 10, 100, 105, 110, 115, 120, 125, 130, 135			

Table 5.2.6 Optimised protocols under the mTE-GRASE scheme with UST mode.

The PLD and TE timings of the output optimised protocols were consistent with where the maximum relative value of the sensitivity functions lies in Figure 5.1.1b. CBFopt and Texopt had generally longer PLDs than BATopt, whose sensitivity functions is at its maximum at the start of the kinetic curve to capture the arrival of the labelled bolus rather than at the peak of the kinetic curve that scales with perfusion.

Texopt had more longer TEs than CBFopt and BATopt, on account of the larger signal difference due to T2 decay at longer TEs to separate the IV and EV compartments.

5.3 Evaluation

5.3.1 Evaluation methods

Simulated ASL images were used to evaluate the root-mean square error (RMSE) of estimating a parameter of interest by the optimised protocols with LST mode. The ASL signals were generated with the two-compartment model from Gregori et al.[16] using ground truth CBF, BAT, and $Texch$ values obtained from three uniform distributions of the parameter ranges listed in Table 5.3.1. Gaussian white noise with fixed SD was then added to the signals. The noise SD was determined by the maximum signal under a typical scenario (CBF = 60ml/100g/min, BAT = 1.4s, $Texch$ = 0.3s) divided by an SNR of 5, a lesser value than in Chapter 3 and 4, considering the typically lower SNR of multi-TE multi-PLD pCASL compared to standard single-PLD pCASL technique.

For both TRUST and mTE-GRASE schemes, the estimation of CBF, BAT, and $Texch$ was performed by the Non-Linear Least Squares (NLLS) fitting function *nlinfit* in MATLAB. For the mTE-GRASE scheme, the estimation of the parameters was additionally obtained by the fabber_asl command line tool (FABBER) with the model configuration of "asl-multite". In both fitting tools, the model to fit the data with was the same two-compartment kinetic model from Gregori et al.[16], but FABBER uses a variational Bayesian method that could incorporate prior information on the parameters to be estimated. The priors used in FABBER are normally distributed with means and standard deviations (SD) listed in Table 5.3.1. All simulations were repeated for 1000 realisations, and the estimated CBF, BAT, and $Texch$ were compared to ground truth values to obtain RMSEs for the parameters under each scheme.

Parameter	Ground Truth Range	Prior mean	Prior SD
CBF (ml/100g/min)	[10, 90]	0	10^6
BAT (s)	[1.0, 2.5]	1.3	0.3
$Texch$ (s)	[0.1, 0.8]	0.3	1.0
T2b (ms)	300	300	0
T2t (ms)	47	47	0

Table 5.3.1 List of parameters ground truths used in evaluation and prior values used in fabber_asl.

5.3.2 Evaluation results

The evaluation results of the optimised protocols under each scheme with LST mode is shown in Figure 5.3.1. Scatter plots of estimated CBF, BAT, and $Texch$ in 1000 simulations against the ground truth values are plotted for the TRUST scheme protocols fitted using NLLS, and the mTE-GRASE scheme protocols fitted using NLLS and FABBER. Generally, each protocol showed good estimation of the ground truth CBF and BAT, indicated by the smaller scale of scattering around the identity lines (cyan lines). The estimation of $Texch$ appeared to be noisier, especially for the TRUST scheme protocols fitted by NLLS. The estimation accuracy by each protocol over the simulated parameter ranges was indicated by the RMSEs shown in the bar plots in Figure 5.3.1. For each fitting model under each optimisation scheme, the protocol that was optimised for a specific parameter always achieved the smallest RMSE for that parameter compared to other optimised protocols and the reference protocol, i.e., CBFopt had the best accuracy for estimating CBF, BATopt for BAT, and Texopt for $Texch$. The ALLopt protocol, which was designed to maintain a balance on the estimation accuracy of all three parameters of interest, had intermediate RMSE among the five protocols. Table 5.3.2 lists the percentage difference in RMSE of estimating the parameters by the optimised

protocols compared to the reference protocols and ALLopt protocols. Texopt had up to 28.0% lower RMSE relative to the reference protocols in the estimation of $Texch$. This demonstrated the effectiveness of the optimal sampling strategy, and that by changing the weights in the optimality criterion, optimised protocols can be generated that result in the maximisation of certain parameter accuracy.

	CBFopt for CBF estimation		BATopt for BAT estimation		Texopt for $Texch$ estimation	
	v. Ref	v. ALLopt	v. Ref	v. ALLopt	v. Ref	v. ALLopt
TRUST-NLLS	48.6%	37.7%	33.7%	33.7%	14.9%	3.9%
mTE-GRASE-NLLS	39.8%	9.87%	27.6%	32.3%	17.2%	17.2%
mTE-GRASE-FABBER	22.2%	20.0%	46.9%	35.0%	28.0%	10.6%

Table 5.3.2 The percentage difference on RMSE of estimating the parameters by optimised protocols compared to the reference protocols and ALLopt protocols using each fitting method.

When fitted by NLLS, the TRUST scheme protocols gave larger RMSEs compared to the mTE-GRASE protocols, which may be because TRUST had fewer numbers of acquisitions than mTE-GRASE for the same optimality criterion, thus less data was used in the fitting. For the same mTE-GRASE protocols, FABBER had larger RMSEs than the NLLS method. This is possibly resulted from the higher systematic bias in FABBER when the ground truth deviated largely from the initial values in the fitting model (for NLLS it is the mean value of the simulated parameter range; for FABBER it is the prior mean). Compared to NLLS, whose standard error was normally distributed and centred at the identity line, the Bayesian method would try to rely on the parameter prior, resulting in a systematic bias with higher ground truth parameter values. This is consistent with the findings in Chapters 3 and 4, where protocols would underestimate CBF and BAT close to the upper boundaries of the optimised ranges.

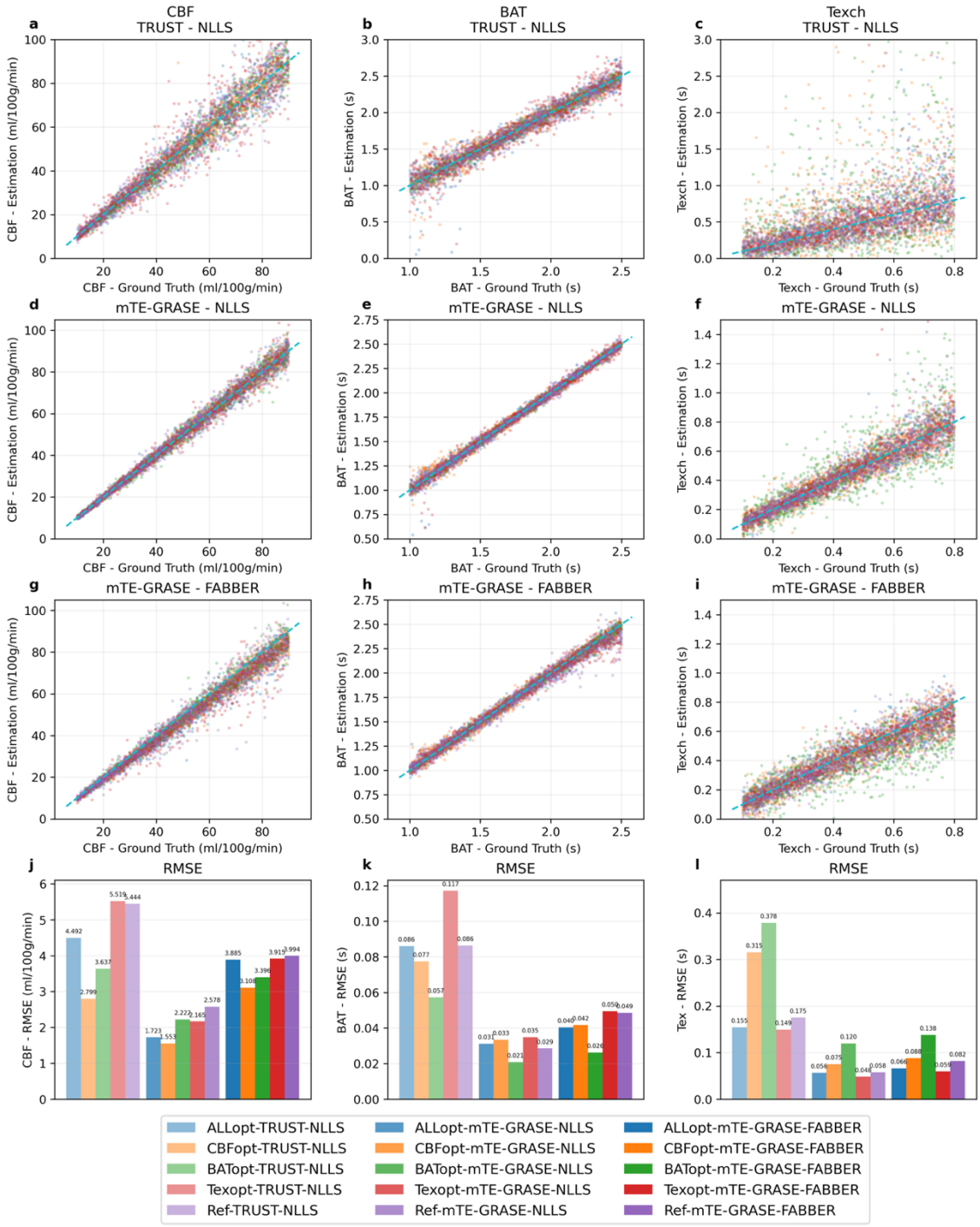


Figure 5.3.1 Evaluation of optimised protocols under each scheme with LST mode. Protocols (optimised and reference) under both TRUST and mTE-GRASE schemes were fitted using NLLS, while those under mTE-GRASE scheme were additionally fitted using the Bayesian inference command line tool, FABBER. The first three rows are scatter plots of CBF (a,d,g), BAT (b,e,h), and Texch (c,f,i) estimation against ground truth values for TRUST-NLLS (a-c), mTE-GRASE-NLLS (d-f), and mTE-GRASE-FABBER (g-i), respectively. The dashed cyan line in each plot indicates identity. The fourth row shows the RMSE of CBF (j), BAT (k) and Texch (l) with each fitting method.

5.4 Discussions

5.4.1 Implications for estimating $Texch$ accurately using OSS

The parameter characterising the exchange time of water molecules from the intravascular to the extravascular compartment, $Texch$, could reflect subtle changes in the blood-brain barrier structural and functional integrity, and thus is a promising biomarker in the early detection of brain pathologies. In this work, we applied the optimal sampling strategy framework in the context of multi-delay multi-echo pCASL and generated protocols with optimised PLDs and TEs, which aimed to improve the quantification accuracy of $Texch$.

As shown in Figure 5.3.1, the optimised protocol Texopt provided the smallest RMSE for estimating $Texch$ across the simulated range among the five examined protocols, under both the TRUST and mTE-GRASE schemes. However, $Texch$ had smaller percentage differences on RMSE compared to CBF and BAT (Table 5.3.2), which is consistent with the low absolute values of the sensitivity functions of $Texch$ (Figure 5.1.1b). If the RMSE of $Texch$ estimation is normalised by the mean of all measured $Texch$, the normalised RMSE (nRMSE) of $Texch$ (10.7%) is an order of magnitude higher than those of CBF (3.1%) and BAT (1.2%) by the method that gave the smallest RMSE, i.e., under mTE-GRASE scheme and fitted with NLLS. Moreover, the weightings chosen for CBFopt, BATopt, and Texopt in Table 5.2.1 represent the upper boundaries we can specify for each parameter, resulting in the minimum RMSE that is theoretically achievable for the corresponding parameters under the simulated conditions. These indicate that $Texch$ was a more challenging parameter to estimate than CBF and BAT, even if the theoretical limit using optimal sampling was reached.

When fitting $Texch$ using NLLS, the estimator is assumed to be unbiased for any given ground truth, therefore the standard error of $Texch$ estimation follows a normal

distribution with zero mean and a standard deviation σ equal to the RMSE of $Texch$. In an approximation, the average RMSE across a range of $Texch$ ground truth could represent the average standard deviation of the standard error across that range. For any change in $Texch$ within that range to be distinguished with a significance level of 0.05, the size of the change, in an individual level, needs to be at least $2 \times 1.96 \times \sigma \approx 3.92 \times RMSE$, the smallest of which is 188.2ms given by the Texopt-mTE-GRASE protocol. In literature such as Shao et al.[26], the measured level of change in k_w using diffusion-weighted ASL was a 28.2% increase in normal vs type-2 diabetes (k_w: 96min^{-1} vs 123min^{-1}, corresponding to $Texch$: 625ms vs 488ms with a difference of 137ms), and a 19.5% increase in normal vs hypercholesterolemia (k_w: 92min^{-1} vs 110min^{-1}, corresponding to $Texch$: 652ms vs 546ms with a difference of 106ms). Therefore, the protocols optimised for 5 minutes under the LST mode could not detect the level of change in $Texch$ that can normally be expected in pathology with 95% confidence in an individual, although it may be possible to achieve the detection in a larger group.

5.4.2 The theoretical RMSE - scan duration curve using the UST mode

The unlimited scan time (UST) mode of the optimisation was used to investigate the trade-off between having lower theoretical RMSE of the parameters of interest and changing one of the experiment conditions, i.e., increasing the available time limit. The optimised protocols obtained with the UST mode has the same number of repeats for each PLD but increasing numbers of PLDs, which leads to longer total scan durations. Figure 5.4.1 shows the RMSE for CBF, BAT and $Texch$ as a function of the total scan duration by different protocols under the three fitting methods, using the same evaluation methods as in Section 5.3.1. The RMSE of all three parameters decreased with

increasing scan times for each optimality criterion, since more simulated images were fed into model fitting.

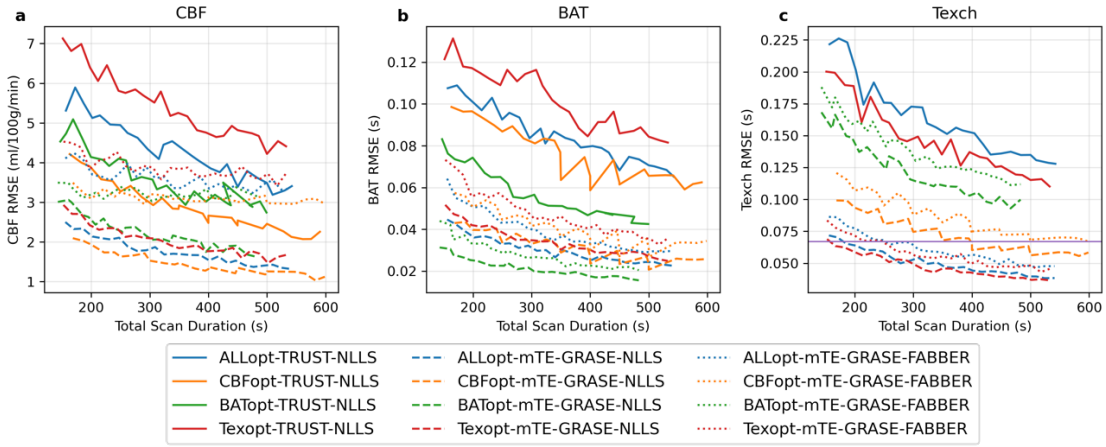


Figure 5.4.1 RMSE of (a) CBF, (b) BAT, and (c) Texch under three fitting methods as a function of the total scan duration of the optimised protocols generated with UST mode. CBFopt-TRUST-NLLS and BATopt-TRUST-NLLS were not shown in (c) due to very high Texch RMSE.

Comparing different optimalities on the estimation of the same parameter, the protocol that was optimised for that parameter could maintain the same level of estimation accuracy with less scan duration. For example, shown in Figure 5.4.1c as the solid horizontal purple line, Texopt-mTE-GRASE could achieve the same level of $Texch$ RMSE by images acquired in 250 seconds as CBFopt-mTE-GRASE in 600 seconds, needing less than half of the scan time. Meanwhile, BATopt-mTE-GRASE could not reach such low RMSE on estimating $Texch$ without further increasing the scan time. Hence, if one intends to reach a pre-defined level of accuracy on a certain parameter, Figure 5.4.1 is useful in determining the minimum scan time necessary with an optimised protocol, if at all the level of accuracy is achievable. For $Texch$ estimation in this study, achieving the accuracy with a normalised RMSE of less than 5% was not possible even if we extended the scan duration to 10 minutes.

5.4.3 Parameter choices in optimisation and simulation evaluation

During optimisation, we used a discrete form of the pseudo-Bayesian optimality criterion in Equation 5.2.2 to approximate the integration over the parameter ranges. In theory, the higher the number of sampling points $|\boldsymbol{\Theta}|$ in the prior ranges, the more accurately the output protocol would represent the true 'optimal' protocol within these ranges. However, increasing $|\boldsymbol{\Theta}|$ comes at a cost of prolonging the computational time exponentially. To find the feasible value of $|\boldsymbol{\Theta}|$, we ran the optimisation for ALLopt under mTE-GRASE scheme with 20 and 33 PLDs and 10 TEs with different $|\boldsymbol{\Theta}|$. Subsequently, two types of summed squared differences (SSD) were calculated for each $|\boldsymbol{\Theta}|_i$: SSD_1 was the summed squared element-wise difference of the output PLDs/TEs between $|\boldsymbol{\Theta}|_{i-1}$ and $|\boldsymbol{\Theta}|_i$; SSD_2 was the summed squared element-wise difference of the output PLDs/TEs between $|\boldsymbol{\Theta}|_i$ and $|\boldsymbol{\Theta}|$=20, the maximum $|\boldsymbol{\Theta}|$. SSD_1 are SSD_2 are both metrics that describe the degree of change in protocol timings when $|\boldsymbol{\Theta}|$ changes. Since SSD_1 and SSD_2 are convergent to zero when $|\boldsymbol{\Theta}|$ approaches infinity, lower values indicate a good approximation of the global optimal protocol. Figure 5.4.2 shows the different output PLDs and TEs of ALLopt with different $|\boldsymbol{\Theta}|_i$ (Figure 5.4.2a-d), SSD_1 (Figure 5.4.2e-h), as well as SSD_2 (Figure 5.4.2i-l). Both SSD_1 and SSD_2 showed a decreasing trend when $|\boldsymbol{\Theta}|$ was less than 10, and stayed close to zero as $|\boldsymbol{\Theta}|$ further increased. Finally, we chose $|\boldsymbol{\Theta}|$=10 for a reasonable trade-off between the accuracy of the output protocol and computational time.

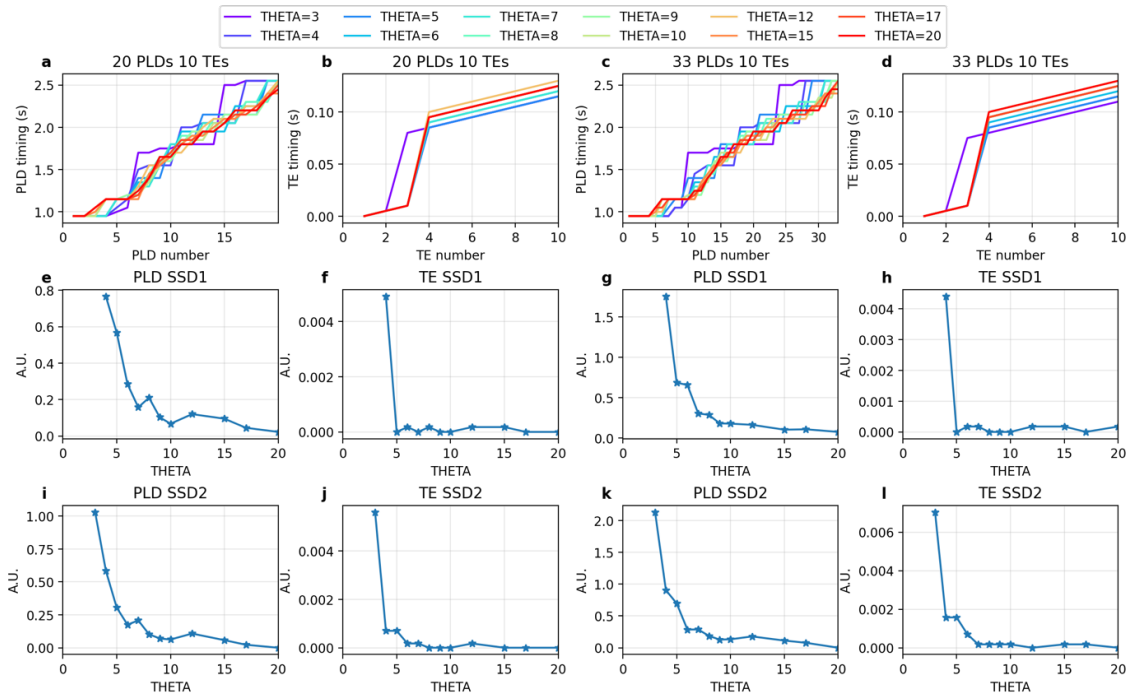


Figure 5.4.2: Different output timings of ALLopt under mTE-GRASE scheme optimised with different $|\boldsymbol{\Theta}|_i$*. (a,b): PLD and TE timings (s) optimised with 20 PLDs and 10 TEs; (c,d): PLD and TE timings (s) optimised with 33 PLDs and 10 TEs. (e-h): summed squared difference (SSD₁) of output PLDs/TEs from the previous* $|\boldsymbol{\Theta}|_{i-1}$*. (i-l): summed squared difference (SSD₂) of output PLDs/TEs from* $|\boldsymbol{\Theta}|$*=20.*

In the evaluation, the theoretical minimum RMSEs of estimating the parameters of interest were determined under an SNR of 5, which made the theoretical RMSEs dependent on the choices of SNRs. We further simulated images with different levels of SNR from 0.5 to 20 for the optimised protocols under the mTE-GRASE scheme fitted with NLLS, and the RMSEs of parameters were plotted against SNR shown in Figure 5.4.3. We observed that the optimised protocols still had the lowest RMSE for their respective parameters under each SNR, but RMSEs increased exponentially with reduced SNR, as one would expect. In this case an intermediate SNR of 5 was chosen, which is less than in the previous work, as a representative SNR for multi-TE pCASL and demonstrating the effectiveness of OSS. However, more accurate RMSEs would be obtained if the SNR is known *a priori*.

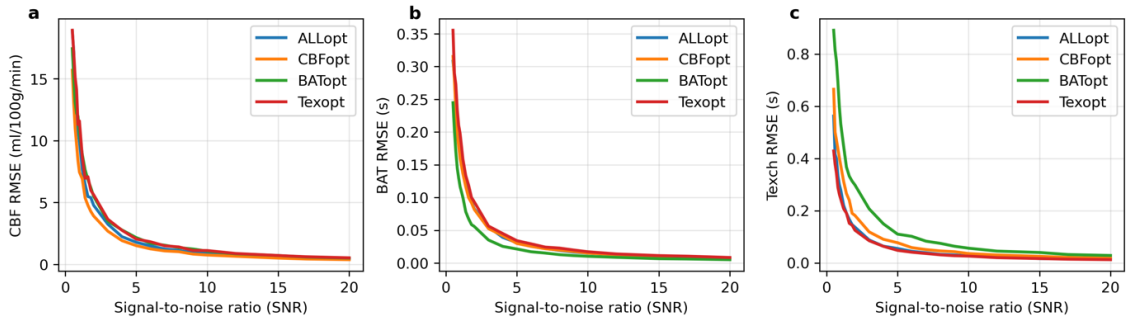


Figure 5.4.3 RMSEs of (a) CBF, (b) BAT, and (c) Texch by optimised protocols under the mTE-GRASE scheme fitted with NLLS with different levels of SNR.

5.4.4 Limitations and future work

There are a few limitations to acknowledge in this work. Firstly, the evaluation of estimation RMSEs was solely based on simulated ASL images. Because of the ongoing COVID-19 pandemic, we were unable to acquire *in vivo* data using the optimised protocols, hence only theoretical minimum RMSEs were derived. The current optimisation framework and evaluation is dependent on the two-compartment kinetic model by Gregori et al.[16], which assumes the equal inflow of the IV and EV compartments, negligible venous outflow, as well as the instantaneous start of exchange from the IV to the EV compartment[4]. However, several models exist to contrast these assumptions[27–30]. Therefore, acquiring *in vivo* data using optimised protocols generated from *different* kinetic models would potentially help evaluate the appropriateness of each model, given that the lowest RMSE would be resulted from both a closest-to-reality kinetic model and the optimal sampling schedule bounded by such model.

Secondly, the T2 values for the IV and EV compartments were fixed as ground truths in the model fitting, and $Texch$ was estimated directly from the entire dataset without extra steps carried out before the fitting. An expansion of the parameters of interest vector from $\{CBF, BAT, Texch\}$ to $\{CBF, BAT, Texch, T2_b, T2_t\}$ was considered in the optimisation and estimation, which only led to an increase of the $Texch$ RMSE

under the same condition. In contrast, a multi-step processing pipeline has been adopted in literature, where $T2_{EV}$ was estimated from control-data[12] to constrain the fitting for Equation 5.1, and multi-delay ASL data with the shortest TE was used to generate voxel-wise perfusion[15] or BAT[13] maps used as prior knowledge in $Texch$ estimation. A useful work in the future would be to investigate the possibility of combining all data from CBFopt, BATopt and Texopt to estimate for $Texch$. CBFopt and BATopt could be optimised for a short scan time to maintain the acceptable total scan duration, while still providing reliable CBF and BAT estimates, which are subsequently used as the priors in Texopt data for $Texch$ estimation.

Currently, the framework is process-oriented, meaning that the user needs to allocate the weightings of the parameters of interest, specify the number of PLDs and TEs for the optimiser to iterate over, generate the optimised protocols under certain experiment conditions, and finally, check the theoretical RMSE lower bound of estimating the parameters using simulation. However, in practice it may be less of interest to adjust the weights and configure the optimisation process itself but more to focus on obtaining a single protocol that provides a desired level of precision on certain parameters. For this reason, the prospect of the optimisation framework is a dictionary that stores the theoretical RMSEs for all possible combinations of weightings, PLD and TE numbers and timings, as wells as the scan duration for each protocol. When the scan time limit and the RMSE requirements on certain parameters are specified, the dictionary would return the protocol within the scan time limit that satisfies the required RMSE level or, if not theoretically possible, one that reaches the lowest achievable RMSE on these parameters of interest. It would greatly simplify the usage of the OSS in research and clinical settings, benefiting the quantification of physiological parameters with limited scan time.

5.5 Conclusion

This chapter used an optimal sampling framework to optimise for both delay times and echo times in multi-TE multi-PLD pCASL, aiming to improve the estimation accuracy of $Texch$, which reflects the exchange time of water molecules across the blood-brain barrier. Optimised protocols were developed under both TRUST and mTE-GRASE schemes, while having different weightings on CBF, BAT, and $Texch$. When choosing the highest weighting for $Texch$, the resulting protocol Texopt reduced $Texch$ estimation RMSE by up to 28% compared with a conventional evenly sampled PLD/TE protocol, under the mTE-GRASE scheme evaluated by the FABBER fitting tool. However, the accuracy in $Texch$ estimation achieved by protocols optimised within five minutes of scanning could not lead to reliable detection of individual pathological change in $Texch$ observed in literature with 95% confidence.

5.6 References

1. Kassner A, Merali Z. Assessment of Blood–Brain Barrier Disruption in Stroke. *Stroke*. 2015;46(11):3310-3315.
2. Minagar A, Alexander JS. Blood-brain barrier disruption in multiple sclerosis. *Multiple Sclerosis*. 2003;9(6):540-549.
3. Desai BS, Monahan AJ, Carvey PM, Hendey B. Blood-Brain Barrier Pathology in Alzheimer's and Parkinson's Disease: Implications for Drug Therapy. *Cell Transplant*. 2007;16:285-299.
4. Dickie BR, Parker GJM, Parkes LM. Measuring water exchange across the blood-brain barrier using MRI. *Prog Nucl Magn Reson Spectrosc*. 2020;116:19-39.
5. Kelly ME, Blau CW, Kerskens CM. Bolus-tracking arterial spin labelling: Theoretical and experimental results. *Phys Med Biol*. Published online 2009.
6. Wang R, Yu S, Alger JR, et al. Multi-delay arterial spin labeling perfusion MRI in moyamoya disease-comparison with CT perfusion imaging. *Eur Radiol*. Published online 2014.
7. Paling D, Thade Petersen E, Tozer DJ, et al. Cerebral Arterial Bolus Arrival Time is Prolonged in Multiple Sclerosis and Associated with Disability. *Journal of Cerebral Blood Flow & Metabolism*. 2014;34(1):34-42.
8. Kim HG, Lee JH, Choi JW, Han M, Gho SM, Moon Y. Multidelay arterial spin-labeling MRI in neonates and infants: Cerebral perfusion changes during brain maturation. *American Journal of Neuroradiology*. 2018;39(10):1912-1918.
9. Amemiya S, Watanabe Y, Takei N, et al. Arterial Transit Time-Based Multidelay Combination Strategy Improves Arterial Spin Labeling Cerebral Blood Flow Measurement Accuracy in Severe Steno-Occlusive Diseases. *Journal of Magnetic Resonance Imaging*. 2022;55(1):178-187.
10. Wells JA, Lythgoe MF, Choy M, Gadian DG, Ordidge RJ, Thomas DL. Characterizing the origin of the arterial spin labelling signal in MRI using a multiecho acquisition approach. *Journal of Cerebral Blood Flow and Metabolism*. 2009;29(11):1836-1845.
11. Liu P, Uh J, Lu H. Determination of spin compartment in arterial spin labeling MRI. *Magn Reson Med*. 2011;65(1):120-127.
12. Wells JA, Siow B, Lythgoe MF, Thomas DL. Measuring Biexponential Transverse Relaxation of the ASL Signal at 9.4 T to Estimate Arterial Oxygen Saturation and the Time of Exchange of Labeled Blood Water into Cortical Brain Tissue. *Journal of Cerebral Blood Flow & Metabolism*. 2013;33(2):215-224.
13. Ohene Y, Harrison IF, Nahavandi P, et al. Non-invasive MRI of brain clearance pathways using multiple echo time arterial spin labelling: an aquaporin-4 study. *Neuroimage*. 2019;188:515-523.
14. Ohene Y, Harrison IF, Evans PG, Thomas DL, Lythgoe MF, Wells JA. Increased blood–brain barrier permeability to water in the aging brain detected using noninvasive multi-TE ASL MRI. *Magn Reson Med*. 2021;85(1):326-333.
15. Petitclerc L, Schmid S, Hirschler L, van Osch MJP. Combining T2 measurements and crusher gradients into a single ASL sequence for comparison of the measurement of water transport across the blood–brain barrier. *Magn Reson Med*. 2021;85(5):2649-2660.

16. Gregori J, Schuff N, Kern R, Günther M. T2-based arterial spin labeling measurements of blood to tissue water transfer in human brain. *Journal of Magnetic Resonance Imaging*. 2013;37(2):332-342.
17. Thulborn KR, Waterton JC, Matthews PM, Radda GK. Oxygenation dependence of the transverse relaxation time of water protons in whole blood at high field. *Biochimica et Biophysica Acta (BBA) - General Subjects*. 1982;714(2):265-270.
18. Liu P, Chalak LF, Krishnamurthy LC, et al. T1 and T2 values of human neonatal blood at 3 Tesla: Dependence on hematocrit, oxygenation, and temperature. *Magn Reson Med*. 2016;75(4):1730-1735.
19. Xie J, Gallichan D, Gunn RN, Jezzard P. Optimal design of pulsed arterial spin labeling MRI experiments. *Magn Reson Med*. 2008;59(4):826-834.
20. Woods JG, Chappell MA, Okell TW. A general framework for optimizing arterial spin labeling MRI experiments. *Magn Reson Med*. 2019;81(4):2474-2488.
21. Woods JG, Chappell MA, Okell TW. Designing and comparing optimized pseudo-continuous Arterial Spin Labeling protocols for measurement of cerebral blood flow. *Neuroimage*. 2020;223(August):117246.
22. Lahiri A, Fessler JA, Hernandez-Garcia L. Optimizing MRF-ASL scan design for precise quantification of brain hemodynamics using neural network regression. *Magn Reson Med*. 2020;83(6):1979-1991.
23. Lu H, Ge Y. Quantitative evaluation of oxygenation in venous vessels using T2-relaxation-under-spin-tagging MRI. *Magn Reson Med*. 2008;60(2):357-363.
24. Günther M, Oshio K, Feinberg DA. Single-shot 3D imaging techniques improve arterial spin labeling perfusion measurements. *Magn Reson Med*. 2005;54(2):491-498.
25. Schmid S, Teeuwisse WM, Lu H, Osch MJP van. Time-efficient determination of spin compartments by time-encoded pCASL T2-relaxation-under-spin-tagging and its application in hemodynamic characterization of the cerebral border zones. *Neuroimage*. 2015;123:72-79.
26. Shao X, Ma SJ, Casey M, D'Orazio M, Ringman JM, Wang DJJ. Mapping water exchange across the blood–brain barrier using 3D diffusion-prepared arterial spin labeled perfusion MRI. *Magn Reson Med*. 2019; 81: 3065– 3079.
27. Parkes LM. Quantification of cerebral perfusion using arterial spin labeling: Two-compartment models. *Journal of Magnetic Resonance Imaging*. 2005;22(6):732-736.
28. st. Lawrence KS, Owen D, Wang DJJ. A two-stage approach for measuring vascular water exchange and arterial transit time by diffusion-weighted perfusion MRI. *Magn Reson Med*. 2012;67(5):1275-1284.
29. Li K loh, Zhu X, Hylton N, Jahng GH, Weiner MW, Schuff N. Four-phase single-capillary stepwise model for kinetics in arterial spin labeling MRI. *Magn Reson Med*. 2005;53(3):511-518.
30. Mahroo A, Buck MA, Huber J, et al. Robust Multi-TE ASL-Based Blood–Brain Barrier Integrity Measurements. *Front Neurosci*. 2021;15.

6 Summary of Findings and Future Prospects

6.1 Summary of Findings

This thesis set out to improve the quantification of the parameters related to cerebral haemodynamics beyond perfusion, using existing and novel multi-PLD pCASL protocols obtained using optimal sampling strategy (OSS). The approach adopted in this thesis to investigate the existing optimised protocols helped to gain a better understanding of their parameter estimation performance and sensitivity to the factors that may be present *in vivo*, and whether accounting for such factors in the model fitting would help reduce the estimation errors. Novel optimised protocols were developed in an extension of the current optimisation framework to incorporate optimised sampling of both PLD and TE. Theoretical implications were drawn on the estimation accuracy of $Texch$ using the lower bound of RMSE obtained through simulation. The findings in this thesis contribute to the wider application of OSS in ASL, while acknowledging its potential pitfalls and limitations.

Chapter 3 aimed to examine the parameter estimation performance by previously optimised protocols to various physiological effects that were not accounted for in the general kinetic model[1,2]. Simulation experiments were conducted to obtain CBF and ATT estimation errors and sensitivity metrics to macrovascular contamination (MVC) for each protocol with different fitting models. The results showed that the presence of flow dispersion, MVC, and prolonged ATT outside of the optimisation ranges led to high parameter estimation errors by all four protocols examined. Among them, CBFopt, a protocol with longer PLD schedules optimised for CBF estimation only, had the lowest CBF estimation sensitivity to MVC, and the lowest CBF estimation error in cases of dispersed bolus profile and long ATT, while maintaining reasonable ATT estimation

accuracy. When the data was fitted with extended kinetic models that accounted for the effects of dispersion and MVC[3,4], the estimation errors of the parameters were largely reduced. Validation using a retrospectively analysed *in vivo* dataset confirmed the evidence found in simulation.

Chapter 4 sought to investigate a group of existing time-encoded CBF-optimised protocols for their sensitivity to MVC and the need to include a macrovascular compartment in the kinetic modelling[5]. The study took a more systematic approach in considering the possible relationships between tissue transit times and macrovascular transit times, and used simulation to generate CBF, ATT and aBV sensitivity maps to MVC over a complete set of combinations of both transit times. Overall, the results strengthened the claim that adding a macrovascular component in the kinetic model could control for MVC effects, regardless of whether we have knowledge about such effect would be present. Furthermore, the sensitivity maps may be of assistance to examining a protocol prior to scanning for potential sources of error incurred by MVC, or interpreting the results after data analysis.

In Chapter 5, the optimisation framework was extended to allow for combined optimisation of PLDs and TEs in multi-PLD multi-TE pCASL, in order to improve the measurement of the water exchange time across the BBB, $Texch$. Optimised protocols with different weightings on the parameters of interest were obtained under two multi-TE schemes, TRUST and mTE-GRASE. The theoretical lower bound of RMSE on $Texch$ estimation was achieved by the Texopt protocol under mTE-GRASE scheme estimated in a nonlinear-least-squares fashion. In addition, the protocols generated with unlimited scan time (UST) mode demonstrated that OSS could maintain the estimation accuracy of $Texch$ while reducing the required scan duration. However, within a five-minute scan, the level of accuracy of $Texch$ estimation by optimal protocols was not

sufficient to reliably detect the expected level of $Texch$ change appeared in pathology in an individual with 95% confidence. Therefore, other factors that contribute to the estimation of $Texch$, such as improving the SNR of the acquisition or having more effective de-noising methods, should be considered alongside sampling-time optimisation.

6.2 Future Prospects

6.2.1 *In vivo* validation of the results

A major future direction of this thesis is to obtain *in vivo* data to substantiate our conclusions. While in Chapter 3 a previously acquired dataset was used for the validation of the findings seen in simulation, the acquisition parameters of the dataset were not designed for such purpose. Specifically, the signal in the macrovasculature was greatly reduced by the application of flow crusher gradients, albeit still detectable in a small number of voxels, presumably due to the remaining signal perpendicular to the direction of the gradients[3]. Also, a group of young healthy volunteers were selected for imaging, limiting the number of voxels that has prolonged ATT values, which are often observed in elderly cohorts or in cerebrovascular diseases[6–8].

The availability of *in vivo* data acquired using optimised protocols would not only help to validate the reported benefits of OSS over conventional timing schedules, but also allow new questions to be answered. For instance, as Section 2.4.2 reviewed, several kinetic models exist that describes the compartmental water exchange across the BBB with different assumptions[9–12]. The optimisation process achieved by Equations 5.2.1 and 5.2.2 also depends on the mathematical expression of ΔM related to $Texch$. Hence, using various modelling of $Texch$ to obtain different optimised protocols, even

though the optimality of prioritising $Texch$ estimation does not change, would give rise to different estimation RMSEs on the *in vivo* data. In theory, the protocol optimised by the kinetic model that bears the closest resemblance to the real exchange process would best sample the haemodynamic response function, thus leading to the lowest RMSE on $Texch$ estimation. This might be a means to probe the underlying mechanism of water exchange by reducing the systematic error of sampling bias, although long scan durations may be needed to achieve sufficient SNR.

6.2.2 Change of simulation conditions

The simulation parameters and prior distributions used in Chapter 3 and Chapter 5 were chosen based on the kinetic model expressions that we assumed to reflect the underlying haemodynamics of the brain, with common values we found in literature[3,4,9]. However, other combinations of the parameters may be possible, with the development of our understanding of the cerebral haemodynamic model formulations, or when applying the simulation to non-neuro ASL imaging.

A recent study introduced an 'intravoxel transit time' (ITT) in an extended two-compartment model to account for the instantaneous start of water exchange when the labelled bolus arrives at the voxel[13]. It releases the model assumption used in Chapter 5, opening up directions for new parameters to be included in the optimisation and simulation. Another aspect that can be changed in the simulation condition is the modelling of noise, for which the thesis assumed to be Gaussian white noise. While it may be justifiable that physiological noise could be more prominent in ASL images, which tends to be Gaussian-distributed, MR noise is more recognised to follow a Rician distribution[14], and the true noise may be a concoction of both. Further modelling of the

noise incorporated into the simulation could provide deeper insight into the arise of noise in ASL images, thus contributing to denoising methods in post-processing[15–18].

Besides the application of ASL in measuring cerebral perfusion, it has been used in other non-neuro organs such as the kidney[19,20]. Compared to ASL in the brain, ASL in the kidneys is more heavily affected by susceptibility and motion artefacts as well as cardiac pulsation, making the optimisation of the acquisition sequence desirable. Future work could inquire into the possibility of developing and testing optimised protocols specifically designed for renal ASL, with corresponding parameter ranges and other conditions such as cardiac triggering[21–23].

6.2.3 Incorporating other parameters in the optimal sampling framework

The ability for the current optimal sampling framework to develop different optimalities makes it particularly suitable for multi-parametric estimation. Apart from the inclusion of ATT and $Texch$ as objectives for estimation in this study, further research could seek to include more parameters of interest, such as T1 and T2, especially when it is not suitable to assume a single literature value on patient groups or conducting ROI analysis. Even if these parameters are not sought to be estimated, the optimality criterion could be incorporated with their prior probability distributions, so that the optimised protocol could account for the variability for each parameter.

In Chapter 3, the relative insensitivity to MVC of protocol CBFopt was regarded as beneficial for estimating CBF when there might be unexpected macrovascular signal present. However, protocols with higher sensitivity to MVC could be useful in estimating the macrovascular contribution, as CBF-ATTopt demonstrated in Figure 3.4.1. Additionally, the optimisation could also incorporate the macrovascular compartment and generate protocols that are optimised for estimating aBV and

macrovascular transit time, which could provide information about vascular function or used to correct for CBF estimates.

6.2.4 Developing the programme for target-based protocol selection

As mentioned in Section 5.4.4, the methods developed in this thesis, whether to examine an existing protocol's sensitivity or find the theoretical estimation limit of a parameter, were orientated by the optimisation process. In other words, one could not start to evaluate the estimation accuracy and sensitivity associated with an optimised protocol, until it is generated by the optimisation process in a pre-defined condition.

However, in a more practical sense, one often requires a level of estimation accuracy on and insensitivity (or sensitivity, depending on if estimation of the parameter is preferred) to certain parameters before the optimisation could commence. Hence, it would be interesting to develop a target-based programme that could optimise for that request, and then select a protocol and the associated theoretical estimation accuracy that fulfils the desired condition if it is attainable, or one that is the closest to the requirements if not. In this case, it is a problem of 'optimising' the optimality criterion, i.e., optimising for the weighting matrix or the number of sampling points in the protocol, etc.

Considering this optimisation would require a rather obscure cost function, a feasible first step might be to build a dictionary that contains a large number of protocols optimised from a near-exhaustive pool of different optimalities by changing the parameter weightings or the number of sampled PLDs (and potentially other parameters). These protocols would have already been evaluated of their theoretical estimation performance through simulation, with the results also stored in the dictionary, which is a process that could be speeded up by the usage of computer clusters or GPU. As a result,

the dictionary will automatically look up and output the appropriate protocol. This programme can simplify the application of optimal sampling strategy, and the computation time of obtaining the optimised protocol as well as its corresponding characteristics, since they have been pre-evaluated, will be greatly reduced.

6.3 References

1. Buxton RB, Frank LR, Wong EC, Siewert B, Warach S, Edelman RR. A general kinetic model for quantitative perfusion imaging with arterial spin labeling. *Magn Reson Med*. 1998;40(3):383-396.
2. Woods JG, Chappell MA, Okell TW. A general framework for optimizing arterial spin labeling MRI experiments. *Magn Reson Med*. 2019;81(4):2474-2488.
3. Chappell MA, MacIntosh BJ, Donahue MJ, Günther M, Jezzard P, Woolrich MW. Separation of macrovascular signal in multi-inversion time arterial spin labelling MRI. *Magn Reson Med*. 2010;63(5):1357-1365.
4. Chappell MA, Woolrich MW, Kazan S, Jezzard P, Payne SJ, MacIntosh BJ. Modeling dispersion in arterial spin labeling: Validation using dynamic angiographic measurements. *Magn Reson Med*. 2013;69(2):563-570.
5. Woods JG, Chappell MA, Okell TW. Designing and comparing optimized pseudo-continuous Arterial Spin Labeling protocols for measurement of cerebral blood flow. *Neuroimage*. 2020;223(August):117246.
6. Paling D, Thade Petersen E, Tozer DJ, et al. Cerebral Arterial Bolus Arrival Time is Prolonged in Multiple Sclerosis and Associated with Disability. *Journal of Cerebral Blood Flow & Metabolism*. 2014;34(1):34-42.
7. Dai W, Fong T, Jones RN, et al. Effects of arterial transit delay on cerebral blood flow quantification using arterial spin labeling in an elderly cohort. *Journal of Magnetic Resonance Imaging*. 2017;45(2):472-481.
8. Fujiwara Y, Matsuda T, Kanamoto M, et al. Comparison of long-labeled pseudo-continuous arterial spin labeling (ASL) features between young and elderly adults: Special reference to parameter selection. *Acta radiol*. 2017;58(1):84-90.
9. Gregori J, Schuff N, Kern R, Günther M. T2-based arterial spin labeling measurements of blood to tissue water transfer in human brain. *Journal of Magnetic Resonance Imaging*. 2013;37(2):332-342.
10. Li K loh, Zhu X, Hylton N, Jahng GH, Weiner MW, Schuff N. Four-phase single-capillary stepwise model for kinetics in arterial spin labeling MRI. *Magn Reson Med*. 2005;53(3):511-518.
11. Parkes LM. Quantification of cerebral perfusion using arterial spin labeling: Two-compartment models. *Journal of Magnetic Resonance Imaging*. 2005;22(6):732-736.
12. St. Lawrence KS, Owen D, Wang DJJ. A two-stage approach for measuring vascular water exchange and arterial transit time by diffusion-weighted perfusion MRI. *Magn Reson Med*. 2012;67(5):1275-1284.
13. Mahroo A, Buck MA, Huber J, et al. Robust Multi-TE ASL-Based Blood–Brain Barrier Integrity Measurements. *Front Neurosci*. 2021;15.
14. Gudbjartsson H, Patz S. The rician distribution of noisy mri data. *Magn Reson Med*. 1995;34(6):910-914.
15. Restom K, Behzadi Y, Liu TT. Physiological noise reduction for arterial spin labeling functional MRI. *Neuroimage*. 2006;31(3):1104-1115.

16. Bibic A, Knutsson L, Ståhlberg F, Wirestam R. Denoising of arterial spin labeling data: Wavelet-domain filtering compared with gaussian smoothing. *Magnetic Resonance Materials in Physics, Biology and Medicine*. 2010;23(3):125-137.
17. Xie D, Li Y, Yang H, et al. Denoising arterial spin labeling perfusion MRI with deep machine learning. *Magn Reson Imaging*. 2020;68:95-105.
18. Carone D, Harston GWJ, Garrard J, et al. ICA-based denoising for ASL perfusion imaging. *Neuroimage*. 2019;200:363-372.
19. Odudu A, Nery F, Harteveld AA, et al. Arterial spin labelling MRI to measure renal perfusion: a systematic review and statement paper. *Nephrology Dialysis Transplantation*. 2018;33(suppl_2):ii15-ii21.
20. Nery F, Buchanan CE, Harteveld AA, et al. Consensus-based technical recommendations for clinical translation of renal ASL MRI. *Magnetic Resonance Materials in Physics, Biology and Medicine*. 2020;33(1):141-161.
21. Cutajar M, Thomas DL, Banks T, Clark CA, Golay X, Gordon I. Repeatability of renal arterial spin labelling MRI in healthy subjects. *Magnetic Resonance Materials in Physics, Biology and Medicine*. 2012;25(2):145-153.
22. Cox EF, Buchanan CE, Bradley CR, et al. Multiparametric Renal Magnetic Resonance Imaging: Validation, Interventions, and Alterations in Chronic Kidney Disease. *Front Physiol*. 2017;8(SEP).
23. Nery F, de Vita E, Clark CA, Gordon I, Thomas DL. Robust kidney perfusion mapping in pediatric chronic kidney disease using single-shot 3D-GRASE ASL with optimized retrospective motion correction. *Magn Reson Med*. 2019;81(5):2972-2984.

Appendix A Parameter estimation errors and sensitivity maps to MVC of protocols

A.1 CBF and ATT estimation errors under the assumption ‘percentage’

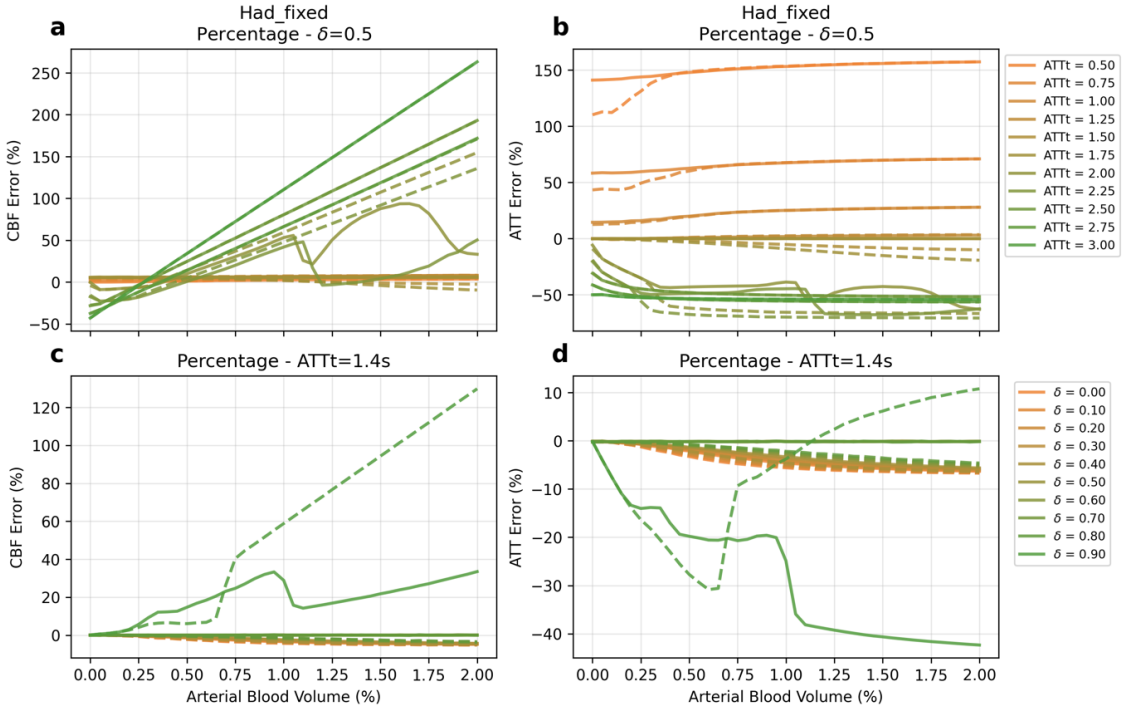


Figure A.1.1 CBF and ATT estimation errors of Had_fixed using gkm (dashed lines) and gkm+mvc (solid lines) under the percentage assumption. (a) and (b): δ = 0.5 while varying ATT_t; (c) and (d): ATT_t = 1.4s while varying δ.

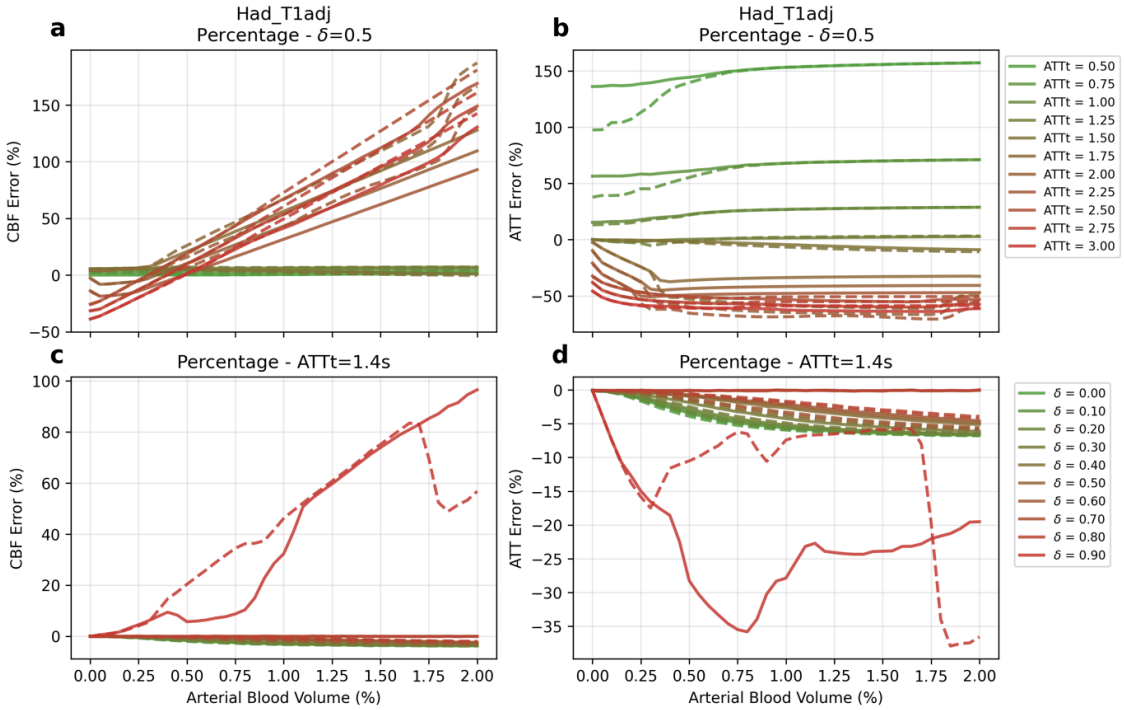


Figure A.1.2 CBF and ATT estimation errors of Had_T1adj using gkm (dashed lines) and gkm+mvc (solid lines) under the percentage assumption. (a) and (b): δ = 0.5 while varying ATT_t; (c) and (d): ATT_t = 1.4s while varying δ.

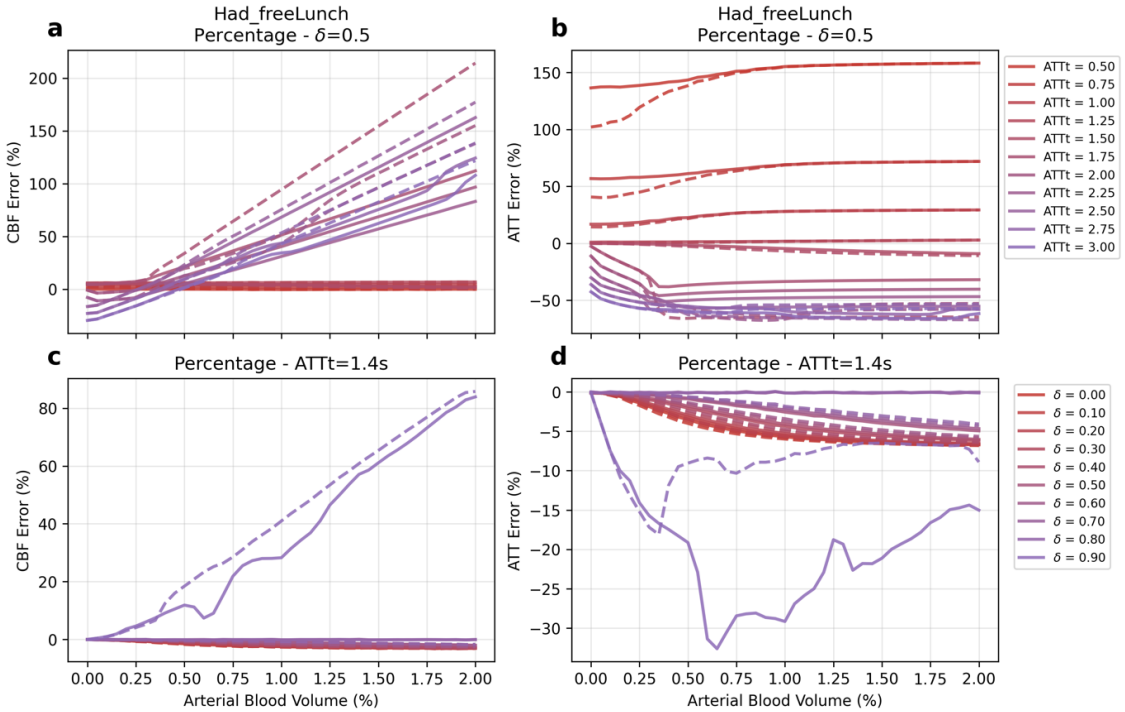


Figure A.1.3 CBF and ATT estimation errors of Had_freeLunch using gkm (dashed lines) and gkm+mvc (solid lines) under the percentage assumption. (a) and (b): δ = 0.5 while varying ATT_t; (c) and (d): ATT_t = 1.4s while varying δ.

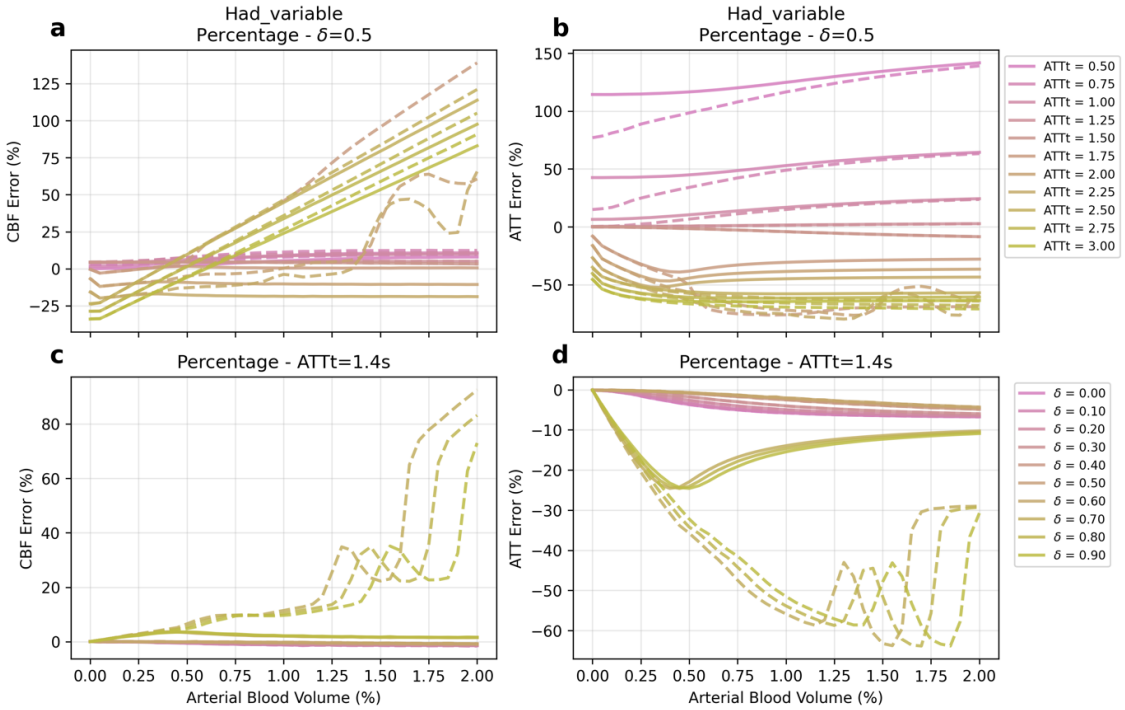


Figure A.1.4 CBF and ATT estimation errors of Had_variable using gkm (dashed lines) and gkm+mvc (solid lines) under the percentage assumption. (a) and (b): δ = 0.5 while varying ATT_t; (c) and (d): ATT_t = 1.4s while varying δ.

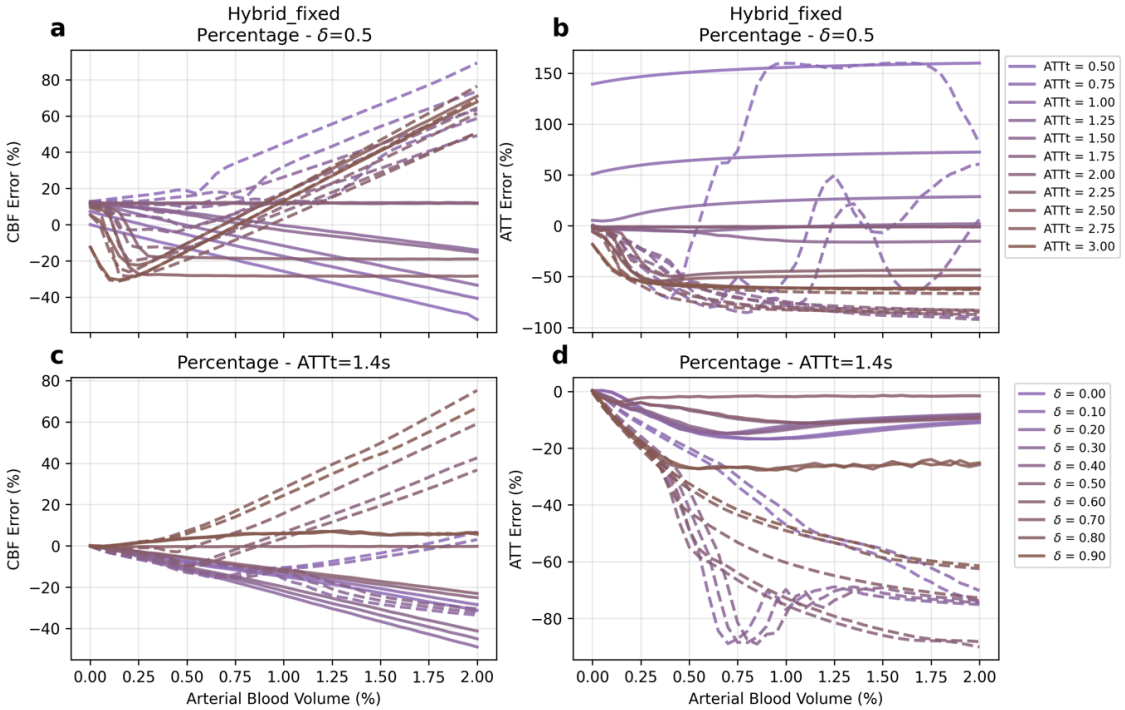


Figure A.1.5 CBF and ATT estimation errors of Hybrid_fixed using gkm (dashed lines) and gkm+mvc (solid lines) under the percentage assumption. (a) and (b): δ = 0.5 while varying ATT_t; (c) and (d): ATT_t = 1.4s while varying δ.

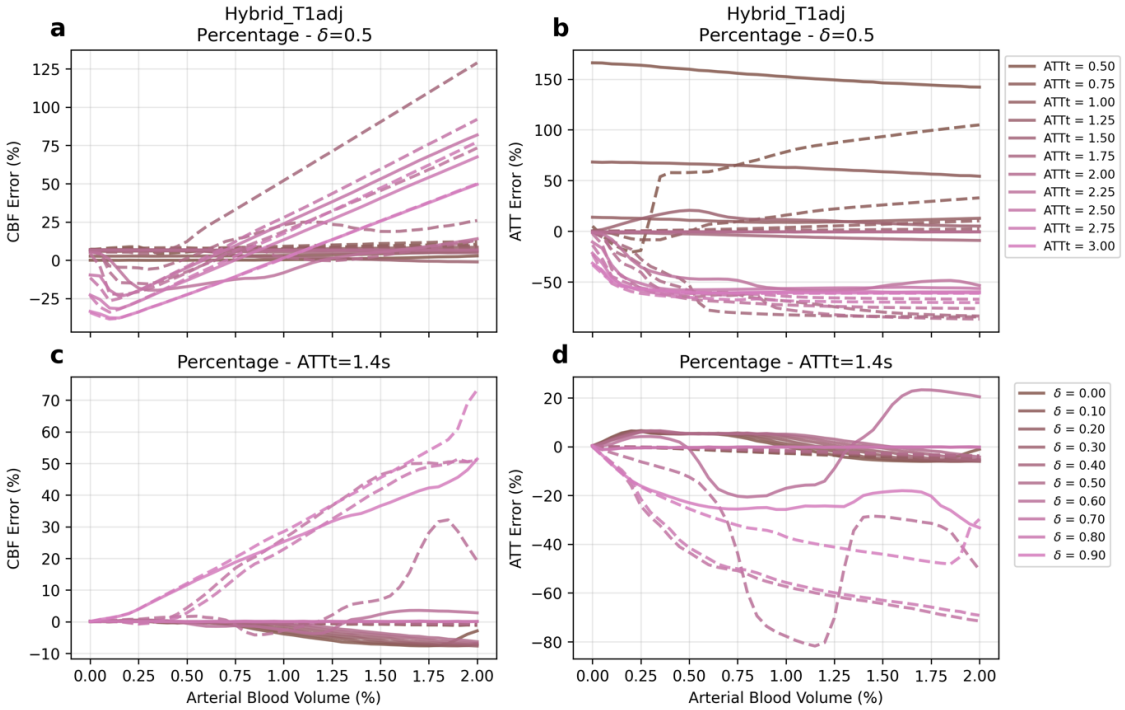


Figure A.1.6 CBF and ATT estimation errors of Hybrid_T1adj using gkm (dashed lines) and gkm+mvc (solid lines) under the percentage assumption. (a) and (b): δ = 0.5 while varying ATT_t; (c) and (d): ATT_t = 1.4s while varying δ.

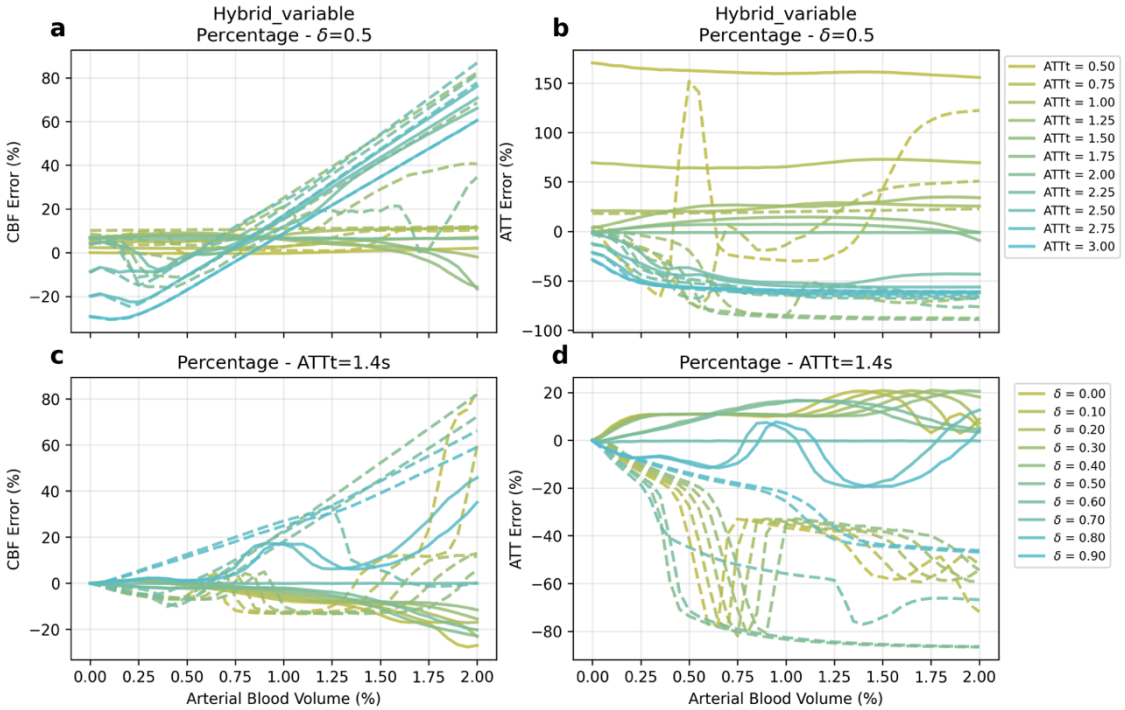


Figure A.1.7 CBF and ATT estimation errors of Hybrid_variable using gkm (dashed lines) and gkm+mvc (solid lines) under the percentage assumption. (a) and (b): δ = 0.5 while varying ATT_t; (c) and (d): ATT_t = 1.4s while varying δ.

A.2 CBF and ATT estimation errors under the assumption 'fixed'

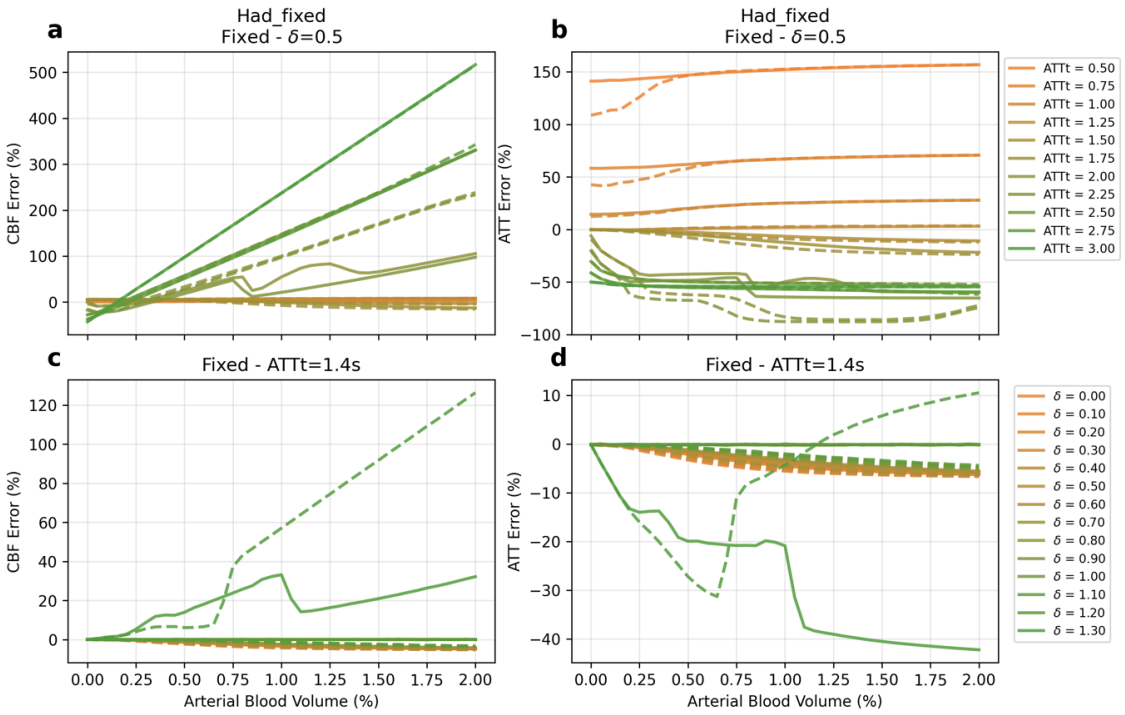


Figure A.2.1 CBF and ATT estimation errors of Had_fixed using gkm (dashed lines) and gkm+mvc (solid lines) under the fixed assumption. (a) and (b): δ = 0.5 while varying ATT_t; (c) and (d): ATT_t = 1.4s while varying δ.

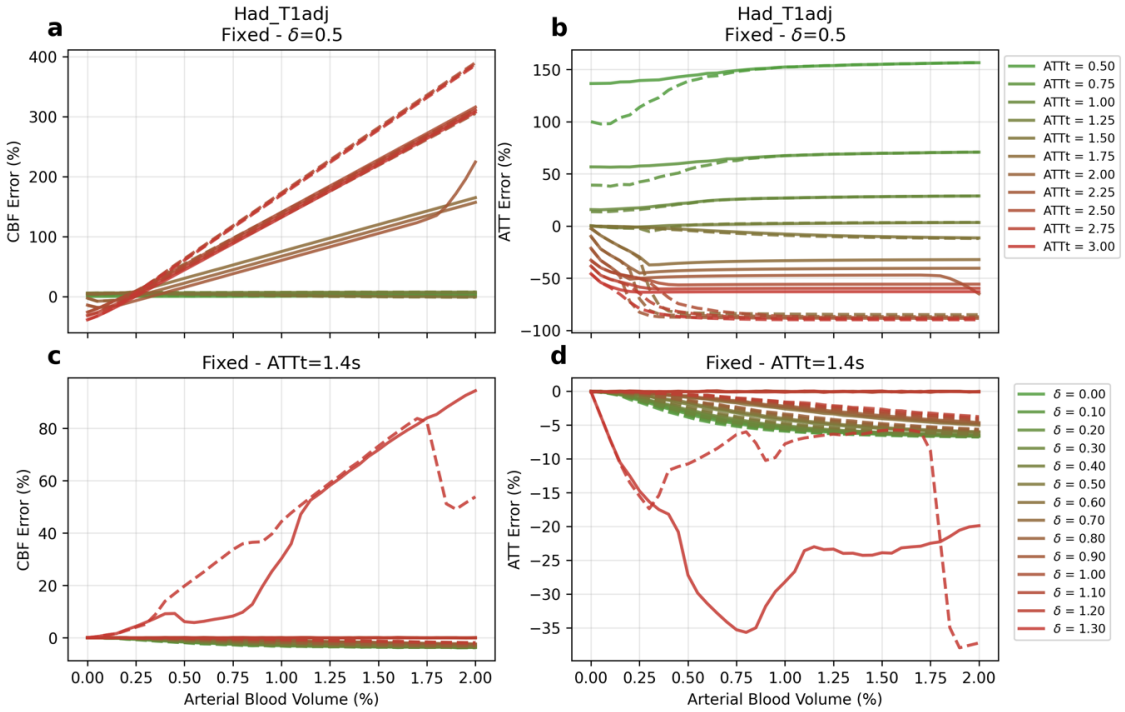


Figure A.2.2 CBF and ATT estimation errors of Had_T1adj using gkm (dashed lines) and gkm+mvc (solid lines) under the fixed assumption. (a) and (b): δ = 0.5 while varying ATT_t; (c) and (d): ATT_t = 1.4s while varying δ.

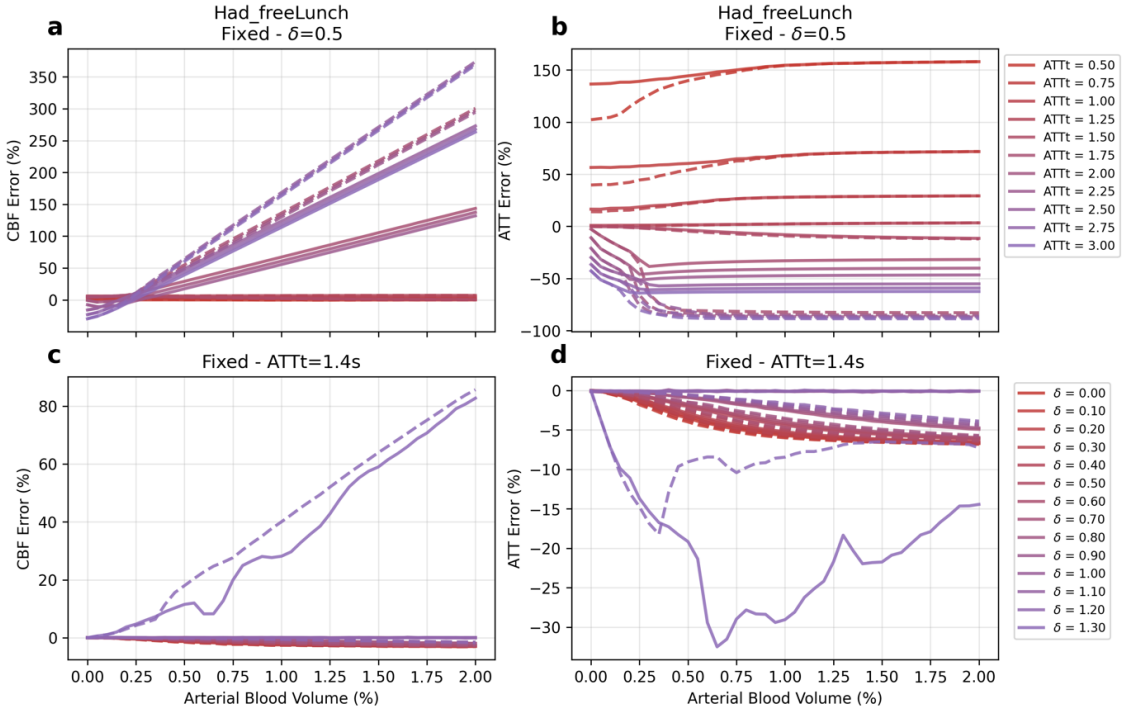


Figure A.2.3 CBF and ATT estimation errors of Had_freeLunch using gkm (dashed lines) and gkm+mvc (solid lines) under the fixed assumption. (a) and (b): δ = 0.5 while varying ATT_t; (c) and (d): ATT_t = 1.4s while varying δ.

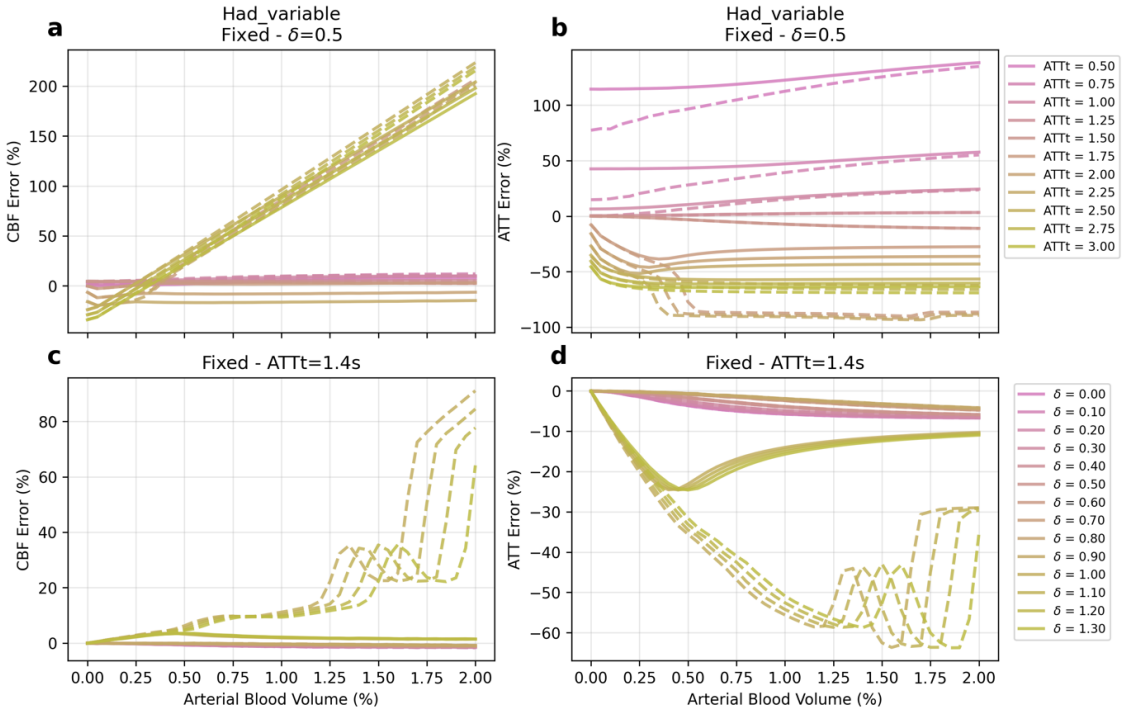


Figure A.2.4 CBF and ATT estimation errors of Had_variable using gkm (dashed lines) and gkm+mvc (solid lines) under the fixed assumption. (a) and (b): δ = 0.5 while varying ATT_t; (c) and (d): ATT_t = 1.4s while varying δ.

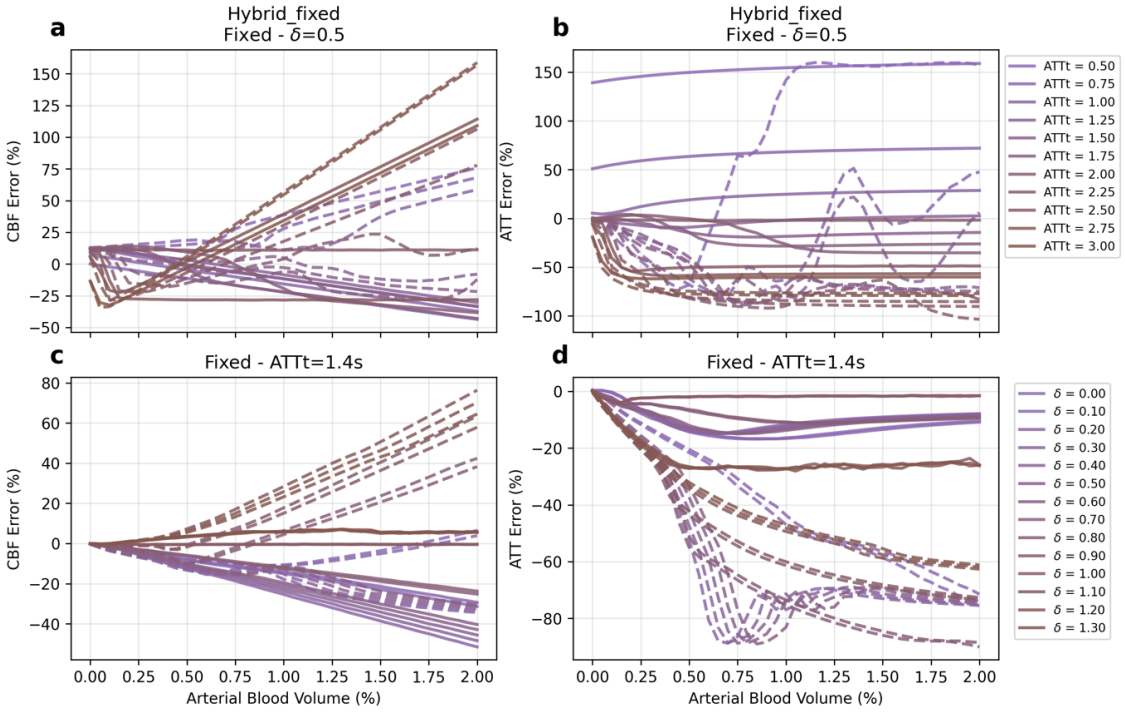


Figure A.2.5 CBF and ATT estimation errors of Hybrid_fixed using gkm (dashed lines) and gkm+mvc (solid lines) under the fixed assumption. (a) and (b): δ = 0.5 while varying ATT_t; (c) and (d): ATT_t = 1.4s while varying δ.

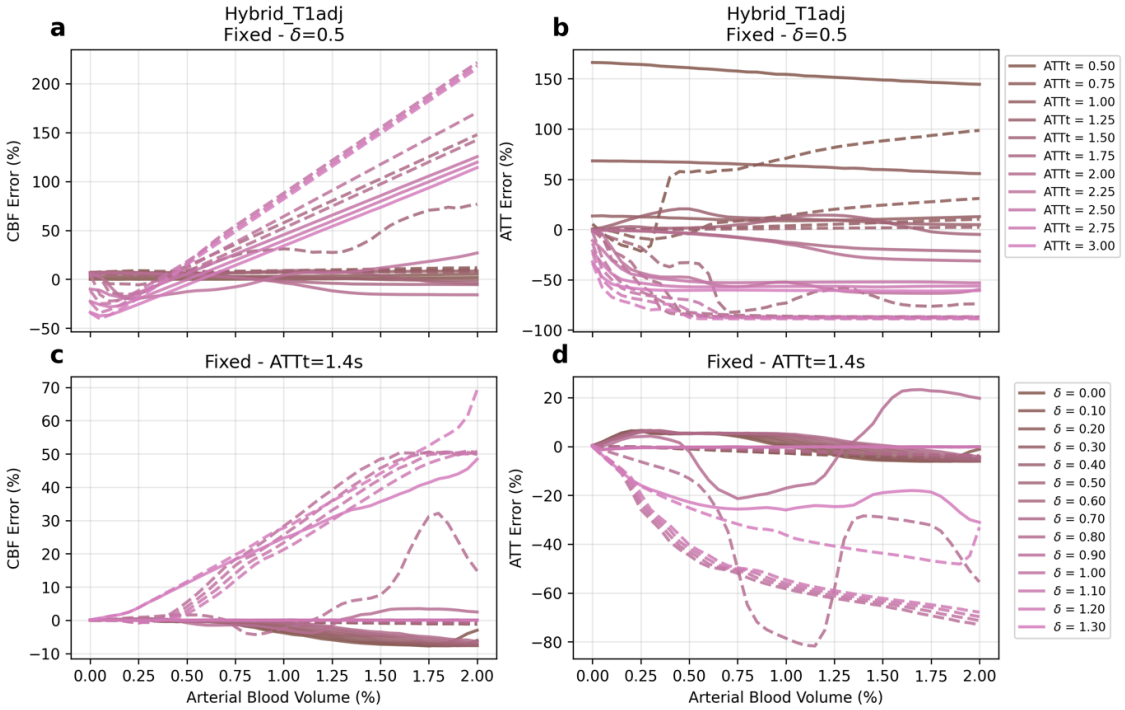


Figure A.2.6 CBF and ATT estimation errors of Hybrid_T1adj using gkm (dashed lines) and gkm+mvc (solid lines) under the fixed assumption. (a) and (b): δ = 0.5 while varying ATT_t; (c) and (d): ATT_t = 1.4s while varying δ.

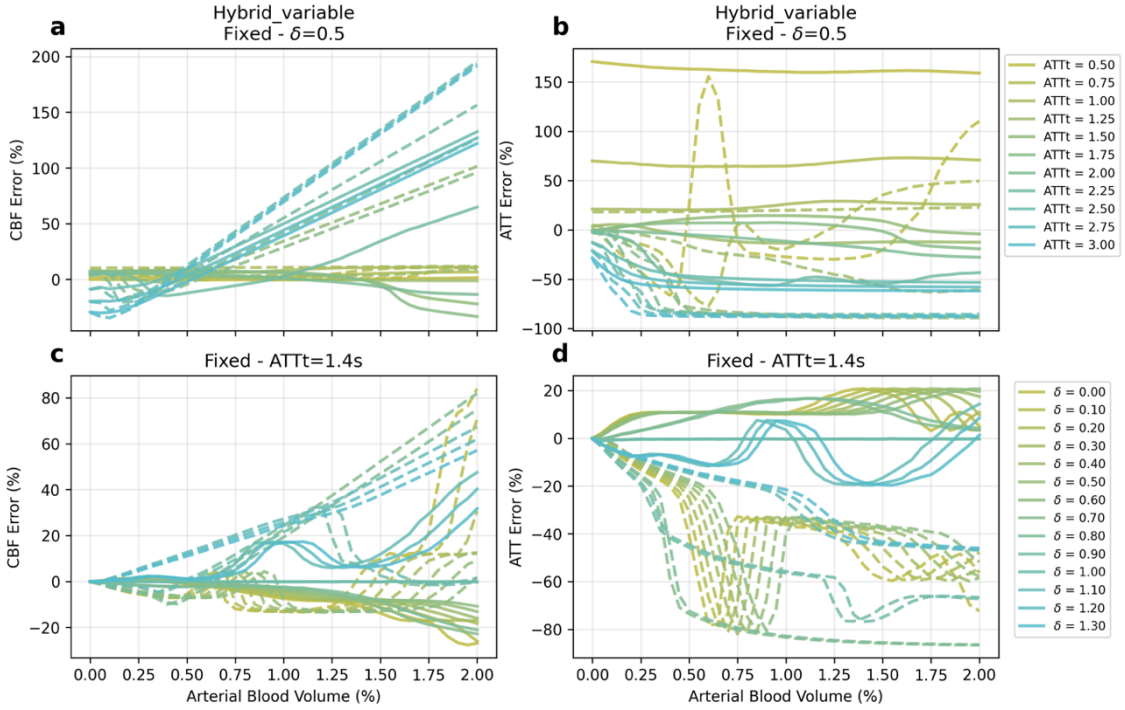


Figure A.2.7 CBF and ATT estimation errors of Hybrid_variable using gkm (dashed lines) and gkm+mvc (solid lines) under the fixed assumption. (a) and (b): δ = 0.5 while varying ATT_t; (c) and (d): ATT_t = 1.4s while varying δ.

A.3 CBF and ATT estimation errors under the assumption 'fixed_interval'

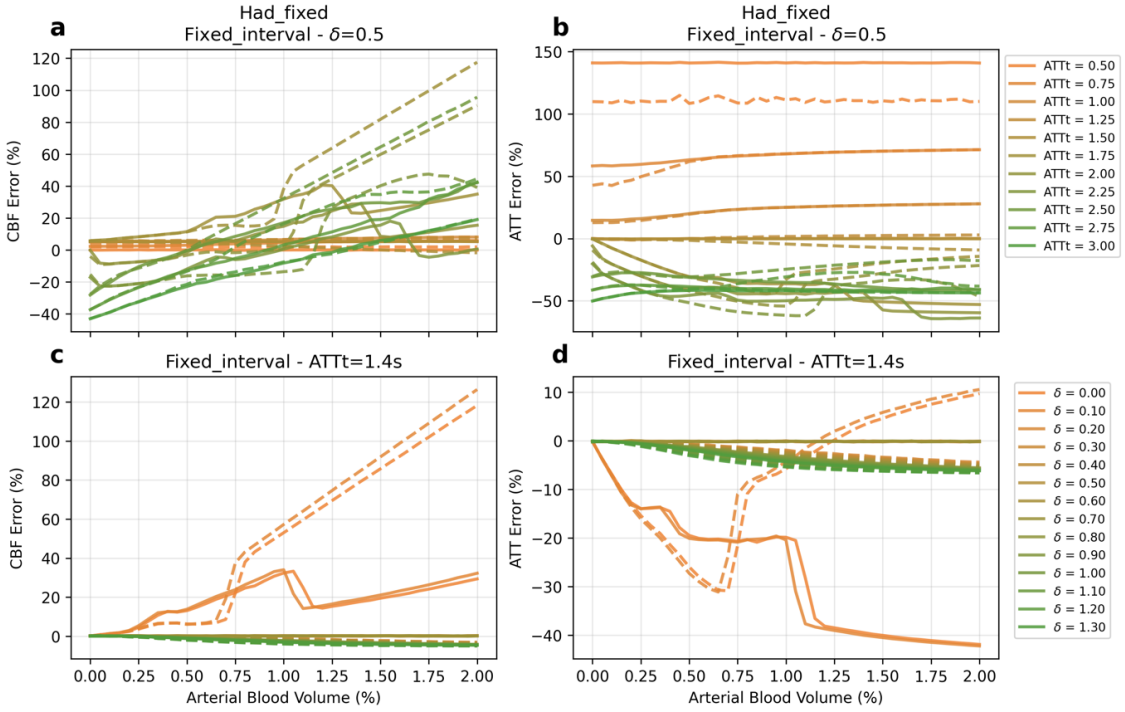


Figure A.3.1 CBF and ATT estimation errors of Had_fixed using gkm (dashed lines) and gkm+mvc (solid lines) under the fixed_interval assumption. (a) and (b): δ = 0.5 while varying ATT_t; (c) and (d): ATT_t = 1.4s while varying δ.

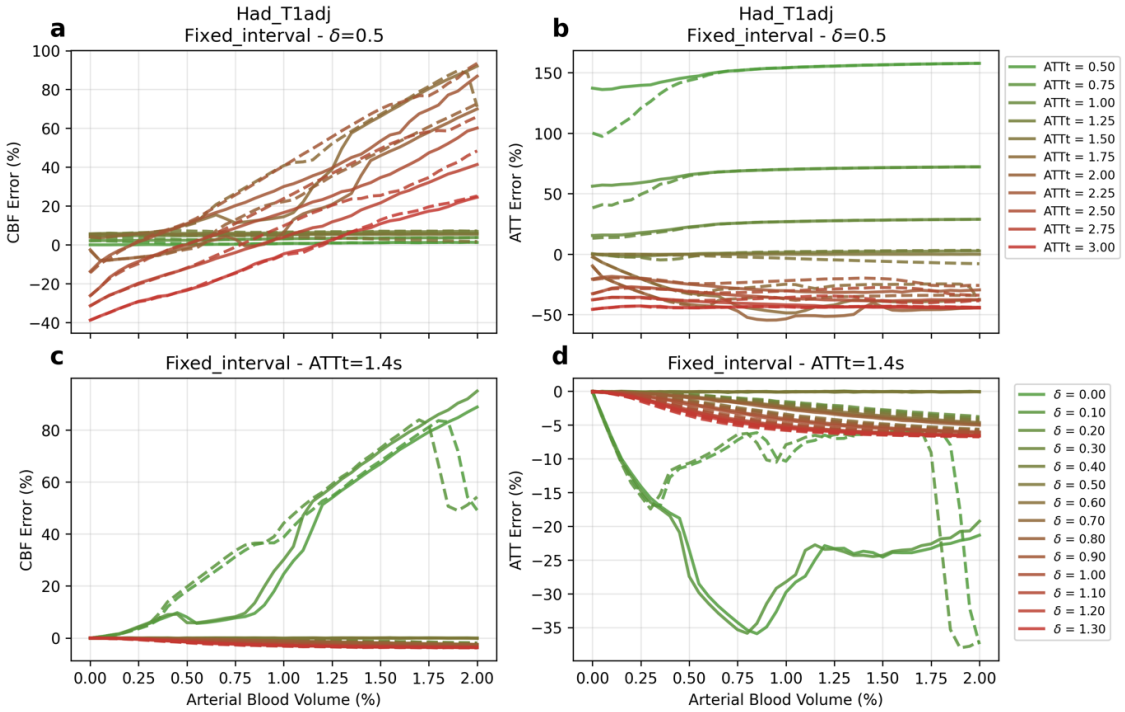


Figure A.3.2 CBF and ATT estimation errors of Had_T1adj using gkm (dashed lines) and gkm+mvc (solid lines) under the fixed_interval assumption. (a) and (b): δ = 0.5 while varying ATT_t; (c) and (d): ATT_t = 1.4s while varying δ.

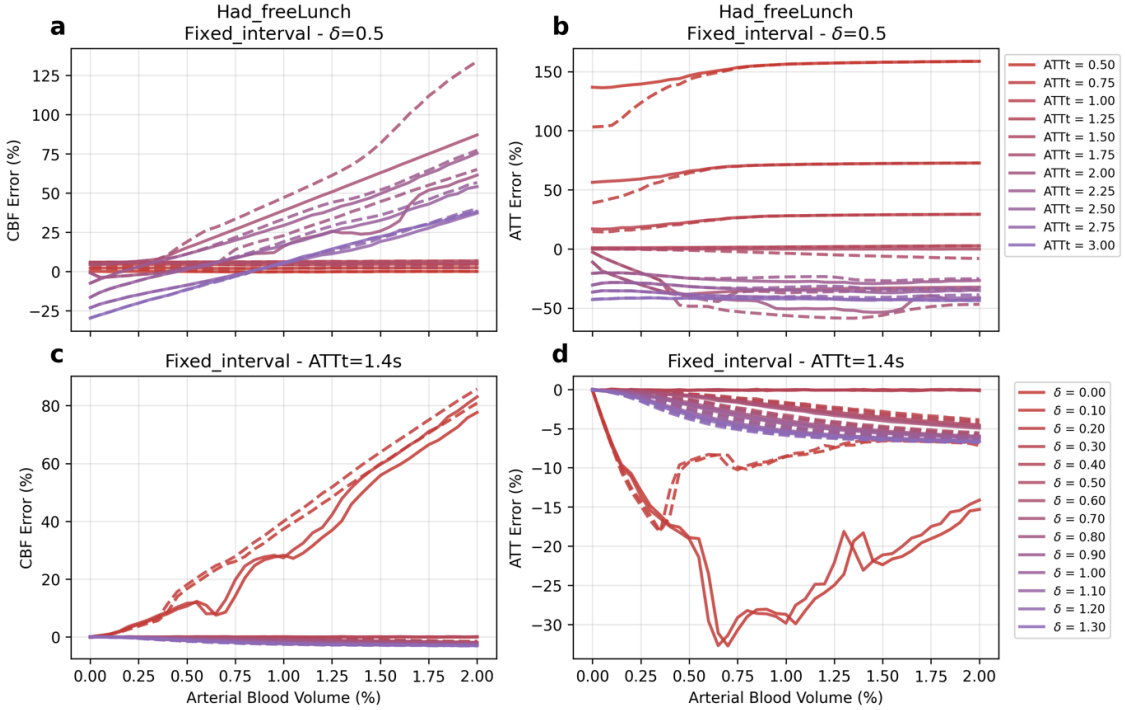


Figure A.3.3 CBF and ATT estimation errors of Had_freeLunch using gkm (dashed lines) and gkm+mvc (solid lines) under the fixed_interval assumption. (a) and (b): δ = 0.5 while varying ATT_t; (c) and (d): ATT_t = 1.4s while varying δ.

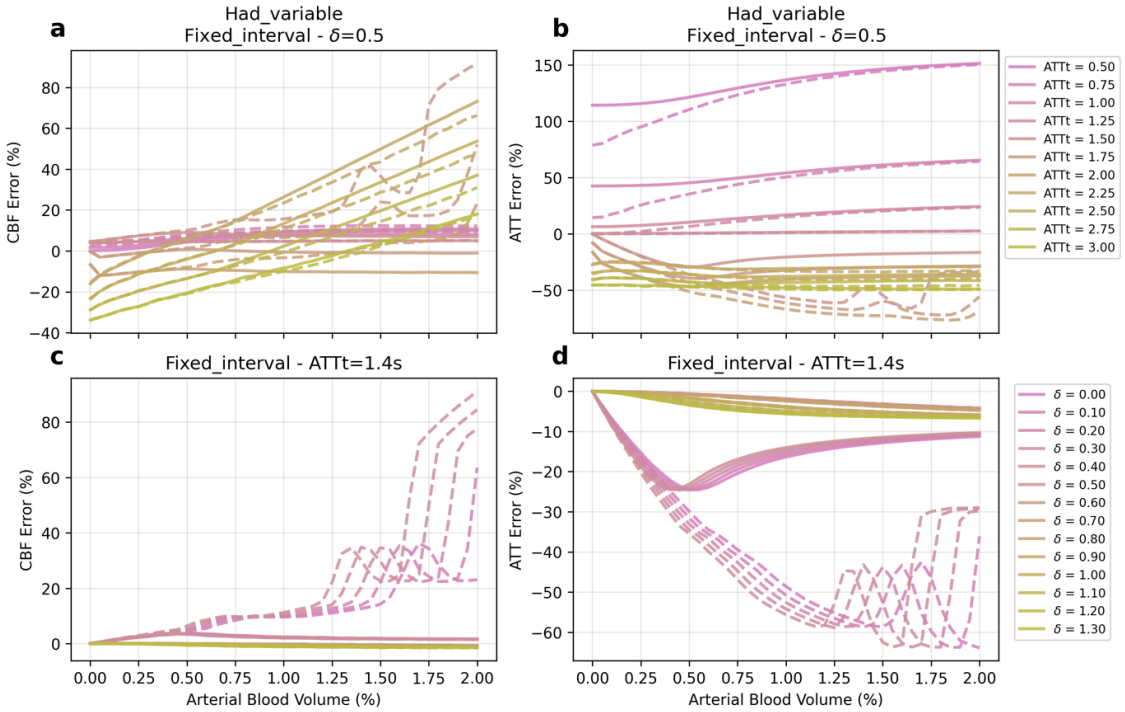


Figure A.3.4 CBF and ATT estimation errors of Had_variable using gkm (dashed lines) and gkm+mvc (solid lines) under the fixed_interval assumption. (a) and (b): δ = 0.5 while varying ATT_t; (c) and (d): ATT_t = 1.4s while varying δ.

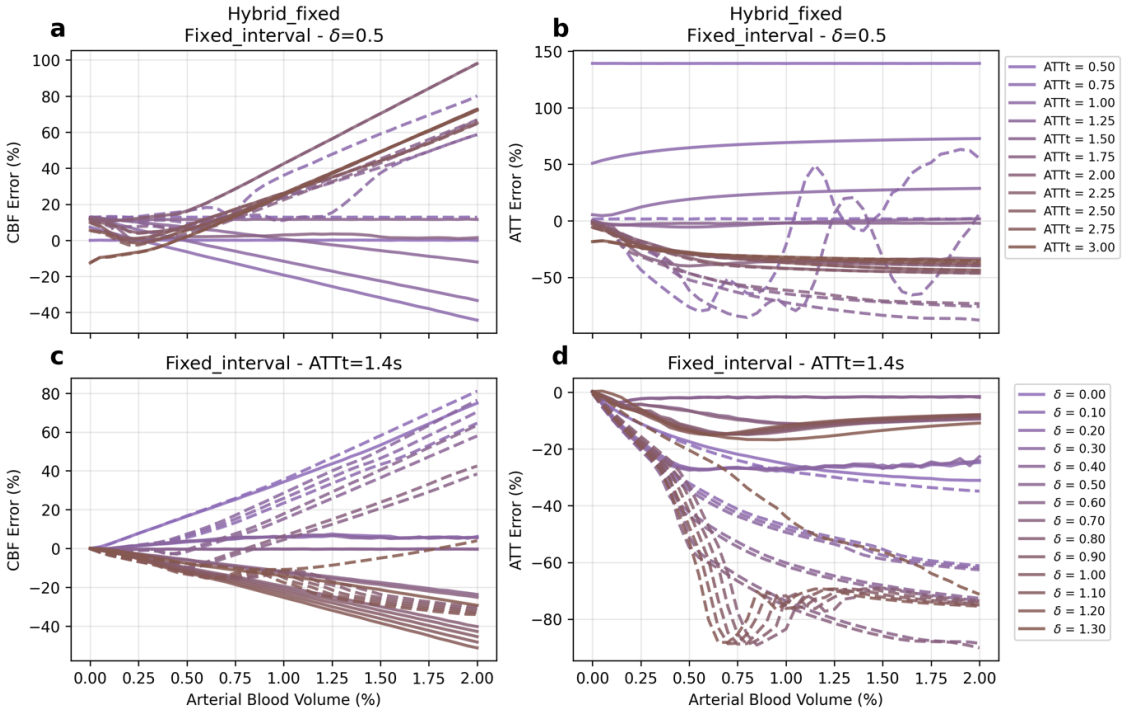


Figure A.3.5 CBF and ATT estimation errors of Hybrid_fixed using gkm (dashed lines) and gkm+mvc (solid lines) under the fixed_interval assumption. (a) and (b): δ = 0.5 while varying ATT_t; (c) and (d): ATT_t = 1.4s while varying δ.

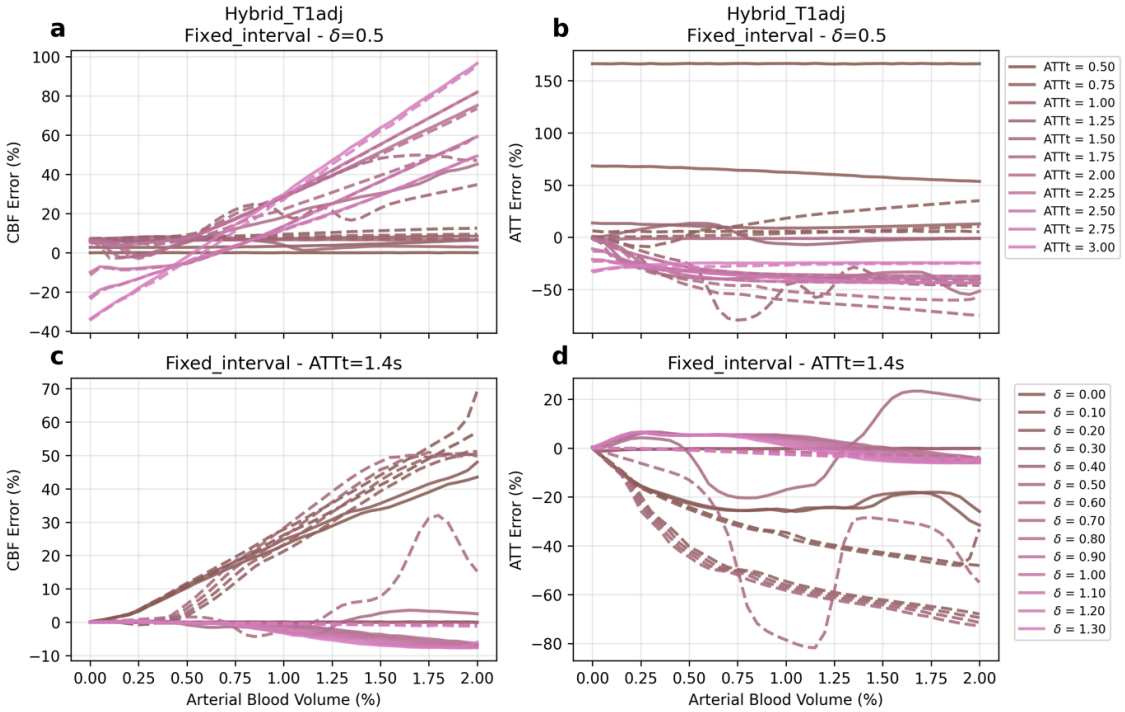


Figure A.3.6 CBF and ATT estimation errors of Hybrid_T1adj using gkm (dashed lines) and gkm+mvc (solid lines) under the fixed_interval assumption. (a) and (b): δ = 0.5 while varying ATT_t; (c) and (d): ATT_t = 1.4s while varying δ.

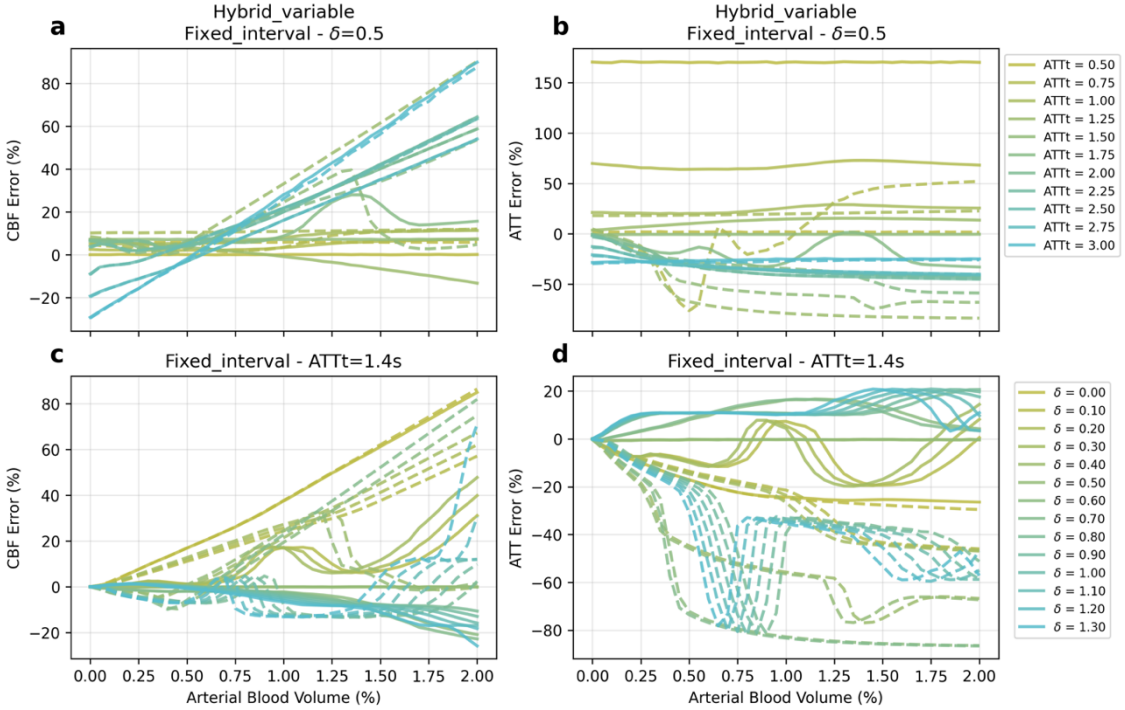


Figure A.3.7 CBF and ATT estimation errors of Hybrid_variable using gkm (dashed lines) and gkm+mvc (solid lines) under the fixed_interval assumption. (a) and (b): δ = 0.5 while varying ATT_t; (c) and (d): ATT_t = 1.4s while varying δ.

A.4 CBF, ATT, and aBV sensitivity maps to MVC

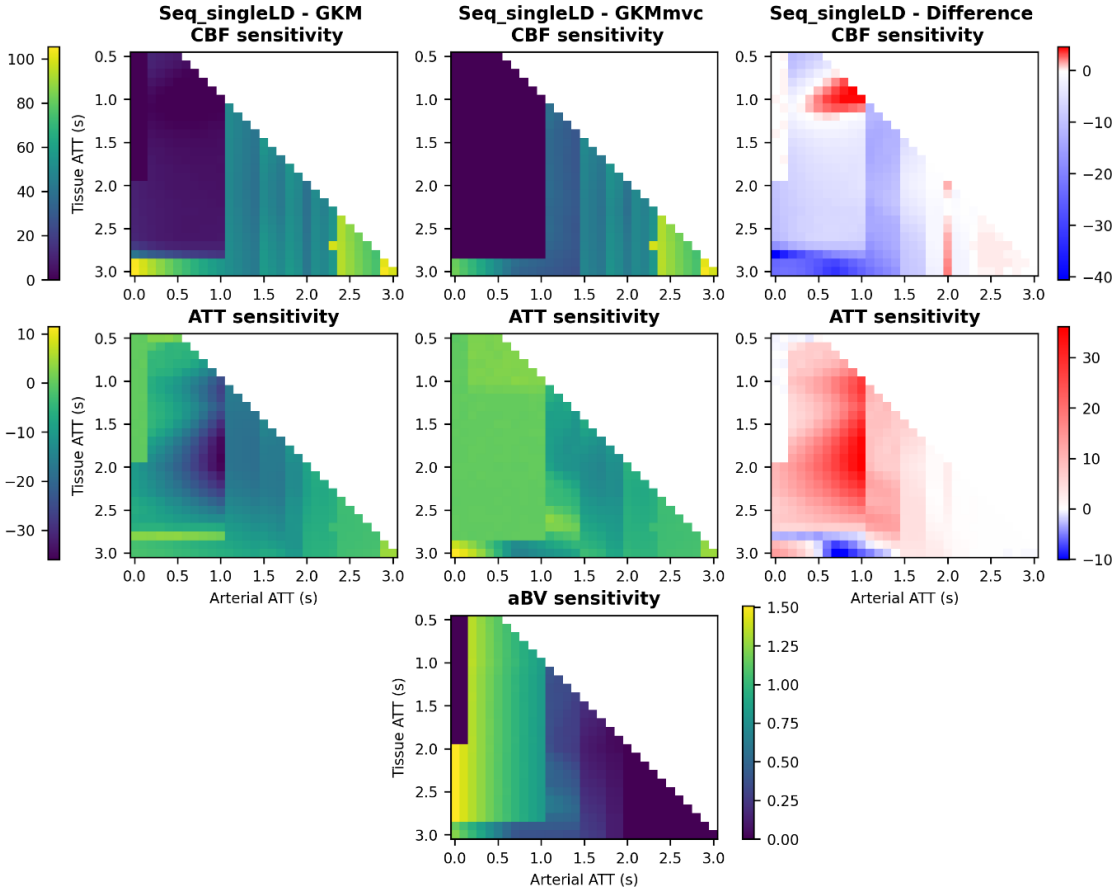


Figure A.4.1 CBF, ATT, and aBV sensitivity maps to macrovascular contamination using gkm (first column), gkm+mvc (second column), and their difference (gkm+mvc - gkm, third column) by the protocol Seq_singleLD.

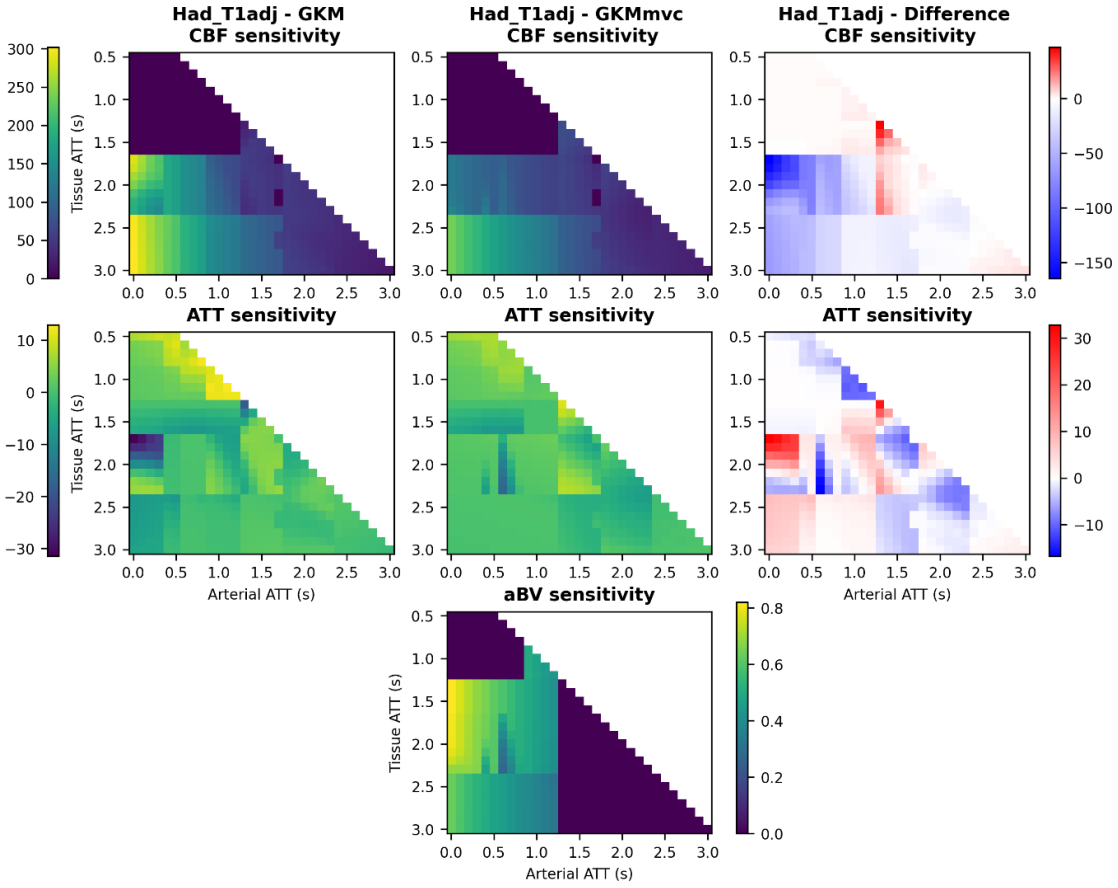


Figure A.4.2 CBF, ATT, and aBV sensitivity maps to macrovascular contamination using gkm (first column), gkm+mvc (second column), and their difference (gkm+mvc - gkm, third column) by the protocol Had_T1adj.

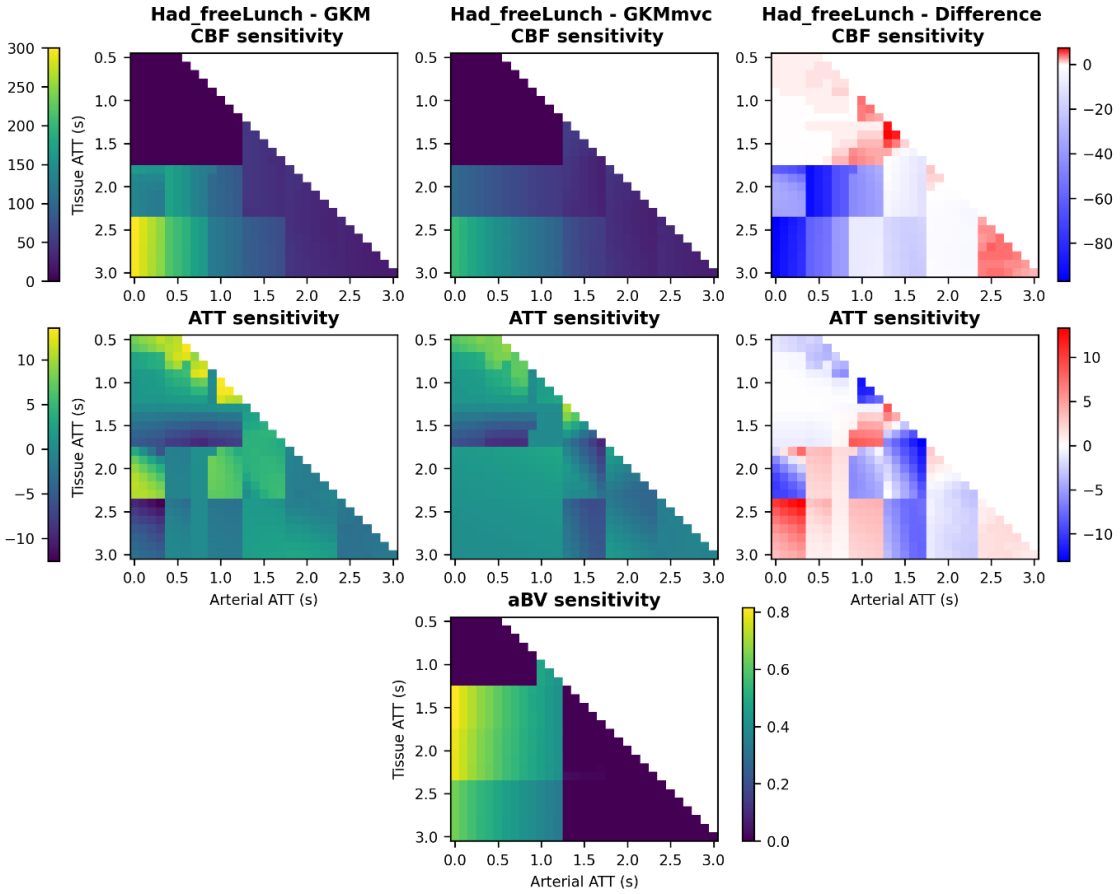


Figure A.4.3 CBF, ATT, and aBV sensitivity maps to macrovascular contamination using gkm (first column), gkm+mvc (second column), and their difference (gkm+mvc - gkm, third column) by the protocol Had_freeLunch.

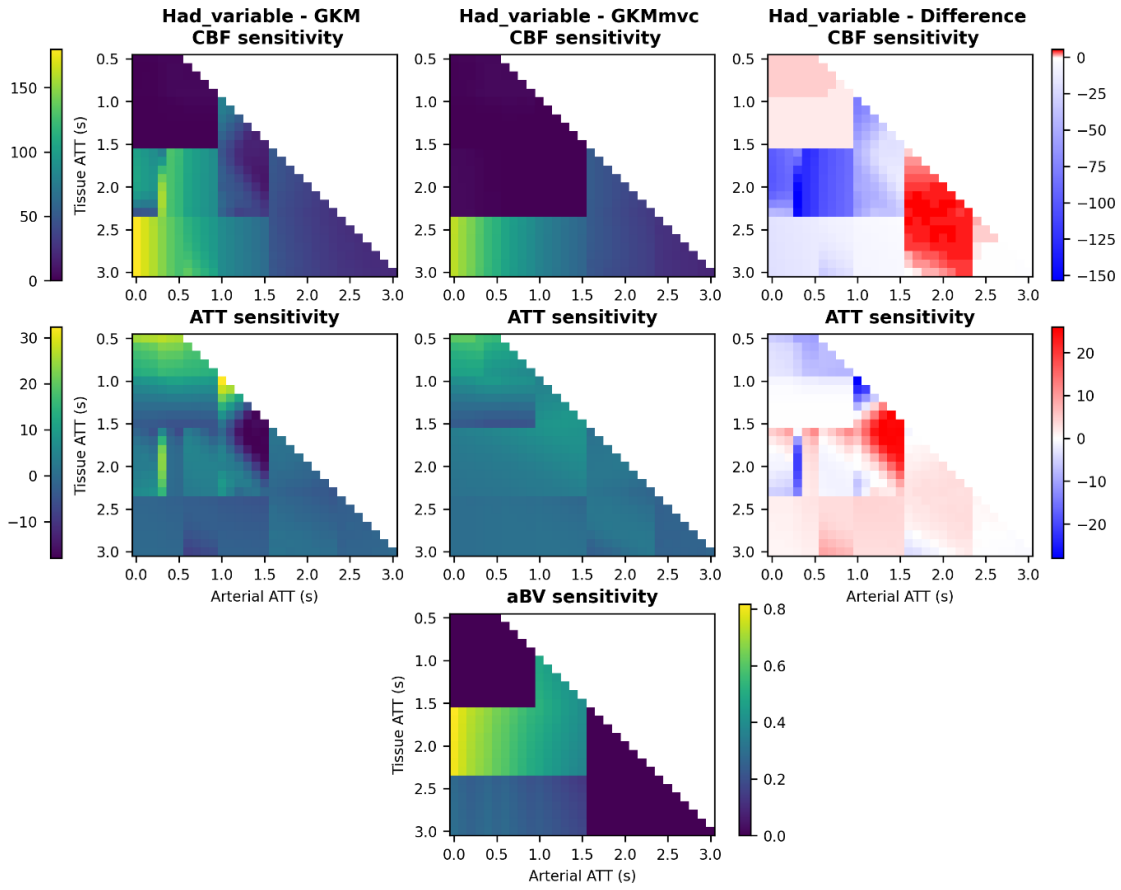


Figure A.4.4 CBF, ATT, and aBV sensitivity maps to macrovascular contamination using gkm (first column), gkm+mvc (second column), and their difference (gkm+mvc - gkm, third column) by the protocol Had_variable.

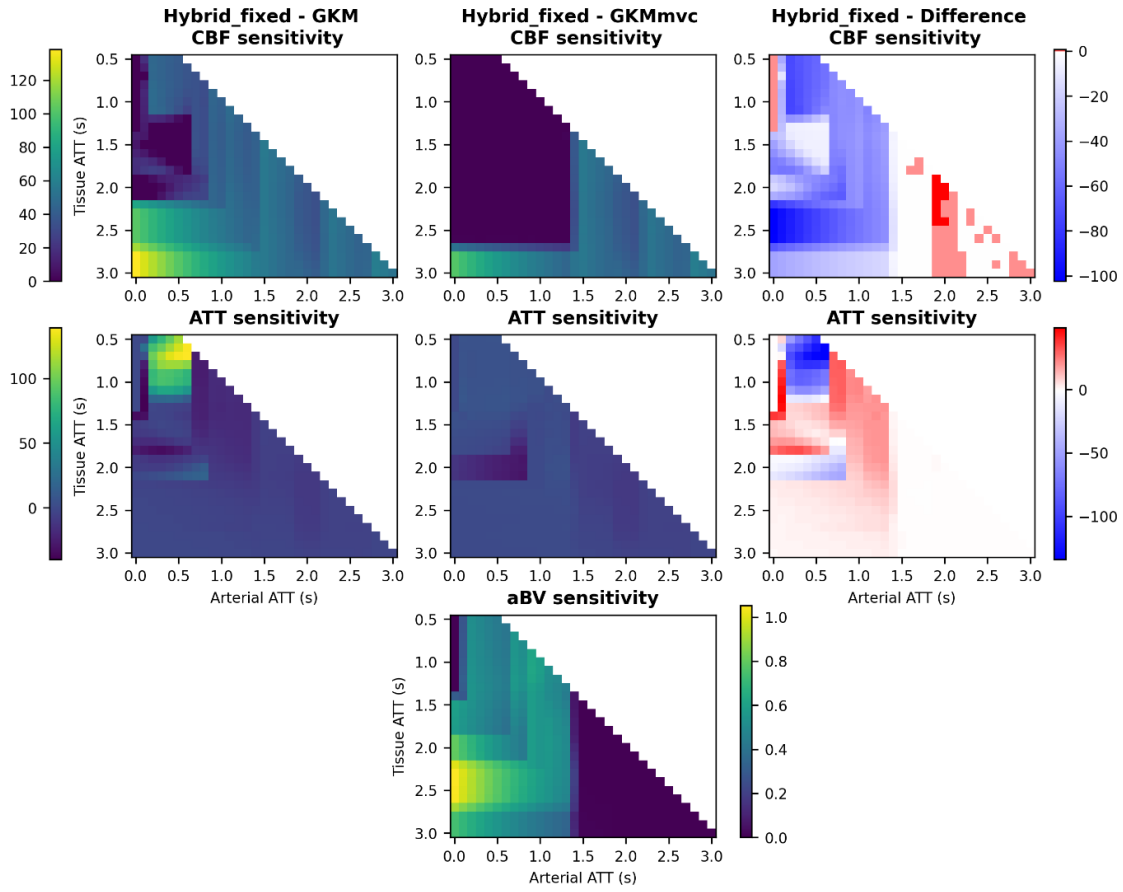


Figure A.4.5 CBF, ATT, and aBV sensitivity maps to macrovascular contamination using gkm (first column), gkm+mvc (second column), and their difference (gkm+mvc - gkm, third column) by the protocol Hybrid_fixed.

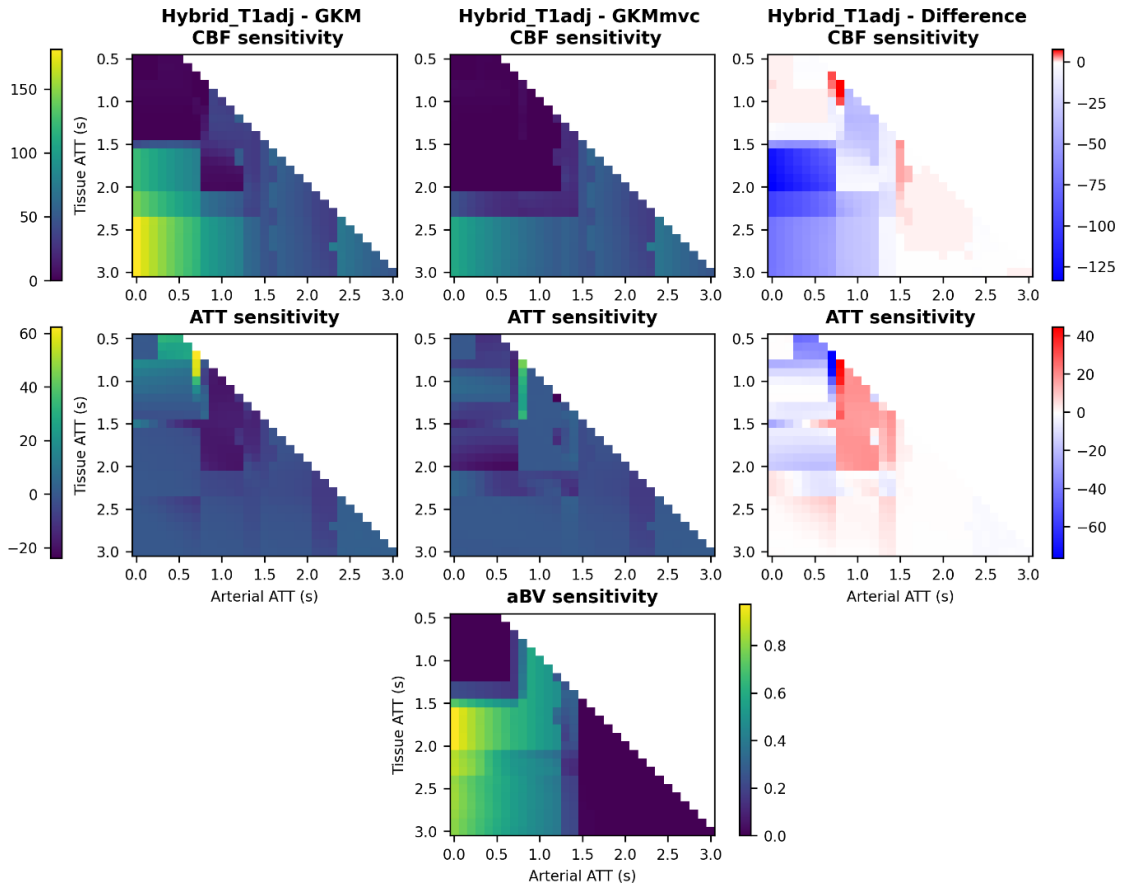


Figure A.4.6 CBF, ATT, and aBV sensitivity maps to macrovascular contamination using gkm (first column), gkm+mvc (second column), and their difference (gkm+mvc - gkm, third column) by the protocol Hybrid_T1adj.

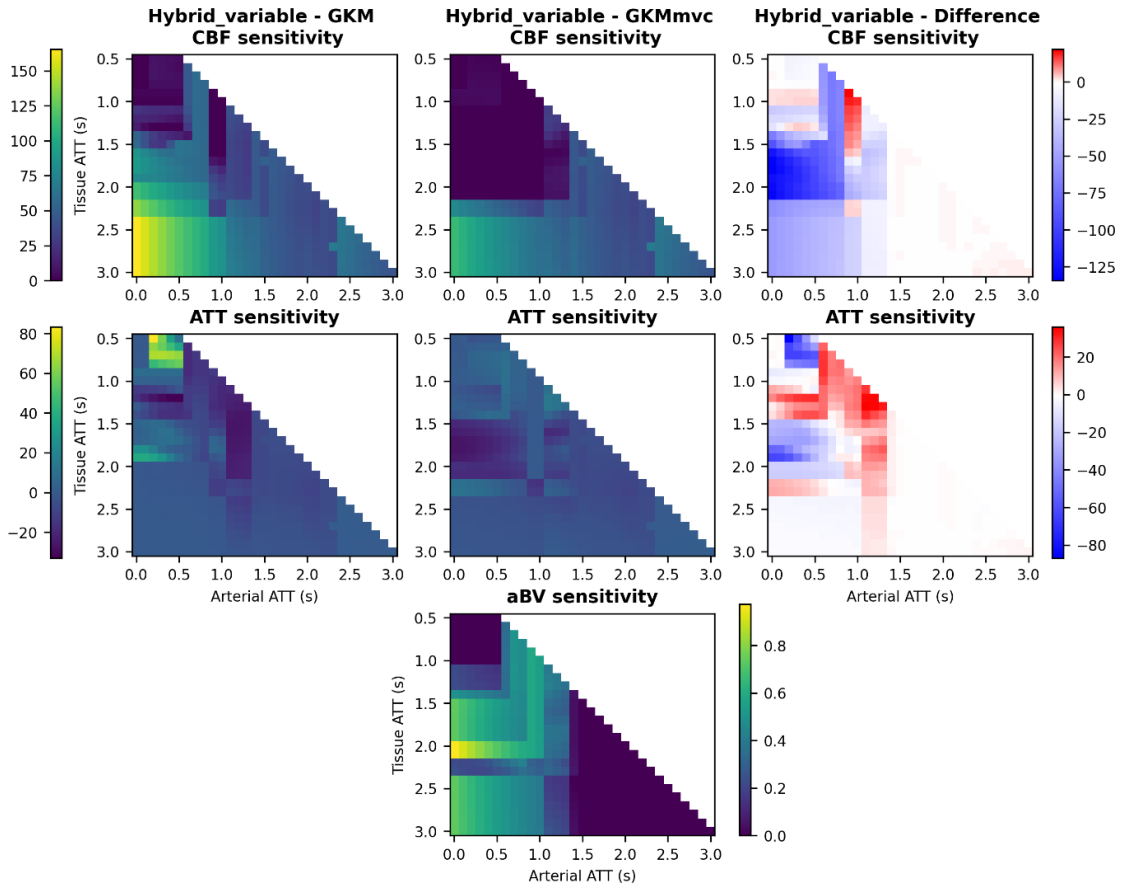


Figure A.4.7 CBF, ATT, and aBV sensitivity maps to macrovascular contamination using gkm (first column), gkm+mvc (second column), and their difference (gkm+mvc - gkm, third column) by the protocol Hybrid_variable.

A.5 ATT sensitivity maps to MVC according to different metrics

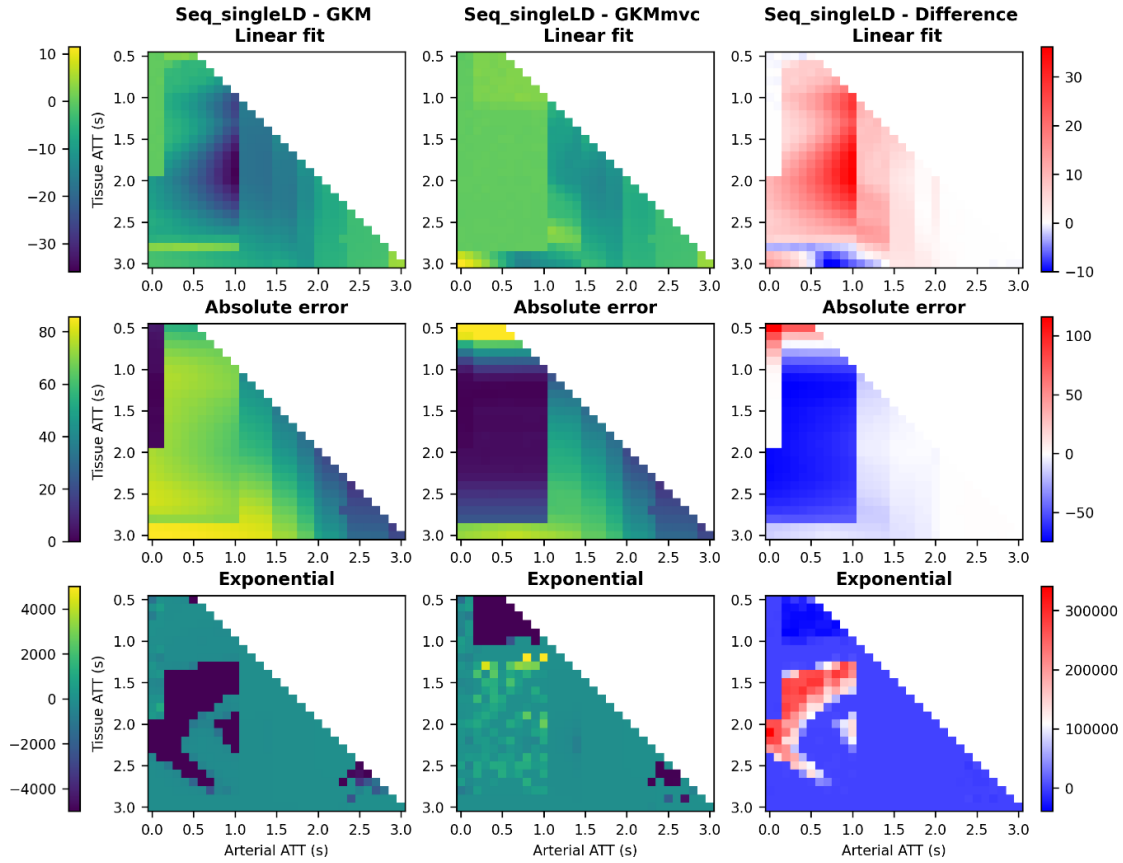


Figure A.5.1 ATT sensitivity maps to macrovascular contamination using gkm (first column), gkm+mvc (second column), and their difference (gkm+mvc - gkm, third column) by the protocol Seq_singleLD according to different sensitivity metrics: linear fit (first row), absolute mean error (second row), and exponential fit (third row).

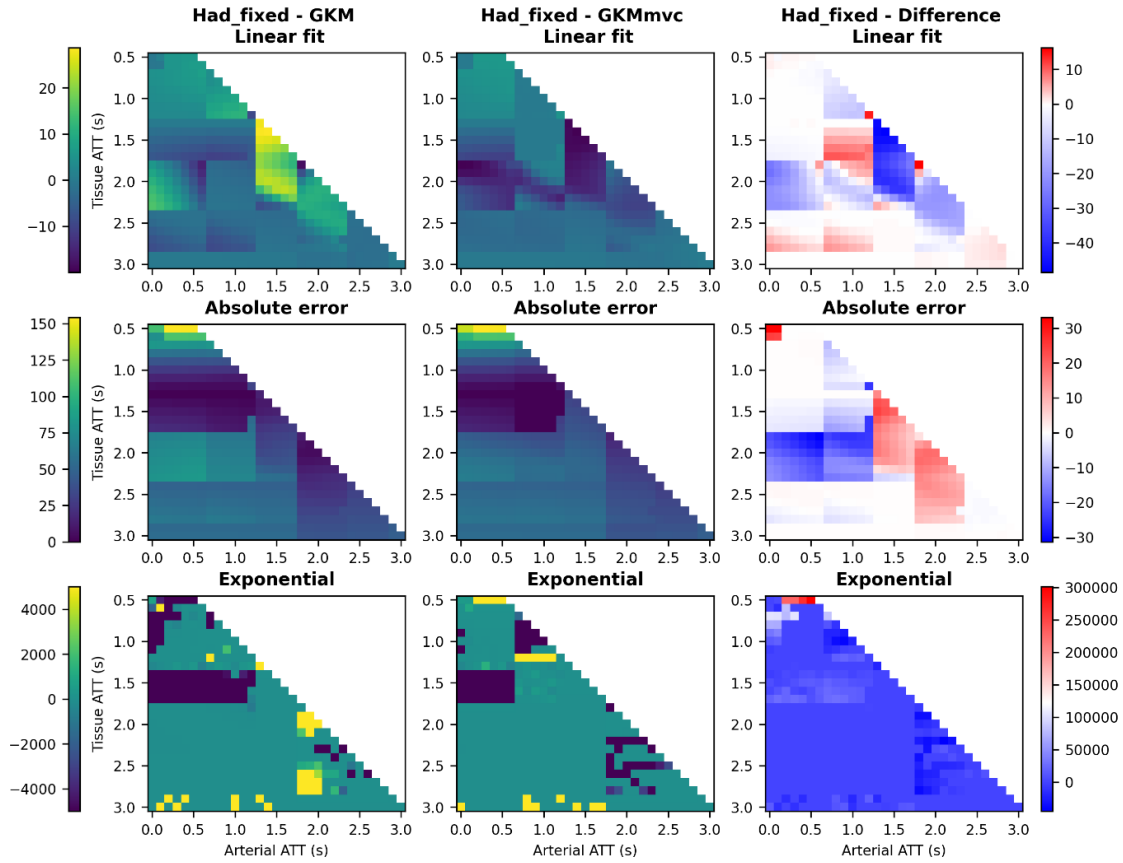


Figure A.5.2 ATT sensitivity maps to macrovascular contamination using gkm (first column), gkm+mvc (second column), and their difference (gkm+mvc - gkm, third column) by the protocol Had_fixed according to different sensitivity metrics: linear fit (first row), absolute mean error (second row), and exponential fit (third row).

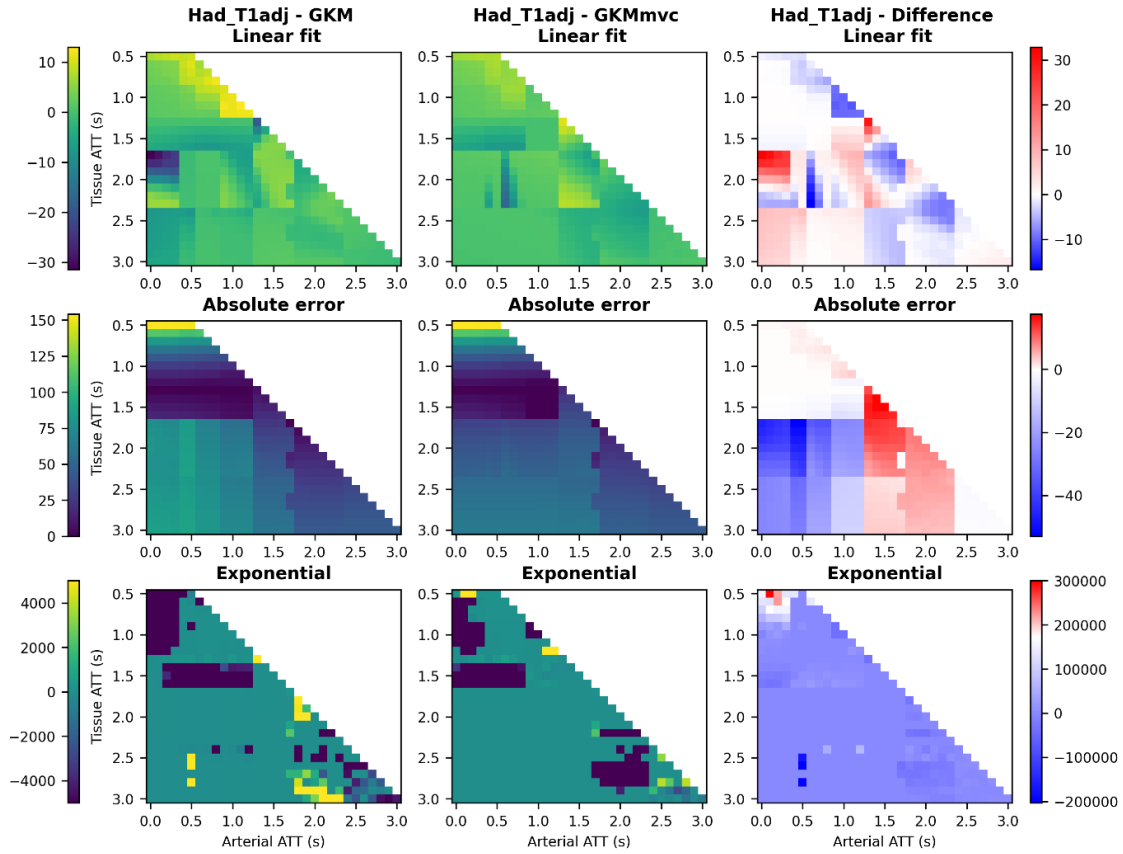


Figure A.5.3 ATT sensitivity maps to macrovascular contamination using gkm (first column), gkm+mvc (second column), and their difference (gkm+mvc - gkm, third column) by the protocol Had_T1adj according to different sensitivity metrics: linear fit (first row), absolute mean error (second row), and exponential fit (third row).

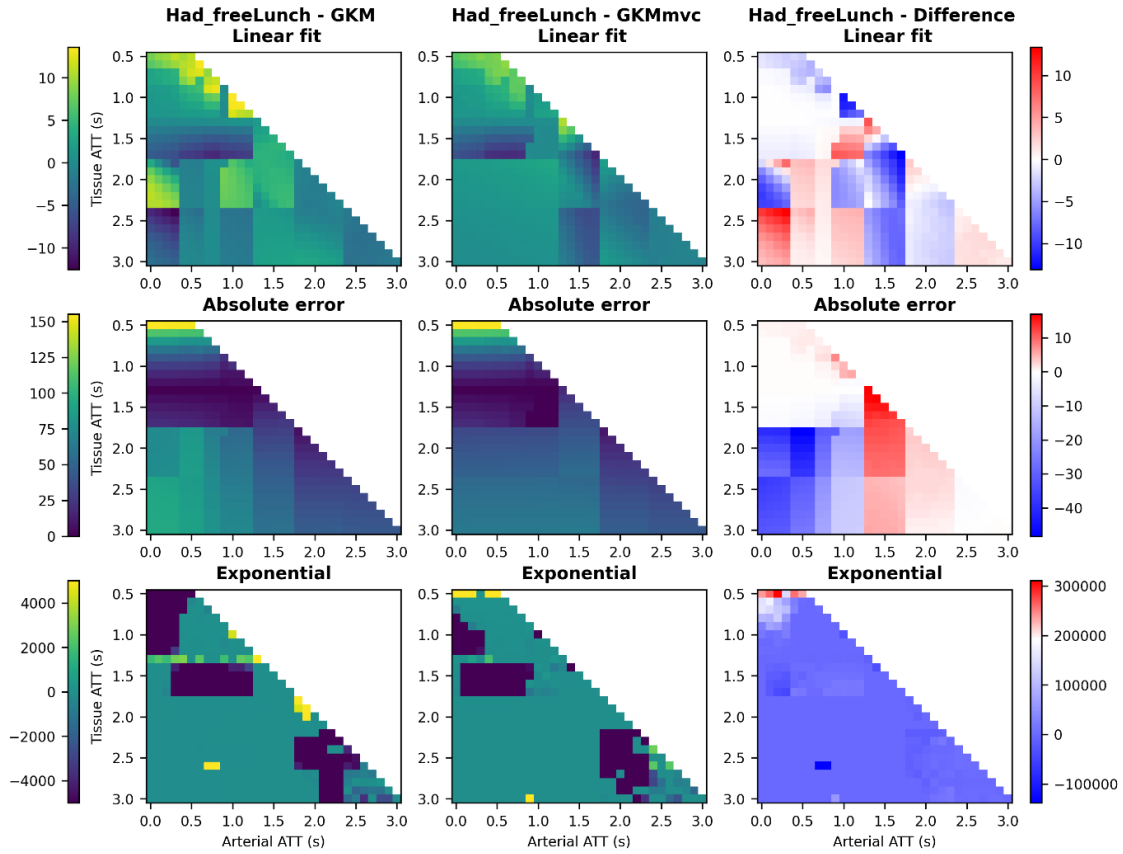


Figure A.5.4 ATT sensitivity maps to macrovascular contamination using gkm (first column), gkm+mvc (second column), and their difference (gkm+mvc - gkm, third column) by the protocol Had_freeLunch according to different sensitivity metrics: linear fit (first row), absolute mean error (second row), and exponential fit (third row).

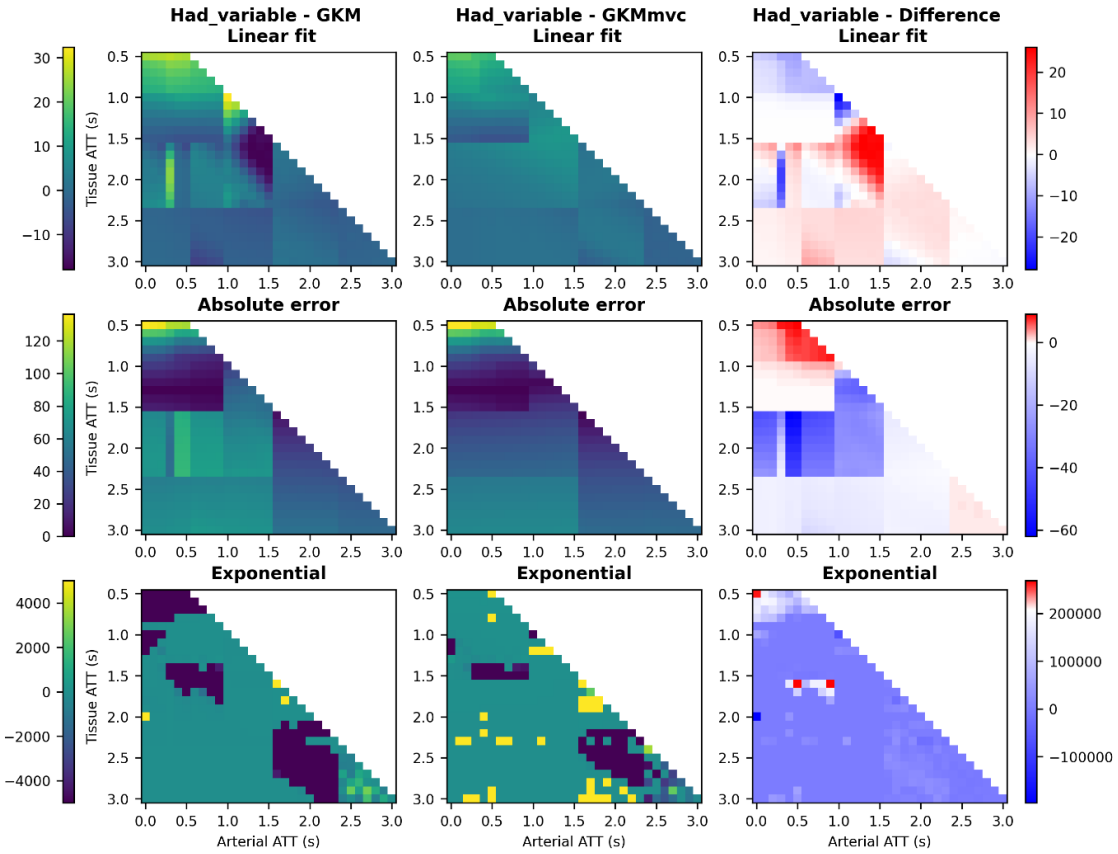


Figure A.5.5 ATT sensitivity maps to macrovascular contamination using gkm (first column), gkm+mvc (second column), and their difference (gkm+mvc - gkm, third column) by the protocol Had_variable according to different sensitivity metrics: linear fit (first row), absolute mean error (second row), and exponential fit (third row).

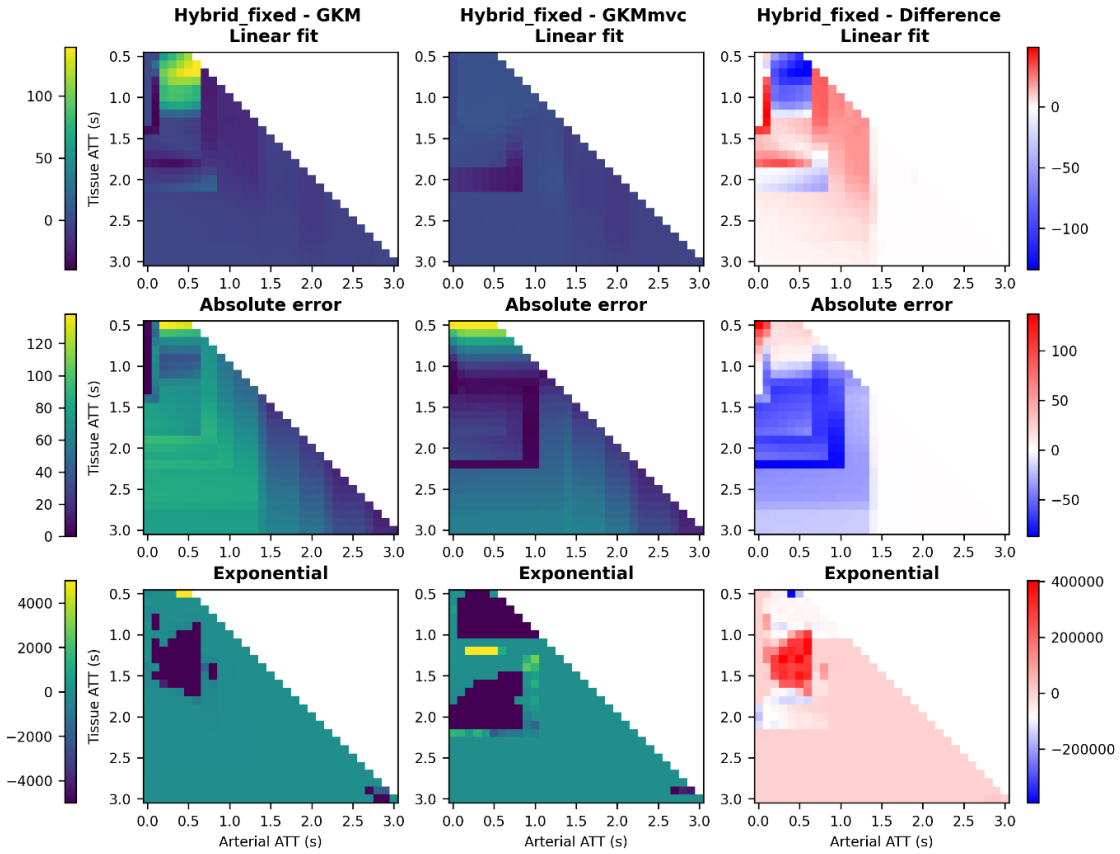


Figure A.5.6 ATT sensitivity maps to macrovascular contamination using gkm (first column), gkm+mvc (second column), and their difference (gkm+mvc - gkm, third column) by the protocol Hybrid_fixed according to different sensitivity metrics: linear fit (first row), absolute mean error (second row), and exponential fit (third row).

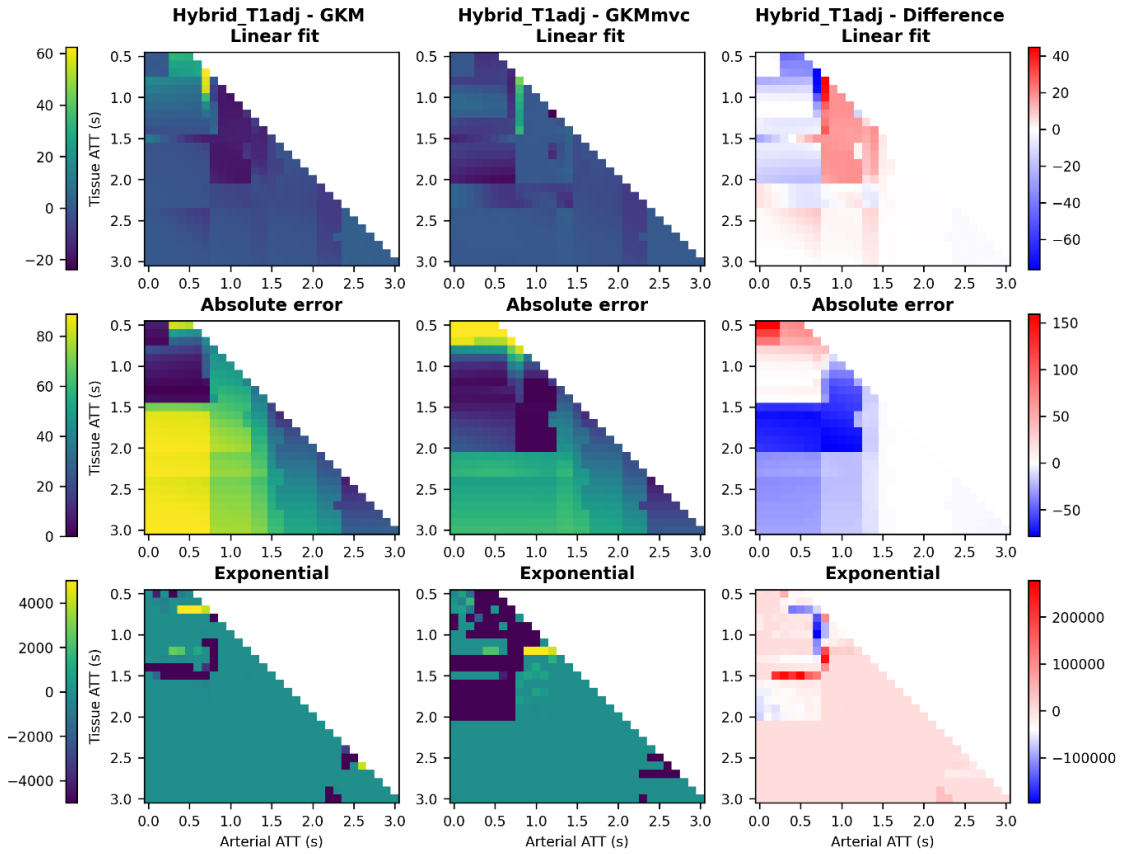


Figure A.5.7 ATT sensitivity maps to macrovascular contamination using gkm (first column), gkm+mvc (second column), and their difference (gkm+mvc - gkm, third column) by the protocol Hybrid_T1adj according to different sensitivity metrics: linear fit (first row), absolute mean error (second row), and exponential fit (third row).

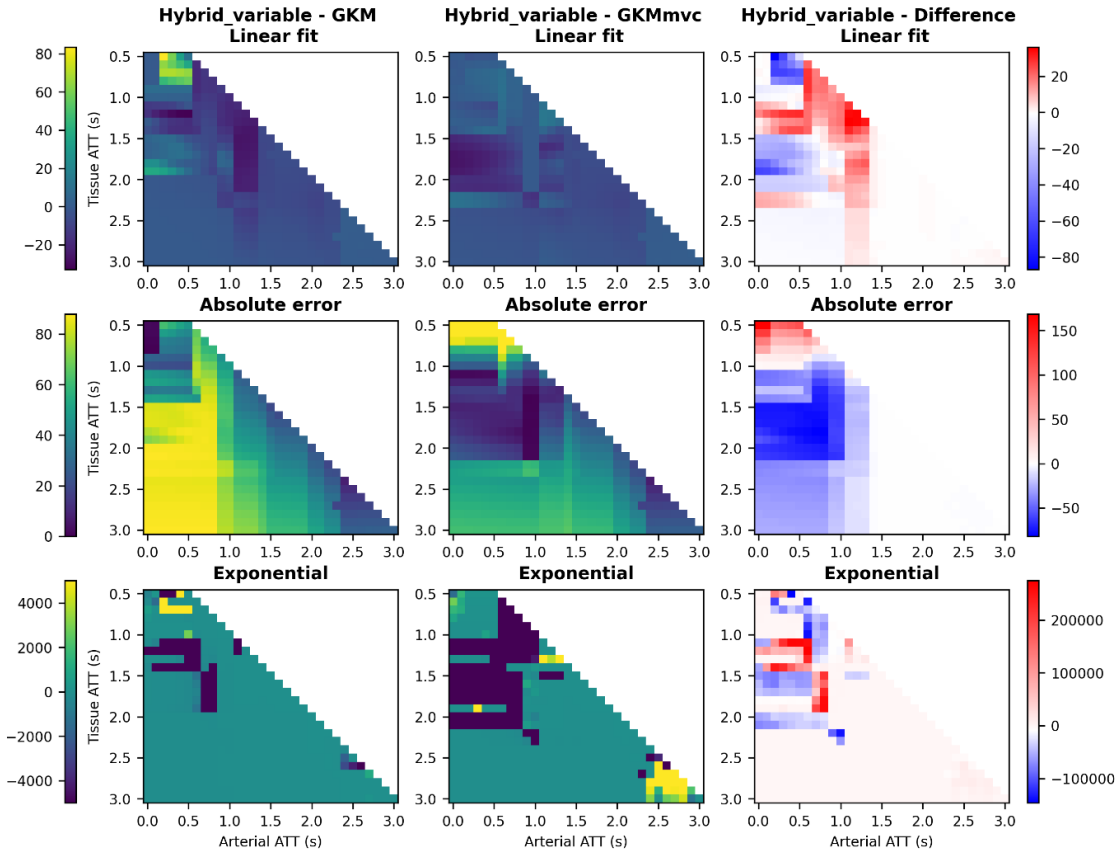


Figure A.5.8 ATT sensitivity maps to macrovascular contamination using gkm (first column), gkm+mvc (second column), and their difference (gkm+mvc - gkm, third column) by the protocol Hybrid_variable according to different sensitivity metrics: linear fit (first row), absolute mean error (second row), and exponential fit (third row).